

**Mechanics of Compaction and Dilatancy in Triaxially  
Stressed Rocks, Under Simulated Crustal Conditions  
Studied by Pore Volumometry.**

by

**Peter Charles Aves.**

A thesis submitted to the University of London  
for the degree of Doctor of Philosophy.

Dept. of Geological Sciences,  
University College London.

September 1995.

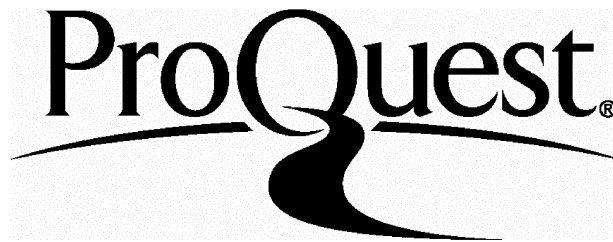
ProQuest Number: 10017156

All rights reserved

INFORMATION TO ALL USERS

The quality of this reproduction is dependent upon the quality of the copy submitted.

In the unlikely event that the author did not send a complete manuscript and there are missing pages, these will be noted. Also, if material had to be removed, a note will indicate the deletion.



ProQuest 10017156

Published by ProQuest LLC(2016). Copyright of the Dissertation is held by the Author.

All rights reserved.

This work is protected against unauthorized copying under Title 17, United States Code.  
Microform Edition © ProQuest LLC.

ProQuest LLC  
789 East Eisenhower Parkway  
P.O. Box 1346  
Ann Arbor, MI 48106-1346

## **Abstract**

Triaxial and hydrostatic deformation experiments have been conducted on Darley Dale sandstone, Penmaenmawr microgranodiorite and Gypsum, to investigate,

- (i) compaction and dilatant mechanisms occurring during deformation under a variety of stress conditions, (triaxial and hydrostatic),
- (ii) the effect of confined fluid flow conditions (*undrained*), on triaxial deformation characteristics of sandstone,
- (iii) the effects of varying the Upstream Reservoir Volume - URV, (necessary to measure pore fluid pressure), under undrained conditions on the deformation characteristics of sandstone. The different volumes are analogous to different permeabilities of surrounding (capping) rocks in the crust, since a degree of fluid flow is permitted into the URV depending the URV size.
- (iv) the effects (mechanical and chemical) of fluid (water) on deformation by varying pore fluid pressure and temperature during suites of drained and undrained triaxial deformation experiments, and,
- (v) the mechanisms occurring during drained dehydration of gypsum, and during the triaxial deformation of undrained dehydrating gypsum.

Results from drained and undrained hydrostatic compaction of Darley Dale sandstone show a smooth concave hydrostat indicating no pore collapse up to a confining pressure of  $\approx 450\text{MPa}$ . The unloading curves indicate restricted fluid outflow - a consequence of compaction induced low permeability. The elastic and inelastic components of pore volume loss under this pressure

range is determined. Mean stress induced compaction is shown to be chiefly elastic below 500MPa confining pressure. Analysis of the data using established poro-elasticity theory shows that from experimental and published rock bulk moduli data, and corrected Skempton B co-efficients (from undrained compaction data), *drained* pore fluid volume loss under a uniform mean stress can be predicted. Drained compaction results on Penmaenmawr microgranodiorite are also presented.

Drained pore volume compaction data is also used in conjunction with pore volume data from triaxial deformation experiments to examine the components of pore volume change attributable to compaction and to dilatancy. The results indicate that under cataclastic flow the majority of compaction is deviatoric stress induced and is largely inelastic. The form of the dilatant pore volume increase curve during brittle faulting deformation at the onset of acoustic emission is found to be exponential, corroborating its connection with acoustic emissions which also initially increase exponentially.

Results on drained and undrained triaxial deformation experiments on Darley Dale sandstone indicate that a confined fluid mass environment (low permeability in surrounding/capping rock) causes a variation in effective confining pressure during deformation which can change the deformation mode from brittle faulting failure to cataclastic flow. A large fluid system volume necessary to monitor fluid pressure (the Upstream Reservoir Volume - URV) causes transitional deformation behaviour between that expected under completely undrained conditions and drained conditions. Extrapolation of the URV variation data has allowed an attempt at determination of a URV correction factor to predict pore fluid pressure change under *zero* URV. The pore fluid pressure change due to the initial application of differential stress (divided into deviatoric stress and effective mean stress) is presented in three dimensional space. The plot allows compaction as a function of either of these stresses to be viewed. The result is valid only for the suite of tests used, although the *method* is valid for all conditions, and indeed is used in this study for a large suite of experiments.

A suite of drained and undrained triaxial deformation results are analysed in 3-D space of pore fluid volume, deviatoric stress, and effective mean stress. The results show how the effect of the URV on effective and deviatoric stress causes the rock to behave with different *apparent* poro-elastic properties. The drained surface (plotted independently of undrained data), confirms that deviatoric stress causes compaction (under constant effective mean stress) during cataclastic flow, and dilatancy during brittle faulting failure. Quantification of the surface has implications for rock poro-elastic behaviour prediction under any stress field.

The effect of elevated temperature of the deformation on sandstone and microgranodiorite is presented, and a decrease in the brittle/cataclastic transition pressure with temperature of 1MPa/11°C is found. The effect is attributed to thermal cracking of the rock matrix.

Finally, results of a study on the factors affecting the dehydration of gypsum is presented. The results indicate a complicated interaction of chemical dehydration, compaction assisted fluid flow, and pressure assisted permeability increase restricting fluid flow, as found by other workers. Disentanglement of this interaction is not attempted since it requires further experimentation.

The experimental programme necessitated the modification of a high pressure triaxial deformation cell to allow pore fluid volume and pressure measurements to be made simultaneously with acoustic emissions and axial stress and strain on deforming rock specimens. The modifications, and associated equipment and technique developments are described.

## Contents.

Title.	1
Abstract.	2
Contents.	5
Lists of Figures.	13
List of Tables.	20
Glossary.	21
Acknowledgements.	23
<b><u>CHAPTER 1. INTRODUCTION.</u></b>	<b>24</b>
1.1. Introduction and Objectives of Study.	24
1.2. Experimental Programme.	25
1.3. Equipment Development Component of Project.	26
1.4. Arrangement of Thesis.	27
<b><u>CHAPTER 2. MICROSTRUCTURE OF ROCKS (CRACKS AND PORES), MICRO-MECHANISMS OF FAILURE, FLUID/ROCK INTERACTIONS, AND DAMAGE MECHANICS - A REVIEW.</u></b>	<b>29</b>
2.1. Introduction.	29
2.2. Micro-structure of Rocks.	29
2.3. Poro-Elasticity of Rock.	32
2.3.1. Effective Stress Law for undrained hydrostatic compression.	33
2.3.2. Elastic Constants for Drained and Undrained Deformation.	35
2.4. Deformation Mechanisms and Brittle Behaviour.	37
2.4.1. Introduction	37
2.4.2. Deformation Mechanisms.	37
2.4.2.1. Brittle Mechanisms.	37
2.4.2.2. Ductile Mechanisms.	39
2.4.3. Brittle Behaviour under Compressive Triaxial Stress.	40
2.4.3.1. Overview of Deformation modes.	41
2.4.3.2. Effect of a Hydrostatic Stress Field.	42
2.4.3.3. Effect of a Deviatoric Stress Field.	43

2.4.3.4.	Effect of Pressurised Pore Fluid.	43
2.4.3.5.	Effect of Elevated Pressure on Deformation.	46
2.5.	Brittle Crack Growth in Geological Materials.	47
2.5.1.	Introduction.	47
2.5.2.	Empirical Models.	48
2.5.3.	Single Crack Analysis Approach.	50
2.5.4.	Modifications to Griffith Criterion.	51
2.5.5.	Linear Elastic Fracture Mechanics (LEFM).	53
2.5.6.	Chemical Effect of Pore Fluids- Sub-critical Crack Growth Mechanisms.	56
2.6	Damage Accumulation and Continuum Damage Models.	58
2.6.1.	Introduction.	58
2.6.2.	Continuum Damage Mechanics Models.	59
2.7.	Holistic Studies of Interaction Between Rock Deformation and Evolution of Crack and Pore Micro-structure.	65
2.7.1.	Introduction.	65
2.7.2.	Microstructural Monitoring Techniques.	66
2.7.2.1.	Acoustic Emissions.	66
2.7.2.2.	Elastic Wave Velocity Measurements.	71
2.7.2.3.	Pore Fluid Volumometry.	73
2.7.2.4.	Permeability.	77
2.7.3.	Summary - Brittle Deformation Cycle and Physical Property Changes.	79
<b><u>CHAPTER 3. ROLE OF FLUID-FILLED CRACKS AND PORES IN THE CRUST.</u></b>		<b>83</b>
3.1.	Role of Fluid-filled Cracks and Pores in the Crust.	83
3.1.	Introduction.	83
3.2.	Fluid Driving Forces.	84
3.3.	Crustal Effects on Fluid and Fluid Movement.	86
3.3.1.	Heat Sources and Fluids.	86
3.3.2.	Earthquakes and Pore Fluids.	86
<b><u>CHAPTER 4. DESCRIPTION OF APPARATUS, MODIFICATIONS, AND CALIBRATION.</u></b>		<b>87</b>

4.1.	Introduction and General Description of Equipment.	87
4.2.	Main Triaxial Testing System.	89
4.2.1.	Lower Closure.	89
4.2.2.	Upper Closure.	90
4.2.3.	Servo-Controller Actuator.	91
4.2.4.	Loading Piston.	92
4.2.5.	Load and Stress Measurements, Correction and Calibration.	92
4.2.6.	Strain Rate Correction and Machine Stiffness.	93
4.2.7.	Three Stage Harwood Compressor.	95
4.3.	High Temperature Furnace.	96
4.3.1.	Furnace Arrangement, Operation and Background.	96
4.3.2.	Commissioning, and Logging Modifications.	98
	▶ Conclusion	102
4.3.3.	Rock and Furnace Temperature Calibration.	103
4.4.	Pore Fluid Volumometer and Fluid Pressure Intensifier.	105
4.4.1.	Purpose of Apparatus and General Arrangement.	105
4.4.2.	Servo-Control and Pressure Calibration.	105
4.4.3.	Pressure Intensifier Modification.	106
	4.4.3.1. Modification Objectives.	106
	4.4.3.2. Fluid Compressibility and Hoop Strain Analysis.	107
	▶ Water Compressibility.	108
	▶ Hoop Strain Analysis.	109
4.4.5.	Modified Fluid Pressure Intensifier Arrangement.	109
	4.4.5.1. Fluid Intensifier Modification.	110
	4.4.5.2. Redesign Pore Fluid Ram.	114
	4.4.5.3. Pore Fluid Ram Testing Apparatus.	118
4.4.6.	Results of Modification and Summary.	119
4.5	Acoustic Emission, AE Monitoring and Logging.	120
4.5.1.	Introduction and Acoustic Emissions Overview.	120
4.5.2.	Acoustic Emission Monitoring, Equipment, and Data Processing.	122
	4.5.2.1. Transducer.	122
	4.5.2.2. Transducer Housing.	123
	4.5.2.3. Electrical Signal and Amplification.	123

4.5.2.4. Logging Equipment.	124
4.5.2.5. Processing and Presentation of Data.	125
4.5.3. Optimising Signal and Data.	126
4.5.3.1. Noise sources and elimination.	126
4.5.3.2. Attenuation.	128
4.5.3.3. Transducer Coupling.	129
4.5.4. System Transfer Function.	130
4.6 Data Logging and Processing.	130
4.6.1. Logging System.	130
4.6.2. Logging and Processing Software.	131
4.7. Equipment Development; New Component Designs.	132
4.7.1. Introduction and Background.	132
4.7.2. Pore Fluid and P-wave/S-wave Upper Ram: Design Objectives, Constraints, and Alternatives.	133
4.7.3. Double Sealing Ring Lower Ram: Design Objectives and Constraints.	134
4.8. Safety Arrangements.	136
<b><u>CHAPTER 5. ROCK SAMPLES TESTED, SAMPLE PREPARATION, AND EXPERIMENTAL PROCEDURE.</u></b>	<b>138</b>
5.1. Sample Preparation.	138
5.1.1. Coring and Milling.	138
5.1.2. Determination of Porosity.	138
5.2. Experimental Procedure.	139
5.2.1. Copper Jacket Manufacturing Development.	139
5.2.1.1. Introduction.	140
5.2.1.2. Identification of Annealing Problem.	141
5.2.1.3. Process Development and Equipment Commissioning.	141
5.2.2. Sample Loading into Jacket.	142
5.2.3. Loading the Vessel.	143
5.2.4. Establishing Crustal Conditions and Commencing the Experiment.	144
5.2.4.1. Drained Triaxial Experiments.	145
5.2.4.2. Undrained Triaxial Experiments.	146
5.2.4.3. High Temperature Triaxial Experiments.	147

5.2.4.4.	hydrostatic Pore Volumometry Experiments.	147
5.2.4.5.	Dehydration Experiments on Gypsum.	148
5.3.	Procedural Development - Sample Saturation Procedure.	148
5.3.1.	Background and Objectives.	149
5.3.2.	Saturation System Design Solution and Conclusion.	150
5.3.3.	Full Specimen Saturation Technique Employed.	151
<b>CHAPTER 6.</b>	<b><u>EXPERIMENTAL PROGRAMME, BACKGROUND</u></b>	
	<b><u>AND RESULTS.</u></b>	<b>152</b>
6.1	General Introduction.	152
6.1.1	Introduction and Summary of Experimental Programme.	152
6.1.2.	Description of Rock Types Studied.	153
6.1.2.1.	Darley Dale Sandstone.	154
6.1.2.2.	Microgranodiorite.	154
6.1.2.3.	Gypsum.	154
6.1.3.	Behaviour of Rocks Simulated Crustal Conditions.	155
6.1.3.1.	Darley Dale Sandstone.	155
6.1.3.2.	Microgranodiorite	156
6.1.3.3.	Gypsum.	157
6.2.	Drained and Undrained Conditions, and Effect of Variations in Upstream Reservoir Volume on Deformation Characteristics of Darley Dale Sandstone.	159
6.2.1.	Introduction and Review.	159
6.2.2.	New Equipment.	162
6.2.3.	Programme of Experiments.	163
6.2.4.	Results.	163
6.2.4.1.	Drained and Undrained Triaxial Deformation Experiments on Darley Dale Sandstone.	163
6.2.4.2.	Results of Upstream Reservoir Variations under Undrained Triaxial Conditions.	169
6.2.5.	Discussion and Analysis: Pore Fluid Pressure Rise and URV Compensation Factor.	175
6.2.6.	Future Work.	180
6.3.	Pore Volume and Pressure Change as a Function of Hydrostatic Stress, (Drained and Undrained).	182

6.3.1.	Introduction and Review.	182
6.3.1.1.	Drained Hydrostatic Loading on Sandstone.	182
6.3.1.2.	Undrained Hydrostatic Loading on Sandstone.	184
6.3.1.3.	Microgranodiorite.	186
6.3.2.	Programme of Experiments.	186
6.3.3.	Results and Discussion.	187
6.3.3.1.	Steel Specimens - Calibration Experiments.	187
6.3.3.2.	Microgranodiorite - Drained Experiments.	189
6.3.3.3.	Darley Dale Sandstone - Drained Experiments.	191
6.3.3.4.	Darley Dale Sandstone - Undrained Experiments.	195
6.3.4.	Darley Dale Sandstone - Analysis.	196
6.3.4.1.	Consideration of Skempton's "B" co-efficient for Undrained Hydrostatic Deformation.	196
	▶ Determination of Bulk Compressibilities of Darley Dale sandstone, and of the Pore Fluid (water).	198
	▶ Calculations of Skempton's "B" Co-efficient.	204
6.3.4.2.	Consideration of Variations in Fluid Mass as a Function of Deformation under Drained Hydrostatic Stress Conditions.	207
6.3.5.	Future Work.	214
6.4.	Pore Volume and Pressure Change under Triaxial Conditions (Drained and Undrained).	217
6.4.1.	Introduction.	217
6.4.2.	Programme of Experiments.	218
6.4.3.	Results and Discussion.	219
6.4.3.1.	Analysis of Triaxial Deformation under Increasing Pore Fluid Pressure and Constant Effective Pressure.	219
6.4.3.2.	Analysis of Pore Fluid Pressure/Volume Changes and AE During Triaxial Deformation Experiments at High Confining Pressures.	222
6.4.3.3.	Analysis of Elastic and Inelastic Contribution to Pore Fluid Volume Change During Triaxial Stressing.	231
6.4.3.4.	Analysis of the Mean Stress-Induced and Deviatoric Stress-Induced Pore Volume Change During Triaxial	

Deformation.	234
6.4.4. Future Work.	241
6.5. Effect of High Temperature on Drained and Undrained Triaxial Deformation.	244
6.5.1. Introduction and Review.	244
6.5.1.1. Darley Dale Sandstone.	247
6.5.1.2. Penmaenmawr Microgranodiorite.	247
6.5.2. Programme of Experiments.	249
6.5.3. Results and Discussion.	250
6.5.3.1. Darley Dale Sandstone.	250
▶ Dependence of the Mechanical Behaviour of the Pore Fluid on Deformation during Undrained Triaxial Conditions.	250
▶ Effect of Temperature on Triaxial Deformation.	253
6.5.3.2. Penmaenmawr Microgranodiorite.	256
▶ Drained and Undrained Triaxial Deformation of Microgranodiorite.	256
▶ Effect of Elevated Temperature on Drained Triaxial Deformation of Penmaenmawr Microgranodiorite.	259
6.5.4. Future Work	261
6.5.4.1. Darley Dale Sandstone Experiments.	261
6.5.4.2. Microgranodiorite Experiments.	262
6.6. Studies of Pore Fluid Generation Due To Chemical Dehydration of Gypsum under Differing Confining Pressure and Pore Fluid Pressure.	263
6.6.1. Introduction and Review of Previous Studies.	263
6.6.2. Experimental Programme.	267
6.6.3. Results and Discussion.	267
6.6.3.1. Dehydration Experimental Results.	267
▶ Effect of Confining Pressure.	268
▶ Effect of Effective Confining Pressure.	268
▶ Effect of Pore Fluid Pressure.	270
6.6.3.2. Triaxial Stress and Dehydration Experiment Results.	271
6.6.4. Future Work.	273

<b><u>CHAPTER 7. GENERAL CONCLUSIONS AND FUTURE WORK.</u></b>	<b>275</b>
7.1. General Conclusions.	275
7.2. Future Work.	279
<b><u>APPENDICES.</u></b>	
Appendix A Calibration of Load Cell.	281
Appendix B. Equipment Development: Pore Fluid and P- & S- wave Upper Ram.	282
Appendix C. Equipment Development: Double Sealing Ring Lower End-cap.	286
References.	288

**List of Figures.**

<b><u>Figure</u></b>	<b><u>Page</u></b>
2.3.1.a. Solid subjected to hydrostatic pressure and internal pore fluid pressure.	34
2.4.2.1.a. Geometries that cause cracking.	38
2.4.3.1.a. Sketch of Macroscopically brittle deformation.	41
2.4.3.4.a. Illustration of effective pressure law on sandstone.	44
2.4.3.4.b. Illustration of concept of dilatancy hardening.	45
2.4.3.5.a. Illustration of brittle/Ductile transition (macroscopic).	46
2.5.2.a. Coulomb Failure criterion illustrated by Mohr circle.	49
2.5.2.b. Coulomb criterion in principle stress space.	49
2.5.2.c. Mohr failure envelop.	49
2.5.3.a. Two dimensional representations of Griffith criterion.	51
2.5.5.a. Modes of fracture mechanics.	54
2.5.5.b. R-curve development of crack growth.	55
2.5.6.a. Schematic Diagram of sub-critical stress corrosion cracking velocity/K curve.	57
2.6.2.a. Illustrates crack growth around a pre-existing flaw.	59
2.6.2.b. Photograph of wing crack interaction and bridge formation in PMMT plates.	61
2.6.2.c. Effect of interaction between collinear cracks on the stress intensity factor, pseudo-traction solution.	62
2.6.2.d. Affect of interaction between an array of collinear cracks on the stress intensity factor of penny shaped cracks in a local tensile stress.	62
2.6.2.e. Initial damage surface and failure surface for Westerly Granite.	64
2.7.2.1.a. Acoustic emission event locations leading to faulting.	67
2.7.2.1.b. Dependence of crack growth rate & AE on humidity.	69
2.7.2.1.c. Change in AE amplitude and frequency during failure of sandstone.	70
2.7.2.1.d. FFT results of waveforms before and after deformation.	71
2.7.2.2.a. Variations of velocity during deformation of sandstone.	72

2.7.2.2.b.	Variations in crack density during triaxial deformation.	73
2.7.2.3.a.	Opening of a throat, and increasing aspect ratio.	75
2.7.2.3.b.	Changing aspect ratio for deformation at different confining pressures.	76
2.7.2.4.a.	Permeability reduction with increasing confining pressure.	77
2.7.2.4.b.	Permeability reduction with varying pore fluid pressure and effective confining pressure.	78
2.7.3.a.	Schematic diagram representing the change in physical properties during deformation.	80
3.2.a.	Inflow and outflow of fluids about faulting.	85
4.1.a.	Photograph of apparatus.	86
4.1.b.	Block diagram of the equipment.	87
4.2.2.a.	Diagram of balanced ram system.	90
4.2.5.a.	Strength of annealed copper jackets.	93
4.2.6.a	Specimen strain rate variation with deformation.	95
4.3.2.a.	Schematic diagram of original thermo-couple wiring system, without monitoring or switching system.	98
4.3.2.b.	Effect of temperature on limestone deformation as seen by P-wave velocity measurements.	99
4.3.2.c.	Example of smooth stress/strain curve at 300°C	100
4.3.2.d.	Schematic diagram of new wiring/switching arrangement.	101
4.3.2.e.	Frequency/amplitude graph showing the spikes due to furnace noise.	102
4.3.3.a.	Upper, lower and rock temperature for 0 to 400°C, under zero confining pressure.	103
4.3.3.b.	Graph of Upper, lower and rock temperature for 0 to 150°C, under 100MPa confining pressure.	104
4.4.3.2.a.	Specific volume of water under various pressures.	108
4.4.3.2.b.	Calibration results. Water pressure against volume for a variety of Upstream Reservoir Volumes.	108
4.4.5.1.a.	Photograph of intensifier unit.	110
4.4.5.1.b.	Photograph of close coupled Pp tubing system.	111
4.4.5.1.c.	Photograph of head block and 1/8 <sup>th</sup> tubing.	113
4.4.5.2.a.	Original Upper pore fluid ram	114
4.4.5.2.b.	Diagram of Fluid Distribution plate.	115

4.4.5.2.c.	Redesigned pore fluid upper ram.	116
4.4.5.2.d.	Diagram of redesigned ram/piston connector piece.	115
4.4.5.3.a.	Photograph of pore fluid ram testing device.	118
4.4.6.a.	Effect of URV on pore fluid pressure change.	119
4.5.1.a.	Mechanisms associated with acoustic emissions.	120
4.5.1.b.	Acoustic emission event.	121
4.5.2.2.a.	Cross-section of piston and ram ends.	123
4.5.2.3.a.	Amplitude spectrum of P-wave form through aluminium.	124
4.5.2.5.a.	<i>b</i> -value calculated from different lower thresholds.	126
4.5.4.a.	Schematic diagram of acoustic emission source characterisation.	130
5.2.1.1.a.	Photograph of the ram and copper jacketing system.	140
5.3.1.a.	Results from unsaturated sample under drained conditions.	149
5.3.3.a.	Results fully saturated sample under drained conditions.	151
6.1.3.1.a.	Typical drained stress/strain curve for Darley Dale sandstone under different confining pressures.	155
6.1.3.2.a.	Fracture stress and stress drop against confining pressure for Penmaenmawr microgranodiorite.	156
6.1.3.3.a.	Differential Thermal Analysis of Gypsum.	158
6.2.1.a.	Deformation behaviour of sandstone with different added water volumes.	159
6.2.1.b.	Undrained deformation behaviour under different confining pressure and fluid added.	160
6.2.1.c.	Comparison of drained and undrained conditions on deformation of sandstone.	161
6.2.1.d.	Drained and Undrained experiments on Darley Dale sandstone monitoring pore fluid pressure/volume.	161
6.2.4.1.a.	Drained & undrained results, $C_p' = 20\text{MPa}$ on sandstone.	164
6.2.4.1.b.	Drained & undrained results, $C_p' = 75\text{MPa}$ on sandstone	166
6.2.4.1.c.	Drained & undrained results, $C_p' = 125\text{MPa}$ on sandstone	168
6.2.4.2.a.	Variations in URV on undrained deformation, $C_p' = 20\text{MPa}$ , sandstone.	169
6.2.4.2.b.	Variations in URV on undrained deformation, $C_p' = 75\text{MPa}$ , sandstone.	171
6.2.4.2.c.	Variations in URV on undrained deformation,	

	$C_p' = 125\text{MPa}$ , sandstone.	171
6.2.5.a.	Deviatoric stress/mean stress for four undrained results at $C_p' = 20\text{MPa}$ .	175
6.2.5.b.	Deviatoric stress/normalised mean. stress for four undrained results at $C_p' = 20\text{MPa}$ .	176
6.2.5.c.	Pore fluid pressure rise under various URV's & Dev. stress.	177
6.2.5.d.	Pore fluid pressure rise under various URV's & Mean stress.	177
6.2.5.e.	Two-D representation of pore fluid pressure surface under increasing deviatoric and mean stress.	178
6.2.5.f.	Three-D surface of fig. 6.2.5.e.	179
6.2.5.g.	Comparison of experimental and calculated pore fluid pressure rise.	179
6.3.1.1.a.	Four typical drained compaction hydrostats.	183
6.3.1.1.b.	Determination of critical crushing pressure in hydrostatic compaction tests from Zhang et al. (1990).	183
6.3.3.1.a.	Drained hydrostatic tests on steel samples (calibration).	188
6.3.3.2.a.	Drained hydrostatic tests on microgranodiorite.	189
6.3.3.3.a.	Two (of four) drained hydrostatic tests on Darley Dale sandstone.	191
6.3.3.3.b.	Two (of four) drained hydrostatic tests on Darley Dale sandstone.	192
6.3.3.3.c.	AE results form suite of drained hydrostatic tests Darley Dale sandstone.	192
6.3.3.3.d.	Examination of gradient of Pvol/time curve for drained hydrostatic tests on sandstone.	193
6.3.3.3.e.	As 6.3.3.3.d., for two further drained hydrostatic results.	194
6.3.3.4.a.	Undrained hydrostatic compaction results on Darley Dale sandstone.	195
6.3.4.1.a.	Skempton's B co-efficient from undrained hydrostatic results.	197
6.3.4.1.b.	P- & S- wave velocity results from drained hydrostatic tests on Darley Dale sandstone.	199
6.3.4.1.c.	Stylised <i>Bed of Nails</i> model of Carlson and Ganghi.	199
6.3.4.1.d.	Static <u>and</u> dynamic bulk modulus for Darley Dale sandstone.	200

6.3.4.1.e	Extrapolation of drained hydrostatic compaction data from Darley Dale sandstone.	201
6.3.4.1.f.	Smoothed $B_{(obs.)}$ and $B_{(theor't)}$ for undrained hydrostatic compaction tests on Darley Dale sandstone.	204
6.3.4.1.g.	As 6.3.4.1.g., including $B_{(corr.)}$ .	206
6.3.4.2.a.	Effective confining pressure co-efficient (alpha) for $K_s=27\text{GPa}$ & $15\text{GPa}$ .	208
6.3.4.2.b.	Total, permanent and elastic compaction of Darley Dale sandstone, and calculated pore volume loss ( $\delta v$ ) data.	209
6.3.4.2.c.	Variation in $\delta v$ with B correction factor and $K_s$ .	210
6.3.4.2.d.	Comparison of B co-efficients for different $K_s$ values.	211
6.4.2.a.	Full suite of triaxial deformation experiments.	218
6.4.3.1.a.	Effect of increasing fluid pressure on triaxial deformation.	219
6.4.3.1.b.	Adjusted pore fluid volume curve for chemical activity of high pore pressure fluid.	221
6.4.3.2.a.	Drained triaxial deformation of sandstone, $C_p' = 22$ & $50\text{MPa}$ .	223
6.4.3.2.b.	Drained triaxial deformation of sandstone, $C_p' = 75$ & $100\text{MPa}$ .	223
6.4.3.2.c.	Drained triaxial deformation of sandstone, $C_p' = 150$ & $200\text{MPa}$ .	224
6.4.3.2.d.	Drained triaxial deformation of sandstone, $C_p' = 255$ & $300\text{MPa}$ .	224
6.4.3.2.e.	Triaxial result $C_p' = 20\text{MPa}$ , Adjusted pore fluid volume curves using "PCA" and "MRA" method.	226
6.4.3.2.f	Triaxial result $C_p' = 50\text{MPa}$ , with adjusted pore fluid volume.	226
6.4.3.2.g	Triaxial result $C_p' = 76\text{MPa}$ , with adjusted pore fluid volume.	227
6.4.3.2.h	Triaxial result $C_p' = 100\text{MPa}$ , with adjusted pore fluid volume.	227
6.4.3.2.i	Triaxial result $C_p' = 150\text{MPa}$ , with adjusted pore fluid volume.	228
6.4.3.2.j	Triaxial result $C_p' = 200\text{MPa}$ , with adjusted pore	

fluid volume.	228
6.4.3.2.k. Compilation of figures 6.4.3.2.e, f, & g., PCA method only.	229
6.4.3.2.l. Compilation of figures 6.4.3.2.h, i, & j., PCA method only.	230
6.4.3.3.a. Five triaxial deformation results showing cycling of differential axial stress.	232
6.4.3.3.b. Last (e) curve of 6.4.3.3.a., expanded.	233
6.4.3.4.a. Drained and undrained triaxial deformation data in 3-D space of effective mean stress, deviatoric stress, and pore volume.	235
6.4.3.4.b. View A of fig. 6.4.3.4.a., effect of effective mean stress axis on pore volume, (drained and undrained).	236
6.4.3.4.c. 3-D plot of drained data only, effective mean stress, deviatoric stress, and pore volume.	237
6.4.3.4.d. View B of fig. 6.4.3.4.c., effect of deviatoric stress only.	238
6.4.3.4.e. View D. of 6.4.3.4.c., shows increase in effective mean stress and deviatoric stress with increase in differential axial load.	238
6.4.3.4.f. View C of 6.4.3.4.c., showing effect of effective mean stress on deformation.	239
6.4.3.4.g. 3-D plot of undrained data, effective mean stress, deviatoric stress and pore volume.	239
6.4.3.4.h. View B of fig. 6.4.3.4.g., showing effect of deviatoric stress alone.	240
6.5.1.a. Saturation vapour line for water.	245
6.5.1.b. Specific volume of water, $T=0\rightarrow 250^{\circ}\text{C}$ , variety of pressures.	246
6.5.1.c. Specific volume of water, $T=250\rightarrow 450^{\circ}\text{C}$ , variety of pressures.	246
6.5.1.2.a. Effect of temperature on deformation of Penmaenmawr microgranodiorite.	248
6.5.3.1.a. Effect of fluid under different pressures and temperatures (different mechanical properties) on undrained deformation Darley Dale sandstone.	250
6.5.3.1.b. Effect of temperature on drained triaxial deformation of sandstone, $T=20\rightarrow 400^{\circ}\text{C}$ , $C_p' = 20\text{MPa}$ .	253

6.5.3.1.c.	Effect of temperature on drained triaxial deformation of sandstone, $T=20\rightarrow 200^{\circ}\text{C}$ , $C_p' = 45\text{MPa}$ .	255
6.5.4.1.d.	Suite of drained triaxial deformation results displaying effect of temperature on strain hardening/softening.	255
6.5.4.2.a.	Drained and undrained triaxial deformation of microgranodiorite.	257
6.5.4.2.b.	Effect of temperature on drained triaxial deformation of microgranodiorite, $T=20\rightarrow 400^{\circ}\text{C}$ .	259
6.6.1.a.	Sigmoidal curve of drained dehydration of gypsum.	264
6.6.1.b.	Dependence of drained dehydration on pore fluid pressure and confining pressure.	265
6.6.1.c.	Sigmoidal curve of undrained dehydration of gypsum.	266
6.6.3.1.a.	Results of drained dehydration of gypsum.	267
6.6.3.1.b.	Effect of effective confining pressure and pore fluid pressure on reaction rate.	269
6.6.3.2.a.	Undrained triaxial deformation of dehydrating gypsum.	271
A.1.	Calibration of load cell.	281
B.a.	Redesigned upper ram for P- & S- waves velocity and pore fluid volumometry measurements.	285
C.a.	Redesigned double sealing ring lower ram.	287

**Tables.**

<b><u>Tables.</u></b>		<b><u>Page.</u></b>
4.4.3.2.a.	Increase in cross-sectional area for different <i>hp</i> tubes under effect of pressure.	109
6.3.1.2.a.	Results from previous work on Skempton's B co-efficient.	184
6.3.2.a.	Outline of experimental programme for section 6.3.	186

## Glossary

$a_0$	Initial crack radius.
$\alpha$	Effective stress coefficient.
$\alpha$	Ratio ( $c/R$ ) - initial crack length/grain radius.
AE	Acoustic emissions.
B	Skempton's B co-efficient.
c	Microcrack length.
$C_p$	Confining pressure, ( $=P_c$ ).
$C_p'$	Effective confining pressure, ( $=P_c'$ ).
C	Bulk compressibility of rock, ( $=1/K$ ).
$C_w$	Bulk compressibility of water, ( $=1/K_f$ ).
$C_s$	Bulk compressibility of solid part of rock, ( $=1/K_s$ ).
$d_i$	Initial spacing between interacting cracks.
D	Damage parameter in cracked solid.
D	Fractal dimension for crack size analysis.
$\epsilon$	Bulk strain.
$\epsilon_{kk}$	Volumetric strain in a given orientation (kk).
$\epsilon_{kk}$	Bulk strain in a given orientation (kk).
$\delta\epsilon_{kk}$	Increment of bulk strain in a given orientation (kk).
$\epsilon$	Dimensionless crack density parameter.
E	Young's modulus.
f	Empirically derived scaling constant (eq. 2.6.2.b.).
F	Proportionality factor between crack driving force from crack interaction and deviatoric stress.
G	Shear modulus of porous rock determined in the absence of pore fluid.
GPa	Giga Pascal.
hp	High pressure.
K	Bulk modulus of rock with unfilled pores - the rock "skeleton", ( $=1/C$ ).
$K_s$	Bulk modulus of solid part of rock, ( $=1/C_s$ ).
$K_u$	Effective bulk modulus of rock under undrained regime.
$K_f$	Bulk modulus of fluid, ( $=1/C_w$ ).
$K_m$	Crack tip stress intensity factor ( $m=I, II, \text{ or } III$ )
$K_c$	Critical crack tip stress intensity factor for crack propagation.
K	Rock permeability.
L	Normalised crack extension for propagating cracks.
LVDT	Linearly Variable Differential Transducer.
MPa	Megapascals.
PC	Personal Computer.
$P_p$	Pore fluid pressure, ( $=p$ ).
$p$	Pore fluid pressure, ( $=P_p$ )
$\rho_u$	Change in pore fluid pressure under undrained conditions due to applied stress.
$\delta p$	Pore fluid pressure change due to stress under undrained regime.
$P_v$	Pore fluid volume.
$P_c$	Confining pressure, ( $=C_p$ ).
$P_c'$	Effective confining pressure, ( $=C_p'$ ).
$P'$	Confining pressure at which all microcracks are thought closed.

$P^{**}$	Pore collapse pressure.
$\phi$	Rock porosity.
$\delta\phi$	Change in rock porosity.
$Q$	Seismic quality factor.
$S$	Shear stress.
$R$	Elastic strain constant - measure of change in water content for a change in pore fluid pressure.
$R$	Grain radius.
$\delta V$	Increment of volumetric strain.
$\delta v$	Change in pore volume of rock under drained conditions under stress.
$\sigma_1$	Maximum principle stress.
$\sigma_2$	Intermediate principle stress.
$\sigma_3$	Intermediate principle stress.
$\sigma_m$	Mean stress.
$\sigma_m'$	Effective mean stress.
$\sigma_{kk}$	Hydrostatic stress.
$\mu$	Co-efficient of friction.
URV	Upstream Reservoir Volume.
$\nu$	Poisson's ratio.
$\nu_u$	Poisson's ratio for a porous rock in undrained regime.
$V_p$	Pressure wave velocity.
$V_s$	Shear wave velocity.
$c/a$	crack aperture ratio (min. dim/max. dim.).

## **Acknowledgements**

I would like to thank a number of people in connection with this thesis and with my time spent at University College London.

Firstly I would like to thank Stan Murrell for his scientific advice and guidance, and unmatched enthusiasm for this work; Philip Meredith for his time and effort spent on the details of this thesis, with reviewing conference papers, and with securing overseas conference visits; and Peter Sammonds for assistance with equipment development in the early stages of this project.

Acknowledgement goes out to the crew of Hut 18 who have kept me sane through some of the more frustrating moments of the last few years. This includes, Dave Raistrick, John Bowles, Neil Hughes, and Anita Odedra. Also worthy of the same thanks is the senate house luncheon group, Dave, Anita, Greg Fookes, and Gerald Roberts. Extra thanks to Gerald for time spent explaining the details of structural geology.

Thanks also for scientific advice freely forthcoming from all those in the Rock and Ice Physics lab.; to Tobi for yet more photo's of the equipment; to John and Neil and Steve Boon for equipment modification, developments, machining and general tinkering; and to Henry Tillotson for his time creating the 3-D images used in this thesis.

Finally, a special thanks to Karen de Rochemont. Karen has been patient and supporting in every sense throughout the Ph.D., especially through the last hot summer of 1995. This thesis is dedicated to Karen.

The project was sponsored by the Natural Environment Research Council.

## **CHAPTER 1. INTRODUCTION.**

### **1.1. Introduction and Objectives of the Study.**

The behaviour of crustal rocks as cracked porous fluid filled media under the influence of imposed lithostatic and fluid stress conditions is of vital importance to industries and researchers concerned with understanding and controlling rock deformation in fields such as hydrocarbon extraction, mining, civil engineering, radioactive waste storage, and understanding earthquake nucleation & crustal evolution processes. Furthering the understanding of the mechanisms responsible for brittle deformation is a goal of researchers around the world, and this project makes a contribution to that goal through improved experimental capabilities and examination of dilatancy and compaction mechanisms during deformation under crustal stress and temperature conditions.

Polycrystalline rock is comprised of a matrix of mineral particles, spherical pores, and microcracks. It is the presence of voids in rocks, their effect on local stress concentration due to far field stresses, and the subsequent nucleation, growth and eventual interaction of microcracks, which is responsible for brittle rock deformation. In the laboratory, specimens of rock can be subjected to conditions of confining pressure, pore fluid pressure, and temperature in an attempt to reproduce crustal conditions and study these complex micro-mechanisms. Imposing full triaxial crustal conditions allows the material properties of the rock to be analysed in a natural sub-surface state. Scaling problems often encountered with rock strength analyses (laboratory specimen to crustal scale) are less significant with material property analysis, and so the results obtained are of direct relevance to the earth science industries mentioned above.

The study uses pore volumetry and acoustic emissions to monitor damage accumulation and changing crack and pore volumes in saturated deforming porous crustal rocks to study the effect of fluids on rock deformation through mechanical and chemical processes. Complex feedback mechanisms occur

in rock under undrained conditions concerning the growth of microcracks (pore volume increase); crack growth reduces pore fluid pressure, increases effective stress and hence changes the stresses upon which the mechanisms of microcrack growth depend. Combined with other factors also influential in controlling the deformation process, (i.e. temperature, rock permeability, mineral fracture toughness, fluid flow conditions - i.e. drained or undrained), the mechanisms of fluid/rock interactions are complex.

In order to conduct the experimental programme, the development of equipment capable of controlling and monitoring fluid pressure and volume changes in deforming rock specimens was necessary (section 1.3.). This has allowed a comprehensive experimental study to be conducted to elucidate aspects of fluid/rock interactions in the deformation process, and to examine changing pore and crack volume (due to axial deviatoric stress ( $\sigma_1 - \sigma_m$ , hereafter referred to simply as deviatoric stress), and effective mean stress), during deformation under a range of crustal stress and temperature conditions. The results are analysed and interpreted in terms of established poro-elasticity theory and the behaviour of a cracked porous solid in which cracks/pores may change both elastically and inelastically. Results are presented in detail in chapter 6 and general conclusions are contained in chapter 7.

## 1.2. Experimental Programme.

Throughout the study 199 separate experiments were conducted, logged and analysed. Of those,  $\approx 140$  yielded sufficiently complete data sets to be of use. The range of experiments conducted address a variety of fluid/rock deformation problems. These are described below.

- ▶ A comprehensive series of drained and undrained triaxial deformation experiments on Darley Dale sandstone up to confining pressures of 375MPa and fluid pressures of 350MPa. The results describe the effect of a changing fluid pressure (undrained) on the deformation of porous sandstone compared with constant fluid pressure (drained), and changes in pore volume/pressure during cataclastic flow of porous

sandstone. Analysis of mean stress, deviatoric stress, and pore fluid volume for the suite of experiments has been undertaken to examine deviatoric and mean stress induced changes in pore volume through mechanics of dilatancy and compaction.

- ▶ Extension of the above programme to investigate the effect of temperatures of up to 400°C on the deformation of Darley Dale sandstone and Penmaenmawr microgranodiorite under both drained and undrained conditions.
  
- ▶ An analysis of drained and undrained hydrostatic compaction on both Darley Dale sandstone and Penmaenmawr microgranodiorite under a variety of stressing rates and cyclical peak stresses up to 450MPa. This isolates the mean stress induced compaction component of pore fluid volume loss for analysis independently and in comparison with triaxial deformation results.
  
- ▶ A suite of undrained triaxial deformation experiments varying the fluid system volume outside the vessel (necessary to monitor changing fluid pressure, called the **Upstream Reservoir Volume - URV**). The effect of a variety of URV's on pore fluid pressure change is observed, and results allow prediction of pore fluid pressure changes under zero URV to be attempted.
  
- ▶ A suite of dehydration experiments on gypsum monitoring the increase in fluid volume. Factors affecting dehydration rates and triaxial deformation of dehydrating gypsum are investigated.

### **1.3. Equipment Development.**

The extreme crustal conditions possible using the high pressure gas medium rock deformation cell at the Rock and Ice Physics Laboratory are 1400MPa confining pressure, 1000°C temperature, and 700MPa pore fluid pressure. At the outset of the study, the equipment was set up to measure acoustic

emissions and either, (i) P- and S- wave velocity or, (ii) pore fluid volumetry (pore fluid intensifier sited remotely from pressure vessel). For the proper investigation of dilatancy and compaction under *undrained* triaxial stress conditions the *close coupling* of the pore fluid intensifier with the deformation cell was vital. The integration of previously independent logging systems, a redesigned pore fluid upper ram, a ram-leak testing device, and extensive modifications to the pore fluid supply and pressure transducer arrangement was an integral part of this equipment development programme. The existing high temperature furnace was also recommissioned for the study. The overall equipment development work demanded extensive calibration testing programmes. Prior to the experimental programme, modifications were also carried out to the manufacturing technique of the soft copper jackets (required to protect rock specimens from confining pressure gas), to computer logging software, and to the 1400MPa confining pressure pump. The present study used the equipment to limits of 450MPa confining pressure, 400°C temperature, and 350MPa pore fluid pressure. Details of the equipment development programme are contained in chapter 4.

#### **1.4. Arrangement of the Thesis.**

The thesis is divided into six further chapters following this introduction. They discuss in turn;

- (i) the micro-mechanisms by which dry and fluid filled porous rocks deform and theories describing rock deformation,
- (ii) the effect of fluids in the crust,
- (iii) equipment used and modifications undertaken during the study,
- (iv) techniques developed in the study,
- (v) the experimental programme undertaken, results, discussion and conclusions, and finally,
- (vi) conclusions and comments on the results of the study, and future work possibilities.

The contents of each chapter are presented in more detail below.

*Chapter 2* forms the background to rock deformation studies. It begins by describing the microstructure of polycrystalline rocks. Rock, considered as a matrix of mineral grains, spherical pores, and microcracks, is then discussed in terms of poro-elasticity theory. Deformation mechanisms (for rocks with and without fluids) based on empirical data is then considered, and the theories of brittle crack growth in rock is reviewed. Recent continuum damage models are then reviewed, and the chapter concludes with holistic view of porous rock deformation and the evolution of crack damage as monitored by measurement of changing rock physical properties.

*Chapter 3* briefly describes the role of fluids in the crust. Fluid sources are considered along with fluid driving forces. The effect of fluid both mechanically and chemically on the behaviour of rocks under crustal pressure and temperature conditions is discussed. This chapter attempts to connect problems of fluid in the crust with the experimental rock physics research.

*Chapter 4* describes the equipment used in the study. Calibration of equipment, and modifications to the pore fluid pressure intensifier, to the high temperature furnace, and to the logging system are described. Acoustic emissions technology and techniques are discussed, and new component design and commissioning is presented.

*Chapter 5* describes specimen preparation techniques, experimental procedures, and research techniques developed throughout the study.

*Chapter 6* describes, discusses and analyses the results. It is divided into 6 discrete sub-sections, each of which deals with a certain aspect of rock deformation as monitored by pore volumetry. Each sub-section is self contained with a relevant review section, discussion, analysis, and a note on pertinent future work possibilities. Section 6.1.1. describes these sub-sections in more detail.

*Chapter 7* contains the general conclusions of the study and future work possibilities.

## **CHAPTER 2. MICROSTRUCTURE OF ROCKS (CRACKS AND PORES), MICRO-MECHANISMS OF FAILURE, FLUID/ROCK INTERACTIONS, AND DAMAGE MECHANICS - A REVIEW.**

### **2.1. Introduction.**

The deformation and failure of rocks under stress is complex and depends on many environmental factors such as, confining pressure, pore fluid pressure, temperature, applied differential stress, and rate of stress change. Internally, the porosity and pore structure of the rock affects pore fluid pressure change during deformation and hence alters the deformation characteristics of the rock through the law of effective stress. Whilst much is understood about the response of porous materials to internal fluid pressure and external confining pressure, (presented here), much remains outstanding and the need for experimentation continues.

In order to assist the understanding of this complex interplay of mechanisms, Chapter 2 addresses the physical processes of deformation leading up to rock failure -rock compaction, microcrack nucleation, crack extension & linkage, and coalescence of microcracks. Theoretical models based on these concepts, from the earliest to the most recent, are reviewed, and the application of some of these processes with respect to earthquake faulting and fluid flow in the crust are reported. Finally, experimental methods used in this study and elsewhere, to examine fully these processes during deformation are presented.

### **2.2. Micro-Structure of Rocks.**

Rocks are formed from an assemblage of minerals of different chemical and physical composition. It is the behaviour and interaction of these packed mineral particles, and moreover the pores and microcracks between the grains, that dictate the gross behaviour of the rock. The mode of formation

of a rock has a large effect on pore and crack micro-structures, and hence on the gross behaviour of rock under stress.

*Igneous rock* crystallisation occurs either on the surface of the Earth (volcanic igneous) or beneath the surface (plutonic igneous). Different cooling temperatures and durations control crystal grain size - a smaller grain size resulting from rapid cooling. Because igneous rocks crystallise in-situ, a tight structure without pores generally results (the exception is rock containing dissolved gases - e.g. basaltic magmas - which generate pores from enclosed bubbles). The tight matrix created causes porosity to be as low as 0.1% which is often comprised of fully or nearly closed *intergranular* cracks. Fractures in igneous rocks generally occur subsequent to rock formation, and although they are often of low aspect ratio (minimum dimension  $\ll$  maximum dimension), their interconnecting nature can allow a permeability that is surprisingly high for such a low porosity.

*Sedimentary rocks* are most commonly a collection of previously weathered, eroded and transported (rounded) particles, and the energy of the depositional environment (water or wind blow) dictates the *grading* of the rock particles (grains). A high energy environment causes only one particle size to be deposited at a given location, resulting in a *well graded* rock (high porosity - 0.4-0.45), whilst a low energy environment allows many particle sizes to be deposited at one location, resulting in a *poorly graded* rock (lower porosity). Initial porosity is controlled by three main factors, (i) *grain size*, through enhanced gravity assisted settlement of the larger grains - smaller grain sized sediments do not compact until pressure assisted, (ii) *grain shape*, through frictional resistance to gravitational settlement from rough surfaced grains, and, (iii) *grading*, poorly graded sediments allow smaller grains to fit between the larger grains, therefore reducing porosity without decreasing overall packing of the large grains.

Upon gradual burial, overburden pressure and elevated temperature overcomes grain friction and cohesive forces in the sediment to cause consolidation, compaction and diagenesis.

- ▶ ***Consolidation*** is the rotation and rearrangement of particles reducing the void ratio and expelling interstitial fluid. The amount of consolidation possible is limited by the grain size; larger grains consolidate more up to a minimum porosity of  $\approx 0.4$ . For grains  $< 100\mu\text{m}$ , minimum porosity increases sharply, (Guéguen & Palciauskas 1994) consolidation is less important in sandstones than in other sediments such as shales, due to the high grain friction and large particle size of sandstone.
- ▶ ***Compaction*** is the principle porosity reduction mechanism, and involves the deformation of grains through physical damage and chemical alteration; a mixture of different particles under compressive stress and in a potentially foreign pore fluid creates an environment in disequilibrium which is then the subject of grain fracturing and mineral dissolution/precipitation. The latter process moves mass locally and/or great distances, and is the cause of siliceous and carbonaceous grain cements in sandstones.
- ▶ ***Diagenesis*** is a form of low-grade metamorphism involving the growth of new minerals from fluids leading to the cementation of grains.

The most significant effect of tectonic stressing in the crust is the development of microcracks within rock. Microcracks are openings with two dimensions much larger than the third. They are categorised in groups dependent upon their location and path.

- ▶ ***Grain Boundary or Intergranular cracks*** run between grains, sometimes entering grains at high angles (non-coincident cracks) or remaining between the grains (coincident cracks). They are long, thin, and often closed. Their aperture is usually greater than for intra-granular cracks, and their orientation may vary approaching a grain boundary. In porous sedimentary rocks they may follow stress paths passing between grains at the grain contact points. They are the result of mechanical loading or thermally induced fracturing.

- ▶ ***Intra-granular Cracks*** occur within grains. They are slot like cavities with blunted ends, often tortuous, with an aspect ratio of  $10^{-2}$  to  $10^{-4}$ . Crack aperture is as low as  $1\mu\text{m}$ . They are often known as *cleavage cracks*, which are cracks confined to a particular plane of the crystal lattice, extremely sharp, and parallel except where they merge with uncracked material.

Cracks can have a significant effect on rock mechanical and physical properties - e.g. elastic and inelastic strain under load, peak stress, permeability, elastic wave velocity. Crack population orientations are often anisotropic, in response to an anisotropic stress field, and when considering certain physical properties such as elasticity, permeability and electrical conductivity, values are often directional and scale dependent (within a certain range). For this reason, *effective properties* are often used to describe the mean macroscopic properties of rock for three directions, whilst mini- and microscopic variations are neglected, (Paterson 1978). The internal surfaces of cracks and pores also strongly affect physical behaviour, i.e. *surface roughness* is particularly important.

The importance of *surface roughness* concerns the ability of a crack to open and close elastically with having to crush mismatched asperities and debris; this affects porosity loss under hydrostatic load. Roughness can be characterised by the distribution of asperity maxima. This can be characterised by the use of fractals (Main et al, 1990).

The relationship between rock microstructure and rock physical properties is complex, and requires knowledge of the shape, structure and inter-connectivity of the pores and cracks. This information has to be inferred indirectly from measurements such as porosity, specific surface area, electrical conductivity, and permeability, These physical properties can be measured during deformation, (section 2.7.).

### 2.3. Poro-elasticity of Rock.

In describing the behaviour of porous media under the effect of stress, elasticity must be generalised to *poro-elasticity*, and when considering the effect of a fluid phase on porous media the question of *drained* or *undrained* conditions must be considered; i.e. whether fluid *pressure* or fluid *mass* is the independent variable, (section 2.4.3.4.). Explanation of the effective stress law is necessary before further analysis.

### 2.3.1. Effective Stress Law for Undrained Hydrostatic Compression.

Considering fluid in the pores and cracks of a rock with fluid mass ( $m$ ), and fluid density ( $\Gamma$ ), and fully saturated when fluid volume equals pore volume ( $v = \Phi$ ); compressibility of the fluid component of the two phase (fluid filled) rock system will depend upon the bulk modulus of the fluid ( $K_f$ ), and pore fluid pressure ( $p$ ). The effective confining pressure ( $P_c'$ ) is defined as;

$$P_c' = P_c - \alpha p \quad (2.3.1.a.)$$

Where  $p$  is the pore fluid pressure, and  $\alpha$  is a constitutive relation of poro-elasticity - the effective stress co-efficient. When  $\alpha = 1$ , the effective pressure is equal to the difference between the confining pressure and the pore fluid pressure. Otherwise  $\alpha$  is found by;

$$\alpha = 1 - K/K_s \quad (2.3.1.b.)$$

where  $K_s$  is the bulk modulus of the solid part of the rock, and  $K$  is the bulk modulus of rock with pores - the rock "skeleton" or "frame". This equation is derived from an analysis proposed by Nur & Byerlee (1971), presented below.

Considering a single pore within a medium subject to external pressure  $P_c$  and internal pressure  $p$  as per the illustration in fig. 2.3.1.a. The volumetric strain is a function of the bulk modulus of the *frame* of the rock with empty pores under the effect of the simple effective pressure ( $P_c - p$ ). i.e.

$$\{\delta V/V\}_{(P_c=p)} = (\epsilon_{kk})_{(P_c=p)} = - (P_c - p)/K \quad (2.3.1.c.)$$

When subject to an internal fluid pressure equal to the applied hydrostatic pressure ( $P_c = p$ ), volumetric strain is governed by the bulk modulus of the solid part of the rock, ignoring the pores as full with fluid and of equal pressure to the external applied pressure. Because the modulus of solid without pores is  $K_s$

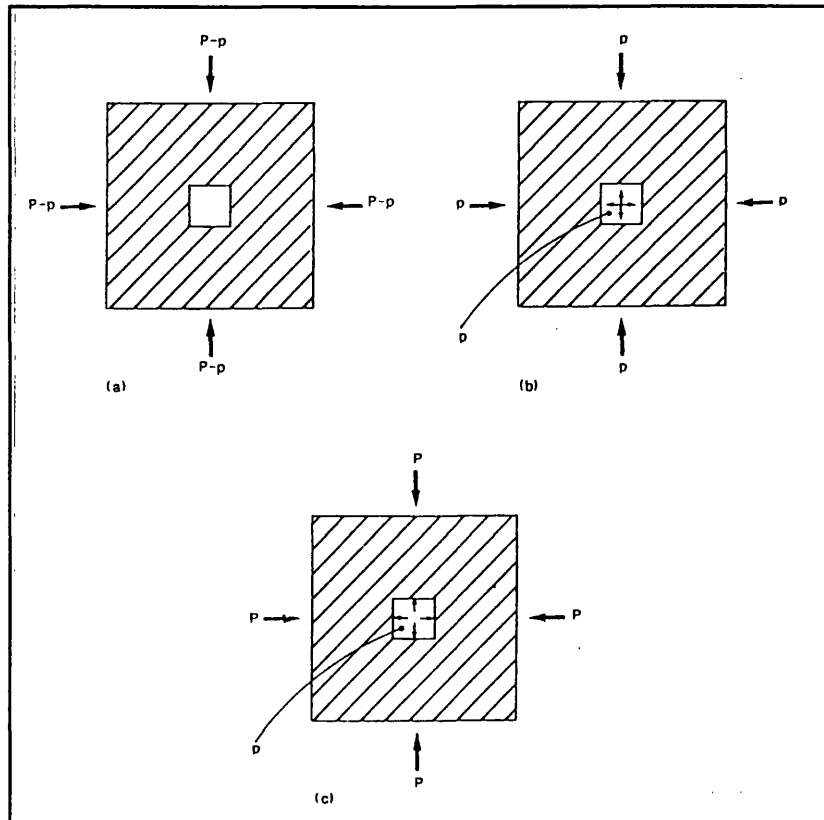


Fig. 2.3.1.a. Solid with pore subject to pore fluid pressure (a) effective confining pressure (b), combined in frame (c), (After Guéguen 1994).

$$\{\delta V/V\}_{(P_c=p)} = (\epsilon_{kk})_{(P_c=p)} = - p/K_s \quad (2.3.1.d.)$$

As linear theory is used, the two conditions can be superimposed when different external and internal pressures exist, such that;

$$\{\delta V/V\}_{(P_c \neq p)} = (\epsilon_{kk})_{(P_c \neq p)} = - (P_c - p)/K - p/K_s \quad (2.3.1.e.)$$

or;

$$\epsilon_{kk} = - (P_c - \alpha p)/K = - P_c'/K_s \quad (2.3.1.f.)$$

where  $\alpha$  is as per equation 2.3.1.b.

For porous rocks when  $K_s \gg K$ , and  $\alpha \rightarrow 0.9$ . However, for rocks of low porosity where  $K \rightarrow K_s$ ,  $\alpha$  can approach 0.6. For Darley Dale sandstone  $\alpha = 0.75 \rightarrow 0.85$  dependent on the effective confining pressure.

### 2.3.2. Poro-elastic Constants for Drained and Undrained Hydrostatic Deformation.

For *drained* conditions, the fluid mass in the rock remains constant whilst its volume varies with deformation. Stress/strain relations are the same as in ordinary elasticity and the law of effective stress applies. Under hydrostatic compression the strain  $\epsilon$  is proportional to the stress  $\sigma$  by;

$$\epsilon = \sigma' / K \quad (2.3.2.a.)$$

Where  $\sigma'$  is the effective hydrostatic stress.

Under *undrained* conditions the value of pore fluid pressure change is determined by the internal deformation of the medium. In this instant *effective* constants (denoted by subscript *u*), are used to describe the behaviour of the *rock/fluid* system under stress. Such that  $K$  is replaced by  $K_u$  - the bulk modulus due to the combined fluid and solid phases, hence;

$$\epsilon = \sigma / K_u \quad (2.3.2.b.)$$

The concept of effective pressure is of little use because the pore fluid pressure is unknown and changes in response to volumetric strain of the rock. The change in pore fluid pressure ( $\delta p$ ), is a function of the bulk modulus of the fluid/rock system  $K_u$ , the bulk modulus of the solid rock matrix  $K$ , and  $\alpha$ , by;

$$\delta p = -\{(K_u - K)/\alpha\} \cdot \epsilon \quad (2.3.2.c.)$$

Combining 2.3.2.a. and b., introducing an independent co-efficient  $B$  called the *Skempton B Co-efficient*, (Skempton 1954), and rearranging for  $B$  results in;

$$B = 1/K_u \cdot \{(K_u - K)/\alpha\} \quad (2.3.2.d.)$$

I.e., the fluid pressure increase can be expressed in terms of an increase in hydrostatic confining pressure for undrained conditions, and the Skempton coefficient.

$$\delta p = -B \cdot (\sigma) \quad (2.3.2.e.)$$

Linear poro-elasticity, therefore depends on the independent rock constants;  $K$ ,  $K_u$ , and  $\alpha$ , (with  $\mu$  - the shear modulus - used in shear stress analysis, although  $\mu_u = \mu$ ).

$K$  can be obtained through drained (or dry) hydrostatic experiment, and  $K_u$  obtained through hydrostatic *undrained* experiments measuring the pore fluid pressure generated.  $K_u$  is a function of  $K_r$ ,  $K$ , and  $\phi$ . Without explicitly deriving  $K_u$ , it can be related to  $K$  when under the special case of  $P_c = p$ . Under these conditions the rock is subject to a homogenous pressure, "appears" homogeneous and without pores, and of bulk modulus  $K_s$ . Based on equation 2.3.1.g., after rearranging for  $K_u$ ;

$$K_u = K + \alpha^2 / [(\phi/K_r) + ((\alpha - \phi)/K_u)] \quad (2.3.2.f.)$$

It should be noted that physically,  $K_u$  is dependent on pore shape although a term accounting for this does not appear in the above relation.

In the drained case, the fluid mass will change during hydrostatic stressing as a function <sup>of</sup>  $\lambda$  bulk strain of the rock and pore fluid pressure. From an internal energy analysis of the rock under infinitesimal strains, (Guéguen 1994), the change in fluid mass can be expressed as;

$$\delta m = m - m_0 = \alpha \cdot \Omega \cdot \epsilon + A p \quad (2.3.2.g.)$$

The constant  $A$  is obtained from the conditions that when  $\delta m = 0$ ,  $p = p_u$  ( $p_u$  is the pore fluid pressure rise under undrained conditions). The fluid volume

change is found by considering the change in density ( $\delta\rho$ ) as a function of  $p$ , where  $\delta m = \rho \cdot \delta v + v \cdot \delta\rho$ , ( $\delta v$  is the change in fluid volume). When fluid volume ( $v$ ) equals porosity ( $\phi$ ), the equation for change in fluid volume with bulk moduli of rock is found;

$$\delta v = \alpha \cdot \epsilon_{kk} + [(\alpha^2 / (K_u - K)) - (\phi / K_f)] \cdot p \quad (2.3.2.h.)$$

$K_u$  can differ substantially dependent upon the relative values of  $K_f$ . If  $K_f \rightarrow 0$ , then  $K_u \rightarrow K$ , whilst if  $K_f \rightarrow \text{infinity}$ , then  $K_u \rightarrow K + (\alpha^2 \cdot K_s) / (\alpha - \phi)$ . The practical analogy is when rock is saturated with a gas compared with a liquid. Theory predicts a lower  $K_u$  for a gas, and this is important for oil and gas industries.

The variations of  $B$  between 1 and 0 concern these two cases; when  $B \rightarrow 1$ ,  $K \rightarrow 0$ , i.e. for a porous, unconsolidated medium, and when  $B \rightarrow 0$ ,  $K \rightarrow K_u$  under circumstances of a very compressible fluid.

## 2.4. Deformation Mechanisms and Brittle Behaviour.

### 2.4.1. Introduction

Rocks deform by a variety of different micro-mechanisms. Environmental conditions are prominent factors in dictating which mechanism is prevalent at any time. Deformation behaviour in rocks as a consequence of these mechanisms can be broadly divided into macroscopically brittle, (faulting failure), macroscopically ductile flow (cataclastic flow), and ductile deformation. The micro-mechanisms operating during these different modes of deformation are outlined below. This section reviews work which describes the brittle microscopic and macroscopic deformation of rock under crustal conditions.

### 2.4.2. Deformation Mechanisms.

#### 2.4.2.1. Brittle Mechanisms.

Brittle crack initiation and growth in poly-crystalline material results from local tensile stress exceeding local tensile strength. This can be mechanically or thermally induced. The multiphase nature of rocks produces stress and strength heterogeneity even under a uniform macroscopic stress. Stress concentrations arise from crack tips and grain contacts geometries (which dictates the location, magnitude and orientation), which then leads to the initiation and propagation of cracks, (fig. 2.4.2.1.a.).

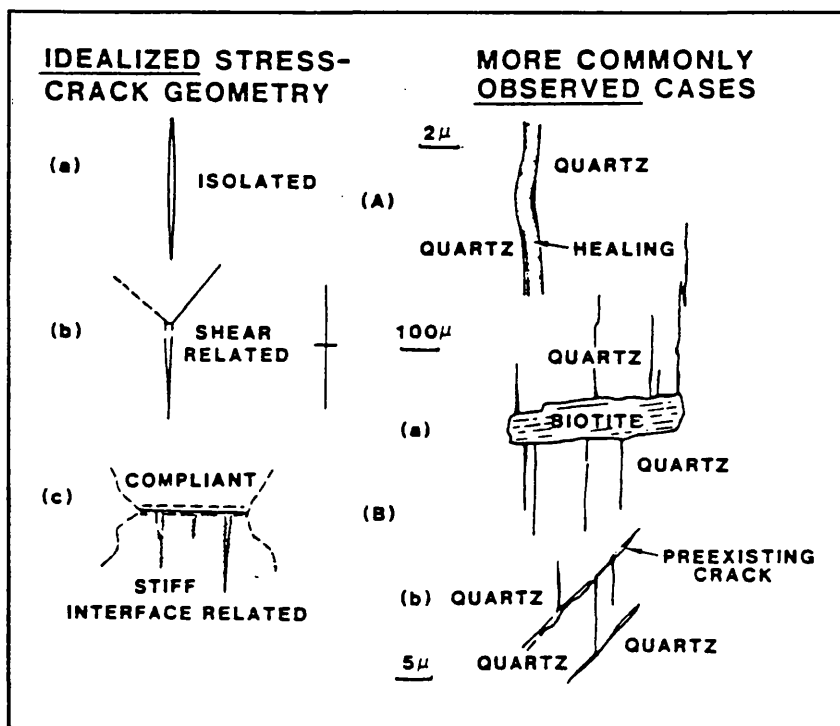


Fig. 2.4.2.1.a. Idealised and observed microcrack nucleation mechanisms, (After Tapponier & Brace, 1976).

- ▶ Movement between twin lamellae generates stress when in contact with grain boundaries and causes crack growth at the twinning site (Olsson & Peng 1976).
- ▶ Microcracks develop normal to kink band boundaries as a result of deformation accommodation problems either side of a kink band, (Carter & Kirby 1978).
- ▶ Cleavage planes represent planes of greatest crack growth vulnerability.

- ▶ Point and line contacts at grain boundaries cause stress concentrations and usually initiate *mode I* extensional cracking.
- ▶ Stress concentrations around cavities, dependent on crack geometry and orientation, initiate cracking.
- ▶ Stiffness mismatch between adjacent minerals under a common stress field can initiate cracking due to differential strain and consequent stress concentration (Dey & Wang 1981). Calculations have shown tensile stresses of the order of 100MPa are possible.
- ▶ Grain rotations and translations can occur under deviatoric stress causing intergranular cracks. The interface strength of quartz and feldspar bonds has been found to be under 10MPa, (Savanick & Johnson 1974). In crystalline rocks rotations and translations are found to be more difficult because of tighter interlocking, although they can occur during cataclastic flow.
- ▶ Wing crack nucleation and growth at the tips of favourably inclined pre-existing flaws, (see fig. 2.7.2.a.).

#### 2.4.2.2. Ductile Mechanisms.

Ductile deformation is prevalent at elevated temperatures and low strain rates ( $\approx 600^\circ\text{C}+$ , and  $< 10^{-9}/\text{s}^{-1}$ , depending on rock type), and the transition from brittle to ductile behaviour is positively correlated to grain size. Whereas brittle fracture results in differential strain in the rock, ductile mechanisms tend to cause uniformly distributed strain throughout the rock. Brittle mechanisms exists up to much higher temperatures in tension than in compressive failure, indeed up to melting point at high strain rates (Murrell 1990). A number of *creep mechanisms* for ductile flow have been identified in rocks despite most of the research, for commercial reasons, being applied to metals. Different ductile mechanisms can act together or independently,

and a brief synopsis of those mechanisms is presented below; for a comprehensive review see Barber (1990).

- ▶ ***Dislocation Gliding.*** Dislocation in material arises from the migration of a flaw by transfer of atomic bonds. By this method the dislocation travels and causes material strain. Dislocation migration inevitably interacts with obstacles (grain boundaries, precipitates), and it is the rate with which the dislocation can overcome these obstacles that governs overall material creep.
- ▶ ***Diffusion Creep.*** This mechanism is predominant at high temperatures and low stresses and can be found in conjunction with Grain Boundary Slippage (GBS). Deviatoric stress causes gradients in chemical potential giving rise to diffusive fluxes of vacancies and atoms. This allows grains to change shape and sliding to occur at grain boundaries. If creep occurs by this process without opening intergranular cracks, material integrity is maintained.
- ▶ ***Grain Boundary Slippage.*** This often occurs in conjunction with diffusional creep, especially when the grain size is small. GBS is not self-sufficient because it produces excess material and voids which must be accommodated by other processes.
- ▶ ***Pressure Solution.*** This is the migration of solids by solution. Dissolution in regions of high pressure, followed by fluid migration and deposition in regions of lower pressure causing mass transfer and resulting in creep behaviour in the rock.

The combination of any or all of these processes causes fracture free strain in geological materials.

### **2.4.3. Brittle Deformation under Compressive Triaxial Stress.**

## 2.4.3.1. Overview of Deformation Modes.

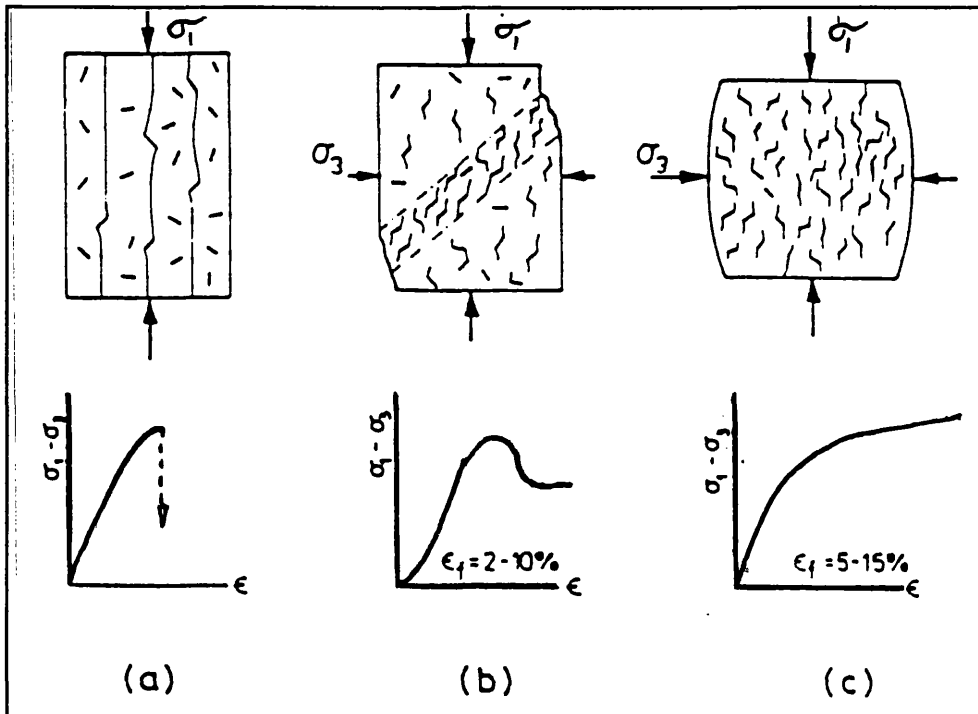


Fig. 2.4.3.1.a. Brittle failure modes under differential axial stress and increasing confining pressure, see text. (After Ashby and Hallam 1986).

The application of confining pressure on rock during deformation has the effect of increasing the ultimate strength of the rock. A number of different deformation *modes* occur in the rock as the confining pressure is increased. These are briefly described below before a more detailed review in later sections. See fig 2.4.3.1.a.

- ▶ Under uniaxial compression (zero confining pressure) the rock fails by tensile crack growth parallel to the axis of maximum principle stress, called *slabbing* or *splitting*.
- ▶ A low confining pressure is all that is required to change the mode of deformation from the above to a shear band inclined to the maximum principle stress at 20°-30° on which all post failure displacement is accommodated. The developments leading to the formation of this fault plane involve the initiation, extension and coalescence of tensile microcracks, and the localisation of displacement on the embryonic

fault plane. Singular dilatant tensile crack growth is inhibited by confining pressure.

- ▶ Higher confining pressure inhibits tensile crack growth to the extent that the development of a shear band is inhibited. This occurs when the shear strength becomes less than the frictional strength (Murrell 1965), and no stress drop occurs. Strain is accommodated throughout the specimen. This is cataclastic flow - macroscopic ductility although internal mechanisms are brittle involving the nucleation but minimal extension of microcracks. Dilatancy and *strain hardening* is reported to occur throughout deformation, (Jones 1988).
- ▶ Finally, when confining pressure and temperature are sufficiently high dilatancy and its associated mechanisms are largely inhibited, and non-dilatant mechanisms such as crystal plasticity and dissolution/precipitation dominates, (Murrell 1990).

Peak strength is slightly strain rate dependent in the brittle field; an increase in strain rate of two orders of magnitude causes a 10% increase in strength, although with the presence of fluid, *dilatancy hardening* must be considered (section 2.4.3.4.). Elevated temperatures affect deformation through partial rock melting or *high temperature embrittlement*. The latter is due to mineral phase changes releasing fluid and affecting the *effective confining pressure* of the rock. A good overview of brittle deformation can be found in Paterson (1978).

#### 2.4.3.2. Effect of a Hydrostatic Stress.

Under the influence of a purely hydrostatic load, existing pores and cracks tend to close causing a reduction in rock porosity. Studies have shown that thermally induced microcracks with well matched but irregular crack faces close easily and fully, whereas mismatched crack faces suffer only partial closure (Batzle et al. 1980). The same study also found that whilst some cracks close, cracks of a different orientation nucleate due to grain rotation

and rearrangement. Kranz (1983) postulated that differential crystal compressibility should produce differential crystal strain, inducing cracking, and Todd (1973) found AE during hydrostatic loading of rock, although he attributed it to grain crushing. In a hydrostatic loading study on sandstone, Zhang et al. (1990), found an inflection point on the stress/strain curve at a certain *critical hydrostatic pressure* signifying pore collapse (grain crushing). The mechanism suggested as responsible was Hertzian cracking at grain contacts. After this point rock porosity fell rapidly under subsequent loading. This critical pressure was found to be inversely related to porosity and grain size, (see section 6.3.1.1.).

#### 2.4.3.3. Effect of a Deviatoric Stress Field.

Under a macroscopic deviatoric stress field, a complex microscopic stress system occurs as a result of structural and mineralogical heterogeneities. Local crack tip stress intensities can be much higher in magnitude than the macroscopically applied stress field, and the principles of fracture mechanics apply for the consideration of crack growth, (section 2.5.5.). Observations show that the realities of crack growth deviate somewhat from model idealisation, (Swan 1975): the vast majority of micro-cracks appear to be extensional mode I cracks - section 2.5.5. although this may be because shear displacements (*modes II and III*) are too minimal in magnitude to be noticed or preserved for post-deformation analysis.

#### 2.4.3.4. Effect of Pressurised Pore Fluids.

Fluids affect rocks both *mechanically* and *chemically*. The early theory of *effective stress* of Terzaghi, concerned the mechanical effect.

A fluid saturated body of rock sufficiently large that its grains and pores do not detract from its being considered homogeneous, under natural conditions, is subject to both a macroscopic stress field and a pore fluid pressure. Both these components are effective in describing the material's gross mechanical behaviour be it elastic, inelastic, shear or consolidation. Dependence on the

separate stress components can be expressed through the *law of effective stress*, (see section 2.3.1.).

There is a great deal of experimental evidence validating Terzaghi's principle. Fig.

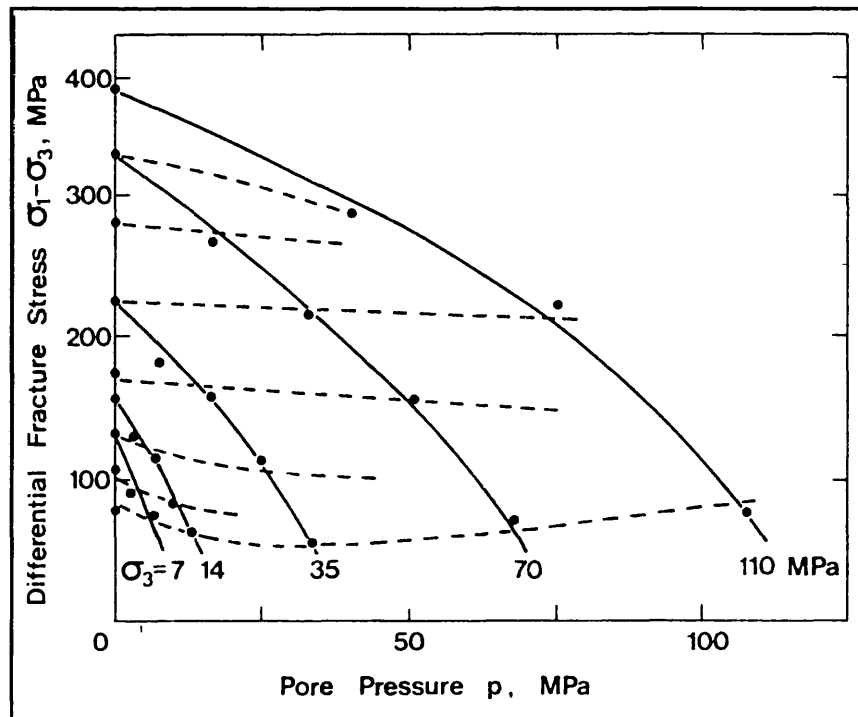


Fig. 2.4.3.4.a. Influence of pore fluid pressure on differential stress at fracture under various confining pressures. (After Murrell 1965).

2.4.3.4.a. shows results of experiments on sandstone at various pore and confining pressures.

It clearly indicates the consistency with which the effective stress law is obeyed. In this situation  $\alpha$  is 1. However, exceptions to this have been noted, for example the value of  $\alpha$  equals four for permeability in Berea sandstone (Zoback & Byerlee 1975a). These anomalies prompted Handin (1963) to note that for  $\alpha = 1$  in the effective stress, the following criteria must be obeyed: (i), that the interstitial fluid is inert, therefore ensuring the fluid/rock interaction is purely mechanical, (ii), that rock permeability is sufficiently high to ensure even and full distribution of pore fluid pressure throughout the rock, (iii), that the rock is a "sand-like aggregate" with connected pore space, ensuring complete fluid circulation and full pressure transmittal throughout the solid phase, and (iv) the rock is fully saturated and the fluid incompressible.

It is pertinent at this stage to briefly explain two modes of triaxial testing involving pore fluid pressure control and measurements;

- **Drained** conditions permit fluid to pass into and out of a specimen of rock during deformation as pore fluid volume varies with crack closure

(compaction) or dilatant crack growth. In this mode pore fluid pressure is kept constant and changes in pore fluid volume are measured (section 4.4.2.). Under natural conditions this mode of experimentation is analogous to deforming rock being surrounded by a highly permeable rock. Hence deformation induced porosity changes prompt fluid flow rather than fluid pressure changes.

- *Undrained* conditions prevent flow of fluid into and out of the rock during deformation, and cause fluid pressure to change under crack closure or dilatant crack growth. In the field this mode is analogous to a highly *impermeable* surrounding rock hence fluid pressure may accumulate and induce weakening of the rock due to a reduced effective stress.

The two experimental conditions above represent extreme conditions of an infinite fluid reservoir connected to the deforming rock (drained), and an fully impermeable capping rock preventing fluid flow (undrained). In natural rock conditions exist somewhere between these two extremes - on compaction porosity reduction induces high pore fluid pressure followed by fluid flow from the region of high fluid pressure to regions of low pore fluid pressure (seismic pumping - Sibson et al. 1975).

A limit to the law of effective stress was found by Rutter (1972a), (and Bernabé & Brace, 1990), in a study on Limestone of 5.3% porosity. At a strain rate above  $10^{-6}/s^{-1}$ , using both a chemically active pore fluid (water) and a chemically inactive pore fluid (acetone), rock *strengthened* relative to lower strain rates. The given strain rate at which a rock was found to strengthen under these circumstances is named the *critical strain rate*. This phenomenon, found

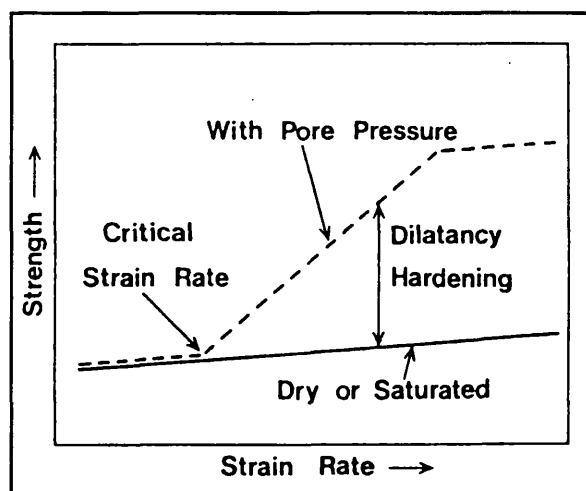


Fig. 2.4.3.4.b. Concept of dilatancy hardening and critical strain rate derived from observations, (After Brace and Martin, 1968).

under drained conditions, is called *dilatancy hardening*. Its mechanism is dependent on permeability, pore fluid viscosity, and strain rate. It is a consequence of sudden increases in dilatant crack growth occurring whilst adequate fluid flow required to equalise fluid pressure throughout the rock is inhibited by permeability limitations. This causes a reduction in pore fluid pressure within zones of the rock and an increase in the effective confining pressure acting on that region. The rock therefore strengthens. Fig. 2.4.3.4.b. schematically illustrates the concept through experimental results.

### 2.4.3.5. Effect of Elevated Pressure on Deformation.

Apparent macroscopic ductility is the result of intense microscopic brittle activity and relative particle movement within the rock. Similar processes (particle movement and associated dilatancy), are found in soils and aggregates. Above certain confining pressure specific to a given rock type, dilatant tensile microcracking is inhibited. The microcracks fail to reach a critical length at which interaction commences (crack length = crack spacing - section 2.6.2.), and strain becomes uniformly distributed throughout the material as cracks initiate pervasively throughout the rock. The material then deforms without gross brittle fracture.

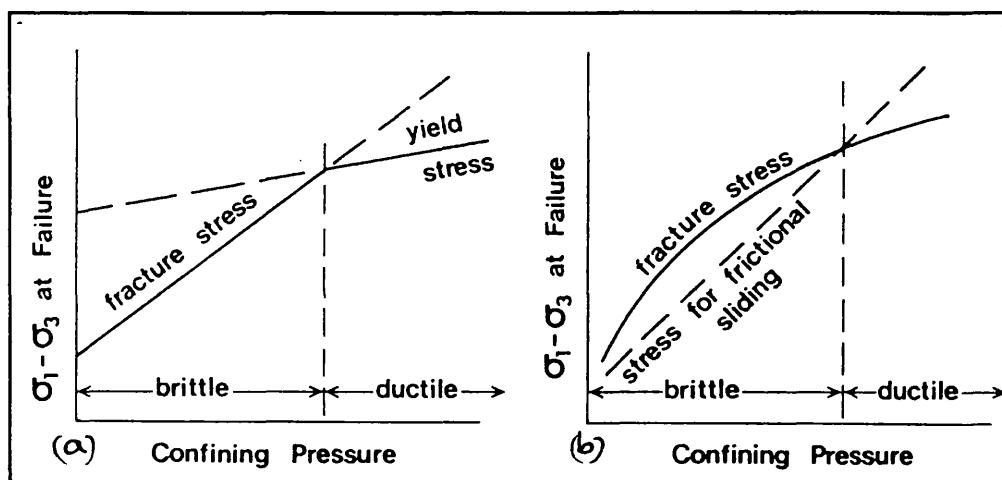


fig. 2.4.3.5.a. Simple model for the brittle/ductile flow (a), and brittle/cataclastic flow transition (b), (After Paterson 1978).

From a purely macroscopic analysis it can be said that the shift from macroscopic faulting to macroscopic ductility occurs "when the confining stress is sufficiently high for the differential stress for faulting failure to equal

the differential stress for frictional sliding", (Murrell 1965). This is illustrated in fig 2.4.3.5.a. The observed effects on deformation of a confining pressure great enough to induce *cataclastic flow*, when compared to brittle faulting is to increase the strain at which peak stress occurs and the differential peak stress. It is further signified by intense post peak AE generated through microcracking, coincident with work hardening under increasing strain.

Broadly, since pressure inhibits dilatancy, confining pressure impedes the formation of a fault plane. Under even higher confining stresses dilatancy associated with cataclastic flow is inhibited and crystalline plasticity becomes dominant: crystal plasticity being a non-dilatant process and therefore non-pressure dependent. Post-peak behaviour under cataclastic flow involves strain hardening - rising resistance to load under increasing strain. A phenomenon known as *high-pressure embrittlement* has been noted by a number of workers; after large cataclastic flow strains (15%), the rock behaves in a brittle fashion. This is thought to be due to a *critical rock density* after which unstable behaviour begins.

The interplay between dilatant crack growth and cataclastic rock compaction is one that makes the transition from macroscopically brittle to macroscopically ductile deformation a gradual one. In this study, experimentation has elucidated details on this interplay, the results of which are in section 6.4.3.

## 2.5. Brittle Crack Growth in Geological Materials.

### 2.5.1. Introduction.

The pursuit of a physical explanation behind brittle behaviour has led to a number of developments. Engineers interested in the behaviour of *rock masses* have concentrated on the joints and bedding planes (planes of weakness) to describe the behaviour of the mass as a series of blocks. Material scientists on the other hand, have concentrated on the behaviour of the material matrix -a poly crystalline aggregate - to investigate physical

processes occurring in rocks which are then used to describe macroscopic material behaviour. Analysis of material behaviour ranges from the empirical approach to recent models based on the physical processes of deformation. Empirical models describe the maximum load a material can withstand before failure with no attention paid to internal physical processes, whilst later models employ *damage mechanics* - the mechanics of the growth and interaction of populations of microcracks - to determine material behaviour and strength.

This section is a review of the initial developments behind the determination of the strength of solids, and an examination of damage mechanics as a tool for describing and predicting the behaviour of geological materials under stress.

### 2.5.2. Empirical Models.

These models are based on a limiting stress or strain that a solid is able to withstand prior to failure. Their function is to provide a basis for calculating the peak strength of a material.

Coulomb (1773) and Mohr (1900) were the first to develop criteria to describe rock behaviour, and their methods are still used extensively. Peak stress is given as a function of maximum and minimum principal stresses ( $\sigma_1$  and  $\sigma_3$  respectively), whilst the intermediate principle stress is disregarded. The Coulomb criterion is based on two variables; the *cohesion*, and the *angle of internal friction*, which are material specific and describe the maximum shear stress a material can withstand. The Mohr criterion can be easily visualised on a graphical plot connecting  $\sigma_1$  and  $\sigma_3$  in shear stress/normal stress space, each point lying on the circumference of a single circle - the *Mohr Circle* (Jaeger & Cook (1979) for more details). Graphically the angle of faulting failure in a specimen of rock can be found from the plot (see fig 2.5.2.a, b, & c.), along with an experimentally derived *Mohr envelope* describing material behaviour under a variety of stress conditions. As can be seen from the figure, the Mohr envelope is concave downwards and describes an increasing

angle between the maximum principle stress and the failure plane - this is borne out experimentally.

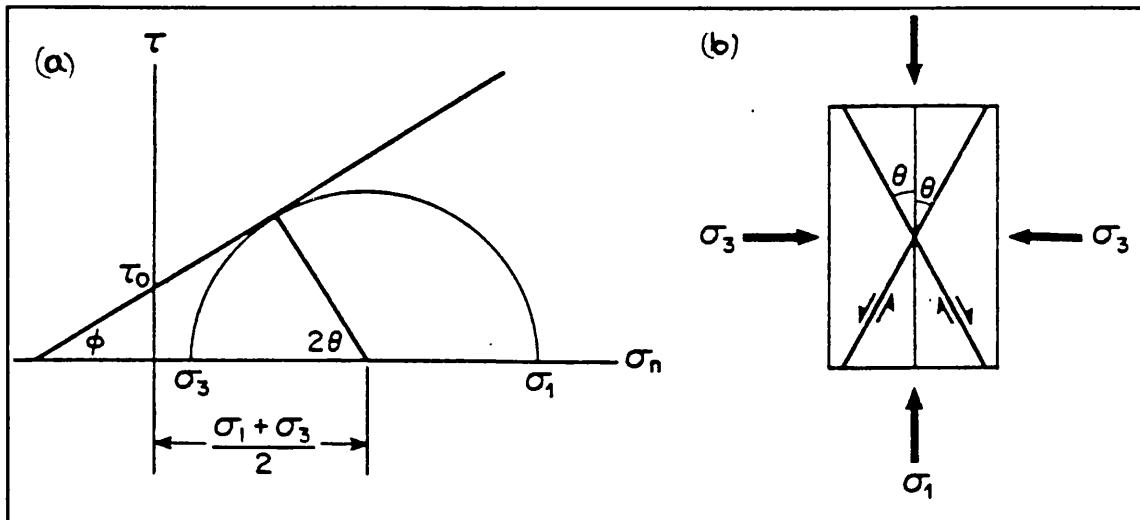


Fig. 2.5.2.a. Illustration of the Coulomb fracture criterion by means of a Mohr circle. Right diagram shows the angular relation between fracture planes and principal stresses, (After Scholz 1990)

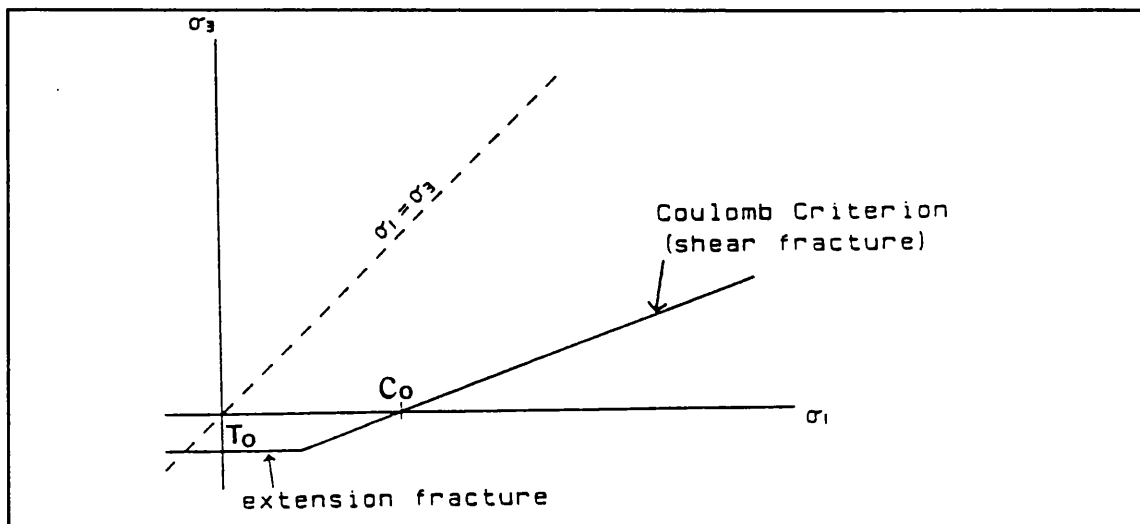


Fig. 2.5.2.b. Coulomb criterion in principal stress space, (After Rist 1989).

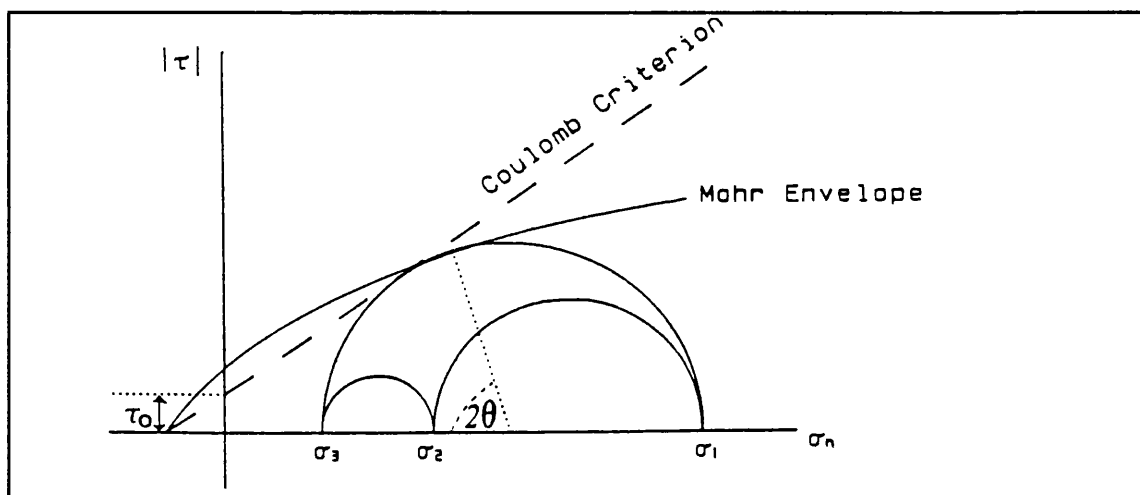


Fig. 2.5.2.c. Mohr failure envelope. (After Rist 1989).

With respect to Mohr Circle rock mechanics analysis the introduction of a pore fluid pressure reduces the maximum and minimum principal stress to the effective maximum and minimum principle stress, shifting the Mohr circle towards lower values of compressive normal stress. It can easily be observed that at sufficiently high pore fluid pressures the Mohr circle touches the fracture envelope, hence the rock fails. By considering pore fluid pressure prior to a Mohr's circle analysis the maximum pore fluid pressure sustainable by a body of rock can be obtained.

### 2.5.3. Single Crack Analysis Approach.

The *Griffith Theory* was the first attempt at describing the physical processes occurring within materials as a cause of failure. Based on experiments on glass, Griffith (1920, 1924) explained the weakness of glass compared to its theoretical atomic bond strength by the existence of flaws and cracks in the glass. Considering a 2-D case in a tensile stress field, stress concentrations around flattened elliptical cracks whose tips have a finite radius of curvature, caused the most favourably orientated crack in a random crack population to propagate. The criterion for crack extension is based on minimising the *Gibb's potential energy*. That is, a crack will propagate if the sum of, (i), the surface energy of the new crack ( $U_S$ ), (ii), change in elastic strain energy of the body ( $U_E$ ), and (iii), change in potential energy of the loading system ( $U_A$ ), is equal to or less than zero. In macroscopic tension local crack tip stress is enhanced by initial crack growth, so that crack growth velocity accelerates, leading to material failure.

Considering rock in compression, crack extension in its own plane can no longer be assumed and indeed evidence to that effect is now available (Brace & Bombolakis 1963). Hence, knowledge of crack growth direction is necessary for precise energy balance analysis. To tackle this Griffith's approach changed from an energy criterion to a tensile strength criterion; this allowed accurate analysis to be conducted for crack growth in any plane.

The *Griffith Criterion* applied to a compressive stress state comprises, (i), establishing the tensile stress in the surface of a cavity in the solid, (ii), determining the crack orientation to yield the greatest local tensile stress and calculating the applied stress for the critical local tensile stress, and (iii), expressing the critical tensile stress as uniaxial tensile strength, ( $T_0$ ).

The form of the Griffith Criterion is as below.

$$(\sigma_1 - \sigma_3)^2 - 8T_0(\sigma_1 + \sigma_3) = 0 \quad \text{if } \sigma_1 > -3\sigma_3 \quad (2.5.3.a.)$$

$$\sigma_3 = -T_0 \quad \text{if } \sigma_1 < -3\sigma_3 \quad (2.5.3.b.)$$

The criterion predicts a compressive strength to tensile strength ratio of 8:1 which is rather less than that found experimentally. However, it accurately predicts propagation of cracks away from the major axis of the existing flaw, towards the axis of major principal stress. Fig 2.5.3.a. represents the above criterion graphically.

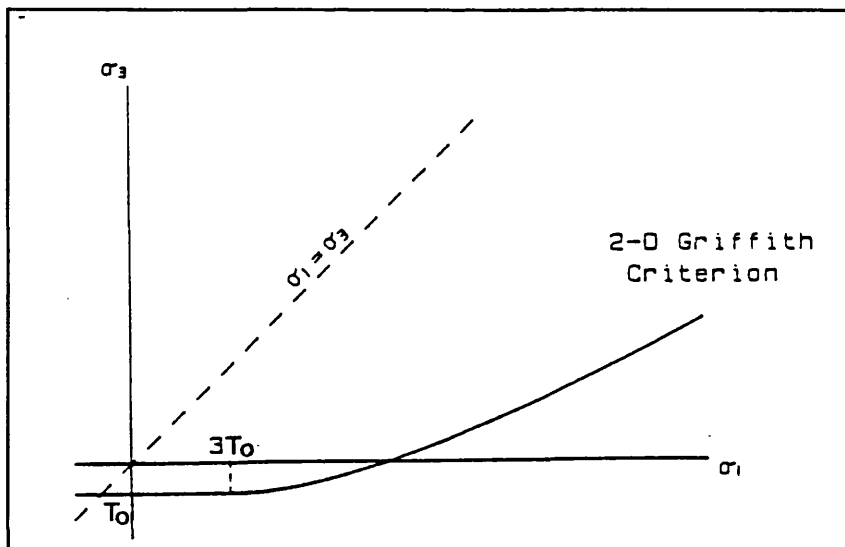


Fig. 2.5.3.a. The two dimensional Griffith criterion expressed graphically, (After Rist 1989).

#### 2.5.4. Modifications to Griffith Criterion.

A *3-D modification* of the Griffith criterion by Murrell (1963), considers the effect of an intermediate principal stress ( $\sigma_2$ ) on rock strength, and gives a

more realistic *compressive : tensile* strength ratio of 12:1. The complete solution for a randomly orientated population of flaws is found in Murrell & Digby (1970). The solution also considers the phenomena of *closed cracks*, and *pore fluid pressure*. The Griffith criterion considers only open cracks and therefore avoids problems relating to inter-crack-face friction and normal forces being transferred across crack faces. In reality, cracks close under a moderate confining pressure and on closing change the physical conditions of deformation. The problem of what force is required to close the cracks, and the transition between the open state and closed state for a population of cracks, is one which has generated much attention over the years. Murrell (1964) calculated the crack closure stress for the 2-D case and Murrell & Digby (1970) did it for the 3-D case.

Whilst the Griffith theories and their subsequent modifications are the first attempts to describe rock fracture on the basis of the microscopic physical processes involved, they do suffer from a number of short comings;

- (i), uniaxial compressive : tensile strength ratios are too low unless an unrealistic value for crack face friction is adopted,
- (ii), the observed effect of  $\sigma_2$  is not fully unaccounted for,
- (iii), the predicted and actual Mohr envelopes do not agree.

These deficiencies are better appreciated when one considers that the models consider only the micro-mechanical behaviour of single micro-cracks. In reality rock failure in compression involves the complexities of the growth and linkage of multiple populations of cracks, with crack growth in compression beginning at deviatoric stresses far lower than the final macroscopic failure stress. This last simple fact helps explain why rocks in compression are so much stronger than in tension.

The following points are not addressed in the above criteria but are important considerations for more rigorous analyses of rocks failure in compression.

- (i), propagating microcracks in a compressive stress field grow out of plane due to rock heterogeneities and so lose the most favourable orientation for growth,
- (ii) as the deviatoric stress increases, less favourably orientated flaws will undergo crack extension and the final rock structure will be a matrix of assorted cracks lengths - the fault plane will be the result of the interaction of an ensemble of cracks under their modified stress fields,
- (iii) cracks perpendicular to  $\sigma_2$  are inhibited under the influence of  $\sigma_2$ , and
- (iv), initial crack size variations and random orientations will contribute to anisotropy and specimen size effects. These points are the basis for a later generation of deformation models covered in section 2.7.

As mentioned above, the energy balance approach meant that the energy gained by the creation of a new crack surface ( $U_E$ ), equalled the strain energy lost in the material and in the loading system ( $U_M$ ) as a consequence of the growth of the crack. In reality, much more mechanical energy is absorbed through irreversible processes involved in separating the material, i.e. materials displayed different *degrees* of brittleness, (Lawn 1993).

### 2.5.5. Linear Elastic Fracture Mechanics (LEFM).

The theory of *Linear Elastic Fracture Mechanics* relies on analysing stress levels in the immediate vicinity of a given crack from the macroscopic stress field through classical linear elasticity theory, and the resistance of the material body to this level of stress. The following assumptions are made when analysing the crack tip stress intensity; (i), any zone of non-linear behaviour around a crack tip (*process zone*) is negligibly small compared to crack length, (ii) the crack tip has a radius of atomic dimensions, and (iii) the crack walls are traction free. A full treatment of this subject is found in Lawn (1993). This analysis yields equations 2.5.5.a. and 2.5.5.b., which show near-field material stress and displacement respectively about a crack tip where in

polar co-ordinates;  $i$  and  $j$  are components of the stress tensor,  $r$  and  $\Theta$  are radial distance and angle from the crack tip, and  $f(\Theta)$  is a well defined function of  $\Theta$  that depends on loading geometry.

$$\sigma_{ij} = K_m \cdot (2\pi r)^{-1/2} \cdot f_{ij}(\Theta) \quad (2.5.5.a.)$$

$$u_i = K_m \cdot (2E)^{-1/2} \cdot (r/2\pi)^{1/2} \cdot f(\Theta) \quad (2.5.5.b.)$$

The term  $K_m$  is the *stress intensity factor* and describes the intensity of the stress field at any point about the crack tip. The subscript ( $m$ ) denotes one of three *modes* of fracturing - *I*, *II*, or *III*. These refer to, (i), simple *tensile* loading of a crack, (ii) *shear in the plane* of crack propagation, and, (iii) *shear normal to the plane* of propagation. Fig 2.5.5.a. illustrates these modes pictorially.

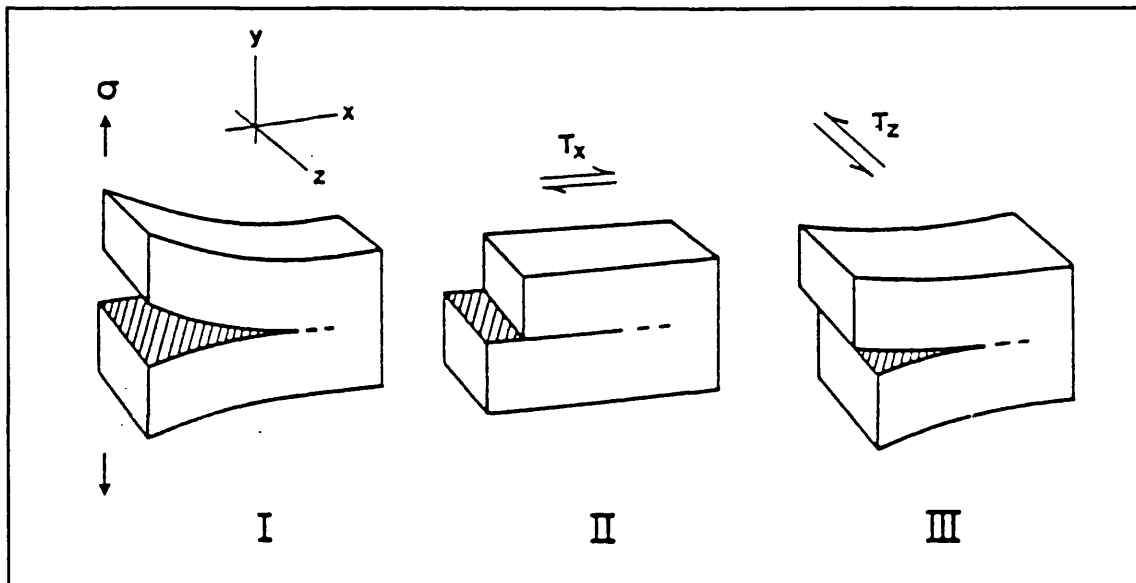


Fig. 2.5.5.a. Basic modes of distortion at a crack tip. Mode I - tensile, mode II - in-plane shear, mode III - antiplane shear, (After Lawn & Wilshaw, 1975).

Crack tip Stress Intensity is found by equation 2.5.5.c. below.

$$K = Y\sigma_r(\pi a)^{-1/2} \quad (2.5.5.c.)$$

Where  $\sigma_r$  is the remotely applied stress,  $a$  is the crack half length, and  $Y$  is a well defined dimensionless geometry and edge effect modification factor. Using the three modes of propagation and converting *stress intensity factor* to *crack extension force*  $G$ , superposition of the modes can describe any combination of modes of propagation. Conditions for crack propagation are met when the stress intensity factor exceeds the *critical stress intensity factor*  $K_c$ . After which crack propagation occurs at sonic speeds, i.e. when  $K_I > K_{Ic}$ , propagation in mode I will occur, and the same for modes II and III. The value of  $K_c$  is material specific and denotes the ease with which fracture can propagate.

In reality, polycrystalline materials present a highly complex situation in which the basic assumptions of LEFM (the limiting size of the region of non-linear deformation), cannot be fully satisfied. If the non-linear region at the crack tip (the *process zone*) is  $>2\%$  of the crack half length ( $a$ ), the magnitude of the crack tip stress field is not completely

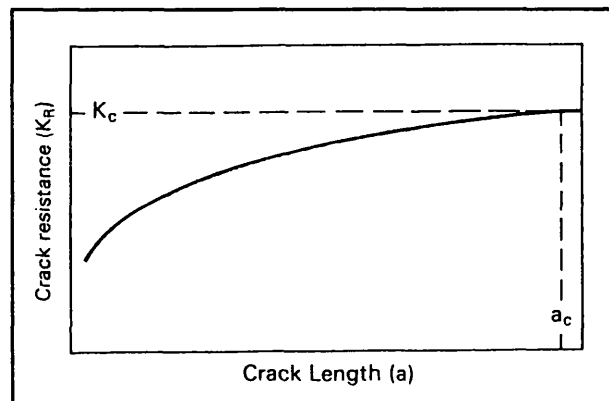


Fig. 2.5.5.b. Schematic diagram illustrating the rising *R*-curve behaviour observed in many polycrystalline materials, (After Barber & Meredith 1990).

characterised by  $K$ . A detailed consideration of the breakdown processes must then be made - resistance to propagation being increased by the presence of the process zone. In this case the term  $K_{eff}$  is used to account this process zone of non-linear behaviour. The zone comprises, (i) intense microfracturing ahead of the crack tip, (ii) crack interface interlocking and traction, and, (iii) ligamentary bridging behind the crack tip. Experimental evidence for this has been obtained from wave velocity measurement across and about a crack tip during propagation, Swanson (1987), and photomicrographs, Freiman & Swanson (1990). A more detailed analysis of process zones and crack propagation is found in Ingraffea (1987).

A final consideration concerns a change in fracture toughness ( $K_c$ ) with crack extension. As a crack grows its resistance to growth increases with length

until  $K_c$  stability is reached (fig. 2.5.5.b.). The value of  $K_c$  can then be assessed as a material property, the process zone having become fully developed, and a portion of the resultant crack having become traction free. This phenomenon is known as the *R-curve*. Prior to this stabilisation,  $K_c$  is a variable dependent not only on the material but on crack length ( $a$ ) hence process zone development.

### 2.5.6. Chemical Effect of Pore Fluids - Sub-critical Crack Growth Mechanisms.

Under the influence of temperature and a reactive fluid (e.g. aqueous), environment the assumptions of LEFM (that of  $K > K_c$ ) break down. Grenet first observed the process that has become known as *sub-critical crack growth* in glass in 1899. Since then its presence has been found in many other materials including polycrystalline rocks (Murrell 1965, and Atkinson 1982). Many different mechanisms can be responsible for this behaviour, and each can occur independently or together depending on specific environmental conditions. The mechanisms are highlighted below:

- ▶ *Stress Corrosion* is the preferential weakening of strained atom bonds (e.g. Oxygen-Silicon bonds) in materials (e.g. silicate rocks), by a chemically active fluid.
- ▶ *Diffusion and Dissolution* (mentioned in section 2.4.2.2.).

Stress corrosion has received attention as the most likely cause of subcritical time dependent failure. Most of the developmental work investigating this theory has centred on tensile crack growth, and "there is no obvious physio-chemical reason why the form of the law used to describe subcritical crack growth, but not necessarily the parameters, should depend on mode", (Das & Scholz, 1981). It is therefore considered applicable to the compressive loading case. It has been employed in many holistic theories for the initiation and propagation of earthquake ruptures and other previously puzzling phenomena, Das & Scholz (1981).

The rate (crack propagation velocity) of stress corrosion cracking is dependent on many factors. Fig. 2.5.6.a. schematically represents the relationship between crack propagation velocity ( $v$ ) and normalised crack tip stress intensity factor ( $K$ ). The normalised  $K/K_c$  axis on the figure indicates crack tip stress intensity between  $K_0$  and  $K_c$  - which are, respectively, the crack tip stress intensity below which sub-critical crack growth ceases, and the crack tip stress

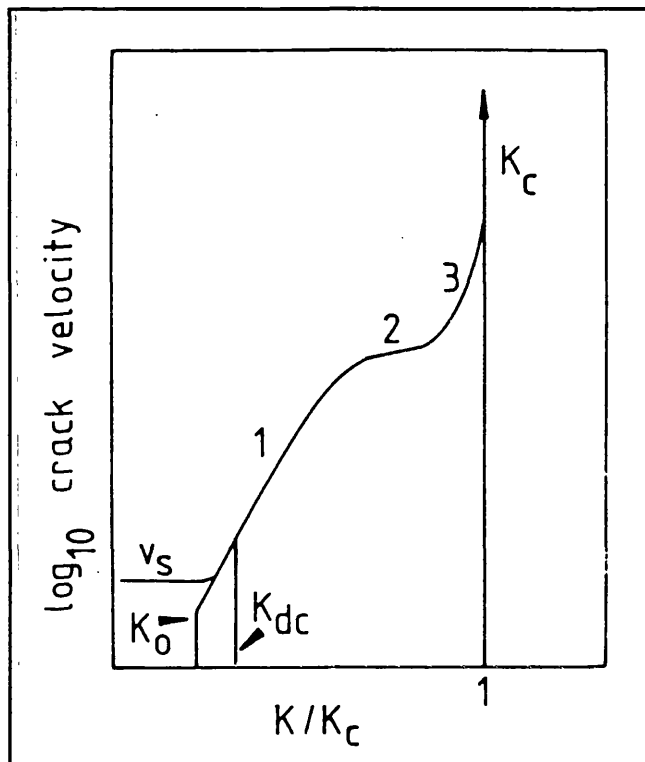


Fig. 2.5.6.a. Schematic crack velocity/normalised stress intensity factor diagram for stress corrosion cracking, see text, (After Atkinson & Meredith 1987)

intensity above which crack growth becomes dynamic. There are three regions within the relationship, depicted as region 1, 2, and 3. In region 1 crack velocity is controlled by the stress corrosion reaction rate, in region 2 the rate of propagation is limited by the rate at which corrosive fluids can replenish *spent* fluids at the crack tip, and in region 3 the approach to critical crack velocity is dominated by mechanical processes, so is unaffected by chemical species. The figure indicates where other mechanisms take over from stress corrosion at low crack tip stress intensities or low crack velocities;  $v_s$  indicates the crack velocity threshold due solely to dissolution, and  $K_{dc}$  indicates the crack growth limit below which diffusion creep dominates.

The effect of temperature on the crack growth rates and hence on the diagram shown in the figure is to shift the curve up the crack velocity axis, i.e., for a given crack tip stress intensity, crack growth velocity is increased. This effect is most marked in region 1 where the heated corrosive fluid are given easiest access to the crack tip, and least marked in regions 2 and 3. Increasing the activity of the corrosive fluid significantly effects crack growth rates in a manner similar to that of temperature - but the effect is sustained

into region 2. Region 3 is unaffected by temperature or chemical activity because it is governed solely by mechanical processes. The effect of confining pressure acts to impede crack velocity in region 2 (limiting active chemical species access to crack tip), increasing the value of  $K_0$  by suppressing the crack tip process zone formation, and has the normal *effective stress law* influence over region 3.

At the microstructural level, as crack velocity decreases, crack growth becomes more intergranular, hence the grain boundary geometry detail controls cracking at geological strain rates.

In this study strain rates were of the order of  $10^{-5}/s^{-1}$ . The results found rock to be far more susceptible to the mechanical effects of pore fluids than chemical effects under these conditions. A programme to isolate sub-critical mechanisms was not specifically conducted, although the effects of chemical activity on pore fluid volume was found during triaxial deformation under high pore fluid pressure, (see section 6.4.3.1.).

## **2.6. Damage Mechanics and Continuum Damage Models.**

### **2.6.1. Introduction.**

Previous sections in this chapter have concentrated on elucidating individual microcrack growth processes. Based on this, *damage mechanics* attempts to relate the physical processes of individual crack growth with gross macroscopic rock behaviour and contemporaneous physical property changes during deformation. In order to achieve this laws concerning the accumulation of damage must consider various mechanisms governing the changing microstructural state of the rock as it deforms. Costin (1987), pointed out that a model to describe the physical state of rock under the accumulation of damage must contain three components; (i), a definition of the state of damage, (ii), an equation to describe damage evolution, and (iii), a constitutive law that relates the state of damage to rock stress and strain.

Broadly the affect of damage on rock can be described by an equation such as the linear one -  $\sigma = E_0 (1 - D)\epsilon$ , where  $D$  represents the state of damage in the material and  $E_0$  represents the *Young's Modulus* of the undamaged rock. Clearly, as  $D$  increases from 0 to 1 - damage density increasing from zero to 100% -  $E$  is degraded. Differentiated where the term  $\delta D$  is damage increment, this yields:

$$\delta\sigma = E_0(1 - D)\delta\epsilon - E_0\epsilon.\delta D \quad (2.6.1.a.)$$

## 2.6.2. Continuum Damage Mechanics Models.

Ashby & Hallam (1986), employed fracture mechanics to describe the growth of *wing cracks* from the ends of existing inclined cracks in a brittle solid. The concept of wing cracks was first postulated by Brace & Bombolakis (1963), to explain dilatancy in rocks. Fig. 2.6.2.a. illustrates crack growth around a pre-existing flaw.

Initial shearing of the flaw under a macroscopic compressive stress field (resisted by friction), loads the tips of the existing crack in the *mode I* fashion. The superposition of this load and the stress concentration around the crack due to the presence of the crack itself initiates crack growth when material fracture toughness ( $K_c$ ) is exceeded. Once initiated crack propagation continues in *mode I*, due to the shearing

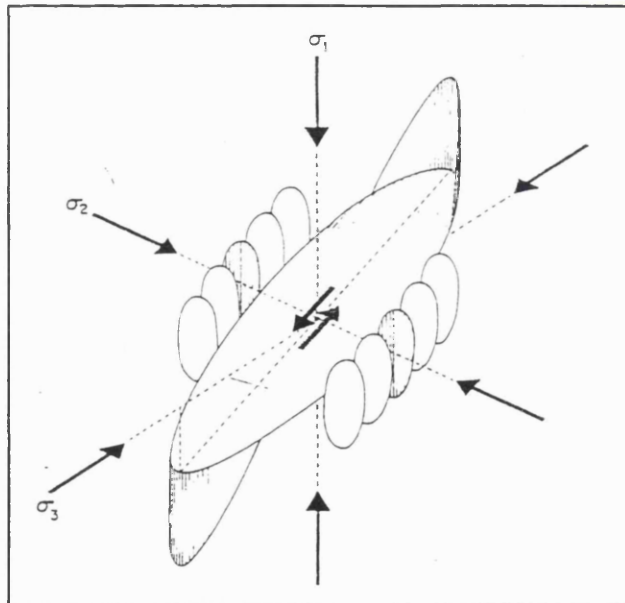


Fig. 2.6.2.a. Schematic illustration of the propagation of shear cracks around an inclined flaw in brittle materials, (After Scholz 1990).

action on the initial flaw. Experiments related to this have been performed by Cox & Scholz (1988b) on *PMMA* (polymethylmethacrylate). Once wing cracks are initiated their driving force is a function of normalised crack extension  $L$ ,

(where  $L = l/a$ ,  $l$  = wing crack length,  $a$  = existing flaw length). When  $L = 0$ , (no growth), the stress intensity factor,  $K$ , is governed by shear on the existing flaw imposing mode I stress on the wing crack tip. When  $L$  approaches unity,  $K$  is governed by the wedging open of the crack by shear strain on the existing flaw. When  $L \gg 1$ ,  $K$  is governed by the confining stress  $\sigma_3$ . If  $\sigma_3$  is large it acts across the entire area of the crack and inhibits further growth, hence crack growth is stabilised. If  $\sigma_3$  is zero or tensional, the mode I stress intensity factor will be enhanced and the crack will *run-away*, i.e. it becomes unstable. Once cracking has become ubiquitous interaction becomes inevitable. In the experiment *beams* or *ligaments* occur between the existing flaws bounded either side by the extended wing cracks (see fig. 2.6.2.b.), and bending of these ligaments adds an additional term to the stress intensity expression. This process leads to axial splitting and slabbing. With the application of only a slight confining pressure, wing crack growth is inhibited, axial splitting prevented, and a transition occurs from slabbing to macroscopic shear failure. The model, whilst addressing the effect of confining pressure on deformation, does not specifically predict the shift to shear failure. Sammis & Ashby (1986) analysed compressive failure of poro-elastic materials by considering tensile crack growth from spherical pores.

The models by Kemeny & Cook (1987), and Horii & Nemat-Nasser (1986) employ wing crack propagation from existing flaws in a similar fashion for their experimental and numerical studies. Kemeny and Cook's model, however, accounts for the curved path the microcracks take during extension (displaying a varied angle to  $\sigma_1$  during extension), which is observed experimentally. The model also addresses the interaction of cracks by the formation of ligaments between the wing crack which support the compressive load through bending and axial compression. Failure then occurs within a single column (axial) or across adjacent columns (shear).

Dilatancy is a fundamental feature of rock deformation and any viable model must be able to reproduce its features. Wing crack growth has been proposed as a mechanism responsible for dilatancy. Models employing this mechanism as an explanation for dilatancy have, however, been criticised for

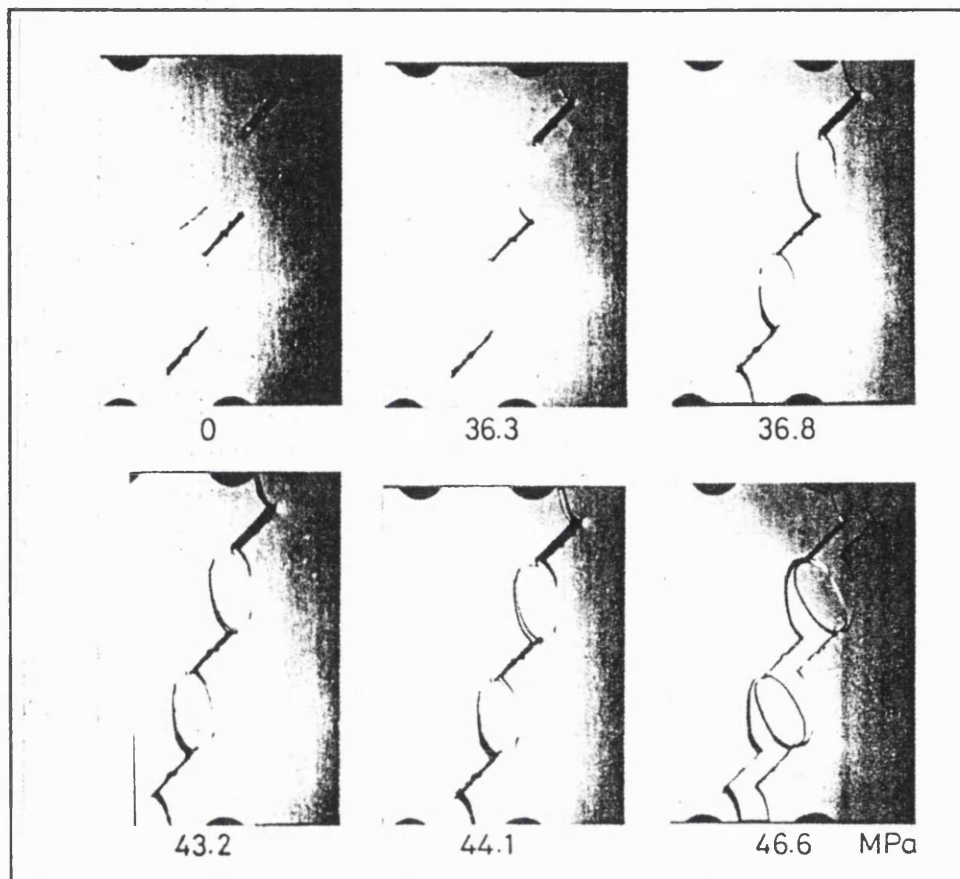


Fig. 2.6.2.b. Sequence of photographs showing crack interaction under an increasing differential stress, (After Hallam & Ashby 1990).

omitting some important observed rock deformation characteristics. For example, elastic wave velocity measurements in granite have indicated immediate elastic recovery upon unloading (immediate crack closure). If wing cracks are the cause of reduced wave velocity during dilatancy, one would expect a certain amount of hysteresis in this measurement due to friction between the faces of the *pre-existing* flaw initially resisting wing crack closure (Stevens & Holcomb 1980). This study has investigated the problem of elasticity and inelasticity of different deformation mechanisms - see section 6.4.3.3.). Furthermore, observations of granite rock sections by Tapponier & Brace (1976), indicate that there are very few well developed sliding surfaces, when compared to cracks with preferred orientations close to the axis of maximum principle stress. In support of this Stevens & Holcomb (1980) show that an array of reversible, axial, tensile microcracks (Griffith cracks), is in better agreement with the observed characteristics of dilatancy, and conclude that this is a more viable model.

Costin (1983, 1985, 1987), developed a model based on single microcrack growth through the principles of fracture mechanics. Local tensile stress, acting normal to the crack, is proportional to the applied deviatoric stress tensor  $S$ , ( $S_{ij} = \sigma_{ij} - 1/3\delta_{ij}\sigma_m$ ), and under triaxial stress conditions this is greatest in those cracks

which have their normal perpendicular to  $\sigma_1$ . It is assumed that the form of the equation describing the response of a single crack is the same as that describing the response of an ensemble of cracks. Hence the model handles a population of collinear tensile microcracks which propagate in their plane parallel to  $\sigma_1$ .

As cracks grow, interaction occurs. Costin uses a different method from Ashby & Hallam for accommodating this, employing instead the "pseudo-traction" technique of Horii & Nemat-Nasser to describe the effect of a decreasing crack spacing on  $K$ .

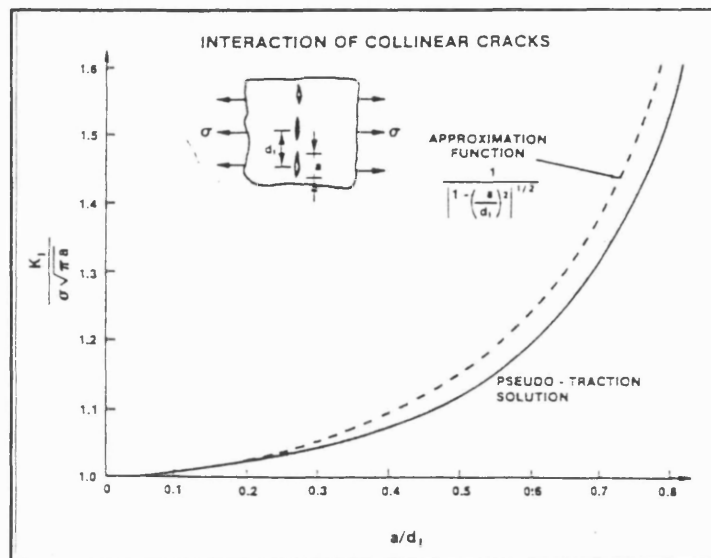


Fig. 2.6.2.c. The effect of interaction between an array of collinear cracks on the stress intensity factor (after Costin, 1985). Pseudo-traction solution (Horii & Nemat Nasser, 1985).

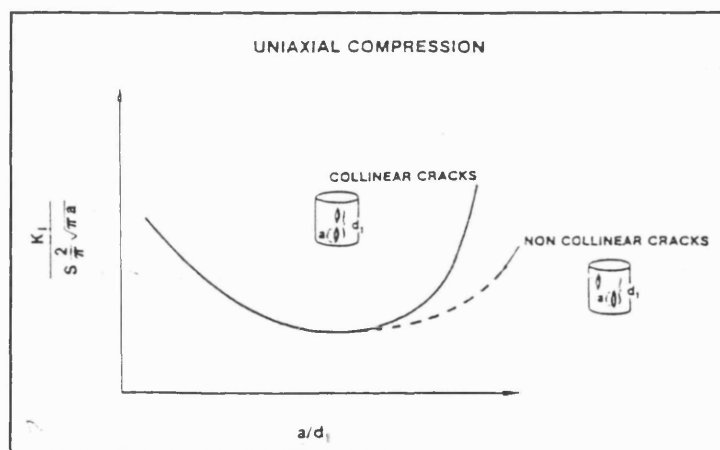


Fig. 2.6.2.d. The affect of interaction between an array of collinear cracks on the stress intensity factor, (After Costin, 1985).

The method is summarised in Gueguen et al. (1990). Figure 2.6.2.c. illustrates the changing stress intensity factor relative to intercrack distance. As the crack length increases, (approaching the intercrack distance),  $K$  increases. Four separate contributions are then considered for computation of overall  $K$ ;

(i) crack interaction effect, (ii), the effect due to the mean stress acting on the matrix to inhibit crack growth, (iii), the deviatoric stress, and (iv), the diminishing stress intensity due to crack extension. Assuming cracks are penny shaped,  $\kappa$  associated with each crack is given by;

$$\kappa_i = \left\{ (2 \cdot (\pi \cdot a \cdot n)^{1/2}) / \pi \right\} \cdot \left\{ \sigma_m + F(a, n, d, d_i) \cdot S \cdot n \right\} \quad (2.6.2.a)$$

The relation can be considered in two parts. The term on the right is an expression for local tensile stress, where  $F$  is the proportionality factor between crack driving mechanisms of crack interaction and deviatoric stress (see equation 2.6.2.b. below),  $d$  the nominal size of the tensile region,  $d_i$  is the initial spacing between interacting cracks,  $S$  is the applied deviatoric stress, and  $a \cdot n$  ( $=a$ ) is a vector whose magnitude  $a$  is proportional to the mean size and density of cracks with normal  $n$ . The other values are also to be thought of as averages. The term on the left is due to the presence of the mean compressive stress,  $\sigma_m$ .

Fig 2.6.2.d. illustrates the changing normalised stress intensity factor  $\kappa$  against crack growth and hence spacing reduction. Initially,  $\kappa$  decreases for an increasing crack length - stable crack growth - a consequence of crack extension relieving crack growth driving force. A certain *critical microcrack length* is then reached after which the effect of crack interaction dominates and  $\kappa$  *increases* with increasing crack extension causing unstable crack propagation. The effect of a decreasing deviatoric stress increment required to maintain  $\kappa_c$  means that damage accumulation (overall crack population extension), can continue under a decreasing compressive stress, leading eventually to failure. *Strain softening* is found experimentally.

Later developments by Costin (1987), consider time-dependent damage accumulation by stress corrosion cracking. The conclusion to the work involves the development of constitutive equations relating stress to strain through the state of rock damage during deformation. These relations are also useful in mapping *damage surfaces* in a  $(\sigma_1 - \sigma_3) / \sigma_3$  space, or a  $s / \sigma_m$  space. That is, an *iso-damage* line in this space connecting points of equal

damage accumulation for a variety of stress conditions based on experimental data indicating damage (e.g. onset of AE, dilatancy). From eq. 2.6.2.a., the gradient of these straight lines was predicted to be 1/the proportionality factor (F), where;

$$F = f \cdot [ \{d/a_o\} \cdot \{1 / [1 - (a_o/d_i)^2]^{1/2}\} ] \quad (2.6.2.b.)$$

Where  $f$  is an empirically derived scaling constant. So, as damage increases,  $F$  decreases, and the *iso-damage* lines become steeper.

Peak strength data can be used to construct a fracture envelope (replacing  $a_o$  with  $a_f$  (failure)), although this is not necessarily a surface of constant damage in the model sense, because the real stress state in a rock is very

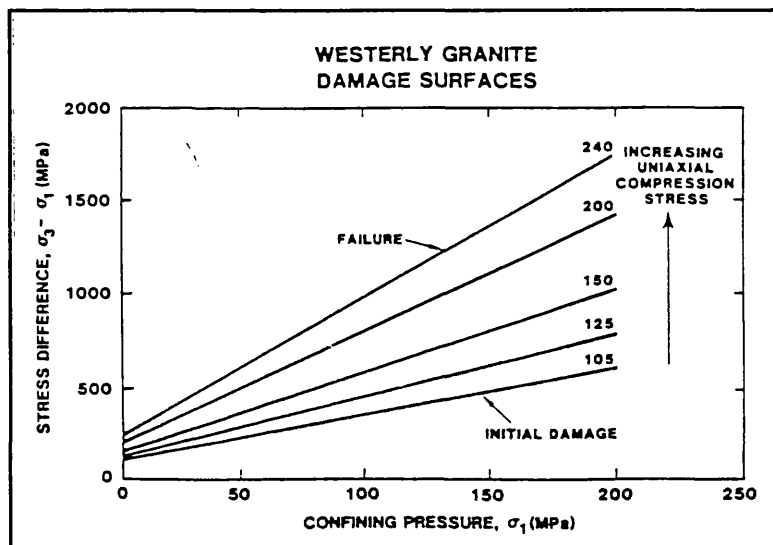


Fig. 2.6.2.e. Lines of constant damage as a function of differential stress vs. confining pressure, (After Costin, 1985).

inhomogeneous. Holcomb & Costin (1986) and Stuart (1992), used the *Kaiser Effect* (The effect relies on the fact that AE only occurs when *new* fractures are formed. Thus AE will only begin after a previous stress level has been exceeded.), to monitor the commencement of damage accumulation for a variety of stress conditions, and found the loci of points for a variety of stressing states were, indeed, straight lines, see fig 2.6.2.e. confirmed Costin's predictions. Stuart (1992) pointed out that the damage state was also dependent on the stress path.

All the models developed to date utilise a simple array of uniform sized microcracks in order to handle the complex problem of failure in geological materials in compression. However, observation of rocks (Kranz 1983), and experimental AE and earthquake seismicity data (Meredith, Main & Jones 1990), indicate a power law crack size distribution. Clearly, modelling rock deformation in compression is complex and has much development work outstanding. Shortfalls to date lie with the description of an initial distribution of crack populations, with time dependent cracking effects, and with a realistic model of the interaction of extending microcracks. Nevertheless, attempts so far have gone some way to describing the nucleation and growth of microcracks which then coalesce to bring about macroscopic rock failure.

## **2.7. Holistic Studies of Interaction Between Stress, Rock Deformation, and Evolution of Crack and Pore Microstructure.**

### **2.7.1. Introduction.**

Directly observing microstructural developments during rock deformation is a desirable although extremely difficult task to undertake. Some SEM studies have been done (Swanson 1987), although they are possibly rather unrepresentative due to the vacuum environment required (no chemical activity), and very small samples size necessary. Another direct observation techniques involves removing the specimen after a certain amount of deformation, preparing a *section* of the sample, and examining it under either optical or electron microscope. This method has been used extensively and has yielded some interesting results. It does, however, suffer problems concerning the preparation technique (cutting, grinding), affecting the state of damage in the sample, and the unknown effect on rock microstructure of removing the rock from the stress field.

Hence a number of techniques have been developed over the years which are capable of monitoring internal microstructural processes contemporaneously

with deformation through remotely monitoring the physical changes in the rock. They include (i) acoustic emissions, (ii) elastic wave velocity, (iii) pore fluid pressure or volume changes, and, (iv) permeability. The following subsections address these techniques. Some recent experimental results are described, and attempts to use these *external indicators* of internal microstructural change to describe rock deformation are reported. In the present study acoustic emissions and pore fluid volumetry are used.

## 2.7.2. Microstructural Monitoring Techniques.

### 2.7.2.1. Acoustic Emissions.

Acoustic activity during deformation was first noticed by Obert & Duval (1942) when they loaded rocks in compression. They attributed the activity (correctly) to *micro-cracking*. The obvious similarity between AE and field micro-seismicity has led to laboratories throughout the world making significant advances in the pursuit of AE research. Being a natural by-product of brittle crack formation and growth, it presents itself as a useful tool for investigating the mechanics of brittle failure in rocks.

The study of brittle processes has developed in a number of directions and these are briefly covered below. Section 4.6. discusses the terminology and AE phenomena that are used to monitor damage accumulation.

*Fracture Event Location.* Employment of four or more transducers and analysis of elastic wave arrival times allows the 3-D location of cracking events to be mapped. Fifteen or more transducers are commonly used for greater accuracy, allowing the source event to be located to within 2mm. The method is analogous to seismic networks for locating earthquakes. Using an AE feedback system to control axial stress and hence AE event rate (to slow down the localisation of events and strain), Lockner et al. (1992) successfully mapped fault nucleation and development, (see fig 2.7.2.1.a.).

The results show pre-nucleation activity, fault nucleation and fault propagation clearly. During fault growth the fault front was seen to propagate erratically, sometimes accelerating and sometimes decelerating at different segments of the fault.

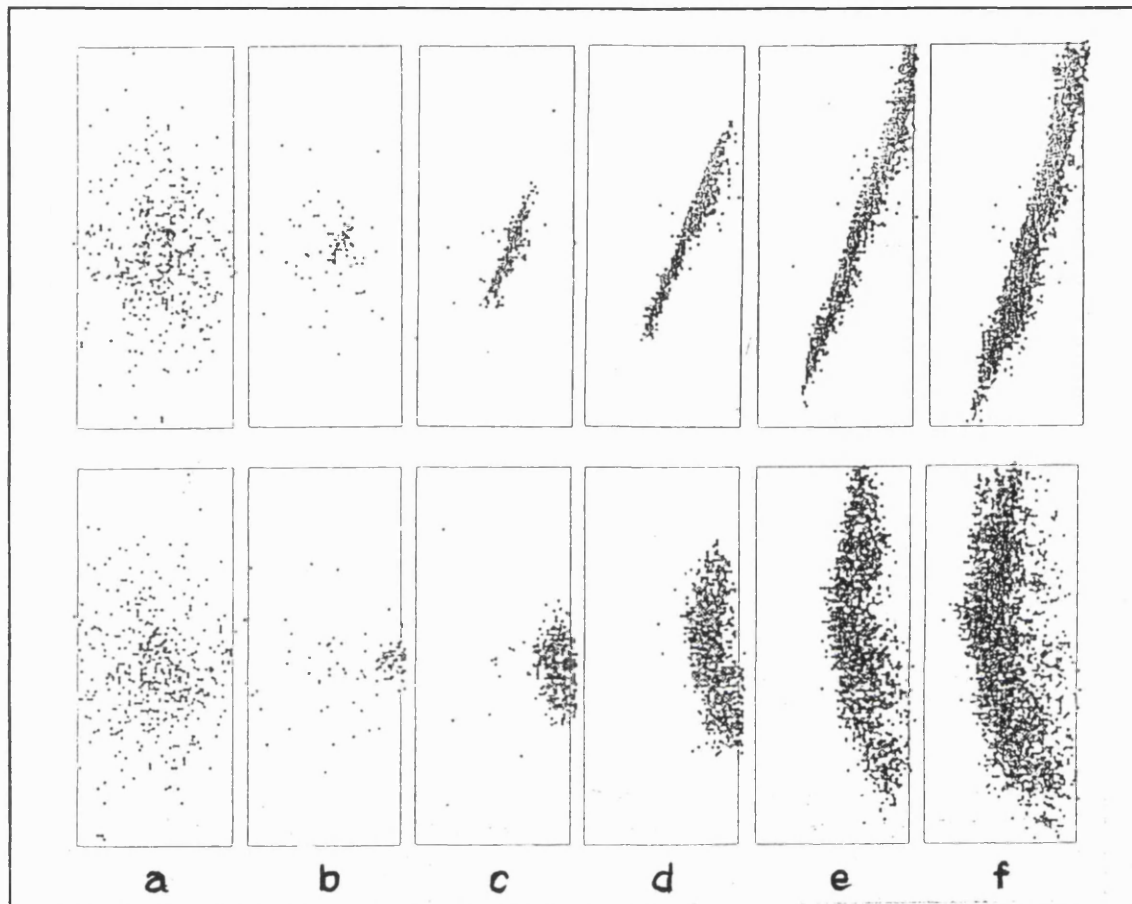


Fig. 2.7.2.1.a. Time sequence of AE events showing the complete fault formation process, the two rows are views orthogonal to each other, (After Lockner 1993).

*Cumulative AE, Event rate and seismic b-value analysis.* Cumulative number of AE events and the event magnitude are the simplest parameters to record (requiring only one piezo-electric transducer), and hence have been used most extensively in rock deformation studies. Scholz, (1968a, b, & c), by increasing the frequency response of a *barium titanate compressional mode transducer* and employing faster monitoring equipment, improved the sensitivity of the AE recording system by two or three times compared with previous workers. This paved the way for more detailed micro-seismic activity studies. His study confirmed earlier work by Brace et al. (1966), which pinpointed the onset of dilatancy in rocks under increasing stress, and also revealed AE to be closely related to stress/strain behaviour; dilatancy

began at about one third to two thirds of peak stress, initially randomly distributed, followed by rapidly increasing micro-fracturing prior to the formation of the fault. *Cumulative AE* gives an indication of the total damage accumulated in the specimen through dilatant cracking, and can be used to correlate brittle crack growth with dilatant volume increase.

A statistical model devised by Scholz successfully predicted the pattern of micro-cracking in laboratory specimens. The Griffith criterion for failure was deemed inapplicable to crystalline rocks on the basis of this work due to rocks' heterogenous nature and hence its microscopically heterogeneous stress field. These internal stress fluctuations cause microcrack growth at much lower macroscopic stresses than in homogeneous materials, and arrest cracks shortly after they have initiated. Hence, unstable runaway microcrack propagation and material failure does not occur until higher stresses. In 1968 Scholz also related the commencement of fault formation within a stressed and fractured medium to it reaching a *critical crack density*.

From statistical analysis of the numbers of AE events of different magnitude a microseismic *b*-value can be determined, (section 4.5.). It has been used to correlate earthquake activity with laboratory specimen behaviour (Mogi 1962b, Main et al. 1989). Mogi's hypothesis regarding the striking similarity between *b*-values in earthquake ruptures and laboratory specimens was further upheld by Scholz (1968b). Scholz, however, also found *b*-values to be closely dependent upon stress levels, and Fonseka, Murrell & Barnes (1985), showed the *b*-value to decrease to a minimum at failure.

Meredith & Atkinson (1983) found a good correlation between AE data and crack tip stress intensity factor in tensile crack growth experiments on Whin Sill dolerite. They conclude that stress intensity factor and crack growth rate have an identical functional relation to AE (see fig. 2.7.2.1.b.), and hence AE event rate can be used as a remote monitor of crack velocity (in tensile mode I fracture mechanics tests). It was further found that because the size distribution of AE events obeys a power law function, Meredith, Main & Jones (1990), showed that this implies that a power law distribution of crack sizes produces the AE, characterised by the fractal dimension, *D*, ( $N(a) = C \cdot a^{-D}$ ), and

$D$  varies with stress. In compressive tests, however, AE events prior to ultimate sample failure come from cracks which eventually stabilise, and subsequent AE is due to the growth of new cracks.

Physically, a high  $b$ -value represents emissions dominated by small events and a low  $b$ -value represents emissions dominated by large events. Test conducted in water showed consistency higher  $b$ -values in the lower  $K$  range ( $0.4 > K/K_c > 0.8$ ) when compared with dry experiments. SEM studies indicate a predominance of transgranular cracking at high crack velocities and in low humidity (high  $K$ ), and intergranular cracking at low velocities and high humidity (low  $K$ ). This is attributed to chemically induced cracking at grain boundaries, since grain boundaries provide the main conduits for fluid movement. Good correlation has also been found between inelastic strain, cumulative AE, and rock damage. Hatton (1992), found sudden jumps in strain during creep tests on granodiorite correlated well with bursts of AE.

Cox & Meredith (1993) related AE data to microcrack forming events. The data is used to represent a damage state variable. Damage accumulation models by Bruner and Walsh are then used to successfully predict physical property changes in the rock during deformation. Whilst the work leaves one or two details outstanding (e.g. an independent calibration of the scaling relation between the acoustic emission parameters and the microcrack geometry), the work demonstrates how quantitative analysis of AE data may be used to infer the mechanical behaviour of rock experiencing damage in compression.

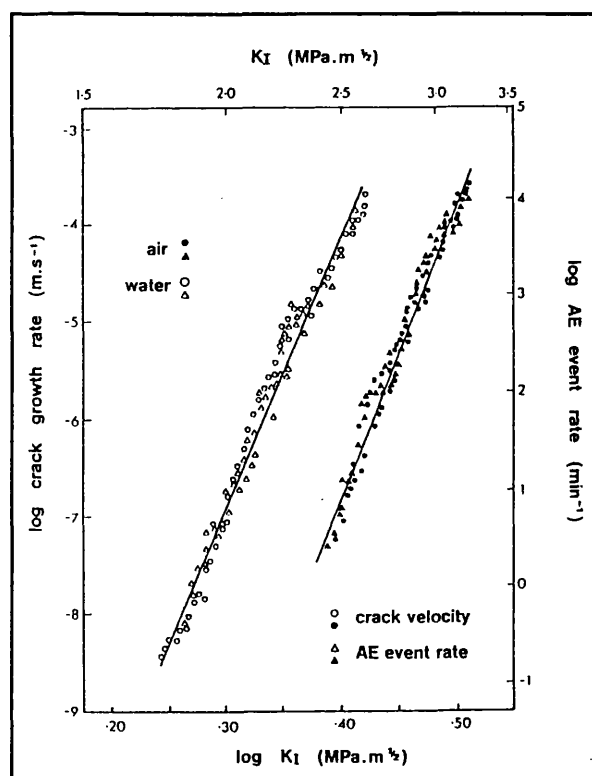


Fig. 2.7.2.1.b. The dependence of crack growth rate and AE event rate and crack tip humidity on  $K_I$ , see text, (After Meredith & Atkinson 1983).

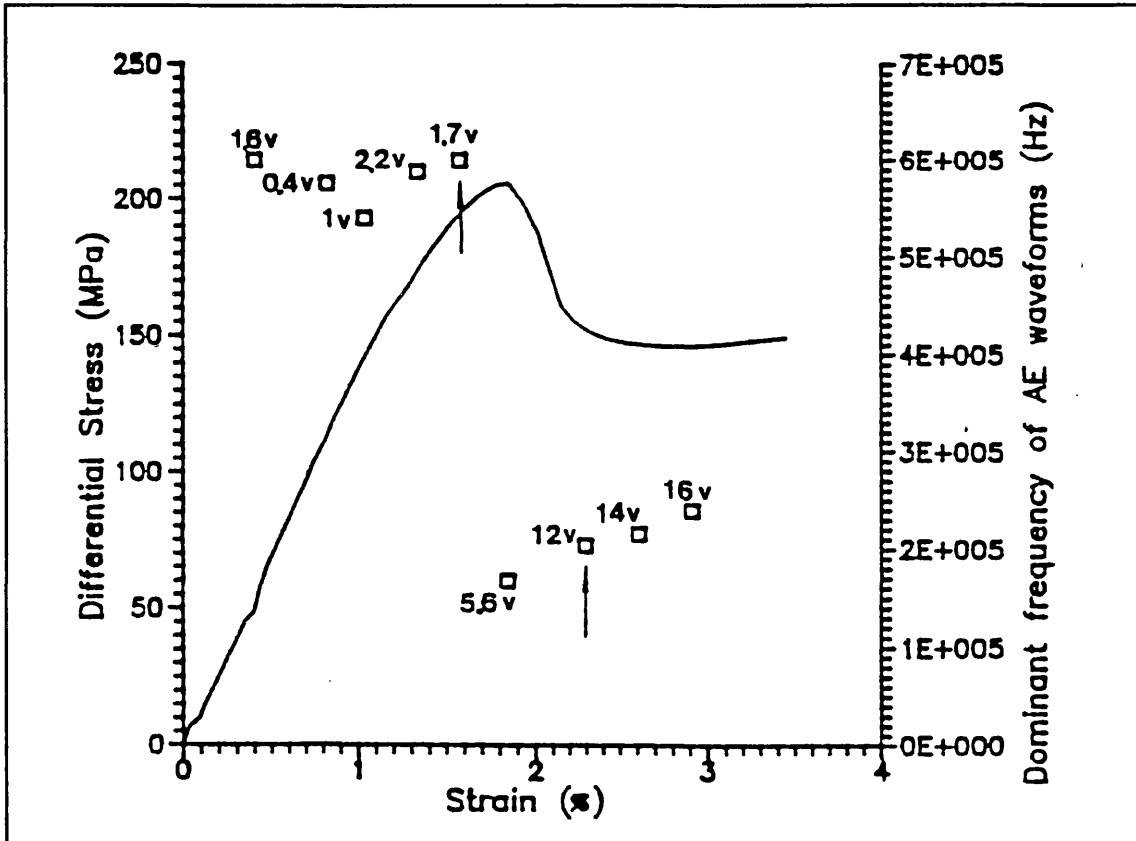


Fig. 2.7.2.1.c. Differential axial stress and dominant AE magnitude changing through dynamic failure, (After Read et al. 1995).

Read et al. (1995) investigated the AE event magnitude and frequency changes that occur in water saturated samples of Darley Dale sandstone during triaxial deformation. By recording the waveform of individual events signal, a Fourier transform was made which allowed the examination of the event's component frequencies. Fig 2.7.2.1.c. shows the change in dominant frequency and magnitude that occurs at peak stress, and fig. 2.7.2.1.d. shows the frequency distribution of each waveform just prior and just after peak stress. Based on the assumption that "a larger effective source dimension leads to an increase in the amplitude of seismic wave and a concurrent decrease in dominant frequency" (Savage 1972), the change in AE characteristics suggests a change from small crack growth increments to large growth increments. In making the above assumption, consideration is given to the fact that increased heterogeneity in the sample through extensive damage accumulation leads to the attenuation of higher frequencies (although this does not explain the *sudden* change shown in fig 2.7.2.1.c.), and a shift in the dominant frequency (600kHz. and 200kHz.). These frequencies correspond to wavelengths of half the width and half the length of the

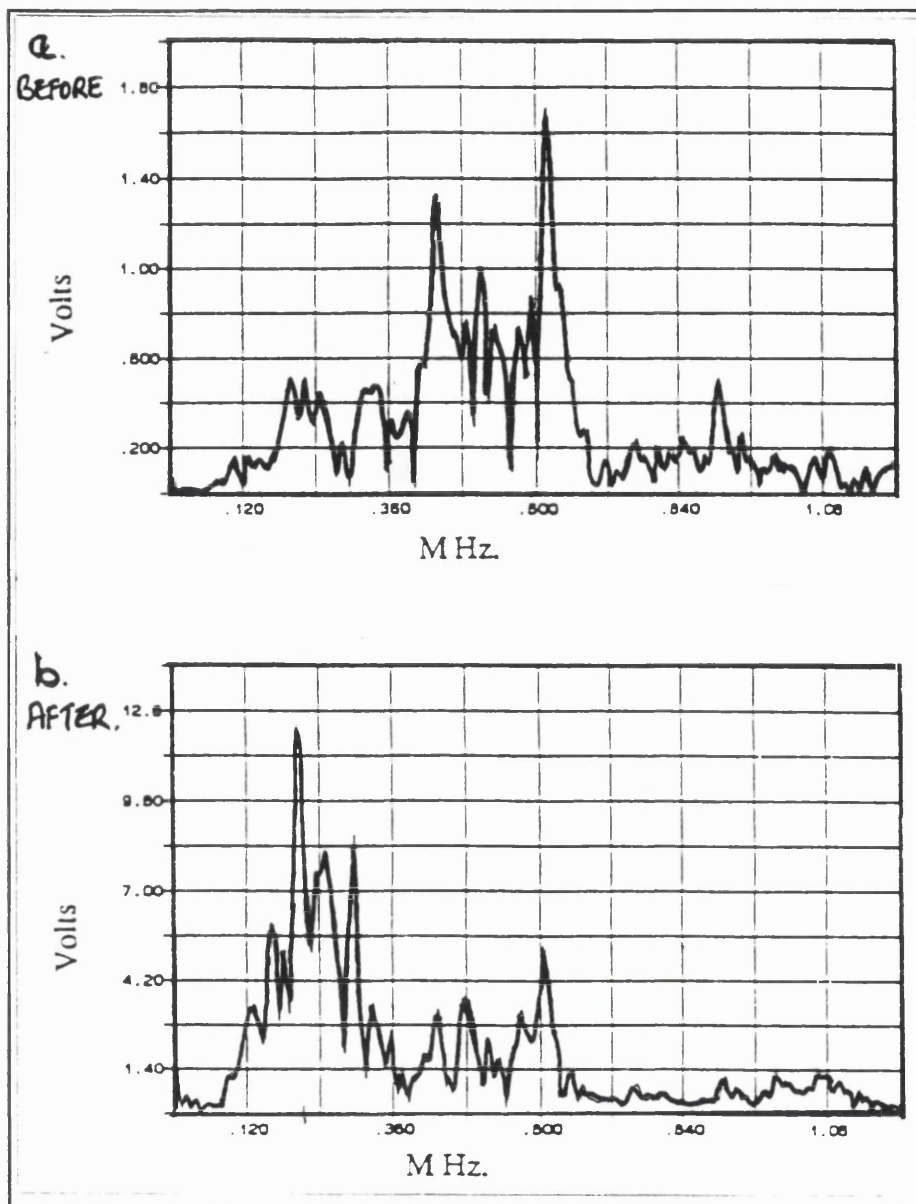


Fig. 2.7.2.1.d. FFT results of AE event waveforms before and after dynamic failure (arrows on fig. 2.7.2.1.c.) see text, (After Read et al. 1995).

specimen (wave velocity = 4km/s), respectively - therefore the energy peaks can be related to horizontal and vertical standing waves in the specimen.

The above reports of the use of AE in rock deformation illustrate the technique's ability to monitor microstructural changes during deformation. In this study, AE is used as an indicator of the onset of new dilatant crack growth and of the rate of damage accumulation.

### 2.7.2.2. Elastic Wave Velocity Measurements.

Another approach for indirectly monitoring microstructural changes is the measurement of P- and S-wave velocities in a rock specimen during deformation. The amount of damage in the specimen (crack density) affects the wave velocity; different waves being affected by different crack orientations whether cracks are dry, or partially, or fully

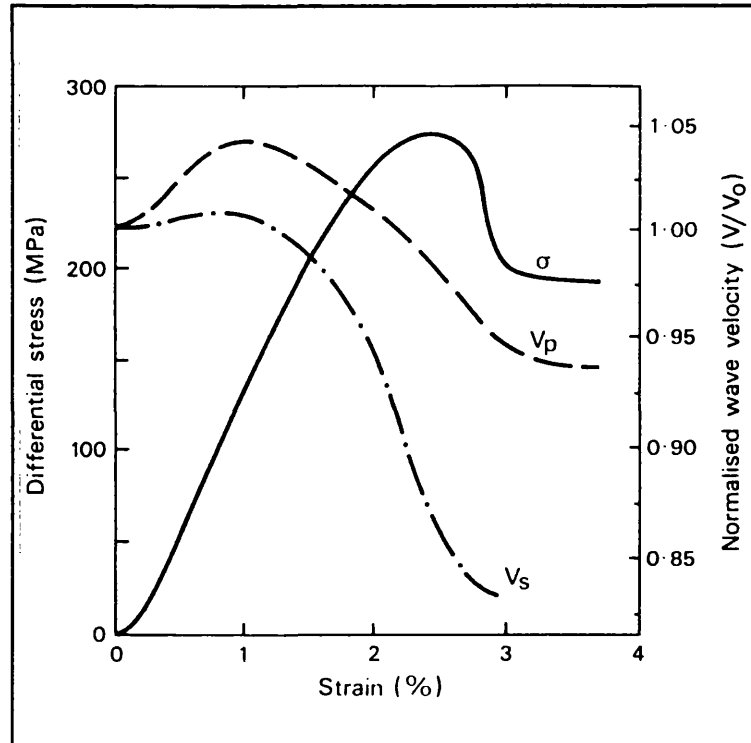


Fig. 2.7.2.2.a. Variations in  $v_p$  and  $v_s$  during the triaxial deformation of dry Darley Dale sandstone, (after Sammonds et al. 1989).

saturated.  $V_p$  and  $V_s$  are related to elastic moduli by well known equations. The variation of P- and S-wave velocity parallel with the maximum principle stress during triaxial deformation of dry Darley Dale sandstone is shown in fig. 2.7.2.2.a.  $V_p$  initially increases more than  $V_s$  due to the closure of cracks with their planes orientated perpendicular  $\sigma_1$ . At the onset of dilatancy ( $\approx 1/2$  peak strength),  $V_s$  is more affected by the opening of dilatant crack perpendicular to  $\sigma_1$ , and hence falls off relative to  $V_p$ . Post dynamic failure both  $V_p$  and  $V_s$  remain constant due to a constant stress level in the rock and hence no change in crack density.

Ayling et al. (1995), conducted experiments on dry Darley Dale sandstone measuring both compressional and shear wave velocity ( $V_p$  and  $V_s$ ) parallel to the maximum principal stress. This allowed the calculation of dynamic elastic moduli, *crack density parameters*, and *Seismic Quality Factor (Q)*. Crack density parameters were calculated using the methods by O'Connell & Budiansky (1974), and by Soga et al. (1986). O'Connell and Budiansky's method considers high density arrays of randomly orientated cracks, whereas the method by Soga et al. (1986) considers orthogonal arrays of non-

interacting penny shaped cracks and yields crack density parameters in three orthogonal directions.

The values for crack density parameters in directions *parallel* and *perpendicular* to the direction of maximum principal stress ( $\epsilon_x$  and  $\epsilon_z$ ) throughout deformation are given in fig 2.7.2.2.b. The figure shows a slightly falling  $\epsilon_z$  throughout deformation indicating continually closing cracks with normals parallel to  $\sigma_3$ , and a rising  $\epsilon_x$  from the onset of dilatancy until peak stress indicating the extension of dilatant cracks with normals perpendicular to  $\sigma_1$ .

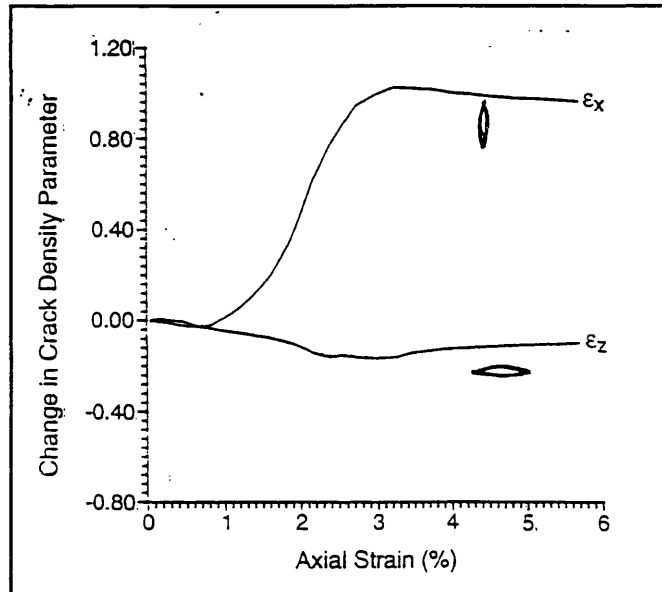


Fig. 2.7.2.2.b. Variations in crack density in two orthogonal directions ( $\epsilon_x$  and  $\epsilon_z$ ), during deformation, (After Ayling et al. 1995).

Work by Jones (1989) further illustrates the use of changes in  $V_p$  in elucidating deformation mechanisms not apparent from inspection of only the stress/strain data. In experiments on Solnhofen limestone at temperatures ranging from 20°C to 300°C, the stress/strain curve shows little concerning a change in mechanisms during deformation throughout the temperature range, (see chapter 4., fig. 4.3.2.b.).  $V_p$  data, however, illustrated that at 20°C microcracking was ubiquitous throughout deformation, whereas at the highest temperatures  $V_p$  increases throughout deformation indicating that crystal plasticity was responsible for deformation rather than microcracking. In this study  $V_p$  and  $V_s$  results from dry experiments have been used to determine the dynamic Young's modulus ( $E$ ), of Darley Dale sandstone throughout deformation for poro-elastic analysis of drained hydrostatic deformation, see section 6.3.4.1.

### 2.7.2.3. Pore Fluid Volumometry.

The first accurate measurements of rock volume changes during deformation were made by Brace, Paulding and Scholz (1966), using the *strain gauge method*. The method involves attaching a number of strain gauges to the surface of a rock specimen and measuring linear strain along different axes, from which total specimen volume change can be found. A second technique, used by Edmond & Paterson (1972) uses a *dilatometer*. The apparatus is capable of externally measuring the total specimen volume change by volumetric displacement of fluid from a sealed chamber surrounding the sample. The system is also confining pressure compensated. A third method, the *pore fluid method*, has been developed more recently and is used in this study. The system relies on no attachments to the surface of the sample, and thus can be used under elevated confining pressures and temperatures. Fluid flow into and out of a specimen is monitored during deformation, and hence specimens are required to have adequate permeability during deformation. The method is advantageous as it allows pore fluid pressure under either drained or undrained conditions to be introduced to the sample, which, combined with elevated temperature and confining pressures, more accurately simulates crustal conditions, see section 4.4.

Edmond & Paterson (1972), used the dilatometer to investigate the deformation of a number of rocks at different confining pressures up to 800MPa. Gosford sandstone showed some initial compaction at all confining pressures. The change from compaction to dilation was also present under all conditions. Volume changes (compaction and dilatancy) were attributed to micro-structural changes - grain rearrangement and the development of internal cracking, respectively. Dilatancy is thought to occur simultaneously with grain rearrangement, otherwise unnecessary work would be done against the confining pressure. Finally, dilation during stress release is attributed to the general loosening of the granular structure, leading to fracturing under the influence of contact stresses established during deformation. Similar results are discussed in section 6.4.

Fischer & Paterson (1989), used pore volumetry to investigate dilatancy during deformation at elevated pressures *and* temperatures in Gosford Sandstone. Positive dilatancy was observed to be qualitatively similar under

all conditions, although the onset of dilatancy became more marked and began earlier at higher pressures. This earlier commencement is a consequent of initial compaction occurring under the application of the elevated confining pressure. All specimens showed some barrelling with the superimposition of a shear zone. The effect of temperature is to reduce strength (at 10% strain), under all conditions, this effect being markedly reduced with greater effective confining pressure. A number of different mechanisms are cited to account for the volume changes; (i) opening or closing of microcracks, (ii) relative movement of grains causing changes in intergranular void space, (iii) collapse of initial porosity due to high confining pressures, and (iv) changes in connectivity.

Microstructural changes have implications for permeability, and hence permeability was investigated by Fischer & Paterson (1992) using a sinusoidal fluid pressure pulse technique. A sinusoidal pulse is applied to one end of the sample, the attenuation and phase retardation recorded at the other end is related to permeability and storage capacity. Results found permeability to be closely related to porosity within and between rock types - permeability increasing as pore fluid pressure increases. Storage capacity initially decreases under an increasing pore fluid pressure (for a fixed confining pressure), responding to a decreasing

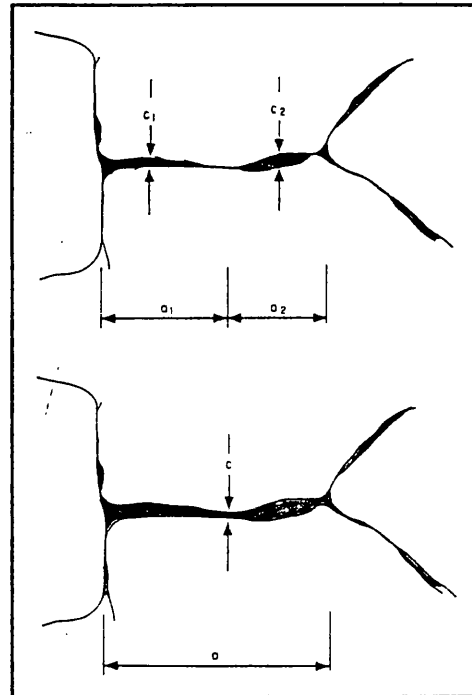


Fig. 2.7.2.3.a. Schematic diagram showing how crack aspect ratio increases with crack throat closure, see text, (After Paterson & Fischer 1992).

compressibility of the pore fluid (argon), and then increases with a further increase in pore fluid pressure, responding to increasing porosity and increasing volumetric compliance of the pore space. Modelling the results with reference to the pore structure yields an decrease in aspect ratio with increasing pore fluid pressure. The opening of a closed throat between two cracks under an increasing pore fluid pressure would have the effect of increasing aspect ratio markedly, see fig 2.7.2.3.a.

Pore fluid volume data is used in conjunction with previously obtained crack density measurements by Read et al. (1995), to yield the aspect ratio of deforming Darley Dale Sandstone. By subtracting the pore volume change due to compaction (assumed to have a linear relationship with applied stress - initially the result of elastic pore closure), from total pore volume change, the pore volume change due solely to dilatancy is obtained. Assuming a narrow range in aspect ratio at any given time within the crack and pore population, the aspect ratio ( $c/a$ ) during deformation is calculated from the crack density ratio ( $\epsilon$ ) and crack porosity ( $\Phi$ ) as below.

$$\Phi/\epsilon = (4\pi/3).(c/a) \quad (2.7.2.3.a)$$

The results (fig 2.7.2.3.b.) for the experiment under an effective confining pressure ( $C_p'$ ) of 50MPa show the aspect ratio starting comparatively low (reflecting the component of porosity comprised of cracks), increasing slightly as the cracks initially bow with the application of differential stress, then decreasing under crack extension. For the experiment under  $C_p' = 100\text{MPa}$ , the aspect ratio starts higher than at  $C_p' = 50\text{MPa}$ , reflecting the fact that under this higher confining pressure many of the cracks have closed, hence pores make a larger component of rock porosity. Upon the application of differential stress cracks initially open elastically (no AE detected), followed by new crack extension. Absolute pore volume change data indicates dilatant porosity increase in experiments

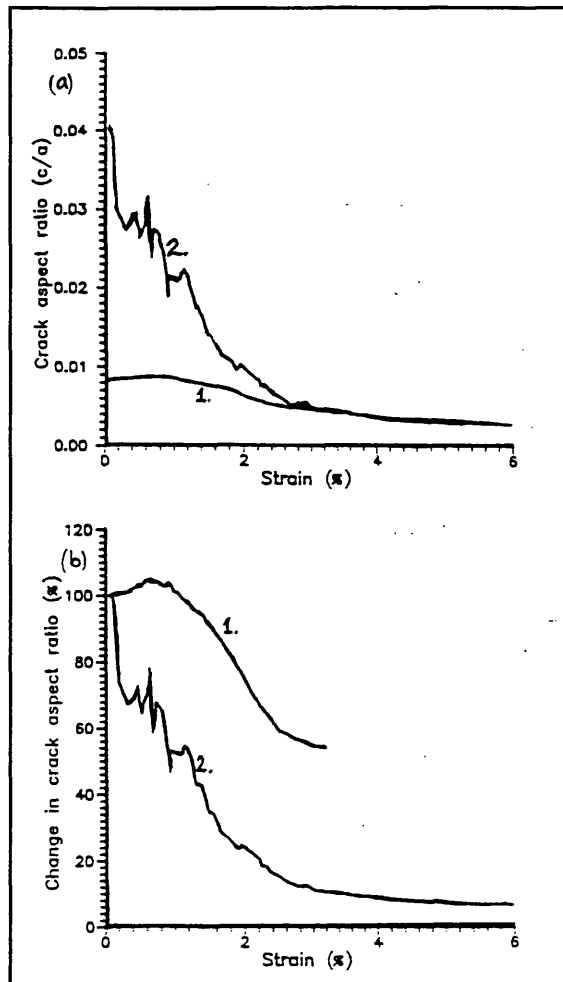


Fig. 2.7.2.3.b. Changing aspect ratio (a), and normalised aspect ratio (b), during triaxial deformations under (1)  $C_p' = 50\text{MPa}$ , (2)  $C_p' = 100\text{MPa}$ .

at  $C_p' = 100\text{MPa}$  of four times that for experiments under either  $C_p' = 50\text{MPa}$  or  $C_p' = 20\text{MPa}$ . The higher differential stress supported by samples subjected to higher confining pressure confirms that the application of confining pressure encourages crack growth of a small distributed nature, and prevents *runaway* growth and crack coalescence. Whilst the reservations of combining results from two separate experiments is noted in this study, the work illustrates the use of pore fluid volumetry in understanding certain aspect of the micro-mechanics of rock deformation.

#### 2.7.2.4. Permeability.

The measurement of *Permeability* ( $K$ ) is achieved by measuring fluid or gas flow (for low permeability measurements), through rock samples. Permeability is perhaps one of the most important rock characteristics, affecting hydrocarbon recovery rates, geothermal energy extraction efficiency, and subsurface radioactive storage efficacy.

Measuring  $K$  in the laboratory can tell much about the shape of pores and cracks making up rock porosity. Whether low aspect ratio cracks, equi-dimensional pores, or a mixture of both make up the connected porosity markedly affects the response of permeability to changing stress conditions. The

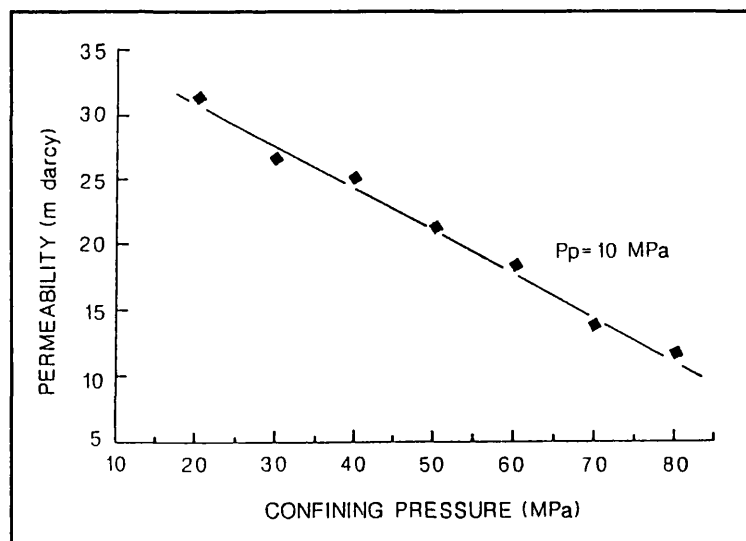


Fig. 2.7.2.4.a. Variation of  $K$  with  $C_p$  for Fontainbleue sandstone ( $\phi = 12\%$ ) consisting mainly of pores, (After David & Darot, 1989).

The resistance to rock fluid flow depends on viscous drag supplied by rough crack walls (hence to crack aperture), and the tortuous pass followed by fluid in flow. Flow studies have shown that crack aperture has a much greater effect on  $K$  than tortuosity, (Walsh 1981).

Increasing confining pressure reduces  $K$  through porosity reduction, but the nature of  $K$  reduction depends upon the initial porosity and its micro-structure. Fig. 2.7.2.4.a., & b. illustrate the reduction in  $K$  with increasing confining pressure for sandstones

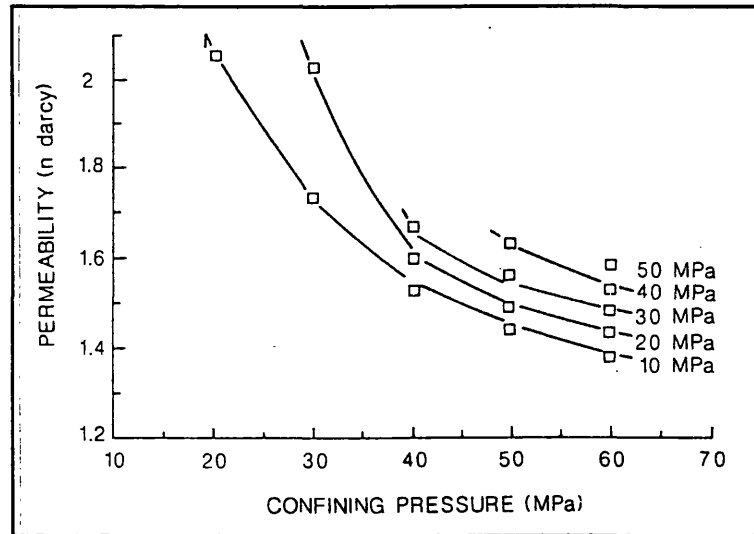


Fig. 2.7.2.4.b. Variation of  $K$  with  $C_p$  for different pore fluid pressures on Fontainbleau sandstone ( $\phi = 6\%$ ) consisting mainly of pores, (After David & Darot, 1989).

of low and medium porosity, respectively. Permeability clearly responds to the different components of porosity (cracks and pores) for each rock type - cracks closing easily, pores offering greater resistance. Permeability reduction also depends upon whether the fractures being closed are required to maintain pore inter-connectivity. Another consideration is that crack closure is governed by two processes; initial elastic closure, followed by final closure governed by surface roughness. Permeability reduction becomes increasingly difficult with increasing confining pressure due to the latter mechanism. Furthermore, cycling the application of confining pressure quickly results in permanent microstructural rearrangement and porosity reduction, (see section 6.3.3.3.).

Permeability increases in response to a pore fluid pressure rise. Fig. 2.7.2.4.b. illustrates  $K$  reduction under an increasing  $C_p$  for different pore fluid pressures (indicated in the body of the graph). It can be seen that the effective stress law (eq. 2.3.1.b.) applies, but the value of  $\alpha$  does not equal unity. Indeed,  $\alpha$  varies for a given pore pressure, rock type, and confining pressure. Often  $\alpha$  is found to increase during confining pressure increase. It seems the efficiency with which pore pressure maintains porosity *increases* with confining pressure; after the closure of the weakest component of porosity, deformation of the porous network becomes more and more sensitive to internal pressure (David & Darot, 1989). Whilst permeability is not measured

in this study, knowledge of how its magnitude responds is important for analysis of the pore volumetry results (e.g. section 6.3.3.2.).

### **2.7.3. Summary - The Brittle Deformation Cycle and Physical Property Changes.**

The measurement of all these changing physical properties is schematically summarised for the deformation of a porous sedimentary rock under conditions conducive to brittle faulting failure in fig 2.7.3.a. Differential axial stress, cumulative AE, permeability, normalised  $V_p$  and  $V_s$ , and  $P_v$ , against strain are shown. The axial strain axis is divided into five regions. Each characterises particular macro- and micro-mechanical deformation behaviour. These regions are described below.

*Region I* is the highly non-linear region of initial compaction. The closure of pre-existing microcracks under the influence of an increasing differential stress causes the material to become stiffer with increasing stress. The stress/strain curve displays this through an upwards concave shape. The elastic wave velocity increases;  $V_p$  increases proportionally more than  $V_s$  due to its sensitivity to the above mentioned cracks. Pore volume decreases, indicating sample compaction (although this is partially due to reduction of ram/sample interface volume), and a slight decrease in  $K$  occurs as connected porosity is decreased. Acoustic emission activity is low throughout the region.

*Region II* is known as the region of *linear elastic deformation*. Deformation is thought to be elastic and recoverable. Actual behaviour depends largely on rock porosity - the higher the porosity the larger the initial compaction region (region I) relative to the linear elastic portion. Inelasticity through cracks reopening and closing, and grain sliding is illustrated by stress/strain curve hysteresis is found in this zone, and static elastic moduli measurements have indicated that the region is not purely elastic and an amount of inelastic deformation does occur (Bernabé et al. 1994). Walsh (1965) attributed this to frictional sliding on the surfaces of the grains. Batzle (1980), described

how cracks with mismatched surfaces (mismatched asperities) partially close or crush debris lodged inside cracks, during closure. This increases the energy requirement during compression which is then irrecoverable on unloading. Furthermore, pore fluid volume measurements (this study), show continued pore and crack volume reduction during this stage of deformation, indicating continued porosity reduction and perhaps crack closure, adding further weight to

Batzle's observations, (see section 6.4.3.2.). AE output is still low during this period, and  $V_p$  and  $V_s$  increase slightly as porosity decreases and rock density increases. Permeability and electrical conductivity gradually decrease in this region.

*Region III* begins at the onset of AE (usually between  $\frac{1}{2}$  and  $\frac{2}{3}$  of peak stress), and continues until peak stress. Deviatoric stress is sufficient at this stage to initiate microcrack growth primarily parallel to the maximum principle stress. Initially dilatant crack growth is distributed throughout the volume of the specimen (although this is absent at the ram/sample interfaces), and of small growth increments. The growth of both intergranular and intragranular cracks occur in response to local crystallographic heterogeneity. It can now

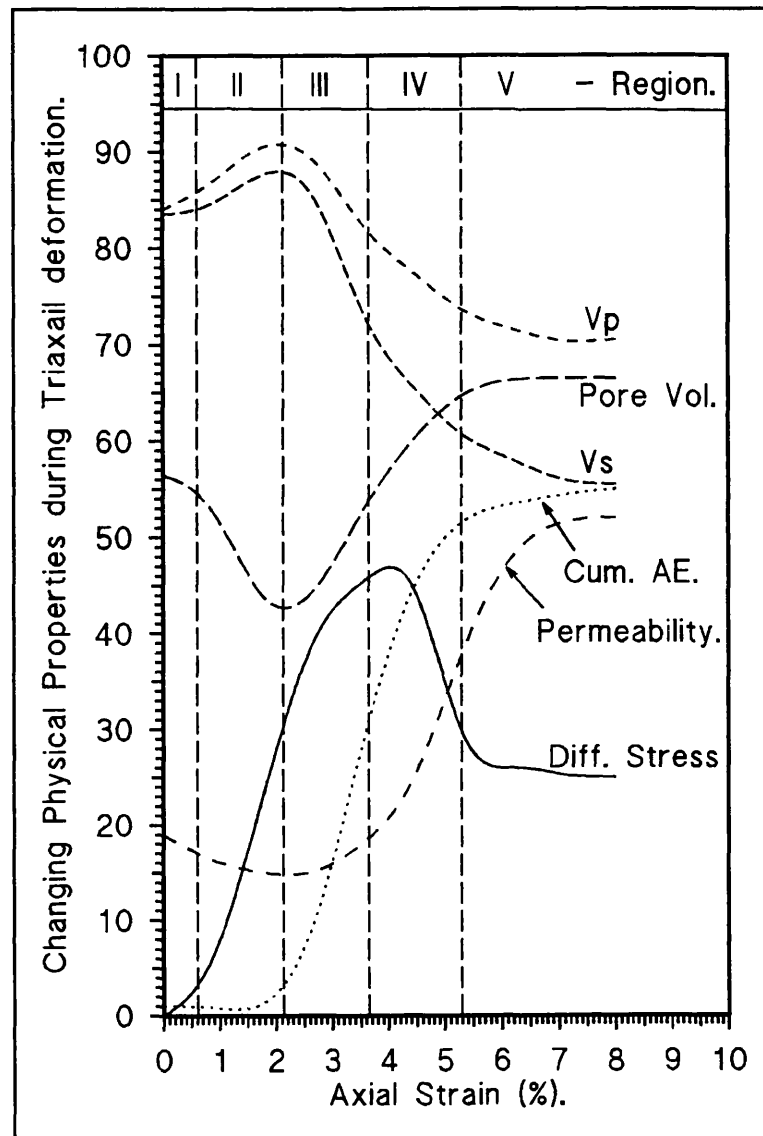


Fig. 2.7.3.a. Schematic illustration of changing physical during triaxial loading of a porous sandstone, see text.

be seen from the broad, smooth minimum in the pore fluid volume curve at the change from region II to III, that a gradual change from compaction to dilatant crack growth occurs. After this change the pore fluid volume ( $V_p$ ) curve becomes linear, increasing steadily.  $V_s$ , being more sensitive to cracks aligned parallel to  $\sigma_1$ , decreases more during this region compared to  $V_p$ . AE increases exponentially with dilatant cracking. At  $\sim 80\%$  of fracture stress  $K$  increases markedly.

Studies using holographic interferometry have elucidated precursory bulging of the rock associated with eventual faulting zone at stresses as low as 60% of peak stress (Spetzler et al. 1974), however most studies have found the majority of dilatant cracking occurs very near to peak stress.

*Region IV.* As deviatoric stress peaks, the *driving mechanism* for crack growth (crack tip stress intensity) also peak and the crack population (or *accumulated damage*) reaches a point where crack growth cannot occur without interaction with other nearby microcracks; *crack linkage* begins, and  $V_p$  and  $V_s$  continue to decrease. Cracking and interaction now undermines the integrity of the rock to the extent that only a *decreasing* load is sustainable under increasing strain - *strain softening*. Growth between zones of extensive crack coalescence on the embryonic fault plane begins decreasing the *average* Young's modulus of the rock even further. The failure plane now forms and the rock fails suddenly. Cumulative AE continues with a maximum rate of change indicating maximum damage accumulation.

*Region V.* Once strain has localised, stress in the body of the rock away from the fault zone decreases and strain is accommodated through rotation and further fracturing of grains within the fault plane. A zone around the fault plane, the size of which depends upon confining pressure, then suffers the majority of the strain. From this point onwards the *residual shear strength* of the fracture surface is responsible for resistance to strain. Pore volume,  $V_p$ ,  $V_s$ ,  $K$ , and AE stabilised to a low level indicating overall damage in the rock at this stage remains stable. Under a higher confining pressure, behaviour shifts from strain softening accompanied by faulting, to strain-hardening marked by homogeneous deformation, (see section 2.4.3.5.). The explanations for this

lies in consideration of the processes of crack initiation and growth. Brittle microcrack linkage associated with faulting results in run-away cracks creating zones of weakness which then localise strain. Under triaxial stress conditions conducive to cataclastic flow, confining pressure is small compared to fracture initiation stress at crack tips (brought about by the applied deviatoric stress), hence microcracks nucleate. However, microcrack *growth* is inhibited through inter-crack-face friction on the pre-existing flaws from which the microcrack nucleate, (François & Wilshaw, 1968). Deformation occurs under these condition by the rotation and rearrangement of the resultant rock fragments into pre-existing pore spaces. It is this mechanism that is responsible for stabilising the distribution of deformation within the rock and inhibiting localised strain.

Consideration of the stages of crack growth with respect to an increasing confining stress sheds further light on the matter. Initially resistance to *intragranular* crack growth is greater than *intergranular* crack growth, hence crack growth is unstable - jumping around from grain to grain. At higher pressures *intergranular* crack growth is more inhibited than *intragranular* crack propagation, hence crack growth is stabilised at grain boundaries. Furthermore, under this mechanism once full compaction has been achieved the rock may exhibit brittle characteristics; this is comparable to *high pressure embrittlement*.

This chapter shows that whilst much is known about the deformation cycle with respect to internal micro-mechanisms and changing physical properties (potentially of use for far field rock deformation monitoring - Ayling 1991), much remains hypothetical, requiring more experimental data. In the present study a series of experimental programmes have been undertaken using new equipment (described in chapter 4), to further explain the mechanisms of compaction and dilatancy that occur under a variety of crustal stress and environmental conditions. The next chapter (chapter 3) describes the sources and role of fluids in the crust, and attempts to relate some of the mechanisms uncovered from rock physics experimentation to real crustal processes of faulting and fluid flow.

## **CHAPTER 3. ROLE OF FLUID FILLED CRACKS AND PORES IN THE CRUST.**

### **3.1. Introduction.**

This chapter reviews the role of fluids in the crust and research which explains the behaviour of the crust under the influence of tectonic loading, in terms of rock physics principles. Most polycrystalline rocks contain fluid filled pores and cracks (usually filled with water, aqueous solutions, CO<sub>2</sub>, or hydrocarbons), and it is recognised that they play a fundamental part in the evolution and formation of the crust.

Crustal rock porosity may be formed by several processes;

- (i) by burial, compaction and diagenesis of water saturated sediments leading to an interstitial fluid phase,
- (ii) by burial/heating, and uplift/cooling leading to thermal decomposition (e.g. dehydration - releasing water into the rock) or thermal cracking, and,
- (iii) by tectonic processes leading to fracturing.

Rock fluids may originate from magmas or from surface processes. Fluid phases may combine with rock forming minerals to form hydrates, and geochemical interaction between water and rocks can lead to the formation of ore deposits, (Murrell 1989).

Surface exposures show the effects of fluid/rock interactions at all crustal levels, and geophysical studies (electrical resistivity and electromagnetic surveys), borehole analyses (Kola Peninsula 12km deep borehole), seismic reflections, and low seismic wave velocity zones give evidence of fluid activity (hence microfracturing) at depths of up to 10-15km.

Fluid pressure and flow in the crust are the most likely factors in initiating change in rock. The primary dependent variables dictating equations of state for the behaviour of fluids are fluid pressure, chemical composition, and temperature, and the characteristics of a flowing fluid system are determined by the bulk rock permeability, hydraulic pressure gradient, fluid chemical composition, temperature, and available fluid volume.

### 3.2. Fluid Driving Forces.

The driving forces governing fluid flow in the crust are the result of either (i), topographical relief, (ii), tectonic dilation/compaction, (iii), diagenesis, (iv), heat, and (v) the nature of an external fluid source. These are summarised below.

*Topographical relief* flow occurs throughout the upper regions of the crust. Boundaries of fluid flow regions include natural drainage divides and the upper level of the water table (normally between 50m and 100m below ground level). The lower boundary is at some depth in the crust. This type of flow is found in most mature sedimentary basins and is often responsible for elevated fluid pressures in confined aquifers, (Tôth 1963).

*Tectonic Dilation and Compaction* of rock alters pore volume and hence has a profound effect on the pressure of a *confined* mass of fluid. Fluid pressure generated by this process is dependent on the permeability of the rock and the rate of deformation, as is the fluid flow resulting from the elevated pore pressure. Changes in permeability and porosity due to precipitation from mineral rich fluids during flow (crack sealing) can cause a drastic permeability and porosity reduction. Subsequent changes in fluid pressure within the confined fluid mass can then produce a complex alteration of the rock stress state as the magnitude of the effective macroscopic stress field and the pore fluid pressure changes. This then has an effect on deformation behaviour. At a cessation of tectonic loading fluid flow dissipates the elevated pressure as a function of permeability. This mechanism has been suggested for the deposition of hydrothermal ore formations (Sibson et al. 1975), and

outpourings of warm ground water along fault traces following normal faulting and water drawn in during thrust faulting (Muir Wood 1994), see fig. 3.2.a.

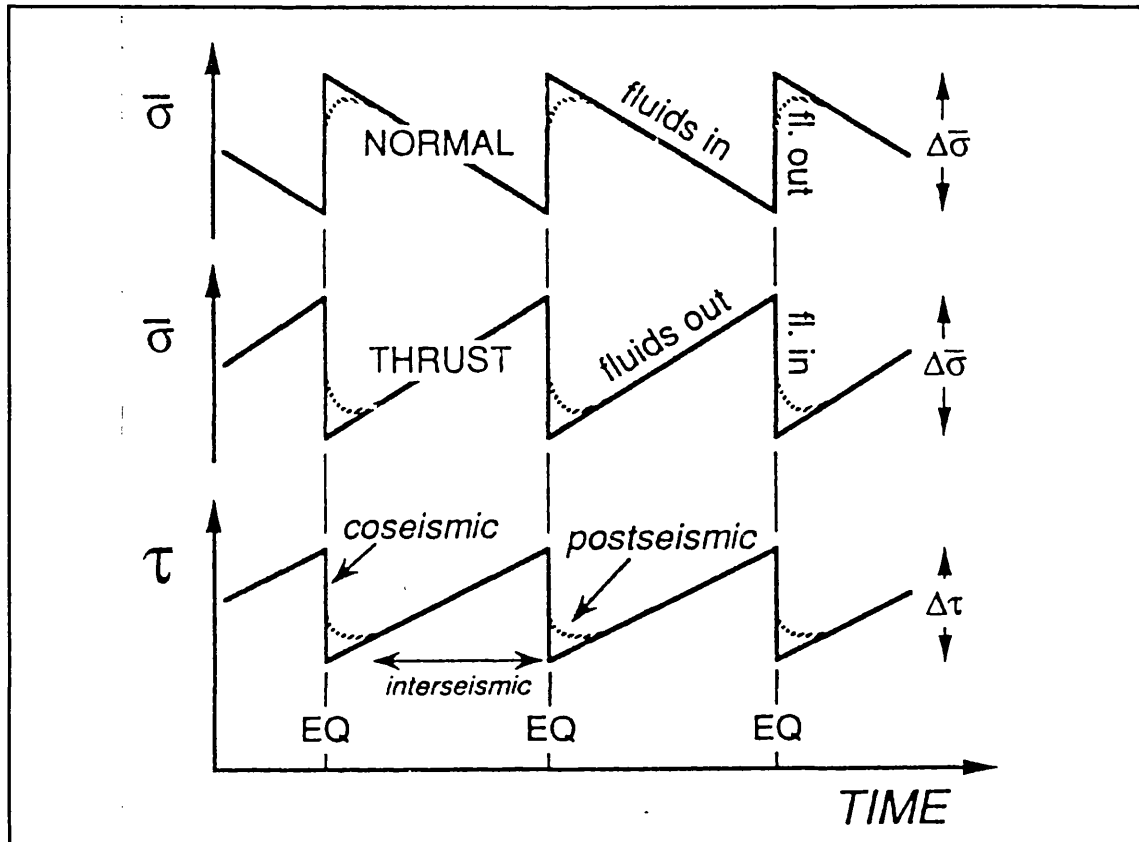


Fig. 3.2.a. Variation in mean and shear stress on faults, and associated fluid flow. Dotted line indicates possible time dependence (After Sibson 1994).

*Diagenesis* causes the closure of pore spaces under burial and compression through heating, sealing, stress induced compaction, and chemical reactions causing loss of fluids into new solid phases (e.g. hydration). Depending on permeability the crust may either dry out or develop elevated fluid pressure. The latter situation exists in the Gulf of Mexico where low permeability sediments (due to clay minerals) are being buried quicker than fluid can escape. In this situation the fluid pressure generated equals the lithostatic stress, hence zero compaction. Once burial ceases elevated fluid pressure becomes a mechanism for fluid flow.

*Heat* as a cause of fluid flow is described in section 3.3.1. One result in this case is intense fracturing around magma bodies and temperature induced pore fluid pressure imbalance. This heat source and the resultant micro-fracturing is of interest to geothermal extraction industries.

*Fluid source* regions are often the locations of elevated fluid pressures. The top few kilometres of the crust are likely to receive fluid through precipitation and topographic flow. Other sources are mantle degassing events, or mineralogical phase changes.

### **3.3. Crustal Effects on Fluids and Fluid Movement.**

#### **3.3.1. Heat Sources and Fluids.**

Practical examples of fluid/rock interactions are numerous. The introduction of a magma body into a rock system initiates heating of the surrounding country rock causing fluid flow through localised elevated fluid pressure. The flow of pressurised heated fluid away from a heat source exerts a strong effect on the cooling of the body and on the mechanical stress state of the surrounding rock. In regions of low permeability hydro-fracture can occur allowing rapid fluid flow and a sudden reduction in pore fluid pressure. As chemical activity (increased under high temperatures) begins to reduce permeability through crack healing and sealing, flow ceases. A cyclical system of flow or "pumping" can be established.

#### **3.3.2. Earthquakes and Pore Fluids.**

Fluids are known to play a large part in the nucleation processes of earthquakes. Indirect evidence of elevated pore fluid pressures is found throughout most of the world's active tectonic areas, at or well above hydrostatic pressure and often approaching lithostatic pressure. Evidence is accumulating that major faults are weak not only in relation to the surrounding country rock but also in relation to the frictional strength of the appropriate geological material (Scholz 1992). Two schools of thought are developing in response to this. One which states the faults are lined with a material of low intrinsic frictional strength, and another that attributes fault weakness to anomalously high pore fluid pressure. Under either condition frictional resistance to sliding is reduced and over-thrusting can occur under much reduced tectonic stresses (Hubbert & Rubey 1959).

Recent experiments by Cox (1993), compared sliding characteristics of quartz rich sandstones under conditions of 1200K temperature, 300MPa confining pressure, and employing different pore fluids at a pressure of 200MPa. Under these conditions the pore fluid (water) is extremely reactive whereas the inert pore fluid remains unreactive. Results show how the chemical effect of the reactive pore fluid effects the frictional resistance of the rock to sliding. During sliding, dissolution and precipitation of the asperity structure, stress corrosion cracking of the asperities, and lubrication of the surface resulted in a co-efficient of friction ( $\mu$ ) on the slip surface of 0.3. In the experiments using the inert pore fluid (argon), the material *slip hardened* during straining and later observations indicated no chemical activity. The co-efficient of friction in the latter case was 0.5.

Sleep & Blanpied (1992) propose a model to explain the reasons behind weak crustal faults in the San Andreas system. The model is based on results of frictional strength experiment by Blanpied, Lockner & Byerlee (1991), which identified failure at anomalously low frictional strengths. In the model compaction of porous fault core material through ductile creep mechanisms during strike slip fault strain elevates fluid pressure. Pore fluid is trapped within the fault zone by an impermeable seal derived from solute laden fluid driven from the fault zone (chemically active mineral deposition) during compaction. Compaction and associated pore fluid pressure rise progressively weakens the fault core until eventual failure occurs at low shear stress. After faulting fluid pressure falls as a result of faulting induced rock fracture and compaction relaxation. Although *long term* fluid pressure within the core of the fault is in equilibrium with the surrounding rock, *short term* fault fluid pressure varies cyclically with faulting. Repeated faulting creates a fine grained gouge material which is then more prone to further ductile compaction.

Chester et al. (1993) after extensive geological studies, arrive at similar conclusions. Their model postulates that the strength of a given fault (within the San Andreas System) is dependent upon the thickness of an "*ultracataclasite* zone of multiply reworked vein material in the faulting zone testifying to repeated episodes of high pore fluid injection". However, both

of these models suffer from a similar restriction; that of the maximum fluid pressure attainable within a rock being limited to the lithostatic pressure - beyond which hydrofracture soon occurs, dissipating fluid pressure.

The models rely on very high fluid pressures to explain movement on fault plane which lies at an angle of between  $60^\circ$  and  $80^\circ$  to the maximum principle stress. Based on these hypotheses, it can be imagined that injection of fluid into the  $\approx 1\text{m}$  thick fault core bounded by the impermeable seal could reduce fault strength sufficiently to induce continual ductile creep and aseismic movement.

These two examples of the effect of fluids on crustal faulting merely touch on a broad and complex problem. They do, however, illustrate both the chemical and mechanical involvement of fluids in the mechanisms of faulting in the crust. This is an area of active interest with attention being paid to both field analysis and laboratory work. Studies are explaining the effect of fluid rock interactions on rock fracturing, permeability and porosity, and the effects of both chemical active and chemically inert fluids on rocks under the full spectrum of crustal stress and environmental conditions.

## CHAPTER 4. DESCRIPTION OF APPARATUS, MODIFICATIONS, AND CALIBRATION.

### 4.1. Introduction and General Description of Equipment.

The high pressure triaxial rock deformation equipment in the Rock and Ice Physics Laboratory, UCL, was used in this study. It was, however, substantially modified to allow pore volumetry experiments to be executed. This chapter describes equipment design, equipment construction, and details of the extensive modifications undertaken by the author. A general introduction to and history of triaxial experimentation can be found in Paterson (1978) and Jones (1989). Figure 4.1.a. shows a photograph of the apparatus and figure 4.1.b. shows a schematic block diagram of the apparatus.

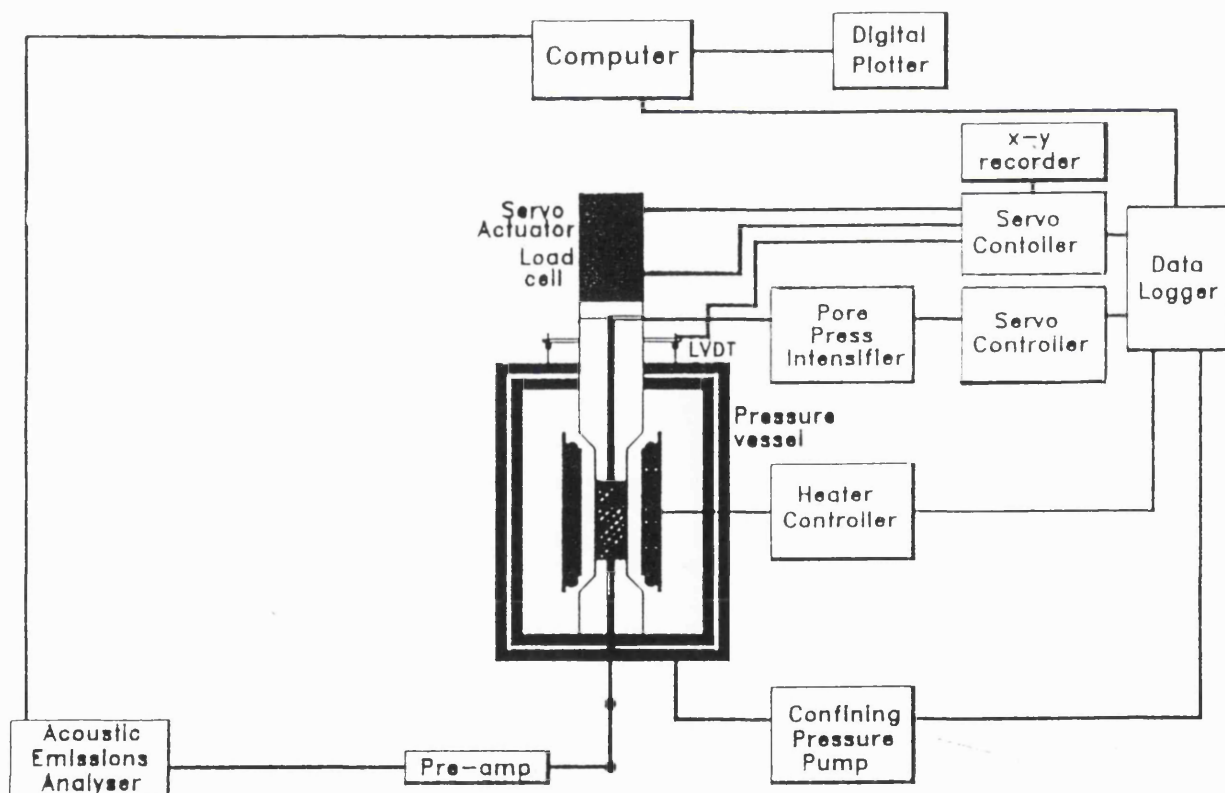


Fig. 4.1.b. Schematic diagram of the apparatus.

The main pressure vessel is designed for pressures of up to 1400MPa. It comprises a cylinder sealed at each end by high pressure sealing *closures*. The vessel contains an internal furnace (capable of 1000°C), and provides for an acoustic emission monitoring system. The acoustic emission signal is

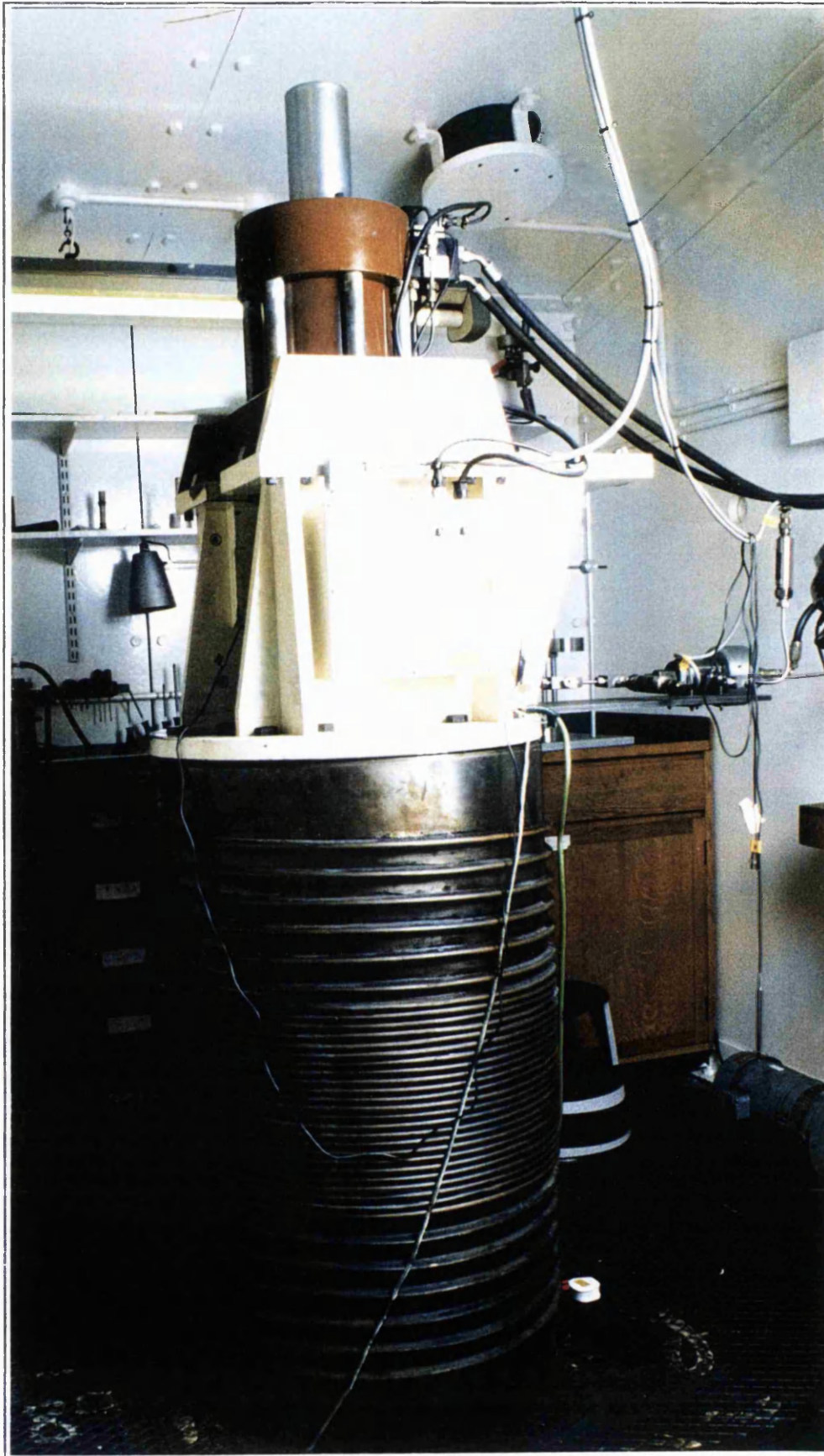


Fig. 4.1.a. Photograph of the high pressure triaxial deformation vessel (modified).

monitored by a piezo-electric transducer sited 6mm from the specimen in the lower ram. The pressurised nitrogen supplied by a Harwood three-stage

compressor stresses the rock hydrostatically whilst a servo-controlled actuator mounted above the vessel superimposes an axial stress on the rock. The actuator can be controlled in either load, displacement, or displacement rate control. Pore fluid pressure in the specimen is provided and measured through a 1/8" (3.2mm) diameter high pressure (*hp*) tube passed down the centre of the loading piston. Fluid pressure up to 700MPa is generated by a pore fluid pressure intensifier connected to the *hp* tube. Confining pressure gas is prevented from entering the specimen by the use of an annealed copper jacket surrounding the specimen. The jacket also serves to keep the pore fluid from escaping. This arrangement allows a specimen of rock to be triaxially stressed under precise control whilst pore fluid parameters and acoustic emissions are monitored. These physical properties are logged and stored on a personal computer.

## 4.2 Main Triaxial Testing System.

The triaxial deformation cell is described by Edmond and Murrell (1973), Ismail (1974), Jones (1989), Ayling (1991), and Sammonds et al (1991). The main body of the vessel, a thick-walled open ended cylinder of  $\approx 64$ cm OD,  $\approx 8$ cm ID and  $\approx 110$ cm long, is of a *duplex* type construction, the design details of which can be found in Ismail (1974). The ends are sealed using *closures* or *end plugs*. These cylindrical plugs use modified Bridgman type seals comprising "O" rings backed by two wedge shaped anti-extrusion rings in addition to the Bridgman unsupported area seal. Originally, an investigation by Ismail (1974) isolated Hall and Hall Silicone "O" rings backed up by anti-extrusion rings as the best arrangement. This functioned well until a new gas compressor was fitted after which they proved insufficient. Jones (1989) further investigated the problem and settled on the modified Bridgman seals.

### 4.2.1. Lower Closure.

The lower closure features a number of high pressure sealed electrical outlets. They allow the passage of three furnace power conductors, three furnace

thermocouple wires, and a further three contacts which are currently not used. The arrangement of the seals with illustrations is found in Ismail (1974). A tenth electrical outlet allows the acoustic emission (AE) signal to pass from the transducer situated in the lower ram, through the closure, to the recording equipment. The confining pressure gas ( $N_2$ ) inlet also passes through the centre of the lower closure. The closure is held in position against the internal load of the confining pressure (which can reach 700 tonnes), by a large screw threaded nut. Due to the multitude of electrical and gas connections the closure is removed only for maintenance purposes. A description of the nut and its principle design considerations is found in Jones (1989).

#### 4.2.2. Upper Closure.

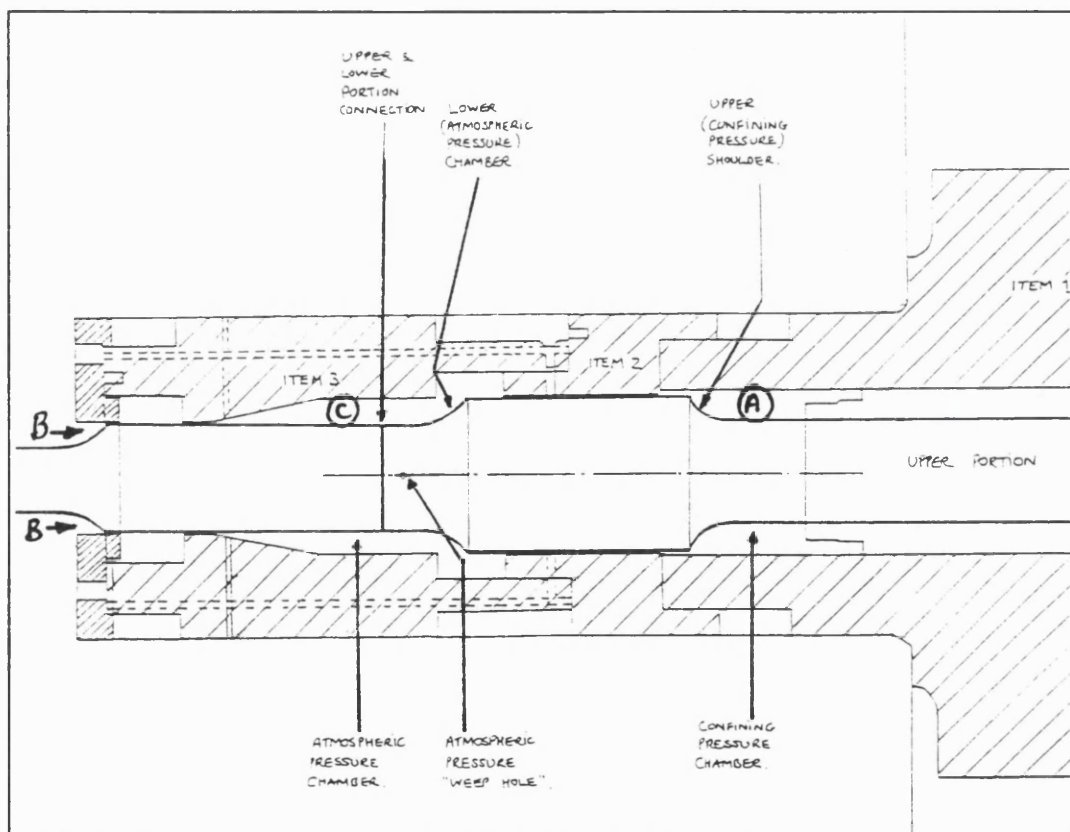


Fig. 4.2.2.a. Diagram of X-section of axial loading ram illustrating the two annular chambers for pressure balancing, see text.

The upper closure incorporates the loading piston which must be free to move axially and which must be removed routinely for emplacement and removal of rock specimens. To complicate the sealing arrangement the piston is

*pressure balanced*. This balancing is achieved by an annulus along the main shaft of the piston, (fig 4.2.2.a.) above and below which are situated two chambers, A and C. Confining pressure gas is fed to the upper chamber (A), and atmospheric pressure is allowed access to the lower chamber (C). The area of the shoulder of the annulus upon which the confining pressure acts is equal to the area of the ram exposed to the working volume of the vessel (B). The net effect is true triaxial hydrostatic stressing under the application of the confining pressure. It also means the load required to axially deform a rock specimen is the differential stress alone, thus the actuator need not be so powerful and the load cell can be more sensitive, see Jones (1989). This complex arrangement requires six modified Bridgman "O" ring seals in order to function.

#### 4.2.3. Servo-Controlled Actuator.

The axial load is supplied by a *servo-controlled actuator*. Its maximum load is 20 tonnes which translates to over 1100MPa differential axial stress on a 15mm diameter sample. The actuator controller includes a *ramp generator* which is used to set rates of change of control signals. Usual settings include *load control*, *displacement control*, and *displacement rate control*. By taking a feedback signal from either a strain gauge built-in to the actuator, a load cell, or two externally mounted Linearly Variable Differential Transducers (LVDT's), one of three loading regimes can be employed;

- (i) constant stress (displacement occurring as necessary as the specimen deforms),
- (ii) constant displacement (load decreasing as the specimen deforms under a fixed displacement), or
- (iii) constant displacement rate (the piston moves at a fixed rate and load is monitored as the specimen resists deformation). With this mode strain rates as low as  $1 \times 10^{-7} \text{s}^{-1}$  are possible.

A detailed description of the actuator, its commissioning, and operation is found in Ayling (1991).

#### **4.2.4. Loading Piston.**

The axial load piston discussed above is constructed in two parts. The upper part (piston) comprises the main shaft with annulus, the lower part (ram) comprises the end cap (rock/ram interface and transducer housing), and pore fluid connection. A full description of the design of the original 10mm ram is found in Ismail (1974). Since the original design the rams have been rebuilt for 15mm specimen size and for a variety of experimental conditions (e.g. high temperature, AE monitoring, P- and S-wave velocity measurement, and pore fluid volumetry experiments), see Jones (1989) and section 4.4.

#### **4.2.5. Load and Stress Measurement, Correction and Calibration.**

Differential load (and therefore stress), is measured directly by virtue of the balanced ram system. However, the load cell, positioned between the actuator and the piston, records the force on the sample and the resistance force provided by the seals and the copper jacket. These components of the measured force are functions of confining pressure and temperature.

Seal friction has been dealt with by Jones (1989). Experimentally seal friction correction is quite straight forward; the load required to push the lower-ram/sample/piston assembly the final few millimetres before the lower ram makes contact with the inside base of the pressure vessel is equal to seal friction. This value is recorded and subtracted from all subsequent load readings before differential stress is calculated. The moment of contact is readily recognised on the load displacement record by a sharp change in slope.

Resistance from the copper jackets has been covered by Ismail (1974). He used an equation previously determined by Murrell and Chakravarty (1973).

These values were recalculated for 15mm jackets by Jones (1989). Fig 4.2.5.a. graphically displays the strength of copper jackets under a variety of temperatures and axial strains. Based on this computer software adjusts the axial stress during data processing, (see section 4.6.2.).

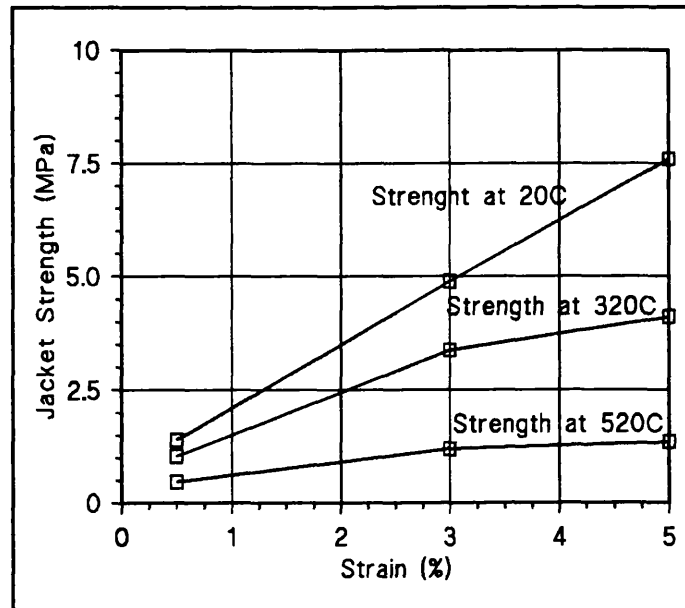


Fig. 4.2.5.a. Strength of annealed copper jackets against axial strain and furnace temperature.

In order to ensure reliable load values during the experimental programme the load cell required calibrating after a maintenance service. A proof ring was employed for this purpose. Siting the ring in-line with the actuator and the newly serviced load cell, readings were taken from the proof ring and load cell at various axial load settings. The results proved to be within allowable limit of 1% of full range. A graph of the calibration is shown in fig. A.1., appendix A.

#### 4.2.6. Strain Rate Correction and Machine Stiffness.

Along with allowing the precise control of deformation conditions, servo-controlled equipment can also analyse and potentially control machine stiffness. Traditional *soft* testing machines have an inherent problem when testing strong rocks; the stiffness of the rock is greater than that of the machine. The result is that during strain softening the system also unloads, transferring its accumulated strain energy to the sample. This strains the sample more than would otherwise be the case with a loading system that had less or no accumulated strain energy. It can lead to dynamic failure in specimens that would otherwise unload more slowly. This has been analysed by Hudson et al (1972), Cook (1981), Rist et al. (1990), and with direct reference to this equipment by Ayling (1991).

Servo-controlled equipment allows the actuator to change displacement rate depending on the rate at which the loading system absorbs or releases strain energy, and this allows the specimen to deform at a constant strain rate. Precise control of specimen strain rate can be achieved by either of two methods; (i), by measuring strain directly at the specimen, or, (ii) by correcting for the apparent elastic strain included in the LVDT signal using electronics in the actuator controller unit. The two methods have been experimentally compared by Rist et al. (1990). The electronic method (ii) involves taking a portion of the load signal and feeding it back in an *outer feedback loop* which reduces the LVDT *inner feedback loop* signal by a proportion representing ram deformation. The proportion was found experimentally (Ayling 1991), for the present apparatus with the servo-hydraulic system.

Neither of these systems is applicable to the test apparatus used in this study. The first method is impracticable since the specimen is surrounded by the confining medium, and the electronic method proved unsuitable (Ayling (1991); negative strains and instability resulted when large loads were required to overcome seal friction without specimen strain. Thus, although the present apparatus is servo-controlled it does not simulate a stiff machine. In the present work ram strain was removed during data analysis. The machine behaved "softly" with some stiff rocks as is seen in section 6.5. on triaxial experiments on Penmaenmawr microgranodiorite.

Fig 4.2.6.a. shows the variation in specimen strain rate throughout a drained experiment on Darley Dale sandstone at  $C_p' = 20\text{MPa}$ . Immediately obvious is the peak in specimen strain rate during specimen failure. It is also interesting to note that once new dilatant crack growth begins and rock elastic stiffness decreases (at  $\epsilon \approx 0.5\%$  &  $1/2$  peak stress), the specimen strain rate increases. Post peak specimen strain rate is constant and as set on the actuator controller because differential stress is constant and therefore the piston strain energy absorption rate is constant.

In order to ensure reliable and repeatable readings the LVDT's were periodically calibrated using a micrometer. A mechanical micrometer is employed as it is

considered more stable and accurate than the LVDT. Setting the LVDT firmly in a micrometer jig, the LVDT is displaced a known distance and comparison is made between the micrometer reading and servo-controller unit voltage

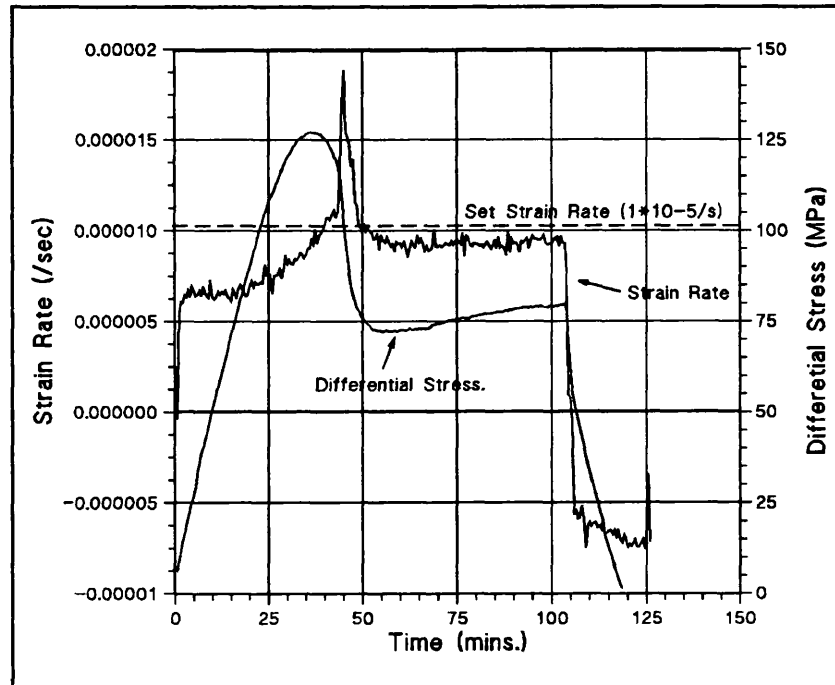


Fig. 4.2.6.a. Specimen strain rate against axial strain, differential stress also shown.

reading. Whilst the LVDT is more accurate at monitoring small displacements than a micrometer, the procedure confirmed, over a 5mm range, that the LVDT was producing reliable large scale displacement measurements.

#### 4.2.7. Three Stage Harwood Compressor.

The Harwood compressor, as summarised by Jones (1989), consists of three stages. The first two (reciprocating) stages of the pump run automatically to a pre-set pressure of up to 350MPa. The single acting third stage is manually operated and takes the maximum pressure up to 1400MPa.

At the start of this project the pump and vessel system was incapable of containing a pressure greater than  $\approx 120$ MPa. This problem prompted extensive work re-grinding and reseating all high pressure seals and junctions, and overhauling or replacing the electrical outlets in the bottom closure of the vessel. Finally, a 1400MPa valve was installed *downstream* of the pump as close to the vessel as possible. This reduced the number of joint and valves required to maintain confining pressure from 24 to 4. The leakage rate was

considerably reduced as a consequence of this work and allowed the experimental programme proper to commence.

To improve recording accuracy and allow the confining pressure reading to be logged automatically a 700MPa Intersonde HP28 pressure transducer and 650MPa safety burst unit was installed in the *hp* tubing system adjacent to the pressure vessel. Accuracy of the pressure measurement system was then increased to 0.25% of full transducer range, ( $\pm 1.75\text{MPa}$ ). The voltage output from the transducer was fed to the data logger to be recorded on the logging computer, (section 4.6.). The modified system allows accurate monitoring of confining pressure and leakages, and tests involving pore volume changes under a changing confining pressure can be logged accurately and automatically.

### **4.3. High Temperature Furnace.**

#### **4.3.1. Furnace Arrangement, Operation and Background.**

The high pressure triaxial deformation vessel is equipped with an internal furnace capable of  $1000^{\circ}\text{C}$ . It is contained within a steel cylinder which slides into the internal chamber of the pressure vessel after the removal of the top closure. Six electrical sockets at the bottom of the furnace make contact with six pins situated in the bottom closure. The contacts provide power for two heating coils and the output from two *R* type thermocouples. The original furnace was designed for 10mm diameter specimens and a full description the main design criteria, design details, diagrams and photographs is given in Ismail (1974). Jones (1989) modified the furnace for 15mm diameter specimens. Following their coverage only a short description is presented here.

A *Viscount* three-term thyristor controls and powers the furnace coils. The two thermocouples measure furnace temperature 10mm apart axially in the furnace, which allows the temperature gradient within the working volume around the specimen to be monitored. Temperature gradients result from

greater convection due to increased nitrogen density when under pressure. This was originally identified by Ismail, and controlled by minimising the working volume around the furnace and using baffles to inhibit the convection of gas from the *hot zone*. The later 15mm diameter specimen size furnace design results in a larger working volume around the specimen and hence a greater convection problem. To counter this, power to the upper coil is reduced compared with the lower coil. This adjustment is carried out by the operator and is dependent on N<sub>2</sub> pressure and furnace temperature.

The three term controller allows power output to be automatically controlled based on the thermocouple feedback signal. The three terms refer to the *integral*, the *derivative*, and the *proportion* of the temperature error (difference between set point and furnace temperature). Furnace temperature is maintained as close as possible to the set temperature based on these functions. The millivolt/temperature relationship for the Pt/Pt 13%Rh (*R* type) thermocouples employed is well documented and used as the basis for selecting the thermocouple feedback millivolt setting on the controller. The setting for the three terms is found by trial and error based on an established procedure detailed in the Viscount operating manual. An apparently complicated system works well once settings are established.

The specimen/ram arrangement used for this study (pore fluid ram and AE transducer lower ram), allows a maximum temperature of  $\approx 350\text{-}400^{\circ}\text{C}$  before the upper ram begins to temper and soften. For higher temperatures a different, high temperature ram manufactured from Nimonic 105 (for temperatures up to  $700^{\circ}\text{C}$ , although limited to 500MPa confining pressure and 750MPa axial load - Jones, 1989), must be employed. The electrically conductive paint used in the lower ram's piezo-electric transducer arrangement is also affected by elevated temperatures. This, combined with the problem of electrical furnace noise affecting the AE signal, renders high temperature experiments ( $300^{\circ}\text{C}+$ ) involving AE monitoring difficult to conduct.

#### **4.3.2. Commissioning and Logging Modifications.**

Before high temperature experiments could be executed the furnace and controller system required servicing and extensive modifications. This work was executed by the author. Servicing involved replacing the Kanthal windings where they had burnt out (see Ismail (1974) for details of winding hot spots), and checking the power and thermocouple extension cables. The original thermocouple monitoring arrangement is illustrated schematically in fig. 4.3.2.a.

As can be seen from fig. 4.3.2.a. the upper thermocouple cables feed directly to the furnace controller. This feedback ensures the set point temperature is maintained at the upper thermo-couple. Whilst both upper and lower

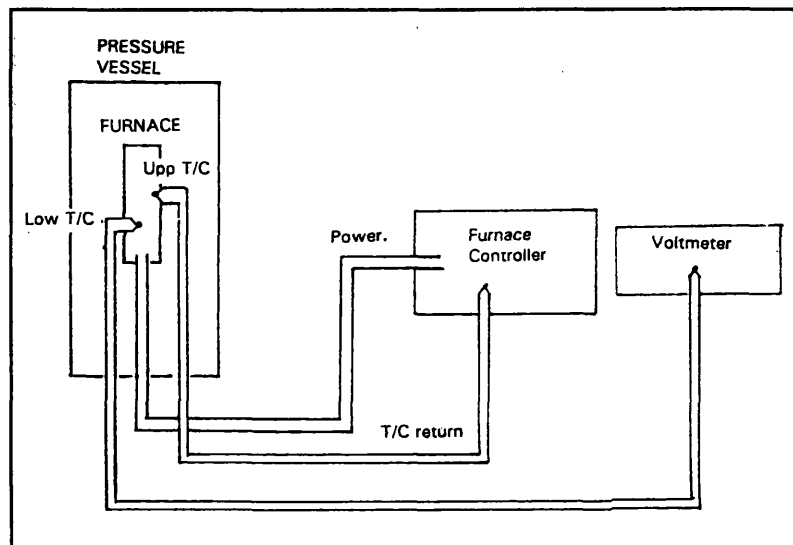


Fig 4.3.2.a. Schematic diagram of original wiring system for furnace temperature control and monitoring.

thermocouples monitor temperature, only the upper thermocouple is used as a signal return to the temperature controller.

The furnace was originally designed and commissioned prior to the introduction of the acoustic emission measurements system and Jones (1989) was the first to experience problems of furnace noise interfering with acoustic emissions and P-/S-wave signals. Fig. 4.3.2.b. shows the results of experiments on Solenhofen Limestone deformed at temperatures between form 20°C and 300°C, Jones (1989). Clearly the wave velocity signal and the stress/strain curve are affected by the high temperature. Jones attributes the oscillating curves to a fluctuating temperature causing expansion and contraction in the loading ram, and hence a fluctuating load. To a lesser extent he attributed the disruption to electrical noise from the furnace. My experiments (see fig 4.3.2.c.), have shown that load fluctuations do not affect the stress/strain curve. Electrical noise from the furnace, however, was found

to significantly affect AE data, to the extent that the data is unusable.

This study required that AE be monitored accurately during high temperature experiments and so a system whereby the furnace is switched off periodically to allow AE data logging was designed and installed. The main objectives of the system are detailed below:

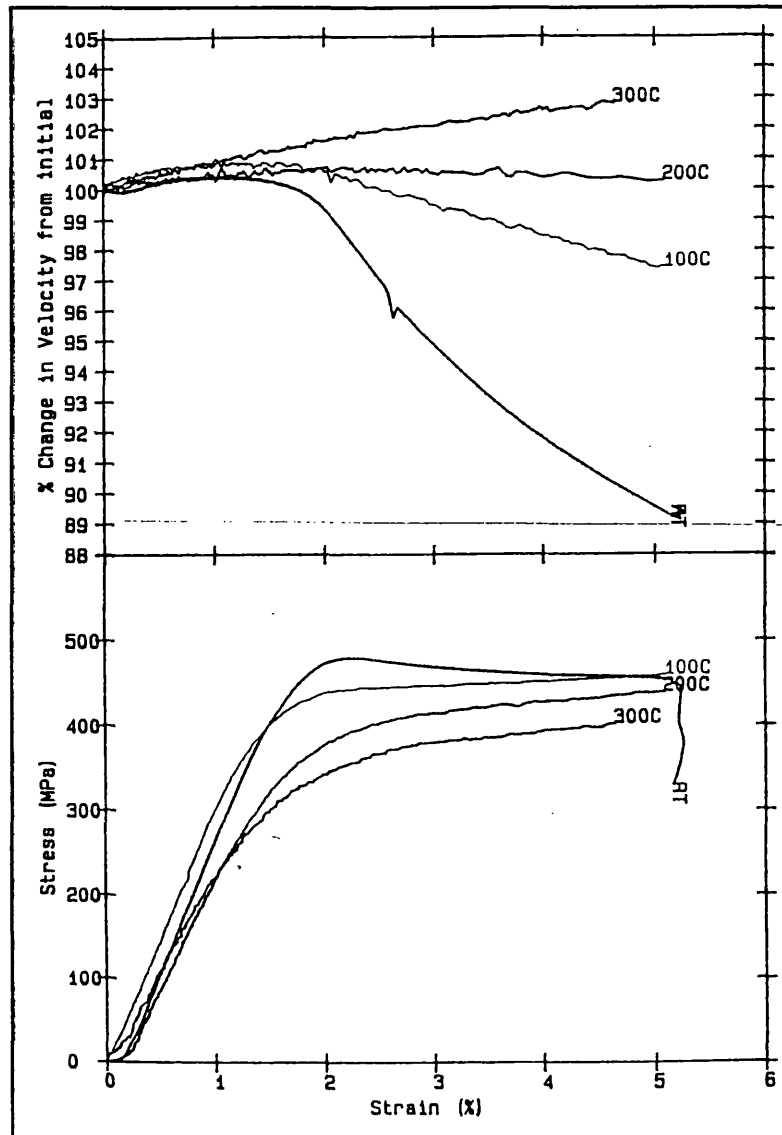


Fig. 4.3.2.b. Limestone deformed at 100MPa and temperatures 0-300 °C.  $V_p$  and Stress plotted against strain, see text and section 2.7.2.2., (after Jones 1988).

- ▶ For the furnace to switch off periodically to allow AE data to be collected.
- ▶ For the switching to be software driven - hence operating automatically during an experiment.
- ▶ For the switching frequency to be variable - allowing high frequency switching (4 cycles/min) - preventing large temperature fluctuations during high temperature experiments ( $\approx 200^\circ\text{C} +$ ).
- ▶ For the upper and lower thermocouple temperature to be monitored and displayed on the computer screen - allowing adjustment of upper and

lower coil power by the operator, hence limiting axial temperature gradient within the vessel.

The furnace switching system is illustrated schematically in fig. 4.3.2.d. As can be seen the *R* type thermocouple extension cables are fed from the reference junction via a *mercury switch* to the *Viscount* furnace controller. The extension cables ensure that only the voltage as a result of the temperature difference between the furnace and the reference junction only is measured. This is

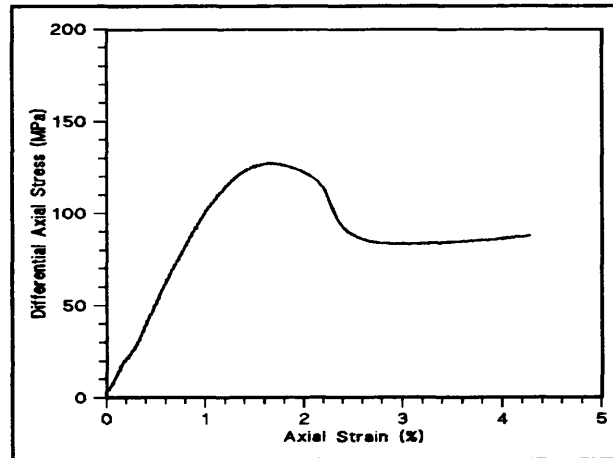


Fig. 4.3.2.c. Drained experiments on Darley Dale sandstone, deformed at  $C_p' = 122\text{MPa}$ ,  $T = 300^\circ\text{C}$ ; stress/strain unaffected by short period temperature fluctuation.

achieved by virtue of the extension cables having similar thermo-electric properties to the thermocouple metals. The mercury switching module used is a *Hewlett Packard 44428A 16 Channel Actuator* installed in the data logger. The *break-before-make* switching system is software driven by a PC via a *Hewlett Packard Interface Bus (HPIB)*. Operating software was written by the author and incorporated into the main logging programme. By activating the mercury switch the return thermocouple signal is disconnected from the *Viscount* controller and power to the coils automatically cut. This permits AE data logging unaffected by electrical noise. The data logger also records the thermocouple signal (section 4.6.), and software converts thermocouple voltage to temperature.

A number of details required addressing before fully commissioning the system.

- ▶ Ensuring junctions in the extension cables did not affect the thermocouple millivolts reading at the *Viscount* controller.
- ▶ Temperature of the cold junction.
- ▶ Timing of the switching between furnace and AE recording.

These problems are discussed below.

1) Thermocouple technology requires that only two junctions exist between two different metals in order to accurately measure a temperature difference - the *hot* and *cold* junctions. The numerous junctions in the

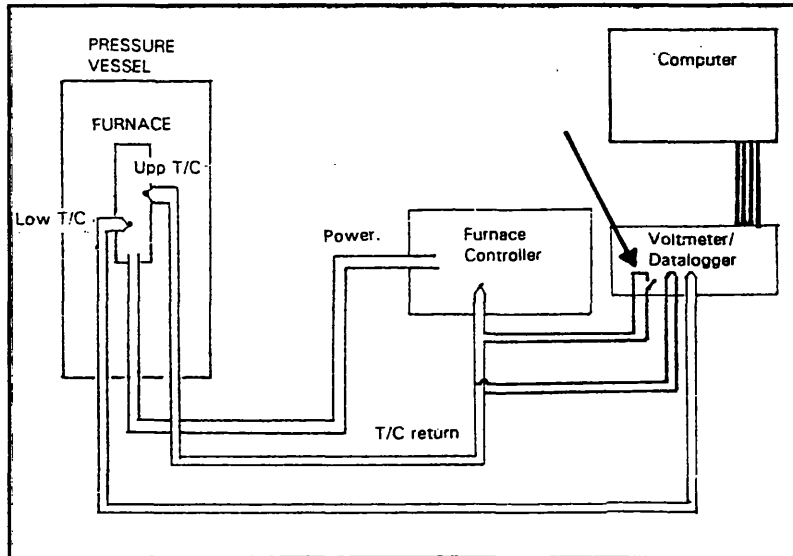


Fig. 4.3.2.d. Schematic diagram of modified T/C wiring system. Mercury switch located in Data logger on Upp T/C return circuit (arrowed).

extension cables due to the switching and logging system could possibly affect the thermocouple millivolt output. A calibration test was conducted whereby the upper thermocouple only was connected to the Viscount controller and the lower thermocouple output was measured independently. Readings for furnace temperature were recorded. Subsequently the logging and switching system was added to the upper thermocouple circuit whilst the lower thermocouple circuit remained unaltered. Again readings for furnace temperature were recorded. Results showed that the addition of the extra junctions in the upper thermocouple extension cables made negligible difference to the lower thermocouple reading, i.e. the temperature of the furnace did not change when the extra connections (logging and switching system) were added.

2) The "cold" junction for the system was physically situated in uncompensated circuitry of the Viscount controller and was taken as room temperature (18°C). This was programmed into the computer software, compensation being made between winter and summer months. Room temperature could be checked at any time using conventional thermometers. A potential room temperature error of  $\pm 3^\circ\text{C}$  is considered satisfactory for the elevated temperature tests.

3) The furnace electrical noise detected by the AE system affected not only the AE hit rate but also the event frequency/amplitude distribution (from which the seismic *b-value* is calculated). Fig. 4.3.2.e. shows the frequency/amplitude distribution for typical experiment. Spikes at the higher end of the amplitude range (50dB → 90dB) are a

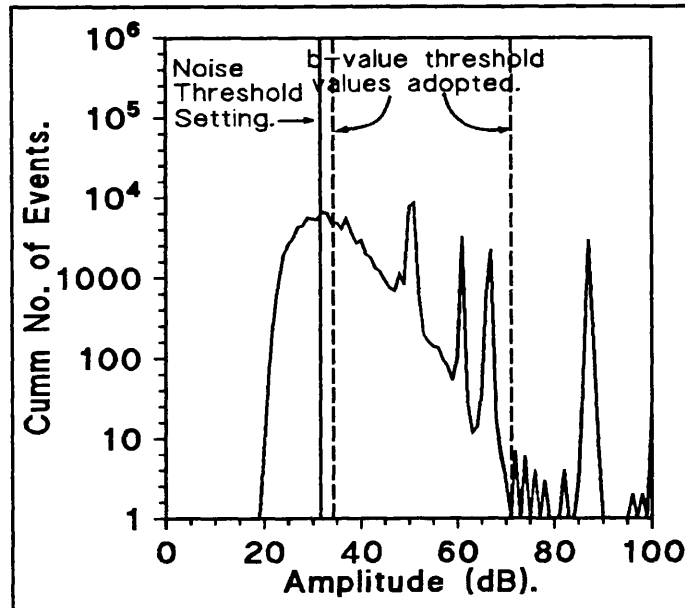


Fig. 4.3.2.e. Cumulative number of AE events against AE amplitude (dB). Spikes are a results of furnace power supply.

result of the furnace turning on only seconds before the end of the AE logging cycle. After further timing adjustments, later tests showed that even the slightest overlap in AE logging and furnace power (<1sec.) was difficult to avoid and produced sufficient events to distort the seismic *b-value* calculations. For this reason, as will be seen, results from high temperature experiments show AE event rate recorded well, whilst *b-value* data are unreliable.

## Conclusion.

Operation of the furnace is now such that it is powered and controlled from the Viscount controller, while the computer keyboard switches the furnace on or off, or triggers the furnace/AE switching system. The switching system allows alternate logging intervals to record AE data or energise the furnace. At temperatures <300°C, the system operates well allowing high temperature conditions and AE data logging. At temperature, >300°C furnace temperature loss during AE logging (perhaps up to 30°C), is such that overall furnace temperature fluctuation is too great and causes thermal expansion problems in the ram and pore fluid similar to those experienced by Jones (1989). Towards the end of the experimental programme, plans were made to adjust

the software such that 10secs. AE recording periods could be taken every 2mins., thus not affecting furnace temperature at elevated temperature. Time constraint meant this was not done.

### 4.3.3. Rock and Furnace Temperature Calibration.

The furnace and rock temperature calibration tests were designed to establish the rock temperature/furnace temperature relationship. A thermo-couple was fed down the loading piston into the middle of a hollow rock specimen and the

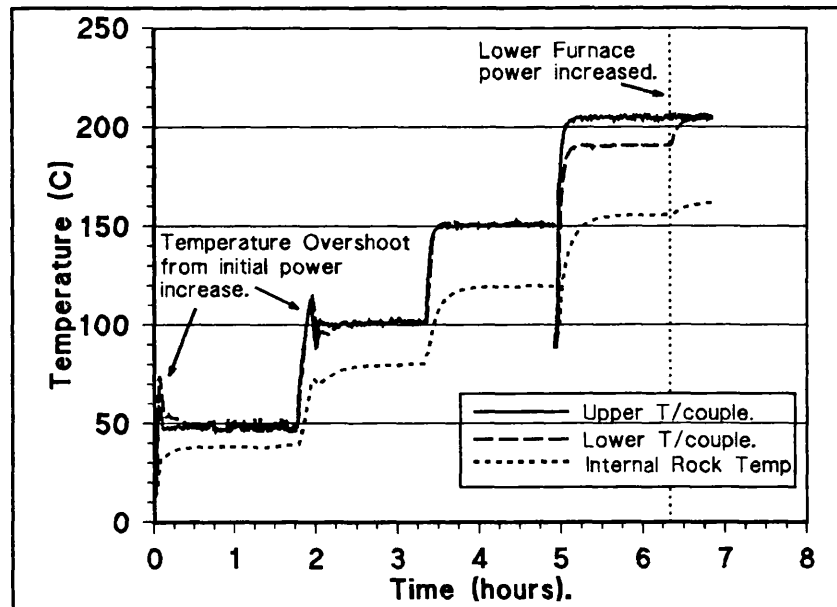


Fig. 4.3.3.a. Upper and lower furnace temperature and internal rock temperature calibration test results for a specimen under zero confining pressure, see text for details.

furnace energised. Ismail (1974) investigated the specimen temperature gradient and the specimen/furnace temperature relationship in the 10mm diameter specimen size furnace using a similar method, although calibration of the enlarged furnace had not been done.

Fig. 4.3.3.a. shows data for the upper thermocouple, lower thermocouple, and rock temperature, for a range of temperatures under zero confining pressure. It can be seen the value of rock temperature in °C reached  $\approx 80\%$  of the value of the furnace temperature. The graph also shows the temperature instability each time the furnace temperature is raised to a new set point. Experience has proved that this instability usually requires upper and lower coil power adjustment. Fig 4.3.3.b. shows a similar experiment. Marked on the graph is the activation of the AE/furnace switching system, and the application of a confining pressure of 100MPa. The introduction of the switching system again

disturbs furnace temperature (although experiments have proved this instability settles down within  $\approx 20$ mins), and again rock temperature in  $^{\circ}\text{C}$  reaches 80% of furnace temperature. The

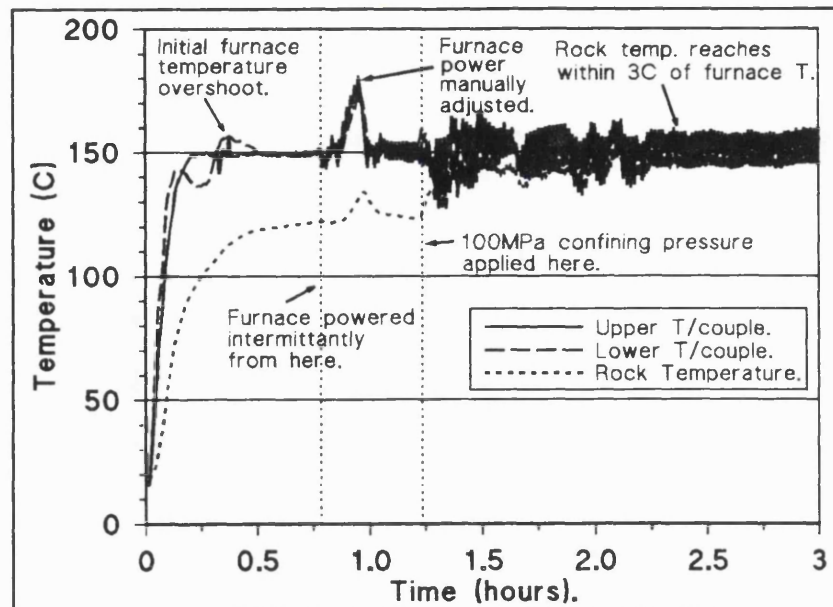


Fig. 4.3.3.b. Upper and lower furnace temperature and internal rock temperature for a calibration test under the effect of 100MPa confining pressure, see text for details.

application of the

confining pressure causes initial fluctuation followed by the rise of the rock temperature to  $\approx 95\%$  of furnace temperature value in  $^{\circ}\text{C}$ . This is attributed to higher  $\text{N}_2$  conductivity and better contact between the copper jacket and rock specimen. From the results, exact rock temperature can be obtained from furnace set point temperature.

Following these modifications, the furnace functioned well. For the first time the high pressure triaxial equipment is capable of monitoring AE data from experiments on rocks under high temperature and pressure conditions.

#### 4.4. Pore Fluid Volumometer and Fluid Pressure Intensifier.

##### 4.4.1. Purpose of Apparatus and General Arrangement.

The *Servo-controlled Pore Fluid Volumometer and Pressure Intensifier* has a basic arrangement comprising two cylinders connected end to end on a single shaft. One cylinder has a large bore ( $\approx 50$ mm diam.), and the other, at the opposite end of the shaft, has a small bore (6mm diam). The large piston is

powered by low pressure hydraulic oil (max. pressure 21MPa), and the small piston moves in response to the large piston generating fluid pressures of up to 700MPa - this is the process of *pressure intensification*. By controlling the low pressure side of the intensifier, high pressure fluid is controlled. A detailed description of this arrangement with diagrams can be found in Read et al. (1989). Low pressure hydraulic oil is generated by a three phase 1.5Kw motor connected to a hydraulic pump. By connecting the high pressure system to a rock specimen in the triaxial deformation cell the intensifier can supply and/or monitor high pressure pore fluid changes during triaxial deformation. ¼" (6.4mm) tubing connects the intensifier to the vessel via a series of valves and pressure transducers.

At the outset of this study the pore fluid pressure intensifier was connected to a hydrostatic testing vessel for a previous rock permeability study. Before the commencement of the experimental programme the equipment was modified and relocated. Details are given below.

#### 4.4.2. Servo-Control and Pressure Calibration.

The intensifier system can operate in one of three modes; *pressure control*, *volume control*, or *pressure pulse permeability testing*.

- ▶ *Pressure Control* involves taking a feedback signal from a fluid pressure transducer. If the system volume (rock porosity and tubing volume) should change as a result of a change in pore and crack volume, a change in fluid pressure results. The resultant error between actual fluid pressure and fluid pressure selected on the servo controller moves the intensifier piston to eliminate the error. This is the *drained* condition, i.e. effective pore pressure is kept constant whilst pore volume changes in the specimen are measured by intensifier piston displacement readings.
- ▶ *Volume Control* involves taking a feedback signal from an LVDT attached to the intensifier piston. The piston position is monitored and

moved, if necessary, to eliminate error between a pre-set value for piston location and the actual piston location. This is the *undrained* condition, i.e. fluid volume is kept constant and any pore pressure change generated as a result of pore and crack volume change is monitored.

- ▶ *Single ended Pressure Pulse Permeability Testing* requires the use of a *one-way check valve*. A pulse of fluid pressure is applied through the check valve to one end of a specimen. The check valve ensures fluid pressure can only drain into the rock specimen, and the decay time of this pressure drop is monitored and related to rock permeability and specific storage, (Read et al. 1989).

Two Intersonde HP28 700MPa pressure transducers are employed in the system and are calibrated regularly; the wheatstone bridge arrangement in the transducers allows this. Accuracy is  $\pm 1.75\text{MPa}$  for a 0-700MPa range. The piston displacement LVDT is regularly checked for maximum and minimum values directly from readings on the control panel.

### **4.4.3. Pressure Intensifier Modification.**

#### **4.4.3.1. Modification Objectives.**

This study requires accurate measurement of pore fluid characteristics during rock deformation. A system to supply fluid under pressure to rock specimens is an integral component of the apparatus. Modifications to the intensifier achieved this by relocating and adapting the pore fluid control & monitoring equipment and the pressure transducers and valves.

The main objectives of the modifications are given here.

- ▶ To *close couple* the intensifier to the triaxial vessel to minimise the Upstream Reservoir Volume (URV) of the system.

- ▶ To connect the intensifier control electronics and logging system to the main data logging system in order to bring all test parameters under one logging time base for easier data analysis.
- ▶ To ensure the system can allow both drained and undrained experiments.
- ▶ To ensure the high pressure tubing system can allow for a variable URV.
- ▶ To ensure the system has the capability for syn-deformational pressure pulse permeability testing.
- ▶ Ensure simple connection and removal of the high pressure tubing to the top axial loading piston, permitting easy emplacement and removal of rock specimens.

#### 4.4.3.2. Fluid Compressibility and Tube Hoop Strain Analysis.

The *close coupling* requirement was prompted by results of early *undrained* triaxial experiments which displayed small changes in pore fluid pressure with initial rock compaction and rock dilatancy during deformation. Because the system was *remotely coupled* to the vessel the volume of fluid under the influence of this changing pore volume (*System Volume*, or URV) approached 25,000mm<sup>3</sup>. Water compressibility and *hp* tubing system hoop strain were thought to be the causes of the reduced pore fluid pressure response and are investigated below.

#### Water Compressibility.

Fig.4.4.3.2.a.shows the relationship between pressure and specific volume of water for water pressure between 0→700MPa. For fluid pressure between 0→200MPa, a change of 5MPa causes a fluid volume decrease of 0.17% (or 0.034% per Mpa). For the whole system of 25,000mm<sup>3</sup> this represents a 50mm<sup>3</sup>

decrease in fluid volume for an increase in pressure of 5MPa.

Fig. 4.4.3.2.b. shows the results of a series of calibration tests examining the effect of different URV's in which the volume change required to produce a given change of pore fluid pressure as measured as a function of URV. The experiments were conducted on the *hp* tubing only.

Clearly fluid compressibility and therefore the URV during *undrained* experiments is crucial to the potential fluid pressure rise and must be reduced to fully examine pore fluid pressure changes during triaxial deformation.

### Tube Hoop Strain Analysis.

Using standard equations for tangential strain on the internal wall of a thick walled tube, the following tube cross-sectional area changes for a 1MPa change in fluid pressure have been calculated.

For a 25,000mm<sup>3</sup> URV with perhaps 95% of the fluid volume contained within *hp* tubes (the remainder contained in elbows, junctions and valves) an increase in fluid pressure of 5MPa represents an increase in system volume of 1.5mm<sup>3</sup>. Tangential hoop strain in the high pressure intensifier cylinder of the

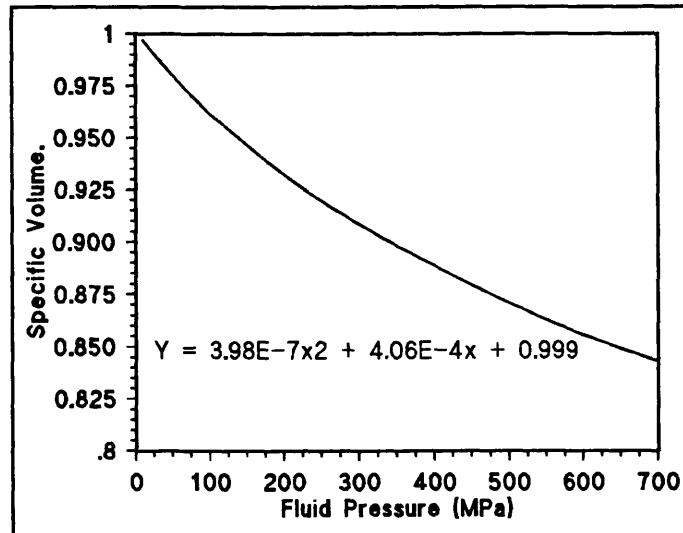


Fig. 4.4.3.2.a. The relationship between specific volume and pressure for water. Taken from steam tables, at 20°C.

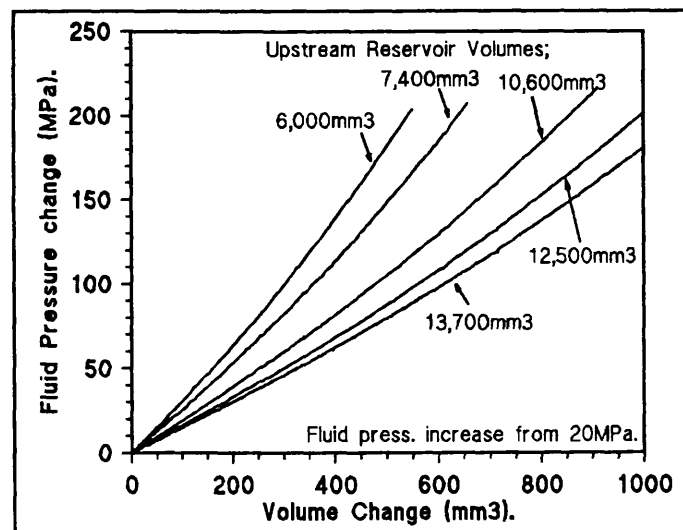


Fig. 4.4.3.2.b. Results from calibration tests showing the relationship between pore volume reduction with increasing fluid pressure, see text.

system was also considered and found to be similarly negligible. This is expected if the high pressure piston seals are to function correctly under all working fluid pressures. Table 4.4.3.2.a. below shows the percentage increase cross-sectional area for different *hp* tubes.

<u>Tube O.D.x I.D.</u>	<u>Tube X-</u> <u>sectional area</u> <u>Increase/MPa.</u>
$\frac{3}{8}'' \times \frac{1}{8}''$	0.00135%
$\frac{1}{4}'' \times \frac{1}{16}''$	0.00130%
$\frac{1}{8}'' \times 0.020''$	0.00200%

Table 4.4.3.2.a.

A fluid pressure changes of 40MPa+ in an URV of 25,000mm<sup>3</sup> represents a 16mm<sup>3</sup> increase in tubing volume. The undrained experiments in this study involved an URV of 1/10<sup>th</sup> of this, representing a tubing volume increase of 1.6mm<sup>3</sup> for a pore fluid pressure change of 40MPa. It can be concluded therefore that the increase in URV size under increasing fluid pressure due to hoop strain is negligible.

*In conclusion*, to fully study the effect of pore fluid pressure change on deformation the URV size must be minimised. This consideration prompted the first four bullet points of section 4.4.3.1.

#### **4.4.5. Modified Fluid Pressure Intensifier Arrangement.**

This section describes the physical arrangement of the modified apparatus plus auxiliary equipment designed and manufactured.

##### **4.4.5.1. Fluid Intensifier Modifications.**

Fig. 4.4.5.1.a. shows the intensifier cylinder, low pressure hydraulic oil system and control manifold located adjacent to the triaxial vessel's safety cell. The fluid pressure signals are fed to the main data logger. The logging software has been re-written to accept more data channels, process extra data and

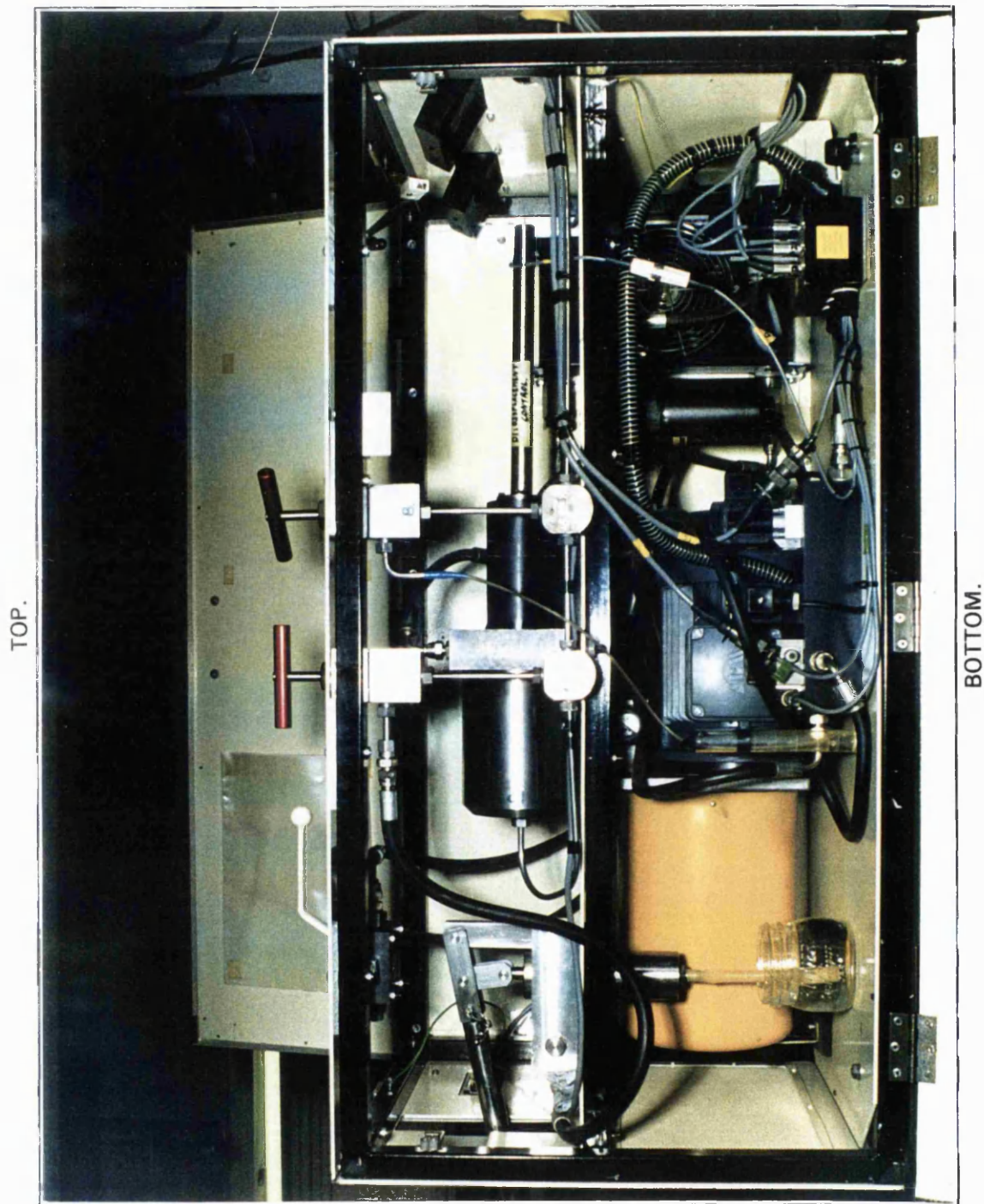


Fig. 4.4.5.1.a. Photographs of the pore fluid intensifier unit, see text for details.

display it continually on a PC monitor.

Figure 4.4.5.1.b. shows a photograph of the high pressure tubing system adjacent to the triaxial cell. Fluid pressure is generated at the intensifier (fig. 4.4.5.1.a.) and high pressure tubing feeds the fluid through to the pressure vessel. The fluid flows to the rock sample through a number of junctions and a remotely operated valve positioned between the intensifier and the rock specimen. Either side of the large valve a pressure transducer is sited; P1

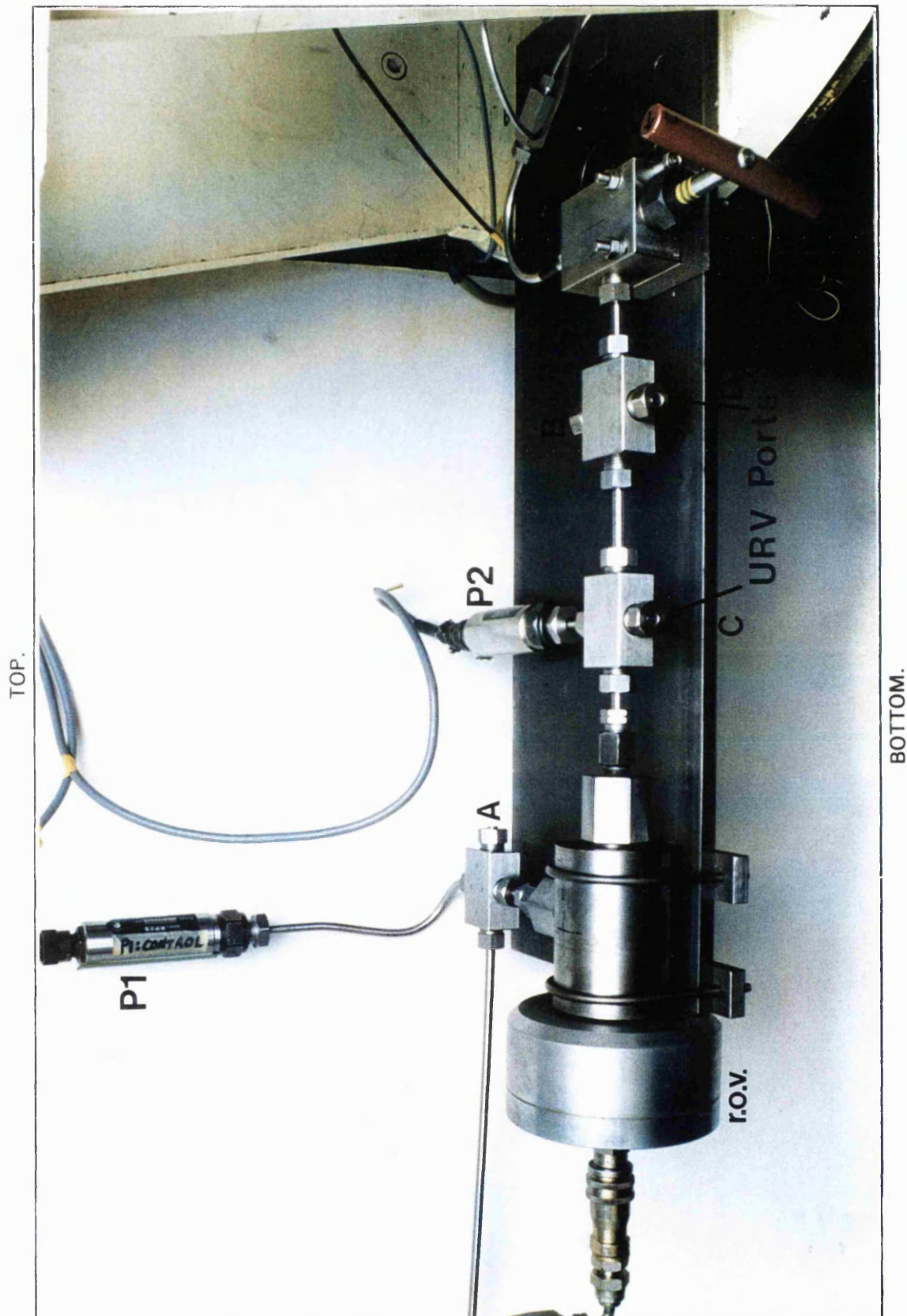


Fig. 4.4.5.1.b. Photograph of *close-coupled* pressure transducers, r.o.v., of pore pressure intensifier system.

furthest, and P2 closest to the specimen. The remotely operated valve (r.o.v.) is positioned close to the specimen such that when it is closed the volume of fluid between the r.o.v. and the specimen is minimised.

When the r.o.v. is closed *undrained* conditions are established. The desired starting pore fluid pressure must be established prior to closing the valve, and once closed, pressure transducer P2 monitors the pore fluid pressure changes. In this condition the URV amounts to less than 2,500mm<sup>3</sup>. This compares with the pore volume of a sample of Darley Dale sandstone of 1,000mm<sup>3</sup>; thus the URV is 2.5x specimen pore volume. The r.o.v. is necessarily remotely operated because it must be closed after the confining pressure and pore fluid pressure have been attained and when safety regulations dictate the triaxial cell must be sealed within the safety cubicle. When the r.o.v. is left open pore fluid pressure is maintained by the intensifier cylinder. Under these conditions the fluid pressure remains constant and pore volume changes in the rock specimen are measured by piston displacement at the intensifier. This is the *drained* condition. In this mode the URV is immaterial to the experimental results as no fluid pressure change occurs.

Between the two pressure transducers (P1 & P2) there are a number of 4-way junctions, the extra ports these junctions provide allow the installation of a one-way check valve for *syn-deformation single ended pressure pulse permeability testing* (between two points marked A. and B.), and of extra URV sections (ports C. & D.).

The additional URV sections consist of lengths of large bore high pressure tubing. The capacity of a one metre length of the HiP 3/8" (9.53mm) O.D. 1/8" (3.18mm) I.D. *hp* tubing is  $\approx 8,000\text{mm}^3$ , hence only a short length of the tube can double the URV for an *undrained* experiment. Sections equalling 3,000mm<sup>3</sup>, 6,000mm<sup>3</sup>, and 9,000mm<sup>3</sup> were manufactured for the experimental programme, and combinations of these are used to conduct experiments examining the effect of the URV on fluid pressure change and deformation, section 6.2.2. & 6.2.4.2.

In order to allow the fluid to flow into and out of the specimen, the fluid must pass down the centre of the piston, through a distribution plate and into the specimen. The system adopted to achieve this consists of an HiP *reducer coupling* allowing the 1/4" tubing to connect to 1/8" tubing. The 1/8" tubing passes down the centre of the piston and connects directly to the ram only

200mm from the specimen. The 1/8" tube is shaped to pass into the piston through the *piston head block*.

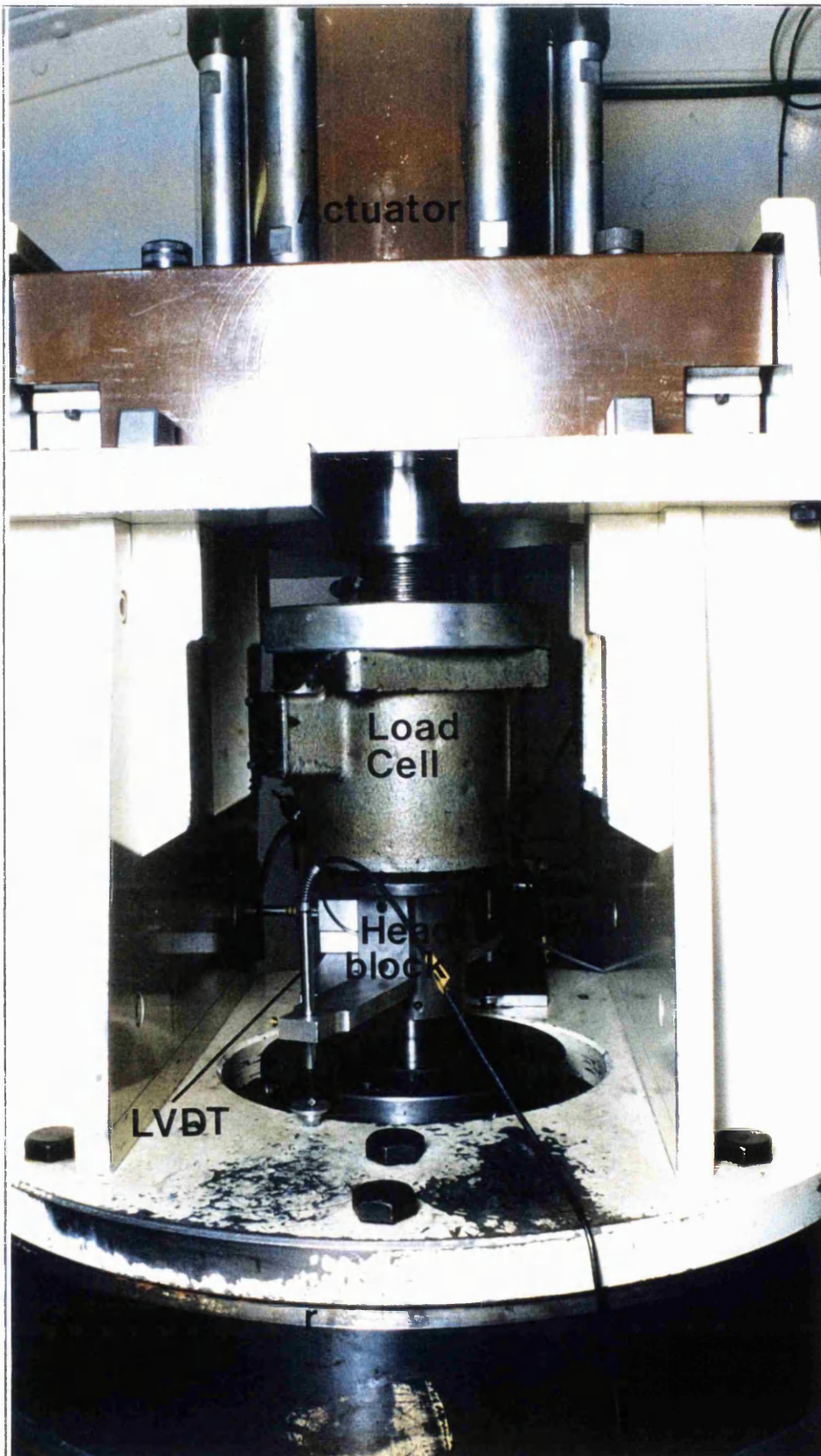


Fig. 4.4.5.1.c. Photograph of axial load actuator, load cell, and piston head block. See text for details.

Figure 4.4.5.1.c. shows a photograph of the *piston head block*, the arrangement of the 1/8" tube is positioned behind the head block.

#### 4.4.5.2. Redesigned Pore Fluid Ram.

The Pore Fluid Ram was re-designed twice for the system. The piston which supplies the axial load to the specimen is comprised of two sections as discussed earlier in section 4.2.4. This arrangement allows for the lower section (ram) to be removed either for maintenance or for the connection of a different ram for different physical property measurements. The two sections are joined by a male/male threaded connector piece. For the previous experimental programme an upper ram similar to the existing AE transducer lower ram arrangement was installed. This gave the facility for P-/S-wave velocity measurement experiments to be conducted. For pore fluid volumetry experiments the ram arrangement as illustrated in figure 4.4.5.2.a. is employed.

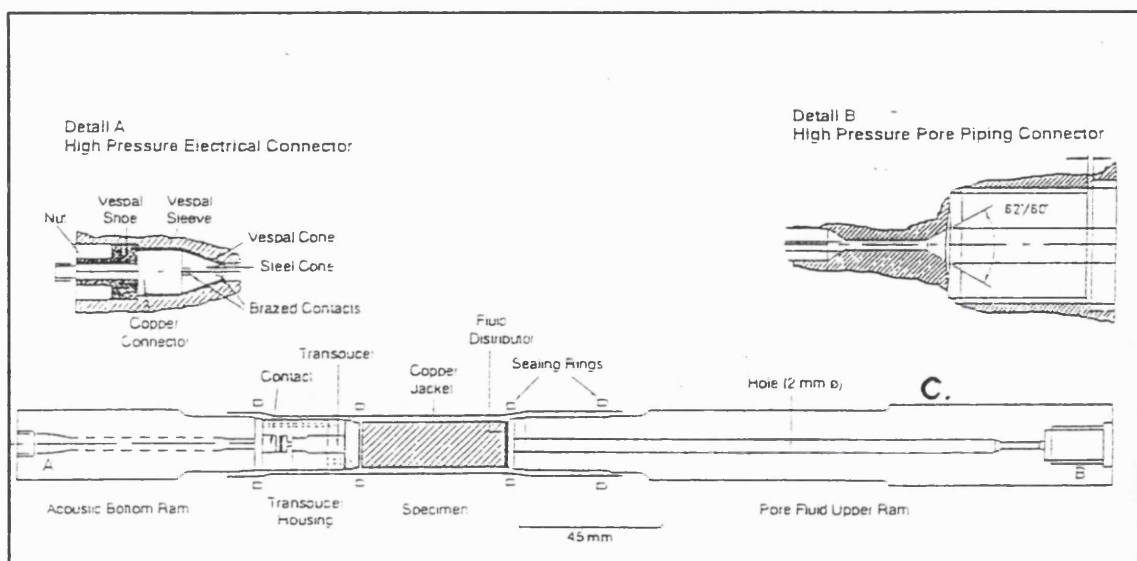


Fig. 4.4.5.2.a. Original pore fluid volumeter upper ram. Position C. indicates position of hair-line crack failure.

The 1/8" tubing is connected to the ram by virtue of a redesigned male/male connector designed by the author. The connector is hollow and the lower section is shaped such that it acts as a high pressure gland nut. The fluid then passes directly from the 1/8" *hp* tube to the inside of the ram. The ram contains a central 2mm diameter bore allowing fluid to flow into the rock



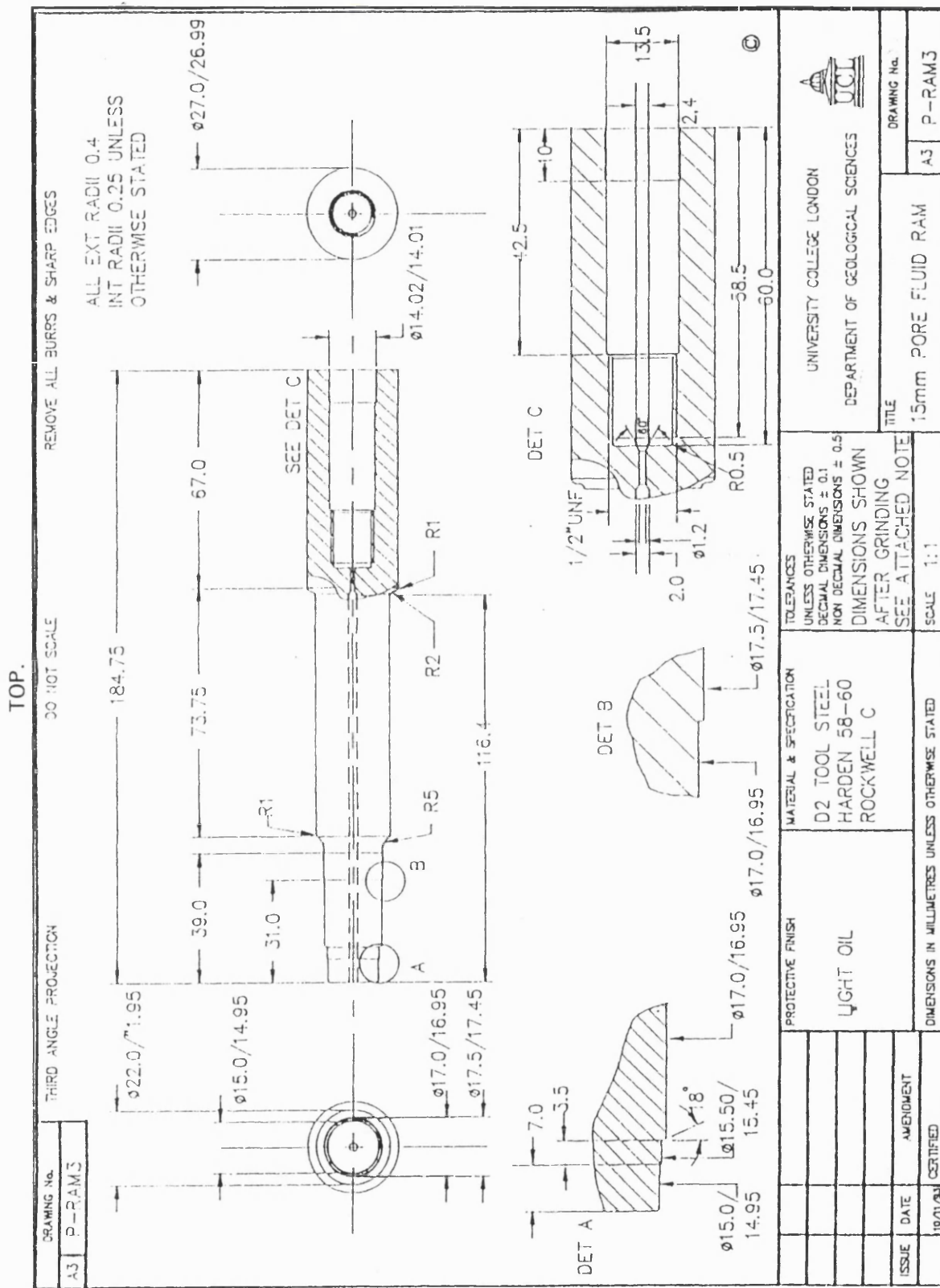


Fig 4.4.5.2.c. Redesigned pore fluid volumetry upper ram. See text for details.

high pressure active aqueous fluid acting on the poorly finished internal surface of the bore promoted vigorous sub-critical stress corrosion cracking. The leak was discovered using the *Pore Fluid Ram Testing Apparatus* (section 4.4.5.3.), and caused considerable delay in the experimental programme. It prompted a redesign of the pore fluid ram.

The re-designed pore fluid ram is illustrated in figure 4.4.5.2.c. The major modifications are detailed below:

- 1) To include a narrower, *honed* bore in the centre of the ram. The thicker wall that the narrower bore provides resists tangential tensile stress better and the smooth internal surface resists the initiation of sub-critical stress corrosion cracking.
- 2) To deep-set the high pressure 1/8" tube connection. (See detail C on fig 4.4.5.2.c.). This ensures that the tangential hoop stress in the bore is reduced by the action of the externally acting confining pressure.
- 3) To extend the length of the final 15mm diameter section of the ram (at the rock/ram interface) from 1.5mm to 7mm. See detail A on Fig. 4.4.5.2.c. The advantages of this are two-fold.
  - ▶ This section transfers compressive axial load to the specimen and experiences the greatest axial stress. The extended length allows for machining, if necessary, for maintenance purposes.
  - ▶ The copper jacket sealing system relies on an interference fit between the ram and the copper at a change in ram diameter from 15mm to 15.5mm. This diameter change has been shifted 5.5mm away from the specimen. This separates two vulnerable locations in the jacket sealing system; the strained copper jacket at the seal, and the rock/ram interface where loose grain cavities in large grain sized rocks *can* cause puncturing of thin walled copper jackets.
- 4) Redesign of the male/male piston/ram connector piece to meet two new criteria. See fig. 4.4.5.2.d.
  - ▶ The design of the collar and gland system of the high pressure 1/8" tube fitting was designed to stricter tolerances after the previous arrangement gave leakage problem at that point.

- ▶ The dimensions of the connector piece required customising to the manufactured pore fluid ram dimensions. This ensures the correct compressive stress simultaneously between the two sections of the piston, and between the 1/8" *hp* tube and the *hp* port.

#### 4.4.5.3. Pore Fluid Ram Testing Apparatus.

A photograph of the pore-fluid-pressure-ram testing frame design by the author is shown in fig. 4.4.5.3.a. The purpose of the

apparatus was to subject the upper piston, 1/8" tube connector and *hp* tube, and the whole of the high pressure fluid system to working fluid pressures whilst outside of the pressure vessel. This allows inspection of all high pressure joints and seals from the intensifier to the *rock/ram* interface. The principle of the apparatus is to apply pressure to the pore fluid hole at the end of the ram (where fluid meets rock), achieve a tight seal, and allow fluid pressure to build up in the system. The ram is mounted vertically above a cone of sealing material. Under an axial load applied by three M16 bolts to the top of the ram, the cone penetrates the hole and deforms to make a seal. Originally a polytetrafluoroethylene (PTFE)

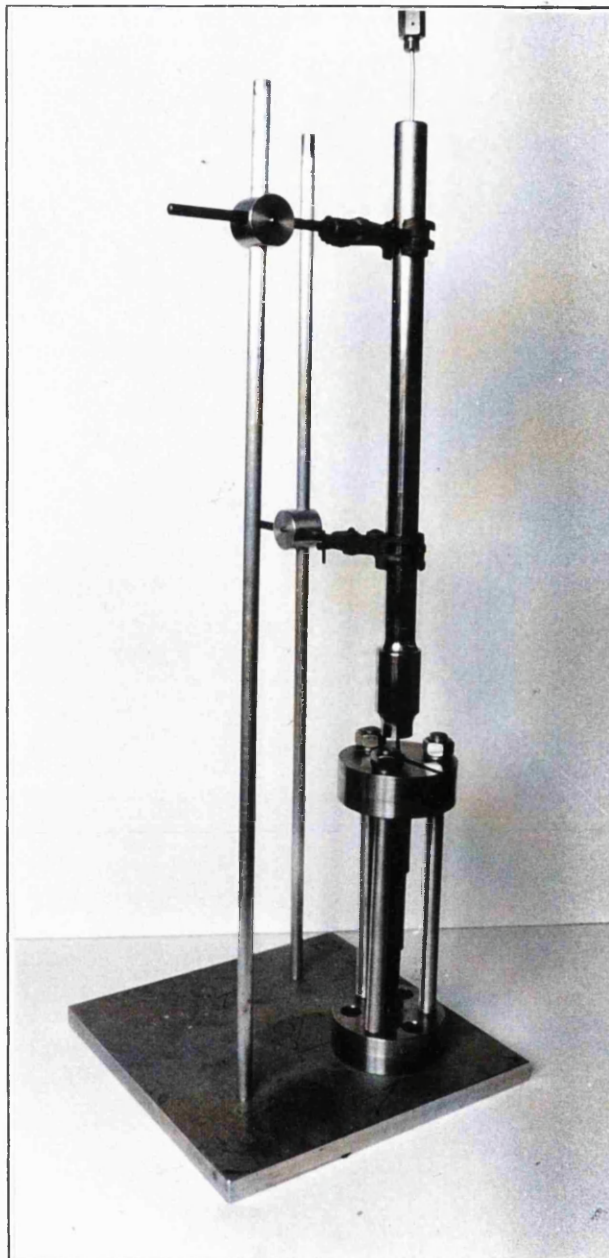


Fig. 4.4.5.3.a. Photograph of Pore fluid ram testing device, see text for details.

cone was used. Whilst the material deformed well into the ram-end hole, it lacked the frictional resistance to form a seal.

A cone of copper was found to be successful; this material deformed and gave a seal against the high pressure fluid. The apparatus allowed the author, after re-seating the *hp* seals in the pore fluid ram to fully check the system for leaks prior to an experiment.

#### 4.4.6. Results of Modification & Summary.

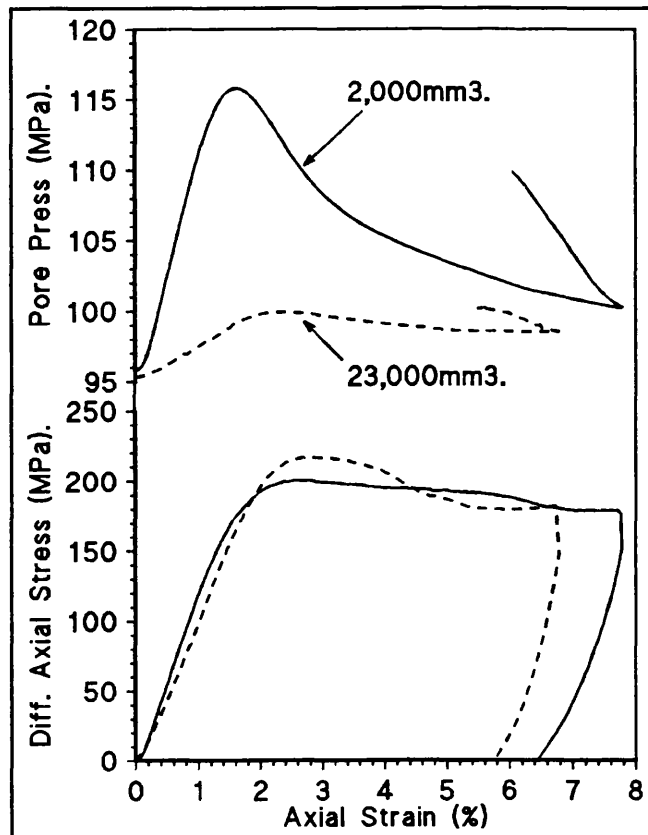


Fig. 4.4.6.a. Results of two triaxial deformation experiments under different URV's.

A comparison between two sets of results before and after

modification clearly illustrates the effect of a reduced URV on deformation. Fig 4.4.6.a. shows the results of two undrained experiments on Darley Dale Sandstone under similar confining pressure and starting pore fluid pressure.

The first test was conducted with an URV at  $23,000\text{mm}^3$  - the URV prior to the modifications - the second test was conducted after the modifications with an URV of  $2,000\text{mm}^3$ . Without venturing too deeply into the results at this stage, it can be seen that the deformation characteristics are clearly different. Results with  $\text{URV} = 2,000\text{mm}^3$  shows a much greater pore fluid pressure generated on initial compaction and greater pore pressure fall during dilatancy. The change in effective confining pressure brought about by this is evident in the shape of the stress/strain curves of the two results. With the modified pore fluid system the URV is variable and allows the implications of these results to be studied in depth, (see section 6.2.4.2.).

## 4.5. Acoustic Emission, Monitoring, and Logging.

### 4.5.1. Introduction and Acoustic Emission Overview.

An acoustic emission, (AE, stress wave generating activity, or microseismic event), is the elastic wave energy produced as the result of a sudden release of strain energy from a stressed defect in a solid medium. In geological materials it is usually a microcrack experiencing growth, a pore collapsing under the influence of stress, twinning, phase transformation, or indeed, on a larger scale, macroscopic failure (the sudden release of large strains). Sensitive AE monitoring equipment is capable of detecting these elastic waves. Careful analysis of the emissions can reveal details of source characteristics and damage induced (both cumulative and instantaneous), by the addition of the new defect to the solid matrix. The different mechanisms responsible for the production of AE are shown in fig 4.5.1.a. In the figure illustration (a) shows a simple tensile microcrack, illustration (b), (c) & (d) show tensile microcracks that are wedged open by a separate shearing process (grain boundary slippage at shearing junction, dislocation pile up, and shearing of a pre-existing crack). Illustration (e) shows pore collapse and the crushing of debris, and illustration (e) shows simple shear.

The terminology used in acoustic emission studies is illustrated in fig. 4.5.1.b. a n d described below.

AE Event is a single energy package as detected by the transducer as a result of a single

increment of crack growth or single pore collapse. Recent terminological

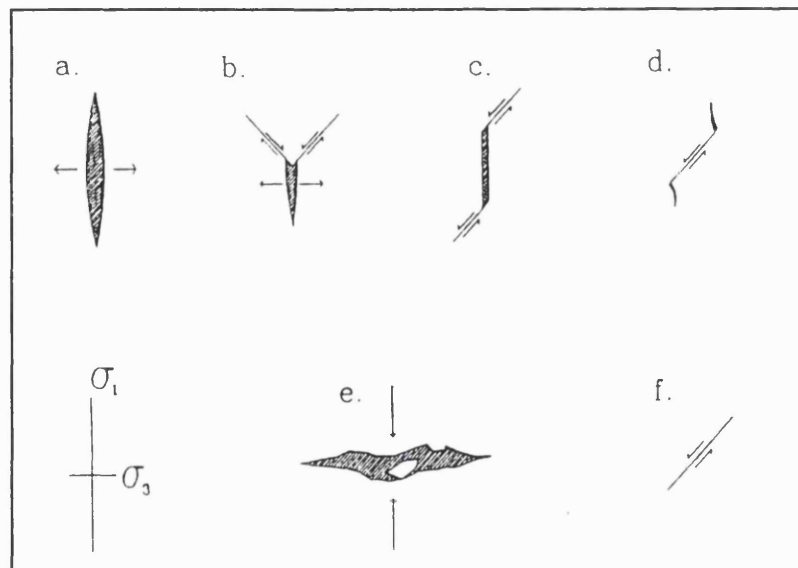


Fig. 4.5.1.a. Mechanisms associated with acoustic emission signals (After Falls et al 1991).

changes following multi-transducer monitoring favour *event* as the *source* of the elastic wave, and *hit* as the received wave at the transducer. However, in this document *event* will be used as only one piezo-electric transducer was employed.

Noise Threshold is the level in dB set on the AE monitoring equipment necessary to eliminate all background noise. In this study the level is usually set between 28dB and 36dB.

Amplitude is the voltage (after amplification), of the highest peak in the wave packet, converted to decibels (in comparison to  $1\mu\text{volt}$  at the piezoelectric transducer). AE amplitudes are usually between 30dB and 100dB after the smallest events (<30dB) have been filtered out.

A Count is a single peak exceeding the threshold. An event may have a number of counts.

Ring-down is the total number of counts in a wave packet.

Dead time is the time after the last count within which no further counts are received. The event is then deemed complete. On event completion the AE monitoring equipment is reset to receive the next event.

Duration is the time from the first count to the last count.

Pulse width is the *signal duration* plus *dead-time*.

Energy is the energy contained within a event, measured under the wave envelope.

In monitoring acoustic emissions high accuracy low noise equipment is required and a number of different characteristics are measured.

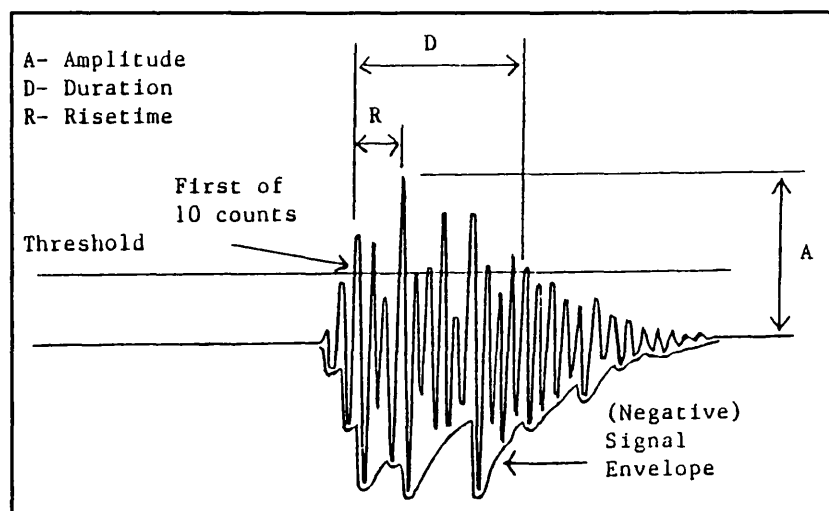


Fig. 4.5.1.b. Schematic Acoustic emission event with characteristics labelled.

#### ► AE Event

*rate*. This is the first and most widely used tool in monitoring AE. It is the number of separate micro-seismic events in a given time period (rate of AE

events). Cumulative AE's are easily obtained by summing events throughout an experiment.

- ▶ *AE amplitude.* Peak amplitude is recorded for events detected and a distribution created of the frequency of each event size at a given axial strain. By relating AE event size to defect growth size a more precise understanding of damage accumulation is gained. From a frequency/amplitude plot the *seismic b-value* is obtained. This is explained later in section 4.5.2.5.

- ▶ *Seismic b-value.* This is the slope of the log occurrence frequency/linear amplitude plot. It yields information on the number of large events relative to the number of small events. The slope can be calculated by a number of methods discussed later in this section.

- ▶ *AE Duration, event energy, pulse width and rise time* are also measurable. It should be mentioned that the duration, pulse width, rise time, and energy (fig 4.5.1.b.), are threshold dependent; the higher the threshold, the lower the calculated values for the above.

The calculated AE characteristics are noise threshold, and system- and medium-transfer function dependent. For this reason quantitative analysis of AE has proven problematic whilst qualitative analysis is common. For this study the AE event rate and event amplitude were recorded throughout triaxial experiments, and down-loaded to hard-disc during every recording interval.

## **4.5.2. Acoustic Emission Monitoring, Equipment, and Data Processing.**

### **4.5.2.1. Transducers.**

In order to detect the kinetic energy of an elastic pressure wave, the wave must be converted to an electrical signal. Piezo-electric materials are used for this purpose. Mechanical deformation of these substances causes a voltage to be established on the surface of the crystal. Certain naturally occurring

substance behave in this manner, quartz being the most well known. Ayling (1991) and Stuart (1992) devote much attention to the selection of optimum transducers for P- and S-wave velocity measurements and AE, and a good summary of transducer technology and selection criteria is contained therein.

#### 4.5.2.2. Transducer Housing.

Based on Ayling's work, a PZT transducer was used in this study. The 6mm diameter, 3mm thick transducer crystal is located 6mm from the rock specimen within a hollowed out ram, (see fig 4.5.2.2.a.).

#### 4.5.2.3. Electrical Signal Transfer and Amplification.

A good bond between the transducer and end-cap is achieved through use of electrically conducting *gold loaded* paint. A high pressure sealed electrical contact (similar to those used for the furnace), is used to transfer the signal (between 1 - 10  $\mu$ volts) out of the high pressure vessel. Immediately below the vessel, as close to the vessel as possible, a Dunegan Endeveco 190B acoustic emission pre-amplifier/filter is employed to amplify the signal by 40dB to the 1-10V range depending on wave amplitude, over the bandwidth of 20KHz to 2MHz. Most of the AE from microcracking in the fine grained rocks studied here is in the range 100KHz to 1MHz, (30mm to 3mm wavelength); the high-pass filter/pre-amp acts to eliminate mechanical noise and mains hum which is chiefly <20KHz. The thickness of the piezo-electric transducer and the speed of the elastic waves through the material determine the natural frequency of the transducer. Reflections off internal surfaces of the crystal cause resonance.

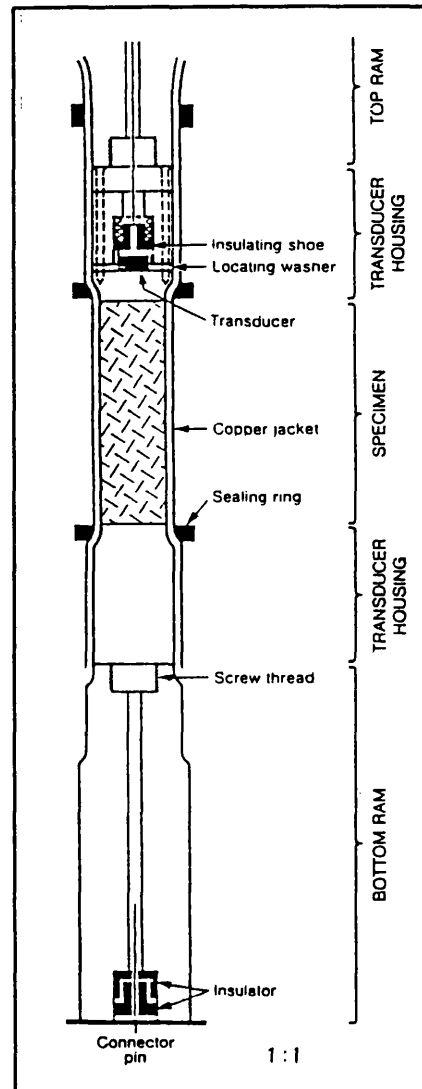


Fig. 4.5.2.2.a. A sectional view of the hollow ram ends. Transducer contact is made using a brass shoe, held in place with gold loaded paint and a spring.

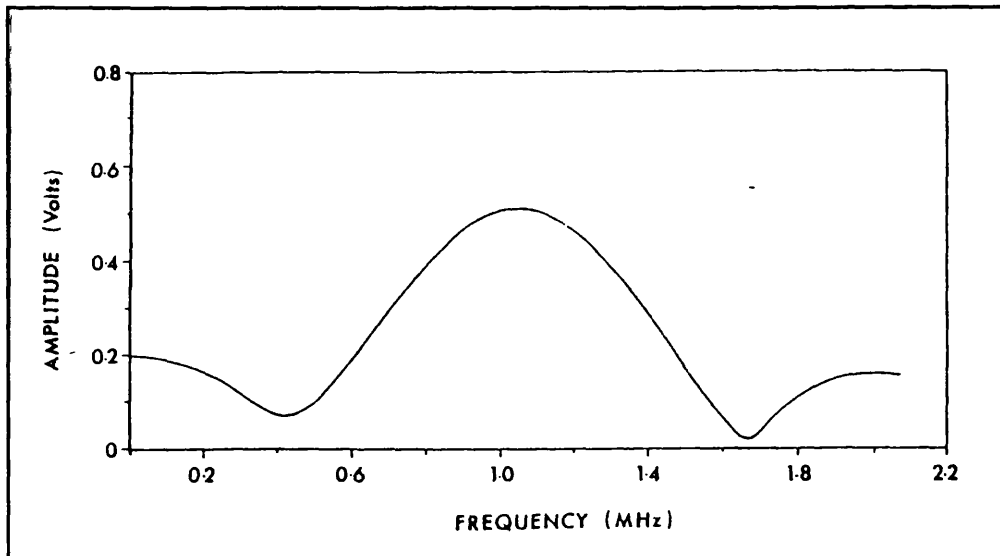


Fig. 4.5.2.3.a. The amplitude spectrum of compressional waveforms passed through sample of aluminium loaded into the equipment, see texts. (After Ayling 1991).

Ayling (1991) examined the frequency response of the AE detection system used in this study by passing pulsed waves through an aluminium sample (low attenuation). Fig 4.5.2.3.a. shows a fast Fourier transform of the output for a compressional waveform. The dominant frequency occurs at  $\approx 1\text{MHz}$ , with large energy responses between  $0.6\text{MHz}$  and  $1.4\text{MHz}$ . This resonant frequency corresponds to a wavelength of  $3\text{mm}$  which coincides with the transducer thickness. Therefore a changing AE dominant frequency can cause an apparent event rate reduction and  $b$ -value change based purely on the AE frequencies falling outside the dominant frequency range of the monitoring system. For this reason a system with a broad band frequency response is advantageous over narrow band frequency response.

#### 4.5.2.4. Logging Equipment.

The amplified signal is fed by co-axial cable to the Dunegan Endevco AE recording system. This modular system is described well in Rist (1989). Briefly, each wave signal is recorded as a single event together with amplitude. The events are summed for a given recording period, usually between 15 and 60 seconds. After a logging interval a seven second period is required to *down load* the AE data to the desk-top computer. The Dunegan system is capable of recording duration, pulse width, counts and amplitude.

#### 4.5.2.5. Processing and Presentation of Data.

The AE data is stored in two computer files; (i) event rate (with main data) and, (ii) number of events of a given amplitude for each logging interval. The logging interval reference number (stored in both files) allows cross-referencing for a common strain rate or time base.

Presentation of the AE event rate and cumulative AE data is achieved through commercially available software.

The event amplitude data reveals extensive information on the relative proportion of large and small events - and hence large and small crack growth increments. In order to achieve this computer software written by the author presents the data for the entire experiment in the form of a log frequency/linear amplitude (amplitude in dB is log voltage and so the plot is in fact, log/log). An example of the data is given in fig. 4.3.2.e. As can be seen the lower instrumental threshold (32dB) does not cause a sharp cut off to event logging. Some events below 32dB are recorded causing a smooth, curved cut-off. For this reason the lower threshold adopted for *b*-value calculations (marked on the figure as dashed line) is set at a greater amplitude than the instrument set noise threshold. This ensures a straight portion of the event distribution curve is selected for analysis. Selecting a threshold too low (including the *roll over* section of the curve) would affect *b*-value results considerably.

Seismic *b*-value analysis for a given set of AE data is achieved by employing a number of methods; Hatton (1992) describes the details of three. Of the three, the *Maximum Likelihood Method* by Aki (1965) is the standard method for scientific AE research and is used in this study. The method requires a full 40dB difference between upper and lower event amplitudes, and for the noise threshold to remain constant throughout an experiment. Aki's method is an improvement over many other methods as it treats each event with equal weight, and is therefore statistically more reliable a method than, for example, a least squares method.

The computer software used calculates the  $b$ -value for a number of different lower threshold level (28dB. to 36dB in intervals of 2dB.). The results of two different lower threshold values are given in fig 4.5.2.5.a. It can be seen how the calculated  $b$ -value is dependent on the selection of a lower threshold from the cumulative AE

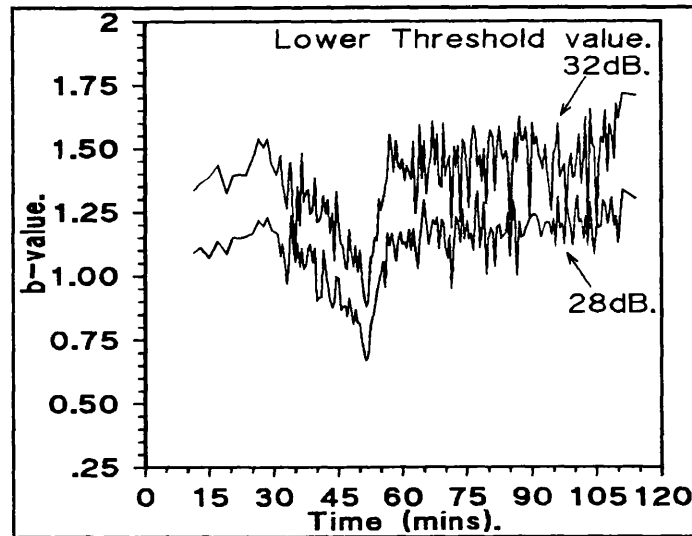


Fig. 4.5.2.5.a.  $b$ -values calculated for different lower thresholds, 28dB. and 32dB. Upper threshold remains at 100dB.

event/amplitude plot. Plots have also shown how selection of the upper threshold (between 75db. and 100db.) is less vital and the few events in those amplitudes affect  $b$ -value minimally.

### 4.5.3. Optimising Signal and Data.

#### 4.5.3.1. Noise Sources and Elimination.

Noise sources, either mechanical or electrical, are detected by piezo-electric transducers and can mask the proper AE signal. For each source of noise there is a specific method for elimination or reduction.

*Mechanical noise* can be due to machinery operating or any other source of physical vibration. Often mechanical noise is of a frequency far lower than AE (20KHz.), and is filtered out by the *high pass filter*. To reduce mechanical noise, sources should be de-activated for the duration of the experiment or suppressed with dampening material, as the pore fluid pressure intensifier motor was. Alternatively the transducer can be mechanically insulated from the vibration locally. Mechanical noise did not present a problem during this study.

*Electrical noise* tends to be a greater problem and can have more obscure and undetectable sources. *White noise*, present in the signal prior to amplification, is inevitable and can be minimised through good pre-amplifier design. It can be eliminated from instrumental measurement by setting an appropriate noise threshold on the monitoring equipment. The noise threshold set on the equipment is established by increasing the dB value until no noise is detected, and then adding a further 2dB. *Electromagnetic noise* is a consequence of machinery or instrument operation. The pressure vessel and cables act as large aerials for these signals which are then transferred to the AE signal wire. To reduce this a number of methods can be employed;

- (i) *special filtering* or *front end filtering* can be employed to detect abnormal signals and identify them as noise.
- (ii) proper *grounding* of the transducer housing and noise source machinery prevents electrical noise signals from getting to the piezo-electric transducer.
- (iii) A *guard sensor* transducer is located near to the AE transducer but sufficiently far from the specimen to avoid AE detection. Noise signals are detected by both the AE and guard transducers, and based on this the "event" is ignored. Proper AE signals, however, arrive only from the AE transducer, and are therefore recorded.

In this study electro-magnetic noise reduction was achieved by particular attention being paid to earthing the monitoring equipment and transducer housing, whilst the transducer itself was properly insulated from electrical noise by ceramic and *tufnol* components. Co-axial cable was adopted to transfer the AE signal 10m or so to the recording equipment, and the cable screen properly earthed. This screening continued around the pre-amplifier by the use of metal foil. The low voltage signal in the first 30cm of cable, unscreened by conventional co-axial cable due to its location inside the pressure vessel, is vulnerable to electronic noise corruption. To minimise this the earthed vessel acts as an earthing aerial and the pre-amplifier/filter is located as close to the vessel as is physically possible.

Furnace noise, which caused a problem for Jones (1989), was eliminated in this study through software driven alternate electronic switching of furnace and AE logging (see section 4.3.2.).

#### 4.5.3.2. Attenuation.

The wave form detected at the recording equipment is a complex result of *attenuation, reflection* and *reverberation* of the *source signal*. Attenuation is discussed here whilst transfer functions are covered in section 4.5.4.

*Attenuation* is caused by two separate effects; (i) geometric spreading of the wave, and (ii) absorption of wave energy by the matrix and the pore fluid. Geometric spreading causes the wave amplitude to decrease with distance from the source and absorption causes the wave to lose energy as heat. Absorption primarily affects higher frequencies and results in a gradual decrease in wave duration. Attenuation occurs to a greater degree in multi-phase media (i.e. crystalline rocks) compared to pure metals, and it dictates whether waves have the amplitude to be detected at the surface of a body, and hence potentially sets sample size limits.

*Reflections* occur when the wave intercepts an interface. Some of the wave is reflected and some is transferred across the interface depending on the acoustic impedance of the two materials in contact. If they are well matched the wave will pass through, otherwise a proportion will be reflected and associated compression and shear components of the wave will be converted. Reflections occur throughout the specimen, transducer and ram components. They cause a single event to be detected more than once and the resultant signal is composed of a number of pulses of diminishing amplitude and arriving at different times; hence the trailing AE event signal. Reflection can be reduced in transducers by *backing*. A material of similar acoustic impedance but with greater absorption characteristics is bonded to the transducer. Instead of event waves being reflected off the inner face of a transducer, they pass into the backing material and are absorbed.

*Reverberation* occurs within a solid object as waves are reflected back from surfaces.

The three phenomena described above change a single simple wave source into a decaying series of peaks of decreasing amplitude and of considerably greater duration than the original source event.

#### 4.5.3.3. Transducer Coupling.

For the AE elastic wave to be transferred from rock specimen to transducer a number of interfaces require bridging - the specimen/ram-end interface and the ram/transducer interface. The transducer cannot be contacted directly to the specimen due to the requirements of pore fluid and confining pressure medium confinement. Hence, the coupling material between these interfaces must be capable of transferring particle motion, and thickness must be < 1 per cent of the wavelength (Ayling 1991 - after pers. comm Dr. Bond, UCL), to reduce the effect of the bond on the wave. In this study the specimens are ground to an accuracy of 0.04mm in length (see section 5.1.1.), and a brass disc is placed between the specimen and the end-cap. The brass disc deforms into any pores or cracks that may be present in the end of the specimen, thus completing a good interface between the two media. Having successfully transferred the wave to the steel end-cap, the thickness of the end-cap should be minimised to reduce attenuation; in this study the thickness was 6mm. An efficient transducer/end-cap bond is then achieved using gold loaded electrically conductive paint and spring loading the back of the transducer. The main functions of the paint are to furnish a thin, stiff and stable bond between the transducer and the polished steel surface, and to earth the front face of the transducer (adjacent to the specimen) to prevent charge build-up. A thin bond is possible by working the transducer in circular motions with the wet paint when applying it to the steel. A bond thickness of 0.05mm is achieved by this method,  $\approx$  1 per cent of event wavelength.

The affect of this method is to minimise contact attenuation as far as possible and provide as clear a signal as possible.

#### 4.5.4. Complete System Transfer Function.

An appreciation of the changes that occur to an event signal between the source and recording equipment is required in order to be able to properly interpret the received signal. If characterised accurately the signal can be inverted to render a meaningful source function.

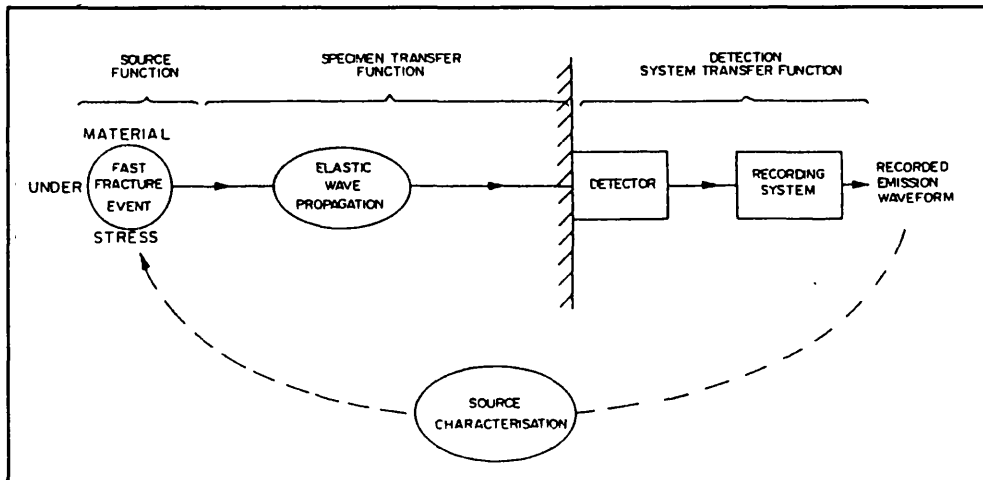


Fig. 4.5.4.a. Schematic representation of acoustic event source characterisation. (After Wadley, Scruby and Skrimpton 1980).

The specimen medium, the piezoelectric transducer and its housing, and the measurement system amplification all contribute to the changes and modifications that the elastic wave experiences. A detailed analysis of source characterisation can be found in Stuart (1992) based on work by Wadley et al (1980), and Scruby (1985). A schematic representation of the considerations necessary are given in fig 4.5.4.a.

#### 4.6. Data Logging and Processing.

##### 4.6.1. Logging System.

In this study, stress, strain, two pore fluid pressure measurements (P1 and P2), pore fluid intensifier piston location (pore fluid volume), furnace temperature (upper and lower), confining pressure, and acoustic emissions data are monitored as described in sections 4.2., 4.3., 4.4., and 4.5. above. The conditioned voltage of all but the AE output is fed to a Hewlett Packard 3497A Data Acquisition Control Unit. The stress and strain signals are also

directed to a Hewlett Packard 7035B X-Y Plotter for direct monitoring of the stress/strain curve.

The Data Acquisition Unit is operated in *remote operating mode* (i.e. computer software initiates and controls the unit), communicating with the computer via an HP-IB. The data logger is capable of logging 20 channels, eight of which are used. The modifications carried out to the furnace, pore fluid system, and the confining pressure monitoring system means six extra channels were added to the two original stress/strain channels operating at the start of the project. The data is recorded on hard disc and printed-out every logging interval.

Acoustic emissions recorded by the Dunegan Endevco Distribution Analyser are down loaded to the computer at the end of each logging interval via a serial RS232 standard interface.

#### **4.6.2. Logging and Correction Software.**

Existing logging and correcting software was expanded to read, process, and display the extra eight channels. Modifications to the software also allowed interaction with the logging system during an experiment, e.g to enable;

- (i) AE logging to be switched off. The AE on/off logging alternative allows for AE recording to be removed from the logging cycle for experiments not requiring AE data, e.g. during very high temperature tests.
- (ii) The logging interval to be changed during an experiment. Necessary during periods of deformation when large stress or strain changes occur, (e.g. at dynamic failure of very stiff rocks).
- (iii) the furnace to be controlled (section 4.3.).

From an examination of the stress/strain curve from the X-Y plotter and the uncorrected data file, the point of contact between the lower ram and the lower closure (contact point) is identified for the zero axial stress point, and from the log frequency/linear magnitude plot of AE events, the AE upper and lower thresholds are selected for *b*-value analysis. The resultant data files are corrected with this information and multiple Y-axes graphs are created using commercially available graphing packages.

## **4.7. Equipment Development; New Component Designs.**

### **4.7.1. Background and Introduction.**

Rock physics experimentation is increasingly concerned with elucidating rock behaviour through syn-deformational measurements of stress, permeability, acoustic wave velocity, elastic stiffness, and pore volume. Recent theoretical developments are emphasising the *number* of physical properties measurable, and for this they require large rock specimens; this is at the expense of the range of crustal conditions possible.

The high pressure triaxial cell used in this study uses a 15mm diameter specimen and is capable of simulating crustal conditions to  $\approx 40$ km depth. These very high pressure conditions necessitate the small specimen size, and this presents a limit to the number of transducers that can physically *fit* into the platens.

The arrangement as it stands allows the measurement of, (i) pore volume changes, AE, stress and axial strain or, (ii) P-wave and S-wave velocity, AE, stress and strain. Equipment allowing both pore volumetry and P-wave/S-wave velocity measurements would aid elucidation of the relationship between these physical property changes during deformation.

This limitation prompted the design of a new upper ram to permit the measurement of a variety of physical properties simultaneously. The design was undertaken solely by the author in consultation with other members of the Laboratory. The design is yet to be manufactured, and there are a

number of design details requiring further attention before the manufacturing stage.

The study meant the author became completely cognizant with the high pressure vessel, its operation, and its design strengths. It became clear that the problem of the leaking copper jackets (section 5.2.1.), required a new lower ram design. Following this a second piece of design work was undertaken by the author; a new "*double sealing ring lower ram*".

#### **4.7.2. Pore Fluid and P-/S-wave Upper Ram; Design Objectives, Constraints, and Alternatives.**

The broad design objectives of the re-designed *multi-mode* upper ram are given below.

- ▶ Allow P-wave and S-wave velocity measurements to be made simultaneously with pore fluid volumetry monitoring.
- ▶ Increase specimen diameter from 15mm to 20mm, affording increased platen area and therefore extra space for the increased number of end-cap components necessary.
- ▶ Maintain minimal distance between the rock/ram interface and the piezo-electric transducer, ensuring maximum P-wave and S-wave signal magnitude.
- ▶ Maintain the provision for AE data recording in the bottom ram. The bottom ram piezo-electric transducer will also act as the receiving transducer for the P-waves and S-waves.

The existing pressure vessel presents a number of design constraints. These are highlighted below.

- ▶ Specimen diameter maximum is limited to  $\approx 20\text{mm}$  due to internal dimensions of vessel and vessel top closure.
- ▶ Limited space available at the 20mm diameter platen for the necessary components (pore fluid access tube and piezo electric transducers).
- ▶ Maintenance of sufficient cross-sectional area of the ram to transfer the axial stress necessary for rock deformation (up to 200KN).

Trying to meet the design objectives within the design and material constraints prompted consideration of a number of alternative designs, one of which was investigated more fully whilst the others remain merely as design concepts. The various designs are given in appendix B with illustrations. Here, only the salient points of the most favoured alternative is given.

The arrangement involves siting the wave-transmitting transducer (manufactured from PZT) centrally in the end-cap, 6mm from the rock/ram interface. This transducer is set in a corrosion resistant adhesive epoxy potting compound to resist the effect of potentially corrosive pore fluids (brine) which pass from the 2mm bored tube down the centre of the ram, around the transducer, and through small diameter holes in the platen to the rock specimen. Both the pore fluid and transducer signal cable pass up the same *hp* 1/8" tube to a redesigned *piston head block*. At this block the wire and pore fluid are separated, (see Appendix C for further details).

#### **4.7.3. Double Sealing Ring Lower End-cap: Design Objectives and Constraints.**

The triaxial testing equipment employs annealed copper jackets to prevent the ingress of pressurised nitrogen into the specimen. They rely on one interference fit between the ram and the copper jacket, (see section 5.2.1.1.). At the outset of this project the procedure for manufacturing copper jackets was empirical and relied heavily on experience. Combined with detrimental

wear and tear to the rams and sealing rings, the success rate for correctly functioning copper jacket was about one out of every three manufactured. The new double sealing ring lower ram design proposed here involves two sealing rings 6mm apart axially, which doubles the chance of a jacket successfully sealing. The double sealing ring arrangement also means a more rigid lower ram/specimen/upper ram arrangement, with less probability of the lower ram separating from the specimen during specimen emplacement and removal.

The design objectives and considerations for the development of a double sealing ring lower end-cap are given below.

- ▶ For the end-cap/transducer housing to be constructed from fewer parts. Previously the numerous parts allowed N<sub>2</sub> to leak between the steel interfaces of the end-cap.
- ▶ To incorporate a second sealing ring further along the end-cap.
- ▶ For the 15mm diameter section of the end-cap (which makes contact with the rock), to be extended from 1.5mm to 7mm in length. This removes the strained section of copper jacket (where the interference seal is made), from the rock/ram interface (where holes from loosened grains in large grain sized rocks can cause the jacket to puncture). These points are as discussed in section 4.4.
- ▶ The steel surface where the receiving transducer is sited (bottom of the *transducer well*), must be polished to provide good acoustic wave transfer.

The design details and drawings are given in appendix C. Only a short description is given here.

The end-cap, previously manufactured from four parts, is constructed from only two parts in this design. The transducer is sited in a *well* in the main body of the end-cap, ≈ 6mm from the rock/ram interface, therefore preserving

wave signal quality. Emplacement and removal is achieved using tweezers. This *well* is necessary if the bulk of the end-cap is constructed from a single piece. The re-designed lower end-cap can be easily modified for a 20mm sample. In this case the main body of the lower ram would also need re-designing to allow equal dimensions at the connection between the end-cap and the lower ram.

#### 4.8. Safety Arrangements.

Any triaxial equipment requires a pressurised medium to apply the confining pressure. This medium contains stored strain energy and rigorous safety precautions are necessary when dealing with it. With pressurised gas (N<sub>2</sub> used with this equipment), more stringent safety standards are required compared with a pressurised liquid.

The primary safety precaution for this equipment is the 25mm thick steel safety chamber in which the triaxial vessel is situated. It is designed to contain the equipment and the pressure wave in the event of a rapid leak. The door of the safety cell is *interlocked* with the pump to prevent operation of the pump without first closing the door. The Harwood 1400MPa three stage pump incorporates a 6mm thick steel guard plate as an instrument panel and additional safety plate surrounding the pump system, and ear defenders are necessary when the pump is under pressure. Two safety valves are built into the pump to prevent the second (automatic) stage generating over-pressures. The setting for the electrically operated and air driven valves is set on the *Foxboro dynalog pressure recorder*. The third stage (1400MPa), is manually operated.

The remainder of the safety precautions are concerned with preventing equipment damage rather than human well being.

The actuator servo-controller incorporates limit settings for maximum tensile and compressive stress, and for maximum positive (higher) and negative (lower) actuator displacement settings. For example, the limits can be set to

**switch the actuator off after 5mm specimen deformation ( $\approx 10\%$  strain) or at a certain compressive load. The use of the limit settings ensures experiments do not exceed stress or displacement limitations and damage equipment components.**

## **CHAPTER 5. ROCK SAMPLE PREPARATION AND EXPERIMENTAL PROCEDURE.**

### **5.1. Sample Preparation.**

#### **5.1.1. Coring and Grinding.**

The three rocks used in this study (described in section 6.1.2.), varied markedly in strength and friability. Sandstone was found to be easy to prepare, being reasonably compliant although sufficiently strong to remain intact through the harsh grinding and coring processes. Microgranodiorite demanded more attention during the coring process to ensure the coring bit did not overheat, and the gypsum demanded a similar degree of attention to ensure the sample did not break apart during coring.

Right cylindrical test specimens were prepared to a length of 45mm ( $\pm 0.25$ mm) with a axial parallelism of  $\pm 0.02$ mm, and a diameter of 15mm ( $\pm 0.1$ mm). The absolute length and diameter tolerances ensure comparability of experimental results and comply with the 3→2.5:1 length to width ratio necessary to reduce "end effects" due to friction between rock specimen and platen, (Jaeger and Cook, 1978). The parallelism criterion is vital to ensure no bending moment is induced in the sample during axial compression.

The samples were cored using a diamond impregnated *coring bit* installed in a floor standing pillar drill. The pillar drill chuck allowed the flow of cooling/lubricating water to the rock during coring. Sample ends were ground parallel using an *Abwood vertical plough grinder* fitted with a diamond impregnated cup wheel. Proper setting of the machine ensured the removal of 0.01mm of rock per pass of the grinding head. This rate of grinding guaranteed smooth specimen ends and avoided grain plucking and edge damage.

#### **5.1.2. Determination of Porosity.**

The porosity of all test specimens was determined prior to testing. This has a dual function of; a) monitoring variability of samples with respect to microstructure and, b) the data can be used during post-experiment data analysis if required (correlation of material behaviour to rock micro-structural parameters). *Saturation and Buoyancy Technique* was used to establish porosity, as detailed in Franklin et al. (1979). Samples were oven dried for 3 days at 70°C. This temperature avoids damage induced through differential thermal cracking that is known to occur above 80°C, (Glover et al 1995). It does mean, however, that complete water removal is questionable. For this reason the porosity was determined for samples subjected to 3, 5, and 7 days of drying at 70°C. The results were constant, and comparable to values obtained for specimens dried at 100°C, thus proving that all fluid is driven off at 70°C and no advantage is gained from extended drying times beyond 3 days.

To determine porosity, firstly the dry weight of the specimens ( $M_s$ ), is taken which gives the weight of the solid rock matrix. Specimens are then saturated with water and weighed in air ( $M_{sat}$ ), and again in water ( $M_{sub}$ ). From the three weights taken, pore volume, rock volume, and hence porosity is determinable from the equation.

$$\phi = (M_{sat} - M_s) \cdot 100 / (M_{sat} - M_{sub}) \quad (5.1.2.a.)$$

Full water saturation during this process is ensured by firstly evacuating the samples in air (1hr.), then allowing distilled water to flow into the evacuated chamber and rock samples. Finally, evacuation is continued for a further hour. The vacuum level attained at each stage using a 0.05 Torr pump with the ballast valve open is 0.3 Torr. The samples are then stored in distilled water until required for experimentation, at which stage they are installed into the vessel as described in section 5.2.3.

## 5.2. Experimental Procedure.

### 5.2.1. Copper Jacket Manufacturing Developments.

### 5.2.1.1 Introduction.

It is necessary to prevent the escape of pore fluids from the sample and the ingression of pressurised nitrogen into the sample to maintain the pre-determined effective confining pressure. The system adopted for this involves sheathing the rock in an annealed copper jacket, (see fig 5.2.1.1.a.). Being malleable in its annealed form and of high melting temperature, copper has proved to be the most appropriate material. *Interference seals* between the copper and the ram are achieved by forcing steel rings over the outside of the copper jacket at a change in diameter of the ram. For example; the first and smallest seal is achieved by forcing a steel ring of internal diameter 15.55mm, over a change in diameter of the ram of 0.5mm - from 15mm to 15.5mm. When considering the jacket thickness of 0.25mm, it is clear that the annealed copper jacket must strain and become thinner at this point. The thinning and *interference* of the copper with the ram ensures the copper fits tightly against the steel ram. Upon application of a moderate confining pressure, the annealed copper is forced against the steel ram, which further improves jacket seal.

The copper jackets are shaped to fit tightly over the 15mm sample and the rams. This complicated shape is manufacturing by repeatedly reshaping the annealed copper tubing using six *mandrels* of increasing size and shape complexity; the sixth mandrel being the same shape as the upper and



Fig. 5.2.1.1.a. Photograph of piston/specimen/lower ram assembly showing jacket and sealing rings.

lower ram. A specifically designed vertical press is used for this purpose.

#### 5.2.1.2. Identification of Annealing Problem.

At the outset of the study, the annealing of the jackets was achieved through heating the copper over two bunsen burners and quenching in dilute nitric acid to remove the oxidised copper. This procedure presented three problems;

- ▶ Heating in an open flame and in an oxygen environment (air) caused the surface of the copper to oxidise heavily. Oxidisation to cupric oxide (black) and cuprous oxide (red) caused scaling over the surface of the copper.
- ▶ Quenching in nitric acid to clean the copper of oxide scale (pickling) caused differential thinning over the surface of the copper due to a non-uniformly oxidised surface.
- ▶ Temperatures attained over the bunsen burners were far higher than the 300→550°C necessary to cause the required physical property changes (annealing). This extreme temperature exacerbated oxidation, thereby worsening the effects described above.

The overall result was a very thin copper jacket of non-uniform thickness which often tore during installation or punctured at the rock/ram interface (where grains had been chipped away during fitting). The success rate for sealing jackets under this system was approximately one in three.

#### 5.2.1.3. Process Development and Equipment Commissioning.

Based on the problems outlined above and readily available data on the properties of copper, specifications for annealing the delicate copper jackets were devised. An inert environment and a constant temperature of  $\approx 550^{\circ}\text{C}$  were found to be the most suitable conditions. To achieve this a controlled

environment carbolite tube furnace was commissioned by the author. Feeding nitrogen under pressure through a pressure control valve and a flow meter to a sealed work tube, a nitrogen environment of  $\approx 25$  psi. pressure was achieved. Bench tests using a probe thermocouple were then conducted to ascertain the furnace work tube temperature gradient between the centre of the furnace and the extreme body of the work tube. At the ends of the extra long ceramic work tube (which protruded  $\approx 400$ mm from the end of the furnace), the temperature was found to be  $\approx 50^\circ\text{C}$ . This permitted the copper jackets to be cooled inside the nitrogen filled tube after annealing at  $550^\circ\text{C}$ . By adopting this cooling method the copper could be annealed for 30mins. at  $550^\circ\text{C}$ , then cooled for 5mins. to below  $\approx 120^\circ\text{C}$  before being removed from the controlled environment, ( $\approx 120^\circ\text{C}$  is the temperature, found experimentally, above which oxidation occurs). Thus the copper jacket emerges from the furnace annealed and completely un-oxidised. Data on copper stated that slow cooling probably made no difference to the annealing process compared with quenching in a cold fluid and this has been found to be true.

The jacket manufacturing procedure now includes proper annealing four times during the reshaping of each end of the jacket. The result is a jacket sufficiently soft to be strained over the rams for adequate interference fit sealing, sufficiently thick to avoid tearing during this process, and sufficiently robust to withstand the treatment it is subjected to during the installation process.

### 5.2.2. Loading Specimen into Jacket.

With reference to fig 4.5.2.2.a. and fig. 5.2.1.1.a., the jacketing procedure can be explained more illustratively.

The rams are initially cleaned with solvent (*inhibiso*). Silicon rubber is then applied at positions where the jacket makes contact with the ram; this results in a more reliable seal. The jacket is first fitted to the lower ram and the sealing rings forced into place using a specifically designed *sealing ring jig*. A 15mm diameter thin brass disc (to aid acoustic contact and reduce

ram/sample interface friction), a fluid saturated rock specimen, and a fluid distribution disc (to improve fluid access from the ram to the sample), are placed into the open end of the copper jacket and pushed *home* to make contact with the lower ram end. The jacket is then filled with water and the upper ram/piston brought firmly down into the flooded open end of the jacket. This ensures no air locks occur in the sealed copper jacket (see section 5.3.3.). The complete ram and specimen arrangement is replaced in the *sealing ring jig* and the upper two sealing rings are forced into position. Finally, more silicon rubber is applied to the rams at the ends of the copper jacket. The arrangement is left over night for the silicon rubber to dry. Although the latter precaution itself is insufficient to seal the specimen against the high pressure confining medium, it does maintain jacket integrity for long enough during the application of the confining pressure for the annealed copper jacket to be forced against the ram and dried flexible rubber. The seal then created by the jacket/silicon rubber/ram seam and the sealing rings is pressure dependent and successfully maintains jacket integrity under very high confining pressures.

### 5.2.3. Loading the Vessel.

Prior to installing the ram and specimen assembly into the vessel a number of checks and operations are performed.

- ▶ The inside of the vessel is inspected for debris. Often fragments of dried silicon rubber contaminate the acoustic emission contact at the bottom closure. These must be removed and the contact cleaned of *Rocol* anti-scuffing paste to ensure a good electrical contact.
- ▶ The ram is coated with *Rocol* anti-scuffing paste at the locations where the ram comes into contact with O' rings. This reduces seal friction.
- ▶ The ram is then carefully loaded vertically through the open upper closure and pushed home until the lower ram makes contact with the lower closure.

- ▶ An effective AE contact is confirmed by "tapping" the top of the piston with a metal tool, the resultant AE being detected by the AE monitoring equipment. Possible AE monitoring problems can be isolated and corrected at this stage.
- ▶ The remaining components of the top ram are put in place and the top breech nut secured.
- ▶ The intensifier system is *primed*, and flushed through with water to avoid air locks. Using the intensifier control electronics the intensifier piston is moved to the end of its stroke (intensifier cylinder full with water), to ensure sufficient motion in the piston remains to provide the necessary fluid pressure for the experiment.
- ▶ The 1/8" *hp* tube emerging from the ram/piston is then connected to the 1/4" intensifier tubing and the necessary valves opened to set the pore fluid in the *hp* system to atmospheric pressure.
- ▶ The *piston head block* is secured in place on the top of the piston and the LVDT's (which record axial displacement) attached.
- ▶ A hemi-spherical dome is greased and placed on top of the piston head block to ensure the load applied to the piston is purely axial.
- ▶ The load cell and actuator are rolled in place vertically above the piston and specimen and secured by tightening four M16 bolts to a torque of 160Nm. This provides the reaction to the axial load exerted on the rock sample.

The vessel is then ready for experimental conditions to be set prior to commencing the experiment.

#### **5.2.4. Establishing Crustal Conditions and Commencing Experiments.**

The equipment is capable of simulating variety of crustal conditions such as temperature, fluid and lithostatic pressure, and stressing or straining rate. In this study a number of different conditions were employed and the experimental procedure adopted to accurately simulate them is presented below.

#### 5.2.4.1. Drained Triaxial Experiments.

Using the actuator control electronics in displacement control, the actuator is brought down to make contact with the piston. A vertical uniaxial load of  $\approx 1\text{KN}$  is applied to the rock sample. This is just enough to ensures good contact between the lower ram, rock specimen, and upper ram. The balanced ram system (as described in section 4.2.) is designed to be slightly imbalanced for calibration purposes. This imbalance is in favour of pushing the piston out of the vessel slightly during the application of a confining pressure. For this reason the servo-controller must remain in displacement control to keep the axial load piston stationary. A load then builds up between the piston and the actuator during confining pressure increase. It is important to note that the specimen does not experience this axial load, though it does experience the hydrostatic load.

A confining pressure of  $\approx 15\text{MPa}$  is applied and held constant. If the copper jacket is going to fail, it will generally leak nitrogen at this pressure. Nitrogen will leak through the pore fluid system, to atmosphere. This is easily monitored and provides confirmation, or otherwise, of a successfully sealed jacket at the outset of the experiment. The pore fluid intensifier system is then closed from atmosphere and "primed" using the hand pump. The confining pressure pump is then started *simultaneously* with the pore fluid intensifier. Pore fluid pressure ( $P_p$ ) is increased along with confining pressure ( $C_p$ ) to ensures the effective confining pressure ( $C_p'$ ) never *exceeds* that value proposed for experiment. This ensures no *additional* damage is exerted on the rock specimen above that expected as a result of the experimental conditions.

Pore fluid pressure inevitably increases as a result of an increasing  $C_p$  and this must be considered during  $C_p$  rise. Also, during  $C_p$  increase, axial load increases due to the balanced ram system (discussed above), this must be monitored and kept below that value expected for seal friction. (Seal friction is a function of confining pressure, and values are well documented.) The reason for this is that if the starting axial load exceeds seal friction, the point of ram/lower closure *contact* will be difficult to determine at the beginning of the test.

Once experimental conditions are set, the system is left to stabilise for 20 to 30mins. This allows fluid pressure variations in the system, due to sudden confining pressure changes, to equilibrate. Pore fluid volume data is logged during this stage. Once fluid flow has stopped i.e. the system is in equilibrium, the pore fluid intensifier controller can be switched to *pressure control* and fluid flow monitored during deformation (see section 4.4.2.). The actuator controller is then switched to *strain rate control*. After checking the correct strain rate and actuator limits are set, the *ramp generator* rate actuator can be started. The actuator begins to move down at the pre-determined rate. Contact is made between the ram and the lower closure and the axial load increases. The frictional stress between ram and seals is recorded prior to this contact point and can be deducted from final axial stress readings, (see section 4.6.).

#### 5.2.4.2. Undrained Triaxial Experiments.

The method for commencing an undrained experiment is similar to method described above. The difference occurs after the equalisation period. At this point the remotely operated valve (r.o.v.) in the pore fluid pressure system is closed. This prevents the flow of fluid into and out of the sample during deformation, allowing the pore fluid pressure to vary during compaction and dilation of the sample. (see section 4.6.2.). After its closure the pore fluid intensifier low pressure pump may be switched off as the unit is no longer connected to the rock specimen.

### 5.2.4.3. High Temperature Triaxial Experiments.

The application of heat to the pore fluid and the nitrogen confining medium increases the pressure of these media through the  $PV/T$  relationship. It is important that the furnace be activated *during* the process of increasing the  $C_p$  and  $P_p$ , so the final  $C_p$  and  $P_p$  attained includes the increase due to the application of high temperature. It is also important to monitor more closely the equalisation period for fluctuations in  $C_p$  and  $P_p$  due to temperature fluctuations.

### 5.2.4.4. Hydrostatic Pore Volumetry Experiments.

Experiments of this nature involve monitoring pore volume or pore pressure (depending on whether drained or undrained conditions are adopted), during the application of only a hydrostatic confining pressure. Early experiments of this type suffered from poorly constrained parameters; the starting procedure and the question of the magnitude of  $C_p$  and  $P_p$  to apply. The problem concerns three conflicting requirements.

- ▶ The need to minimise confining pressure to ensure all voids in the rock sample are open and saturated with fluids prior to the commencement of an experiment. This affects total rock pore volume and hence pore volumetry measurements.
- ▶ The need for the application of a *reasonable* confining pressure ( $\approx 20\text{MPa}$ ) to ensure that no space between the copper jacket and the sample fills with water (pore fluid). This potentially variable total pore fluid volume affects the magnitude of  $P_p$  changes.
- ▶ The need to apply a small confining pressure to the jacketed specimen greater than the pore fluid pressure to prevent pore fluid escape into the pressure vessel.

The second point is also pertinent to undrained triaxial experiments where the pore pressure response under a changing pore volume is important and affected by total fluid volume.

The conflicting requirements of a reasonably high effective confining pressure to ensure the jacket fits tightly, and a low or zero effective confining pressure to allow total pore and crack saturation required calibration experiments to establish a valid experimental starting procedure which could satisfy all these criteria. Section 6.3.3.1. described these calibration experiments and discussed the results.

The solution adopted from the results involves *temporarily* applying an initial confining pressure of 30MPa for  $\approx 5$ mins., raising the  $P_p$  to 20MPa under pressure control, and then slowly reducing the  $C_p$  to 23MPa. The  $C_p'$  then equals only 3MPa. The normal equalisation period of 30mins is allowed before the commencement of the experiment. For undrained conditions the remotely operated pore fluid valve is closed at the end of the equalisation period.

#### 5.2.4.5. Dehydration Test on Gypsum.

Initially 1kN is applied axially using the actuator. The  $C_p$  and  $P_p$  are applied to the saturated gypsum sample as per the drained tests described above. Thirty minutes is then allowed for pressure equalisation. For dehydration experiments the pore fluid intensifier piston is positioned within its cylinder such that the cylinder is mostly *empty* of water, thus water expelled from the specimen during dehydration can be accommodated and measured within the intensifier cylinder. The furnace is then switched on and dehydration begins at the point when the dehydration temperature is exceeded. This style of experimentation was new to this equipment and the method outlined here was established for the purpose of this study.

### 5.3. Procedural Development - Sample Saturation Technique.

### 5.3.1. Background to Problem.

Fig 5.3.1.a. illustrates results of an early experiment using the pore fluid volumometer. The figure clearly shows the increase in pore volume during specimen dilatancy, but fails to show water expulsion during the initial compactive stage of the differential stressing as found by Ayling (1991). Consideration of all possible sources of the problem led to the conclusion that *air traps* in the system or *incomplete saturation* of the rock sample prior to experimentation could be responsible for the anomalous results. The precise effect of mixing air and water

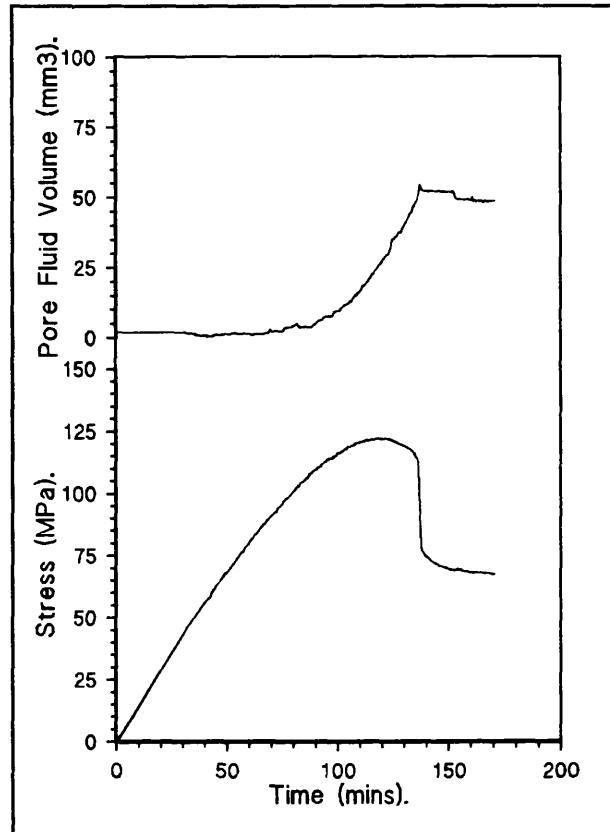


Fig. 5.3.1.a. Results of early undrained triaxial test. Under-saturated sample caused no fluid expulsion on initial compactive stage.

through an under-saturated sample is to change the pressure volume/response of the fluid system. Under the effect of a change in rock porosity during crack and pore closure, air compresses more readily and reduces the fluid pressure increase that would have otherwise occurred. Consequently the experimental results become confused and unreliable. In this specific example, incomplete saturation meant water was not expelled when pores and cracks were initially closed, and upon dilatant crack growth fluid (although reduced quantities) was pumped into the sample.

This prompted a thorough review of the saturation procedure by the author, from initial drying of the sample, through the process of vacuum assisted water saturation, to installation of the sample into the vessel. The result of reviewing the first process is the methods outlined in sections 5.1.2. (Determination of Porosity). The next section discusses the investigation and

water saturation, to installation of the sample into the vessel. The result of reviewing the first process is the methods outlined in sections 5.1.2. (Determination of Porosity). The next section discusses the investigation and trial of a system designed to evacuate and then saturate rock specimens *in-situ* - i.e. once installed inside the pressure vessel.

### 5.3.2. Saturation System Design Solution and Conclusions.

The system designed to evacuate and then saturate the sample *in-situ* consisted of a 0.05 Torr vacuum pump connected into the pore fluid system adjacent to the vessel. After installing a *dry* rock sample in a copper jacket into the vessel, the 1/8" *hp* tubing from the top of the piston is connected to the pore fluid intensifier system as normal. The appropriate valves are operated to allow a vacuum to be generated in the sample. After  $\approx$  1hr. the vacuum valve is closed and water flooded into the sample assisted by the (previously flushed) fluid intensifier.

The system was established and a series of bench tests executed. Head gauges positioned at the pump, at the start of the 1/8" *hp* tube, and at the end of the 1/8" *hp* tube where the sample would be situated recorded vacuum levels. The results are given in table below.

<u>Head Gauge</u>	<u>Vacuum (x 10<sup>-1</sup> Torr).</u>
At Vacuum Pump.	1.2
At head of 1/8" tube	2.8
At Sample position.	10

From this simple bench test it became clear that the frictional resistance to air flow from the inside wall of the 1/8" tube prevented the development of a sufficiently high vacuum at the end of the 1/8" tube where the rock specimen is situated. A vacuum of 10 Torr was achieved at this position, half that required by the International Standard for Rock Mechanics suggested method.

For this reason the system could not be used without the installation of a more powerful vacuum pump or the adoption of a larger bore *hp* tube. For the duration of the study the method outlined in section 5.3.3. was employed to ensure full saturation of the sample.

### 5.3.3. Full Specimen Saturation Technique Employed.

The problem of ensuring full specimen saturation was overcome by filling the volume inside the copper jacket above the emplaced rock specimen with water. The 800mm long upper ram/piston assembly is checked to ensure the *hp* tube is free from obstruction using compressed air, and then flushed with water. The upper ram is then brought down on the flooded lower ram/ jacket/ specimen assembly (as described in section 5.2.3.), and as it is pushed firmly home water is expelled from between the ram

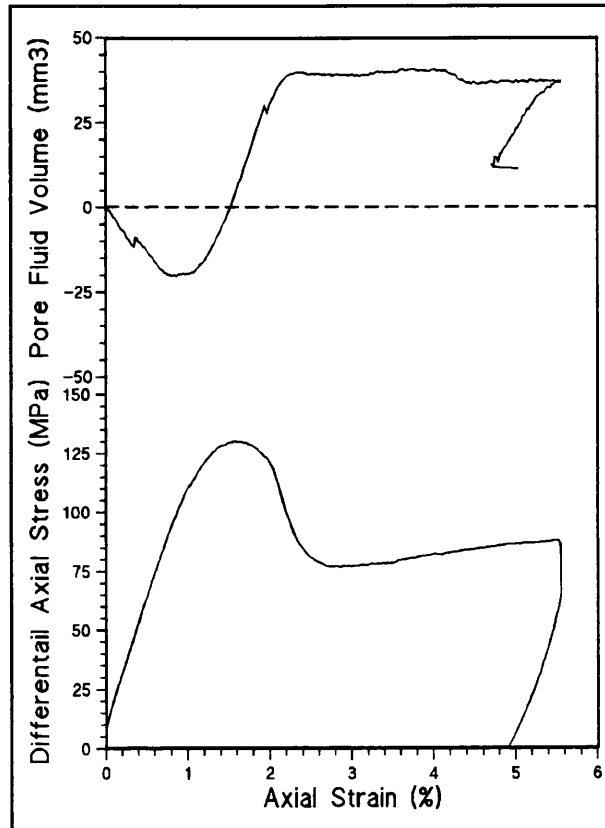


Fig. 5.3.3.a. Results of drained experiment where specimen is fully saturated - fluid is expelled and drawn in during compactive and dilatant stages.

and jacket and from the end of the 1/8" *hp* tube at the top end of the piston. This method has proved to be reliable, and satisfactorily saturates rock specimens prior to experimentation, even when left for 12hr. for the silicon rubber to dry. Fig. 5.3.3.a. shows typical results of fluid volume change during drained deformation of sandstone when the specimen is fully saturated. Compare the results with fig. 5.3.1.a.

## **CHAPTER 6. EXPERIMENTAL PROGRAMME, RESULTS, DISCUSSION, AND ANALYSIS.**

### **6.1. General Introduction.**

Chapter six is divided into six sections. This first section (6.1.) introduces the rocks used in the study and reviews some relevant triaxial deformation data. The subsequent five sections, whilst complying with the main theme of the thesis, are discrete experimental programmes covering a range of problems relating to fluid/rock interaction and rock deformation. Each section employs the same apparatus and is analysed with respect to the deformation micro-mechanisms revealed by the use of pore volumetry. Each section also contains a review on experimental data pertinent to that particular facet of experimental rock physics, a conclusions section, and recommendations for future work. This approach ensures that any section can be read in isolation, if required. All experiments were conducted at a strain rate of  $10^{-5}\text{s}^{-1}$ , found to be sufficiently low to avoid dilatancy hardening and sufficiently high allow experiments to be conducted within a few hours. All samples were examined after experimentation for mode of failure, although microscopy examination was not conducted within this study.

#### **6.1.1. Summary of Experimental Programme.**

Section 6.2. considers the effect of drained and undrained triaxial deformation conditions on sandstone under a variety of effective confining pressures and URV's. The results are analysed quantitatively to obtain a URV correction factor to adjust measured pore fluid pressure for zero URV (undrained conditions). The same results are also used to isolate mean stress and deviatoric stress induced pore fluid pressure increase under the initial stages of triaxial deformation ( $\epsilon=0.0\rightarrow 0.5\%$ ), which yields information concerning which mechanisms are dominant at the initial *compactive* stage of triaxial deformation for the stress regime considered.

Section 6.3. attempts an analysis of pore fluid mass changes under drained hydrostatic compaction. Using experimentally derived values for rock and fluid bulk moduli ( $K$  &  $K_f$ ), and considering a variety of values for  $K_s$  and  $B_{obs}$ . (see Glossary) to meet experimental pore volume compaction data ( $\delta v$ ) a reasonable modelled result is obtained. The analysis fails in parts due to the  $K_u$  values adopted ( $K_u$  obtained from *undrained* experimental data and used in *drained* compaction analysis).

Section 6.4. firstly examines pore fluid volume changes during brittle deformation of Darley Dale sandstone under constant effective confining pressure and increasing pore fluid pressure. From this the chemical effect of a high fluid pressure on brittle deformation is determined. Secondly, the pore fluid volume change due to the application of a deviatoric stress and effective mean stress are considered separately by subtracting drained hydrostatic compaction data (section 6.2.) from triaxial deformation pore volumetry data. Thirdly, a suite of triaxial results are examined in 3-D space of pore volume, deviatoric stress, and effective mean stress, to isolate the effect of each stress on pore and crack volume change for a variety of deformation conditions.

Section 6.5. concerns the effect of elevated temperatures on both the sandstone and the microgranodiorite under triaxial deformation. Also examined is the effect of the pore fluid (water) at temperatures and pressures approaching the critical point of water. The temperature gradient in the *hp* tubing system (rock temperature→room temperature) causes a specific volume change in the fluid and affects fluid pressures generated under undrained conditions.

Section 6.6. investigates dehydration rates of gypsum under various stress states and during *undrained* triaxial deformation, and undrained triaxial deformation of dehydrating gypsum.

## 6.1.2. Description of Rock Types.

Three rocks were used in the this study; Darley Dale sandstone, Penmaenmawr microgranodiorite, and gypsum. The sandstone represents a typical sedimentary sandstone rock of medium porosity ( $\approx 13\%$ ), and a pore structure comprised of pre-existing cracks and spherical pores. The material has been used extensively in the laboratory and a large quantity of experimental data and experience has been accumulated using it. In contrast with microgranodiorite, Darley Dale sandstone displays marked dilatancy and compaction during the deformation cycle. The microgranodiorite was selected as a typical continental crustal rock. Its porosity and micro-structure are  $\approx 1-2\%$ , and comprises mainly of microcracks. Gypsum dehydrates at low temperatures relative to crustal conditions. For this reason its presence and behaviour are important in controlling the deformation of surrounding crustal rocks.

#### 6.1.2.1. Darley Dale Sandstone.

The source for this material is Darley Dale in Derbyshire. It is a well indurated feldspathic sandstone with siliceous cement, of porosity between 12% and 14%. It consists of  $\approx 75\%$  quartz with little or no fracturing,  $\approx 15\%$  feldspar (plagioclase and microcline), and  $\approx 10\%$  other constituents. The rock is poorly graded with angular to sub-angular grains of diameters between 80-800 $\mu\text{m}$ . The grains show a low degree of corrosion and interlocking, (Ismail 1976).

#### 6.1.2.2. Penmaenmawr Microgranodiorite.

This rock comes from Penmaenmawr, Caernarvonshire. Porosity is generally between 1.7% and 2.0%. Altered plagioclase is dominant, with 10-20% free quartz, often graphically inter-grown with the feldspar. Grain size is 50-100 $\mu\text{m}$ , (Murrell and Ismail 1976b). The rock contains a small amount of chlorite and amphibole which decomposes at elevated temperatures. No preferred grain orientation is exhibited. The rock suffers partial melting at  $\approx 700^\circ\text{C}$ .

#### 6.1.2.3. Gypsum.

This rock comes from Glebe Mine, Nottinghamshire. The crystals are fine to medium grained, subhedral to anhedral in shape. Some crystals are elongated and some deformed. The crystals display no preferred orientation. The rock is locally darkened by impurities of clay and iron oxide. Porosity has been measured at between 0.4% and 0.55%, (Murrell and Ismail 1976b).

### 6.1.3. Behaviour of Rocks under Simulated Crustal Conditions.

The rocks described above have been used in previous studies by Ismail (1976), Murrell and Ismail (1976a and 1976b), Edmond & Murrell (1973), Jones (1989), and Ayling (1991). The work conducted demonstrates the stress/strain behaviour of the rock under triaxial stress (both drained and undrained), and temperature. The following section reviews some of the above work which illustrates the brittle/cataclastic deformation behaviour of the rocks under crustal conditions.

#### 6.1.3.1. Darley Dale Sandstone.

The rock is a strong sandstone, and significant compaction and cracking occurs during the deformation process. The rock displays dynamic faulting failure up to a confining pressure of  $\approx 80 \rightarrow 120$ MPa. The initial compaction stage can extend up to 0.3% axial strain, during which very little grain crushing is thought to occur from a low

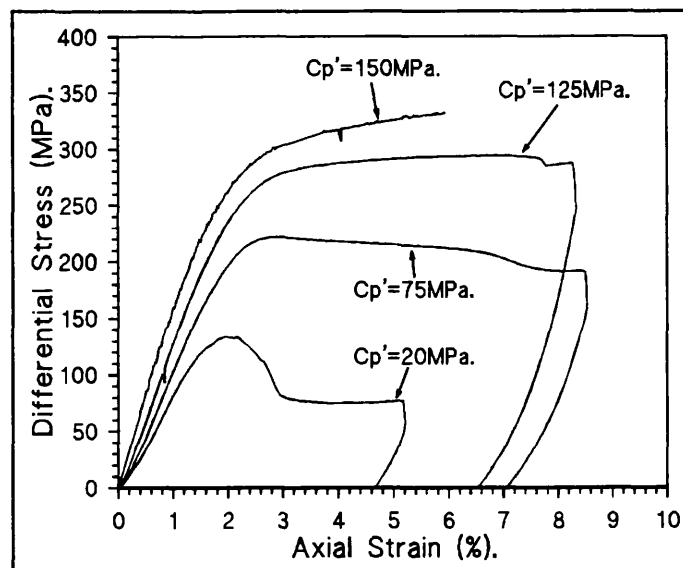


Fig. 6.1.3.1.a. Stress/strain curves for Darley Dale sandstone at various effective confining pressures displaying the change from dynamic faulting to cataclastic flow.

rate of AE. Typical triaxial test results for a variety of confining pressures is

displayed in fig 6.1.3.1.a. It can be seen how peak strength and the strain hardening/softening phase changes with confining pressure. At between  $C_p' = 120\text{MPa}$  and  $150\text{MPa}$  rock behaviour goes through a transition from brittle faulting failure to cataclastic flow. P-wave velocity data measured during the pseudo-linear elastic stage of deformation indicate (in the brittle regime) intense crack closure ( $V_p$  increase), until one half to two thirds of peak stress, followed by dilatant crack growth ( $V_p$  decrease).

### 6.1.3.2. Penmaenmawr Microgranodiorite.

The rock has a high Young's modulus although under the effect of elevated temperatures suffers mineral dehydration and partial melting, which both contribute to weakening.

Fig. 6.1.3.2.a. shows the fracture stress and stress drop plotted against confining pressure. It can be seen that under minimal

confining pressure ( $7\text{MPa}$ ), the fracture strength and stress drop in dry samples is  $\approx 250\text{MPa}$  and  $\approx 200\text{MPa}$ , respectively. Fracture strength increases steadily and stress drop decreases steadily so that beyond  $\approx 700\text{MPa}$  the rock experiences no dynamic failure, only cataclastic flow.

In dry triaxial experiments on microgranodiorite under  $C_p = 100\text{MPa}$ ,  $V_p$  first increased steadily by 3.5% until  $\sigma_{\text{diff}} = 400\text{MPa}$  (2/3 of peak strength), after which it fell steadily at the same rate by 2.5% until fracture. The change from  $V_p$  increase to  $V_p$  decrease was coincident with the onset of acoustic emissions. Fracture strength in this experiment was  $\approx 650\text{MPa}$ , (Jones 1989).

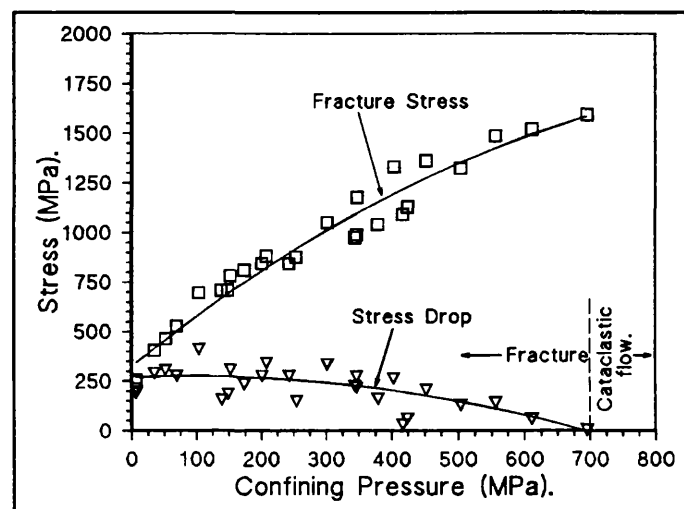


Fig. 6.1.3.2.a. Fracture stress and stress drop plotted against confining pressure. It displays the move from dynamic failure to cataclastic flow. (After Ismail & Murrell, 1989)

With the application of elevated temperatures on dry samples, the rock dehydrates. The reaction equation is given below.



(6.1.3.2.a)

The reaction is known to take place at 500-600°C. Another dehydration reaction is known to occur at  $\approx 320^\circ\text{C}$ , the details of which remain to be elucidated. Dehydration generates high pore fluid pressure in undrained samples and causes marked weakening compared to either drained conditions or experiments at lower temperatures. At 720°C partial melting causes the rock to flow rather than fracture, and reduces strength still further. This has been confirmed by specimen microscopy, (Murrell & Ismail 1976b). Water added to samples prior to experimentation causes embrittlement and dramatic reduction in strength at temperatures below 320°C; the effective confining pressure ( $C_p'$ ) being reduced nearly to zero. Dilatant crack growth in this rock during brittle failure under undrained conditions causes dilatancy hardening.

In the present study, temperatures in the range of 20°C to 400°C are used, and confining pressures used are below that required to cause cataclastic flow in this rock.

### 6.1.3.3. Gypsum.

Under dry conditions the rock experiences dynamic faulting failure to a confining pressure of 40MPa, after which cataclastic flow dominates. Very little linear elastic deformation is evident. P-wave velocity measurements conducted during dry triaxial experimentation indicate an initial compaction phase which decreases in magnitude with increased confining pressure. Following compaction dilatant crack growth causes a  $V_p$  decrease, and the magnitude of the  $V_p$  decrease also *decreases* with increasing confining pressure. This indicates reduced dilatant cracking with increasing confining pressure, (Jones 1989).

Gypsum dehydrates at elevated temperatures. The reaction is as follows; gypsum, to a h e m i - h y d r a t e (bassanite) at between 110°C and 130°C, and then to anhydrite at a higher temperatures of ≈ 190°C, see equation 6.1.3.3.a. below. Fig. 6.1.3.3.a. show the results of a differential thermal analysis of gypsum. Dehydration begins at between 40°C→58°C, but the rate is so slow at this temperature that it is hardly noticeable, (Ismail 1974).

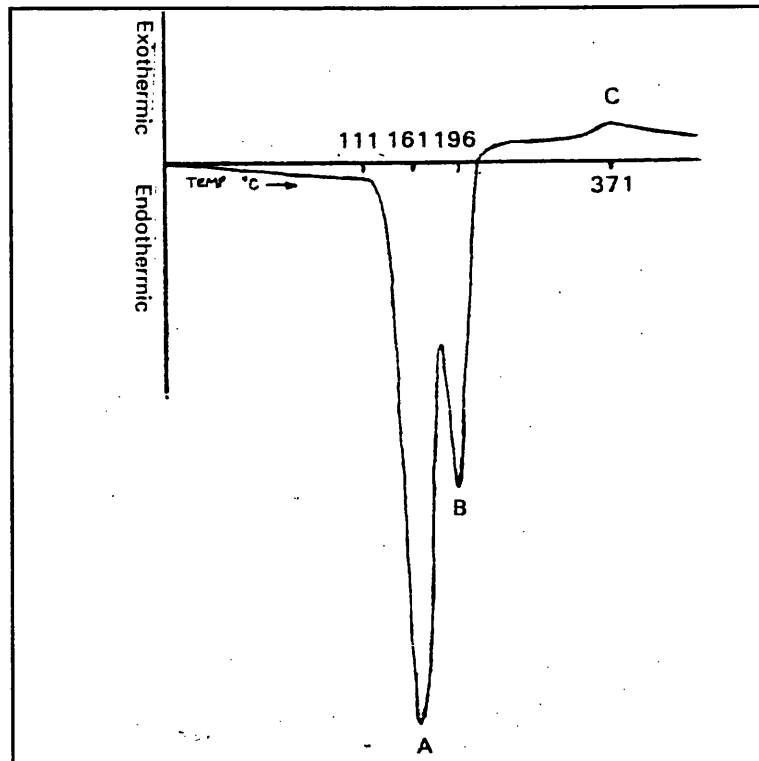


Fig. 6.1.3.3.a. Differential Thermal analysis curve for gypsum. A corresponds to dehydration to hemihydrate, B corresponds to dehydration from hemihydrate to anhydrite. (After Ismail 1974).



(6.1.3.3.a.)

## 6.2. Drained and Undrained Conditions, and Effect of Variations in Upstream Reservoir Volume on Deformation Characteristics of Darley Dale Sandstone.

### 6.2.1. Introduction and Review.

The effect of a constant pore fluid pressure (*drained environment*), on rock deformation under triaxial stress conditions is governed by the mechanical properties of the rock and the law of effective stress. Under these conditions fluids flows into or out of the rock in response to changing pore (and crack) volume. The effect of a constant fluid mass confined within the rock (*undrained environment*) on rock deformation is that pore fluid pressure changes in response to changes of pore (and crack) volume. See section 2.3. which discussed poro-elasticity and effective stress in more detail.

Darley Dale sandstone has been examined with respect to drained and undrained conditions by Murrell (1965) and Ismail and Murrell (1976), respectively. In the latter work specimens of sandstone were deformed under triaxial stress with known volumes of fluid added to the specimens prior to jacketing. The

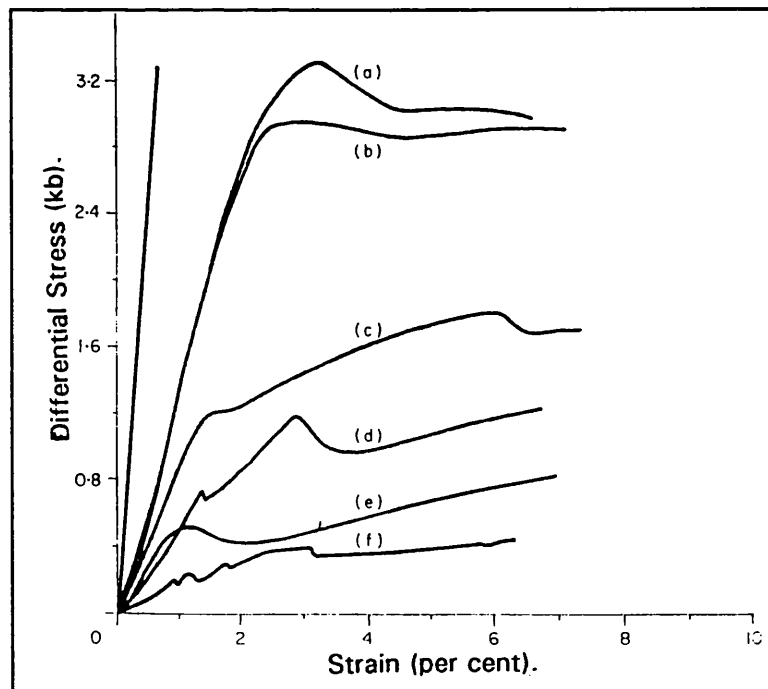


Fig. 6.2.1.a. Undrained tests on sandstone for different quantities of fluid added; a) 0, b) 170 $\mu$ l, c) 264 $\mu$ l (saturated), d) 316 $\mu$ l, e) 325 $\mu$ l, f) 363 $\mu$ l. (After Ismail & Murrell 1976).

different fluid volumes added to the samples corresponded to *under-saturating* the sample (less fluid volume than rock pore volume), *fully saturating* the sample (fluid volume added equals pore volume of sample), and adding more

fluid than the rock can initially hold in the pore/crack spaces - termed *over-saturating*.

The flexible jackets used for these tests meant that the pore fluid pressure ( $P_p$ ), could never rise above confining pressure ( $C_p$ ), as water simply escaped from the rock sample into the space between the jacket and the rock. Fig. 6.2.1.a. shows the effect of added water volumes on the stress/strain curves in tests at fixed confining pressure of 110MPa. Dilatancy hardening is clearly seen.

Fig. 6.2.1.b. shows the effect of different confining pressures and different amounts of water added to samples. The saturation point (where strength drop occurs), is clear.

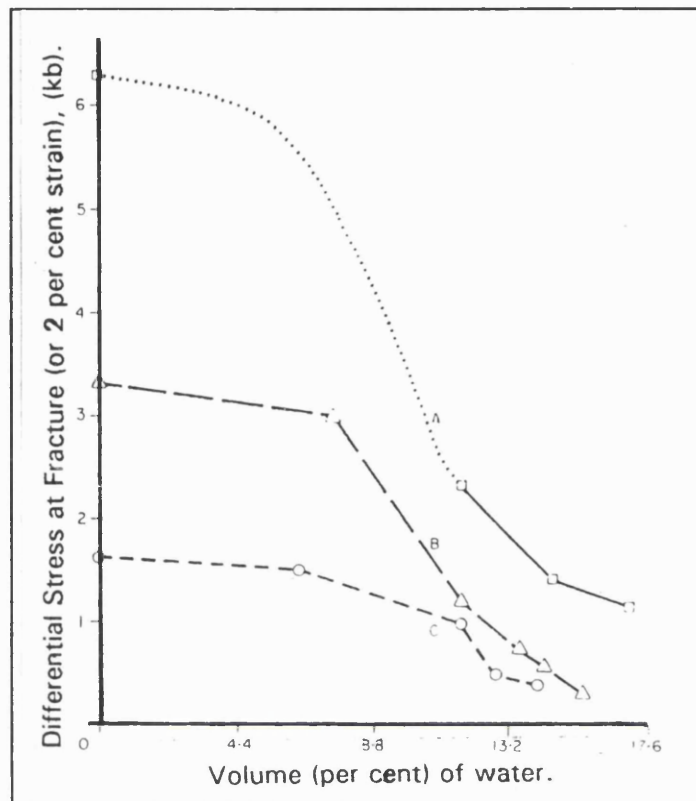


Fig. 6.2.1.b. Strength of sandstone under undrained test for different quantities of fluid added and different confining pressure; A) 441MPa, B) 110MPa, C) 35MPa. (After Ismail & Murrell 1976).

In the study by Ismail and Murrell (1976) the value of pore fluid pressure could not be monitored directly, but by using the law of effective stress, comparison could be made with earlier drained experiments on the same rock. Fig. 6.2.1.c. compares the two sets of data for an external confining pressure of 110MPa, and shows strength as a function of pore pressure in drained tests, and pore fluid volume (mass) in undrained tests.

Jones (1989) conducted work on *over-saturated* Darley Dale sandstone and also showed the same shift from strain hardening to strain softening behaviour with increasing volumes of fluid added. His results showed that the rock also obeyed the effective stress law well under these conditions.

Measurement of pore fluid volume changes in drained triaxial deformation experiments on Darley Dale sandstone have been reported by Read et al (1995), for effective confining pressures ( $C_p'$ ) of 20MPa, 50MPa, and 100MPa. The results are generally similar to those reported in the present study.

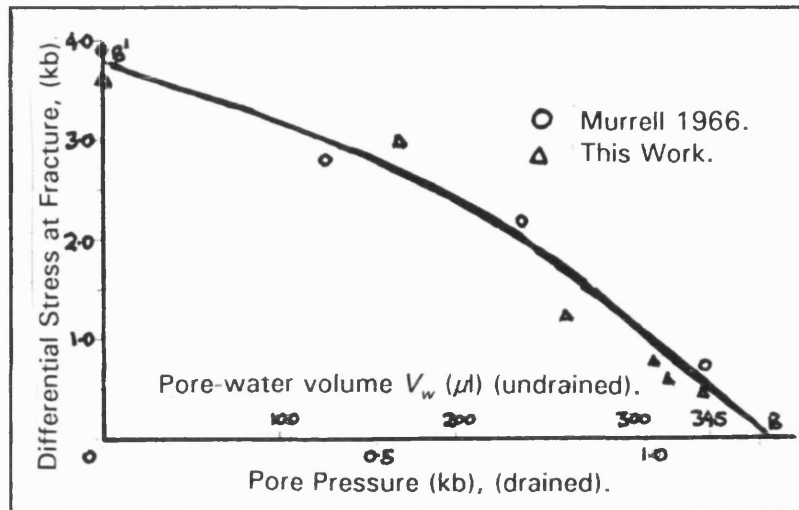


Fig. 6.2.1.c. Comparison of the strength of sandstone under drained, (constant pore pressure, Murrell 1966, circles), undrained (pore fluid added, Ismail & Murrell 1976, triangles).

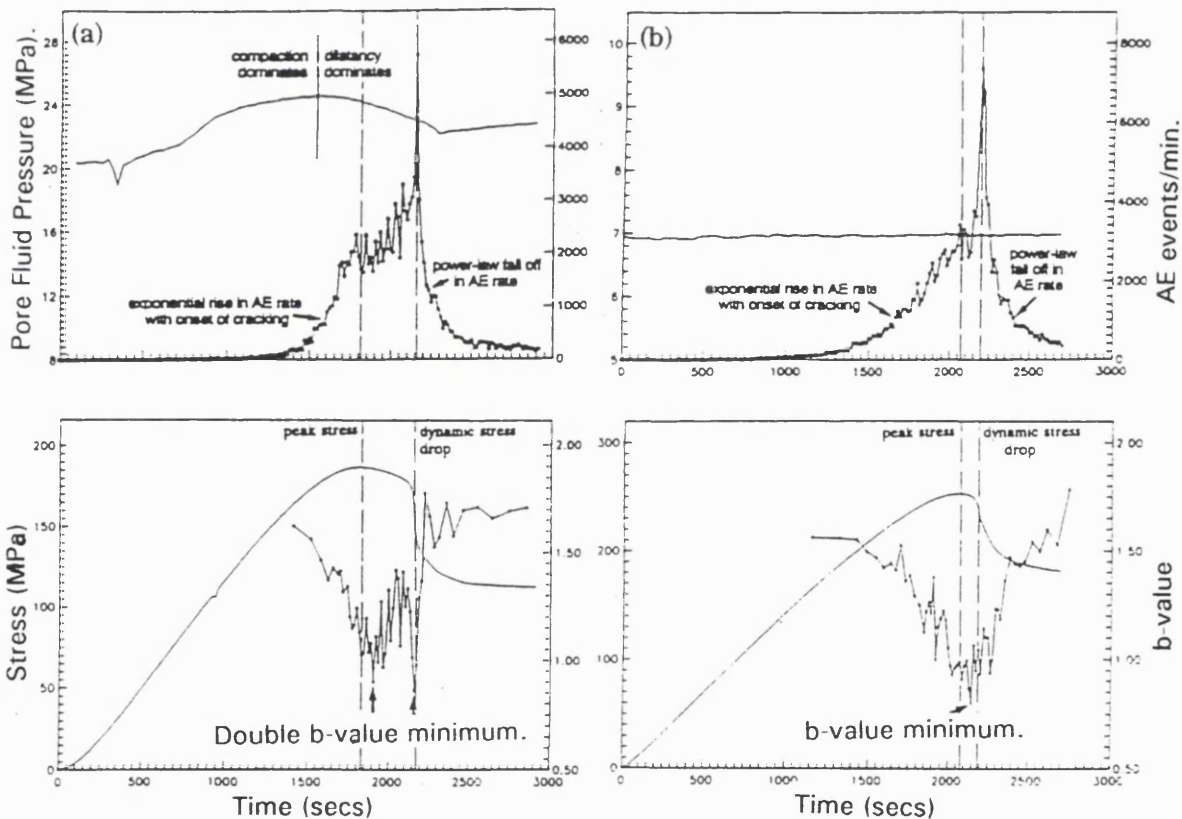


Fig. 6.2.1.d. Sandstone deformed under undrained (a), and drained (b) conditions monitoring pore fluid volume and pressure changes, After Sammonds, Meredith & Main 1992, see text for details.

Acoustic emissions event rate and  $b$ -value measurements have been reported by Sammonds, Meredith and Main (1992) for dry, undrained, and drained experiments on Darley Dale sandstone, (fig. 6.2.1.d.). For all three conditions they report an exponentially rising AE and a high but decreasing  $b$ -value during initial crack growth. The behaviour of the AE event rate and  $b$ -value during pre- and post- peak strength region is where differences were found between the drained and the undrained case. For the drained experiments, the AE event rate increases to a peak at dynamic failure and the  $b$ -value to a minimum of between 1.0 and 0.5. In the drained case (b) the stress/strain curve shows a small roll over relative to the undrained case (a), and an abrupt stress drop. In the undrained case, the AE rise is interrupted by an inflection point coincident with peak strength, before finally rising to a peak as the stress drops sharply during dynamic failure. The  $b$ -value shows a double minimum, one at peak stress and one at dynamic failure. The stress/strain curve showed a much longer period of strain softening.

These three phenomena (AE,  $b$ -value, and extended strain softening), are attributed to dilatant crack growth increasing pore volume in the specimen, causing a falling pore fluid pressure, and an increase in the effective confining pressure. This permits a relaxation of the stress intensity ( $K$ ) at crack tips, reducing the *rate* of damage accumulation, and delaying final dynamic failure.

### 6.2.2. New Apparatus.

The newly commissioned pore fluid pressure intensifier discussed in chapter 4 is essential for this pore volumetry work. In addition to the major modifications already discussed, extra apparatus was commissioned in order to vary the URV for this suite of undrained experiments.

Additional volumes of fluid were connected between the remotely operated valve and the rock specimen see (fig 4.4.5.1.b.). These extra volumes take the form of high pressure tubing of large internal diameter (hence a short length for a given volume), of dimensions 3/8" (9.53mm) O.D. x 1/8" (3.18mm) I.D. rated at 400MPa (purchased from HiP). The tubes are connected to the ports marked

C. and D. on fig. 4.4.5.1.b. via a 3/8"→1/4" connector pieces. The 3/8" *hp* tubing is sectioned into lengths equivalent to 1,500mm<sup>3</sup>, 3,000mm<sup>3</sup> and 6,000mm<sup>3</sup> - equal to approximately 1.5x, 3.0x, and 6.0x the typical pore volume of an unstressed Darley Dale sandstone specimen. Any two of these lengths may be connected to the pore pressure intensifier system at any one time, allowing URV's of between 2,100mm<sup>3</sup> and 13,700mm<sup>3</sup>, in increments of 1,500mm<sup>3</sup> to be employed. Alternatively the whole tubing system and the pore fluid intensifier under volume control can be employed, giving a total URV of ≈ 23,000mm<sup>3</sup>.

### 6.2.3. Programme of Experiments.

Three groups of four or five tests were conducted - groups A. B. & C. The groups were divided according the starting pore fluid pressure used, and hence the effective confining pressure.

Group A -  $C_p = 170\text{MPa}$ ,  $P_p = 150\text{MPa}$ ,  $C_p' = 20\text{MPa}$ .

Group B -  $C_p = 170\text{MPa}$ ,  $P_p = 95\text{MPa}$ ,  $C_p' = 75\text{MPa}$ ,

Group C -  $C_p = 170\text{MPa}$ ,  $P_p = 45\text{MPa}$ ,  $C_p' = 125\text{MPa}$ ,

The temperature was 20°C, and the porosity for the Darley Dale sandstone specimens used in the fourteen experiments ranged from 11.7% to 12.8%. The URV adopted for the six experiments in each group were 22,800mm<sup>3</sup>, 13,700mm<sup>3</sup>, 11,700mm<sup>3</sup>, 2,600mm<sup>3</sup>, and 2,100mm<sup>3</sup>.

### 6.2.4. Results.

#### 6.2.4.1. Drained and Undrained Triaxial Deformation Experiments on Darley Dale Sandstone.

The results for both a drained and an undrained experiment for each of the three sets of conditions (Group A, B, & C), are shown in fig. 6.2.4.1.a, b. & c. The undrained experiments were conducted using an URV of 2,100mm<sup>3</sup>. The stress conditions for each set of results is given in the body of the graph. The graph shows clearly that different deformation behaviour results from a

varying pore fluid pressure during deformation compared with constant pore fluid pressure.

Fig. 6.2.4.1.a. shows that initially the stress/strain curve of the two tests follow generally the same path until  $\approx 50\%$  peak strength. In this first region initial compaction of the rock (closure of pre-existing microcracks) causes a stiffening of the rock (increasing  $E$ ). The "stiffer" (increasing fluid bulk modulus) fluid in the undrained case increases the *undrained bulk modulus* ( $K_u$ ) of the rock, and hence increases the gradient of the stress/strain curve.

In the *drained* case, it can be seen how the stress/strain curve peaks at  $\approx 135$  MPa, followed by dynamic failure at  $\approx 2.5\%$  axial strain ( $\epsilon$ ), and further axial strain takes place on the failure plane formed by the rupture. Dilatant

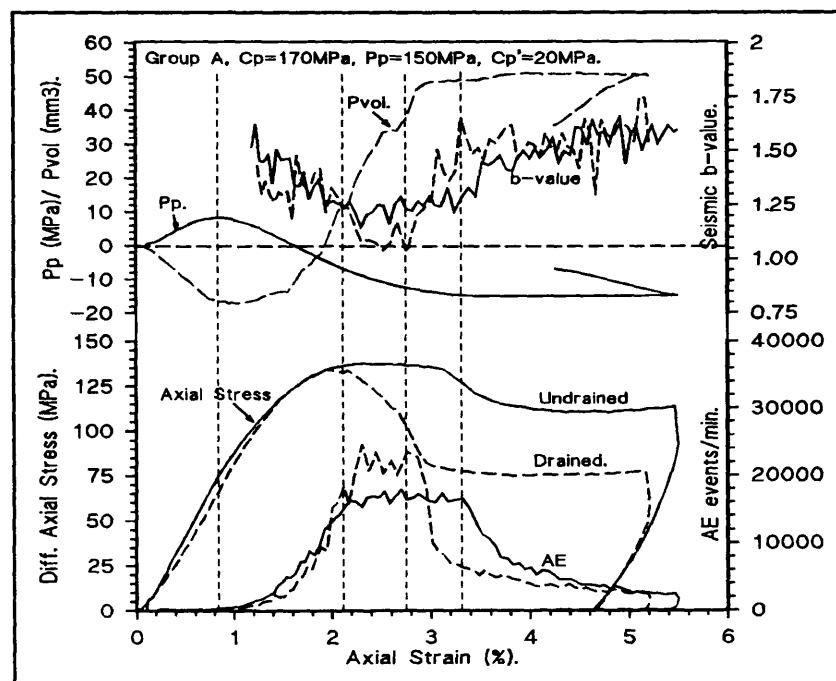


Fig. 6.2.4.1.a. Results of a drained (dashed line), and undrained (solid line) triaxial deformation experiment on Darley Dale sandstone. See text for details.

crack growth occurs steadily from  $\epsilon \approx 1.5\%$  until full dynamic rupture. The AE event rate results shows an exponential increase beginning at the  $\approx 50\%$  peak strength, and a broad maximum from peak strength to dynamic failure. The seismic  $b$ -value shows a decreasing value from  $\approx 1.5$  initially to a broad minimum of 1.0 at rupture, increasing afterwards to its initial value of  $\approx 1.5$ . This response is coincident with the findings of Sammonds, Meredith & Main (1992). The behaviour of the pore fluid volume curve, undulating after showing initial compaction, is thought to be a consequence of competing mechanisms of deviatoric stress induced crack growth and mean stress induced compaction. This is expected at *transitional* confining pressures.

The *undrained case* show different stress/strain behaviour from  $\epsilon = 0.8\%$  onwards. After a differential axial stress of 50% of peak strength, the undrained case begins to display some strain softening - a *rolling over* of the stress/strain curve. This is coincident with the onset of AE and a peak in the pore fluid pressure curve, indicating that dilatant cracking has become the dominant mechanism compared with compaction. The onset of dilatant cracking occurs *slightly* earlier than in the drained case due to the lower effective confining pressure at  $\epsilon = 0.8\%$  (seen from pore volume and pressure minimum and maximum resp.). The increasing effective confining pressure from  $\epsilon = 0.8\%$  on causes a continual strengthening of the rock, and a delay in dynamic rupture until  $\epsilon = 3.1\% +$ . The peak strengths for the two conditions are similar because the effective confining pressure at  $\epsilon = 2.0\%$  are similar. The residual strength of the specimen after rupture is greater in the undrained case due to the higher post-rupture effective stress of  $\approx 35\text{MPa}$  (compared to  $20\text{MPa}$  in the drained case), hence dynamic stress-drop in the undrained case is reduced. The AE event rate data for the undrained case shows a similar pattern to the drained case.

The decreasing pore fluid pressure between  $\epsilon = 0.8\%$  to  $3.1\%$  in the *undrained case* (causing a gradual strengthening of the rock), is worthy of a note. As dilatant crack growth initiates ( $\epsilon = 0.8\%$ ), at an effective confining pressure of  $11\text{MPa}$ , rock pore volume increases causing pore fluid pressure to decrease. From the peak in pore fluid pressure ( $P_p$ ) at  $\epsilon = 0.8\%$ , to  $\epsilon = 3.1\%$ , the falling  $P_p$  causes an increase in effective confining pressure ( $C_p'$ ), which impedes dilatant crack propagation, reducing the rate of damage accumulation, and hence the rate at which pore fluid pressure falls. This causes a gradually decreasing gradient in the pore fluid pressure curve. After a certain amount of damage has been accumulated in the sample, crack density is such that crack interaction is inevitable. For small increments of crack growth, large increases in damage occur in localised areas critical to the integrity of the specimen - i.e. at the embryonic fracture plane. A plane of weakness thus develops which can no longer support the differential axial stress, and failure occurs. In the solid rock surrounding the fault plane, stress is then much reduced and pore volume change (hence pore pressure change), is generally zero during stable sliding.

During sliding, further grain fracture & rotation, and pore compaction continues within the fracture zone. Upon unloading, stress relief in the body of the rock causes dilatant microcracks to close and the pore fluid pressure to rise. This same effect is seen by a fall in pore fluid volume (fluid expelled from rock) in the drained case.

Fig. 6.2.4.1.b. shows the results of a drained and undrained test on the same rock (Darley Dale sandstone) under the same confining pressure but lower pore fluid pressure (95MPa). Similar features can be seen.

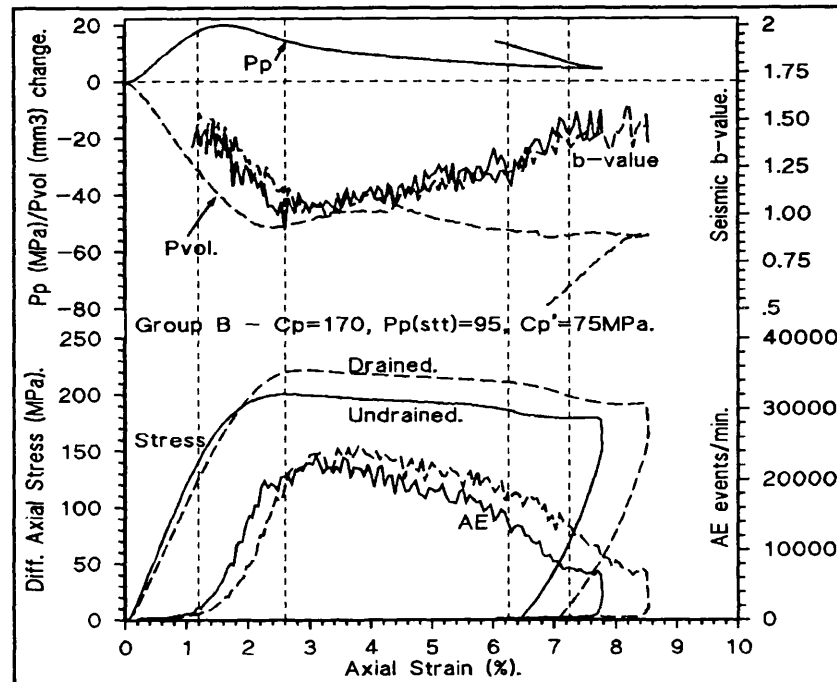


Fig. 6.2.4.1.b. Drained and Undrained triaxial deformation result. Stress conditions in body of graph. See text for details.

- ▶ Stiffer undrained specimen under initial compaction  $\epsilon = 0 \rightarrow 1.5\%$  due to increasing pore fluid pressure initially in the undrained case.
- ▶ Earlier initiation of dilatant cracking in undrained case due to the lower (and decreasing) effective confining pressure,  $\epsilon = 1.4\%$  (undrained),  $\epsilon = 1.8\%$  (drained). This is also evident at axial strains of 3.0+ as the AE curve is retarded in the drained results compared to the undrained result.
- ▶ Exponentially rising acoustic emissions, reaching a maximum at peak stress, then gradually falling with the decreasing rate of damage accumulation.

- ▶ Decreasing  $b$ -value reaching a broad minimum at peak stress in both the undrained and the drained case.
- ▶ Pore fluid expelled during differential stress unloading (at  $\epsilon \approx 8\%$ , pore fluid pressure rise/pore fluid volume fall) due to the closure of dilatant cracks.

The two results shows similar behaviour due to the effective confining pressure of 75MPa at commencement of experimentation, (close to transition confining pressure). If this value were lower (brittle regime), the rock would display greater confining pressure sensitivity, (fig 6.2.4.1.a.). The specimens suffer cataclastic flow and localised faulting, as evident in the stress/strain curve and from post experimental specimen observation. Furthermore the failure plane exhibited little strain compared to the total permanent axial strain throughout the specimen ( $\approx 7.0\%$ ). This confirms the point of dynamic failure of the specimen at  $\epsilon \approx 7.2\%$ , coincident with a sharp decrease in AE event rate and an increase in the seismic  $b$ -value.

In the *undrained* case, the effective confining pressure increases from 55MPa to 70MPa throughout the extended strain softening period ( $\epsilon = 2.6 \rightarrow 6.2\%$ ). Results in this and other studies have shown that Darley Dale sandstone fails in a brittle manner at this confining pressure. The decreasing pore fluid pressure and the relaxation of crack tip stress intensity is producing the extended strain softening region in a similar fashion as seen in fig. 6.2.4.1.a.

Fig 6.2.4.1.c. shows results of an undrained and a drained experiment conducted at a confining pressure of 170MPa, and a commencing (undrained test) pore fluid pressure of 45MPa, (hence  $C_p' = 125\text{MPa}$ ). Many similarities exist between the data in fig.'s 6.2.4.1.a., b., & c. These are highlighted below.

- ▶ AE response, exponential increase and broad maximum, continued AE activity throughout cataclastic flow.

- ▶ Initially stiffer undrained test specimen compared to drained specimen as pore fluid pressure increases between  $\epsilon = 0.0 \rightarrow 1.2$  %.

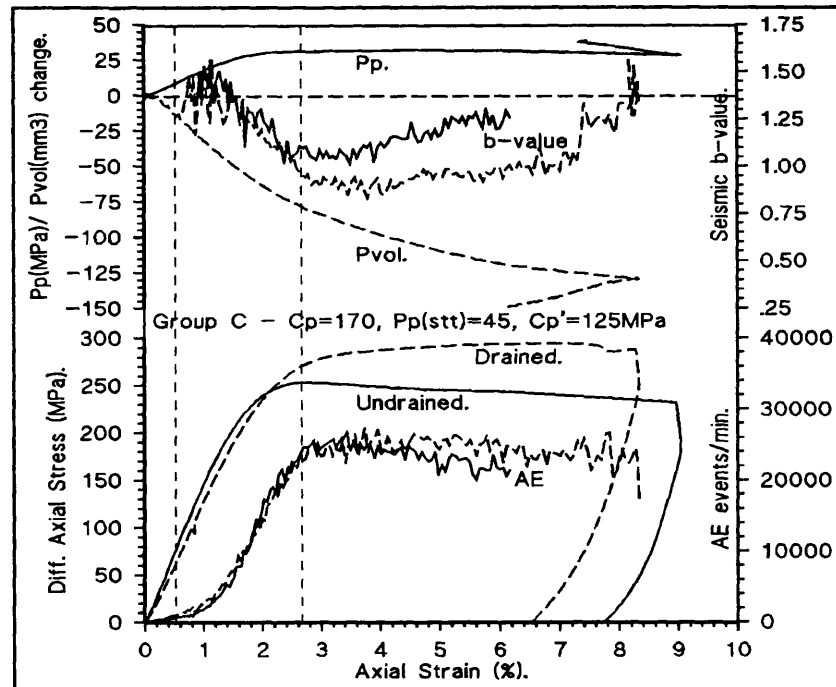


Fig. 6.2.4.1.c. Drained and undrained results of triaxial deformation experiments at conditions shown in body of graph. See text for details.

- ▶ Pore fluid volume decrease and pore fluid pressure increase during differential stress unloading indicates the closure of deviatoric stress induced dilatant cracks.
- ▶ Broad minimum to seismic  $b$ -value.

In both the drained and the undrained test shown in fig. 6.2.4.1.c. the effective confining pressure is  $> 100\text{MPa}$ , and therefore cataclastic flow dominates the deformation process.

The different strengths, and the strain hardening/strain softening differences of the two experiments is a function of the effective confining pressure for each experiment. The drained tests is deforming under an effective confining pressure of  $\approx 125\text{MPa}$ , whereas the undrained tests is deforming under an effective confining pressure of  $\approx 94\text{MPa}$ . Consequently, the drained specimen is strain hardening whilst the undrained specimen is behaving in a transitional manner, showing strain softening but no faulting failure.

*In summary*, an undrained environment affects the deformation of rocks through the mechanical effect of a varying pore fluid pressure. This can bring the rock into the brittle regime from a previously cataclastic deformation stress environment. Furthermore, examination of the pore fluid pressure and volume curves from pore volumetry experiments yields information concerning the micro-mechanisms of deformation. This is covered in more detail in section 6.4.

#### 6.2.4.2. Results of Upstream Reservoir Variation under Undrained Triaxial Conditions.

Fig. 6.2.4.2.a. shows the stress/strain and pore fluid pressure/strain curves for four undrained triaxial experiments conducted under a confining pressure of 170MPa, a starting pore fluid pressure of 150MPa, and hence a starting effective confining pressure of 20MPa. Each experiment is

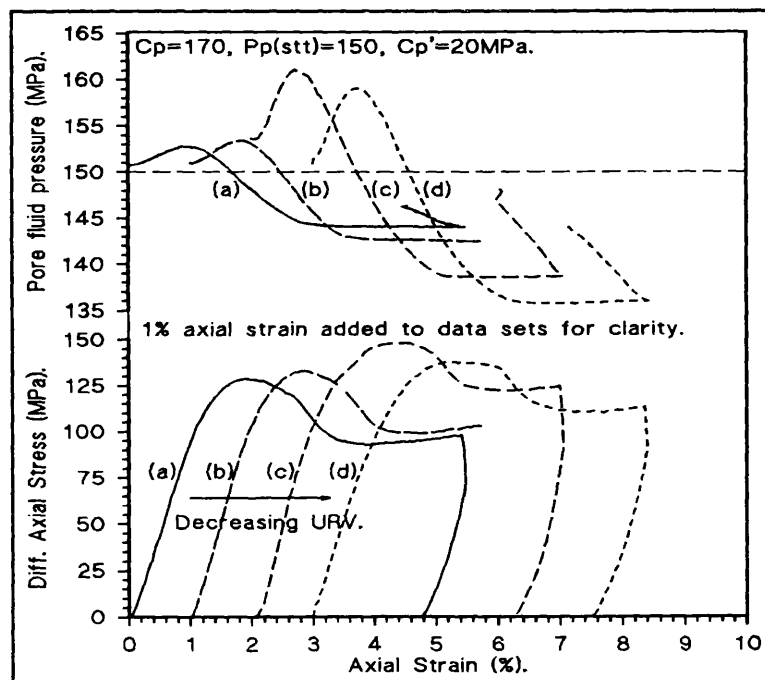


Fig. 6.2.4.2.a. Four undrained test results conducted at different URV's. Details in body of graph and in text.

conducted with a different upstream reservoir volume, (URV). For the stress/strain curves marked (a), (b), (c), and (d), the URV's are; 21,200mm<sup>3</sup>, 13,400mm<sup>3</sup>, 2,600mm<sup>3</sup>, and 2,100mm<sup>3</sup> respectively. The effect of a reduced URV on the pore pressure response during deformation, and hence on the stress/strain curve, is well illustrated in the figure. The points are highlighted below.

- ▶ Exaggerated pore fluid pressure rise and fall with compaction and dilatant crack growth with a decreased URV.
- ▶ Strain hardening (*roll over*), begins earlier in the stress/strain cycle for a smaller URV. This is due to the increasing pore fluid pressure during compaction (decreasing effective mean stress) bringing the rock further into the brittle regime during deformation.
- ▶ A smaller URV causes a larger pore fluid pressure drop, which continues for up to 2% axial strain. This falling pore fluid pressure strengthens the rock during deformation and delays final faulting failure, curve (d), (see section 6.2.4.1.).
- ▶ For a smaller URV, the earlier peak in pore fluid pressure and the more rapid pore fluid pressure drop during dilatant crack growth, the lower the pore fluid pressure at peak strength (higher  $C_p'$ ), and hence the higher the value of peak strength. This same behaviour causes a higher effective confining pressure *after* faulting failure, and hence a higher residual shear strength. Overall this causes a lower stress-drop during faulting failure for a smaller URV.
- ▶ Upon unloading at the end of the deformation cycle, pore fluid pressure rises in all cases due to the closure of dilatant cracks. This pore fluid pressure rise is enhanced by a smaller URV.

Fig. 6.2.4.2.b. shows the results of five triaxial deformation experiments conducted under an effective confining pressure of 75MPa - 50MPa more than in the last suite of experiments. The URV volumes are the same as for 3.2.4.2.a. Some of the deformation characteristic resulting from different URV's are similar to the results in fig. 6.2.4.2.a., and these are summarised briefly below.

- ▶ Pore fluid pressure response much exaggerated for smaller URV.

- ▶ Lower peak rock strength under smaller URV, (due to higher pore fluid pressure attained).
- ▶ Post-peak rate of decreasing pore fluid pressure, (due to dilatant crack growth), is increased for smaller URV, causing delayed faulting failure (extended roll over), and reducing the differential axial stress drop.
- ▶ Pore fluid pressure rise upon differential axial stress decrease at the termination of test, due to the closure of elastically opened dilatant crack, is increased for smaller URV.

Some characteristics particular to the stress conditions adopted for this suite of experiments are detailed below.

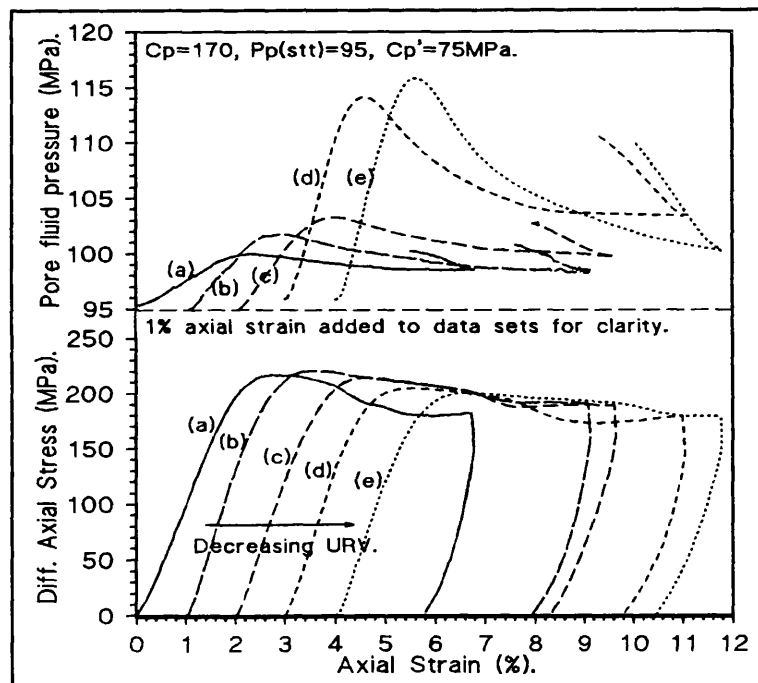


Fig. 6.2.4.2.b. Five experiments conducted at different URV's. Details in body of graph and in text.

- ▶ The effective confining pressure (at start of test) selected for this suite of experiments means that, for the smallest URV, (e) the rising pore fluid pressure upon compaction (falling  $C_p'$ ) causes deformation to move into the brittle regime ( $C_p' = 55\text{MPa}@ \epsilon + 1.5\%$  for e). A falling pore fluid pressure then delays final failure (as before), and brings deformation back into the transition (brittle  $\rightarrow$  cataclastic flow) regime, a factor contributory in causing a smaller differential axial stress drop upon faulting for the smallest URV, curve (e).

- ▶ The slope of the strain softening region of the stress/strain curve varies between (b), (c), (d) & (e), and is generally inversely related to the slope of the pore fluid pressure curve, i.e. for a faster falling pore fluid pressure, the rock strengthens at a faster rate, hence strength decreases at a slower rate.
- ▶ The higher effective confining pressure in this suite of experiments compared to those in fig. 6.2.4.2.a. is responsible for the *lower* rate of pore fluid pressure fall during dilatancy. i.e. dilatancy is inhibited compared to test conditions at  $C_p' = 20\text{MPa}$ , (fig. 6.2.4.2.a.).
- ▶ The results of the experiment (d) & (e) show an anomalous post-peak pore fluid pressure response; final pore fluid pressure in (d) is higher than the results for the smallest URV, curve (e). The earlier plateau in pore fluid pressure achieved for result (d) is prompted by dynamic failure of the specimen, afterwhich differential stress is constant and compaction and dilatant crack growth mechanisms are halted in the solid surrounding rock. The early dynamic failure for *this* specimen is thought due to sample variability.

Fig. 6.2.4.2.c. shows the results from a similar suite of experiments conducted with a variety of URV's under an effective confining pressure ( $C_p'$ ) of 125MPa, (105MPa higher than the first suite of experiments presented). The URV's for the five experiments are the same as before. Under drained conditions the results would all display cataclastic flow and pore fluid volume decrease associated with rock compaction. Under undrained conditions, however, a changing pore fluid pressure causes the effective confining pressure to fall below that required for cataclastic flow, and into that range required to cause transitional behaviour. Many deformation characteristics associated with a confined pore fluid mass and different URV's are similar to the other results (fig.'s 6.2.4.2.a. & b.) and are not repeated here. Characteristic of rock behaviour specific to these stress conditions are noted below.

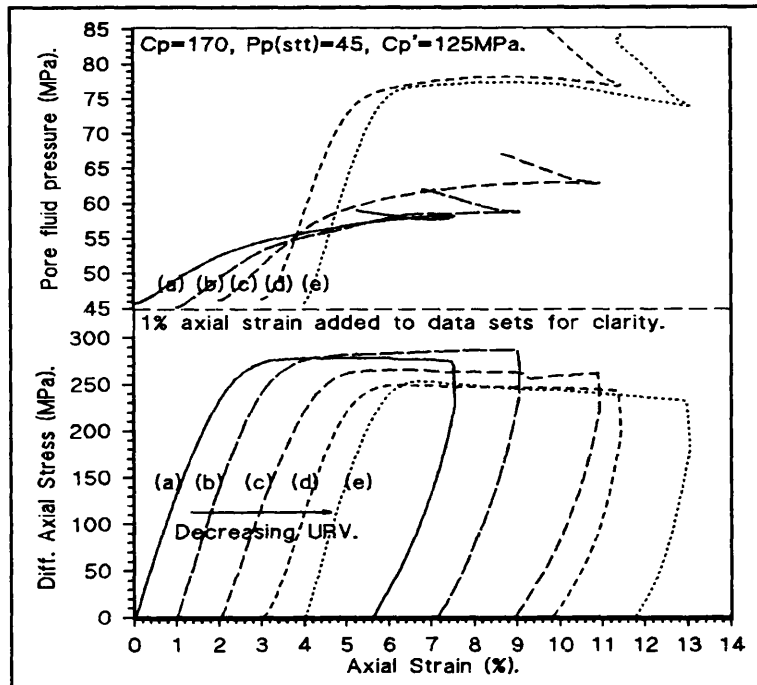


Fig. 6.2.4.2.c. Series of undrained experiments under varying URV. See text for details.

- ▶ The results from experiments employing a large URV's (a), (b), (c) show a small rise in pore fluid pressure upon compaction, as expected. This small rise in  $P_p$  maintains the effective confining pressure above 100MPa, throughout deformation and hence rock behaviour is cataclastic. This is seen in the strain hardening or *flat* response of the stress/strain curves, and continual pore fluid pressure increase. Results (d), and (e), show a large initial pore fluid pressure increase, and a  $C_p'$  fall to 95MPa. Transitional deformation behaviour is seen in the strain softening behaviour of the stress/strain curves, and a plateau followed by a decrease in the pore fluid pressure curve.
- ▶ For curves (b), (c), (d), & (e), upon unloading of the specimen (decrease in differential axial stress), the pore fluid pressure rises for the reasons explained for the two previous suites of experiments. For result (a), however, the pore fluid pressure curve displays a decrease initially, followed by an increase. There are only a few examples of this behaviour seen during this study, and caution should prevail when drawing conclusions. However, consideration of the two mechanisms occurring during deformation - rock compaction and dilatant crack growth - may shed some light on this behaviour.

If both mechanisms occur during differential axial stress increase, it is reasonable to assume that both occur during differential axial load decrease. The response seen here is therefore a result of elastic compaction relaxation, decreasing the pore fluid pressure, and elastically opened dilatant cracks closing, causing pore pressure increase. Traces of elastic compaction recovery can be seen in "flattened initial stages" of the differential stress unloading responses of pore pressure (b), and (c). In case (a), a high effective mean stress means compaction is more dominant during deformation, and therefore compaction relaxation *should* play a larger part during unloading. Hence initially compaction relaxation causes pore pressure decrease, followed by some dilatant crack closure causing  $P_p$  increase.

*In Summary.* Undoubtedly the volume of the upstream reservoir is significant in the behaviour of rock subject to undrained conditions. Some conclusions of these experimental results pertinent to rock failure in the field can be summarised in the following statements,

- ▶ A pore fluid pressure subject to changes resulting from rock pore and crack volume variation can promote cataclastic flow where otherwise brittle faulting would have taken place - hence aseismic creep can occur where dynamic faulting failure may have otherwise been the dominant mechanism.
- ▶ A falling pore fluid pressure during dilatant crack growth under undrained conditions can reduce differential axial stress drop during brittle failure (even though peak stress is increased relative to the drained case), leading to transitional behaviour or cataclastic flow.

The traditional assumption that the introduction of fluid into a rock structure causes a lowering of the effective stress, embrittlement of the rock, and can initiate seismicity needs clarification in light of the above results. In reality the behaviour of rock in the presence of a pressurised pore fluid is highly dependent upon the permeability of the surrounding rock, be it highly impermeable (undrained conditions), highly permeable (drained conditions), or

somewhere between these two extremes. A large upstream reservoir volume in triaxial tests simulates the intermediate condition well by allowing some fluid flow from the rock (to the transducer and *hp* tubing), and some pore fluid pressure changes. Hence, before the exact behaviour of saturated rock under triaxial stress can be predicted information concerning the permeability of the rock under a changing effective stress is necessary.

### 6.2.5. Discussion and Analysis; Pore Fluid Pressure Rise and URV Compensation Factor.

By quantitatively examining the effect of the URV on pore fluid pressure rise during the initial stages of triaxial deformation, a factor to correct the observed pore fluid pressure response corresponding to zero URV can be obtained. In order to achieve this the pore fluid pressure rise for a given set of stress conditions under different URV's must be examined.

The effective mean stress applied to rock induces compaction through elastic pore volume reduction and pore collapse.

Axial deviatoric stress is effective in inducing new crack growth and grain rotation & rearrangement. Both these stress components must be considered in isolation and together when examining pore fluid pressure rise under confined pore fluid conditions and different URV's.

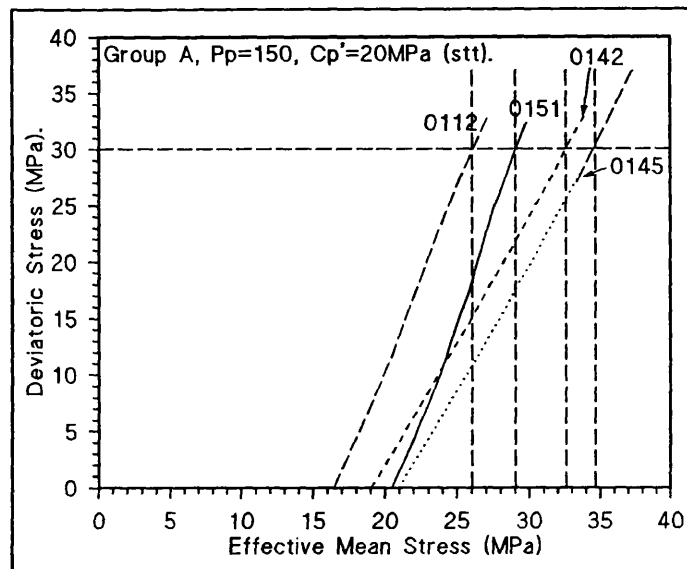


Fig. 6.2.5.a. Increase in deviatoric stress and effective mean stress under the application of a differential load for group A experiments.

Fig. 6.2.5.a. shows the effective mean stress plotted against deviatoric stress for the experiments in Group A, (fig 6.2.4.2.a.). Pore fluid pressure rise in the

early stages of brittle triaxial deformation is considered a result of elastic closure of cracks with their major planes orientated perpendicular to the maximum principle stress (at higher effective confining pressures, new cracking activity can occur at lower differential stresses - section 6.4.3.2.). New crack growth occurs after a critical deviatoric stress is exceeded (crack tip stress intensity), and this second mechanism competes with elastic closure of cracks for the overall effect on rock pore volume and hence pore fluid pressure. This effect can be seen in the smooth peak of the pore fluid pressure curve, and is discussed in chapter 2. For this reason the limited region of deformation in zone 1 ( $\epsilon = 0.0 \rightarrow 0.5\%$  - compaction only) is considered for group A to eliminate the effect of new crack nucleation on the analysis. This renders the results comparable with hydrostatic compression experiments of section 6.3.

The data from fig 6.2.5.a. is presented in figure 6.2.5.b. with the starting effective mean stress set from its actual value of between 16MPa and 21MPa for the four tests, to 20MPa. This simple operation allows better analysis of the *change* in effective mean stress for an increase in deviatoric stress between the four results under consideration. From

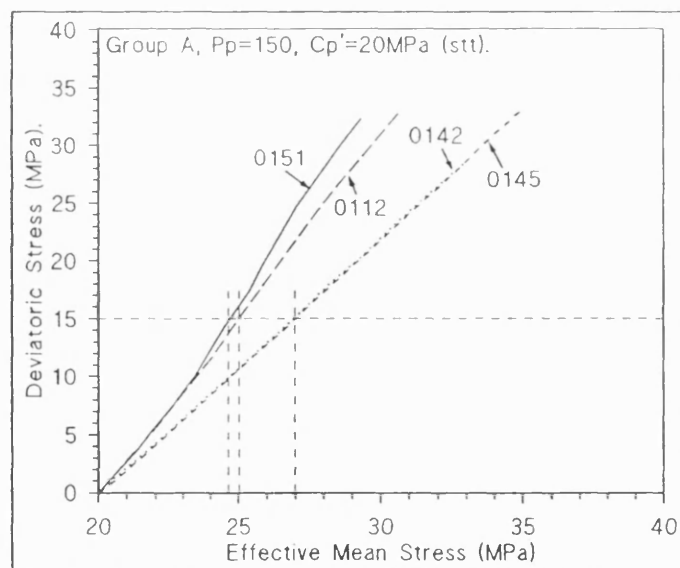


Fig. 6.2.5.b. Results of 6.2.5.a. normalised to 20MPa. Various mean stress recorded for varying effective mean stress and vis versa. See text for details.

this figure, changes in deviatoric and effective means stress can be read. For example, three different effective mean stresses are recorded for a given deviatoric stress, and three different deviatoric stresses for a given effective mean stresses - as shown by the sets of dashed lines in fig. 6.2.5.b. Hence, at a deviatoric stress of 15MPa, an effective mean stress of between 24.5MPa and 27MPa is obtained for the four different tests. The pore fluid pressure is then obtained for this effective mean stress from the experimental data for each test result. This pore fluid pressure (corresponding to a specific mean

stress) is then linearly normalised against effective mean stress for effective mean stresses of 22, 25, and 30MPa. This produces a range of pore fluid pressure rises for a range of effective mean stresses against a fixed deviatoric stress and fixed URV. The different pore fluid pressure rises and mean stress for the different tests is due directly to the different URV's used in the experiments. This linear normalisation is done for an effective mean stress of 22, 25 & 30MPa against a deviatoric stress of 15MPa, and an deviatoric stress of 10, 20 & 30MPa against an effective mean stress 30MPa, hence six sets of data are obtained in total. Whilst normalising pore fluid pressure data assumes a linear relationship between  $P_p$  and  $C_p'$ , it represents an acceptable assumption for the small pressure range considered here.

Fig. 6.2.5.c. shows the normalised percentage pore fluid pressure rise for a mean stress of 30MPa and different deviatoric stresses. The different experiments are represented as different URV's on the horizontal axis.

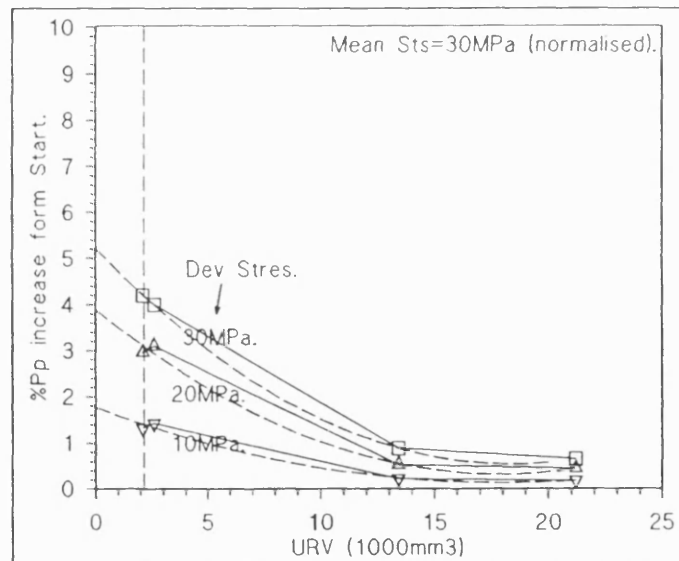


Fig. 6.2.5.c. Normalised percentage pore fluid pressure rise for a range of deviatoric stress (30, 20 & 10MPa), for different URV's, under a mean stress of 30MPa.

Fig. 6.2.5.d. shows the normalised pore fluid pressure rise data for a deviatoric stress of 15MPa and different effective mean stresses.

The two plots show the effect of deviatoric and mean stress on pore fluid pressure rise for any URV. A simple theoretical analysis is performed below to determine a functional form to fit to the data.

The change in fluid pressure is proportional to the change in fluid volume (expressed as strain), such that  $\delta P_p = \kappa_f \cdot \delta P_v$ . Where  $\kappa_f$  is the bulk modulus of fluid,  $\delta P_p$  is the change in pore fluid pressure, and  $\delta P_v$  is the change in pore volume. The bulk modulus of the fluid can be considered constant over the

range of pressures considered in this analysis. Also under the stress levels considered here the majority of pore volume change,  $\delta P_v$ , will be a consequence of a deforming rock matrix and not grain crushing, therefore  $\delta P_v$  is a function of applied effective stress ( $\delta\sigma_3'$ ), and bulk rock matrix modulus ( $\kappa$ ). Since effective stress under undrained conditions can be found from Skempton's A & B co-efficients and applied stress,

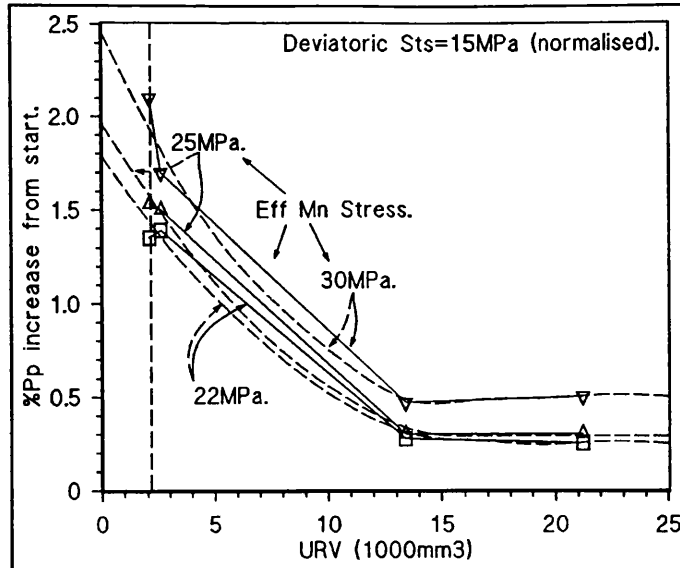


Fig. 6.2.5.d. Normalised pore fluid pressure rise data for various effective mean stress and URV's, for a deviatoric stress of 15MPa. See text for details.

$$\delta P_p = (B[\sigma_3 + A(\sigma_1 - \sigma_3)] \cdot V_r) / (K(v_0 + URV))$$

where  $V_r$  is the rock specimen volume,  $v_0$  is the initial pore volume of the rock under applied hydrostatic stress. Hence the change in pore fluid pressure as a function of URV under a more simplified stress regime of purely uniform mean stress, is,

$$\delta P_p = (K_f \cdot B \cdot \delta\sigma_3 \cdot V_r) / (K \cdot (V_0 + URV))$$

or,

$$\delta P_p = C \cdot \delta\sigma_3 / (V_0 + URV)$$

Where  $C = (B \cdot K_f \cdot V_r) / K$ . Curves of this form are fitted to all the data of a given stress condition and extrapolated to zero URV. More accurate data fitting is prevented by lack of datum points. The percentage pore fluid pressure increase from the initial starting pressure of 150MPa under a zero URV can be read from the vertical axis. These percentage pore fluid pressure increases under certain deviatoric and effective mean stress conditions map a 3-D surface on axes of effective mean stress, deviatoric stress, and percent pore fluid pressure rise.

The three dimensional plot can be visualised from the two dimensional plot (fig. 6.2.5.e.). Line A-A' maps perpendicular to line B-B', with point A' mapping directly onto point B''. A 3-D representation of the results is shown in fig. 6.2.5.f.

The plot represents the Pp rise under increasing differential axial stress separated into effective mean and deviatoric stress components. The effective mean stress data is truncated at a value of 20MPa - representing the commencement of the experiment. It can be seen how under triaxial stressing conditions the pore fluid

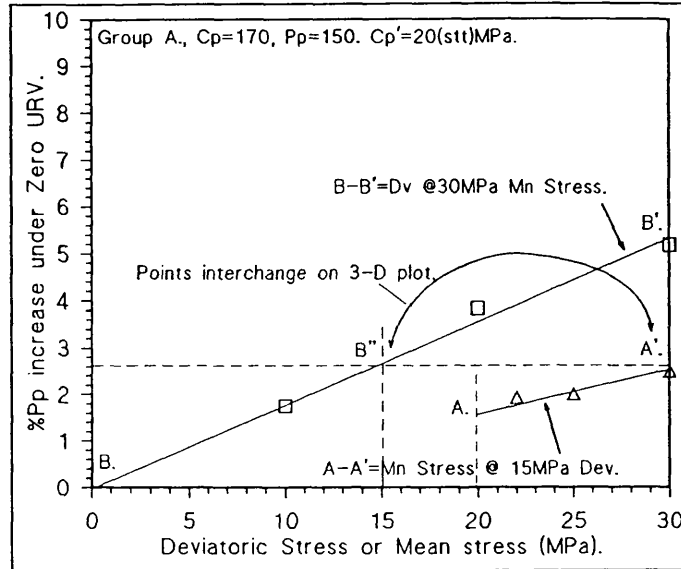


Fig. 6.2.5.e. Surface plot represented in 2-D space. Percentage increase in pore fluid pressure for increases in effective mean stress and deviatoric stress. See text.

pressure rise is more sensitive to deviatoric stress induced crack closure than to effective confining stress induced isotropic compaction. This conclusion is, of course, valid only for the initial pre-dilatant stage of deformation, afterwhich different mechanism (**New Dilatant Crack growth - NDC**), changes the Pp response markedly. The surface can be represented as;

$$\%Pp = 0.006.D_v.\sigma'_m \tag{6.2.5.a}$$

Which, in this simplified analysis shows both AA' and BB' going through the origin. In the equation, %Pp represents the percentage rise in pore fluid pressure,  $D_{v1}$  represents the axial deviatoric stress, and  $\sigma'_m$ , the effective mean stress. To calculate the compensation factor between the pore pressure rise for the minimum URV obtainable experimentally and the pore pressure rise for theoretical zero URV, a plane is plotted for actual pore fluid pressure rises under a URV of 2,100mm<sup>3</sup>, and the equation for the surface calculated.

By comparing the constants in each equation, the correction factor is obtained. Under a starting fluid pressure of 150MPa the URV correction factor is 1.286. The validity of this factor relies on the extrapolation of the data to

By comparing the constants in each equation, the correction factor is obtained. Under a starting fluid pressure of 150MPa the URV correction factor is 1.286.

The validity of this factor relies on the extrapolation of the data to zero URV in figs. 6.2.5.c. & d. A greater number of tests would provide more information for accurately extrapolating the data, and perhaps would give an improved reading for zero URV.

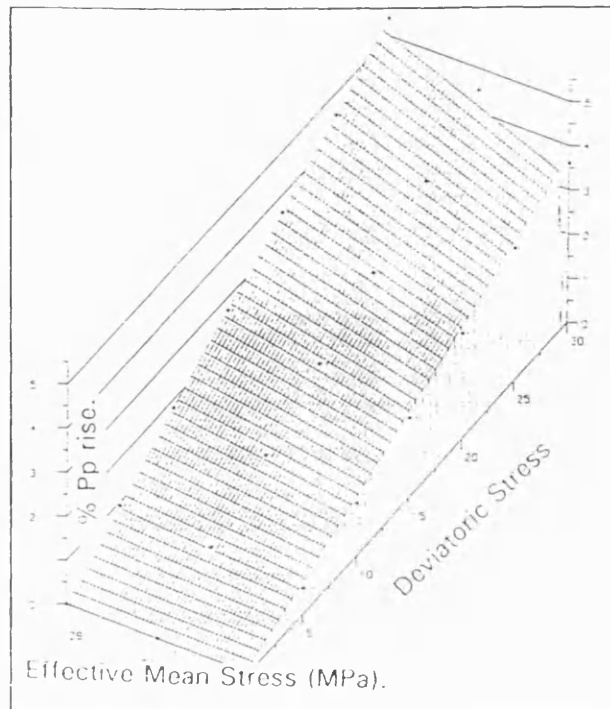


Fig. 6.2.5.f. Three dimensional representation of percentage pore fluid pressure rise for increases in deviatoric and effective means stress for experimental data group A.

To check the accuracy of the calculated surface, pore fluid pressure rises are calculated for the experiment which employed an URV of 2,100mm<sup>3</sup>, and the results are then divided by the correction factor to yield the actual pore fluid pressure rise. The results are given in fig. 6.2.5.g. It can be seen

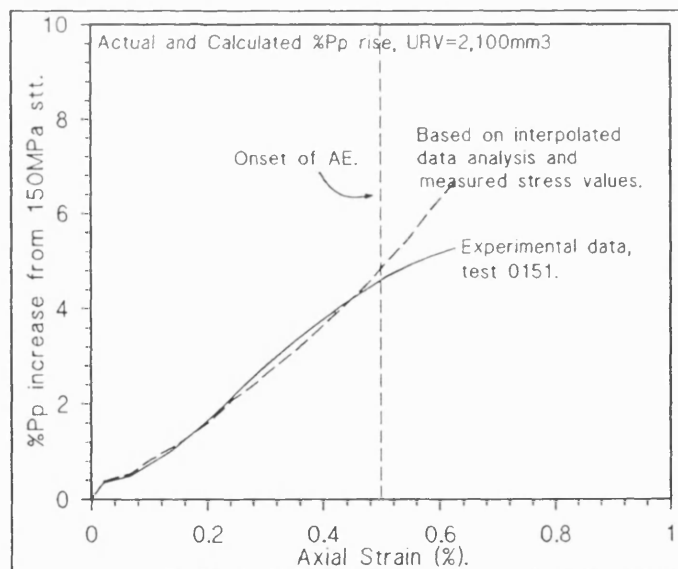


Fig. 6.2.5.g. The experimentally determined surface accurately determines pore fluid pressure rise for test 0151 within group A suite of experiments, see text.

how the results accurately predicts the pore fluid pressure rise until  $\epsilon = 0.5\%$ , beyond which new dilatant crack growth causes the pore fluid pressure curve to *roll over*, whereas the calculated curve continues in the same plane. This is expected considering the assumptions and limitations of the analysis.

*In Summary*, the method of linearly extrapolating experimental pore fluid pressure rise data for deviatoric and mean stress components of differential axial stress during the initial compaction stage of triaxial deformation can be used to determine pore fluid pressure for any given stress path under a known commencing mean stress.

## 6.2.6. Future Work.

Further work to develop this investigation essentially involves a greater number of more complicated experiments. These are highlighted below.

- ▶ Conduct triaxial experiments under *controlled deviatoric and effective mean stress* conditions. This would accurately isolate the effect of both deviatoric and mean stress on pore volume change and hence pore fluid pressure change. Improving control of these stress parameters would also provide more data points on fig. 6.2.5.e. & 6.2.5.f. This could be achieved by accurately controlling the confining pressure during triaxial deformation.
- ▶ *Greater number of URV's*. Conduct more experiments using a wider range of URV's. This would provide the extra data points on the curves in figs. 6.2.5.c. & d.
- ▶ *Investigate different effective confining pressures*. Employ different effective confining pressure conditions during triaxial experimentation, (considering the above comments), to examine the effect of different commencing effective mean stresses on the relationship established in this section. Under cataclastic flow conditions ( $C_p' > 100\text{MPa}$ ), compaction and cracking occur simultaneously during initial triaxial deformation.
- ▶ *Develop equipment* capable of removing the effect of the URV completely during undrained triaxial deformation through the use of the pore fluid intensifier, see fourth bullet point in section 6.4.4., "Future Work".

## 6.3. Pore Volume and Pressure Change as a Function of Hydrostatic Stress (Drained and Undrained).

### 6.3.1. Introduction and Review.

#### 6.3.1.1. Drained Hydrostatic Loading on Sandstone.

When a porous sedimentary rock such as Darley Dale sandstone is subjected to an increasing confining pressure under *drained* conditions a pore volume reduction occurs through compaction of the pore/grain matrix. Strain gauges connected to the surface of a specimen will measure both the bulk decrease in volume of the matrix and pore collapse & crack closure. Pore volumetry measures only pore volume reduction and so gives a more accurate picture of the changes occurring to the pore structure of the rock. This can be deduced from overall bulk strain to determine the magnitude of both contributions.

Generally compaction is non-linear. Several types of hydrostats (volumetric change against confining pressure), are shown in fig. 6.3.1.1.a. Curve (a)

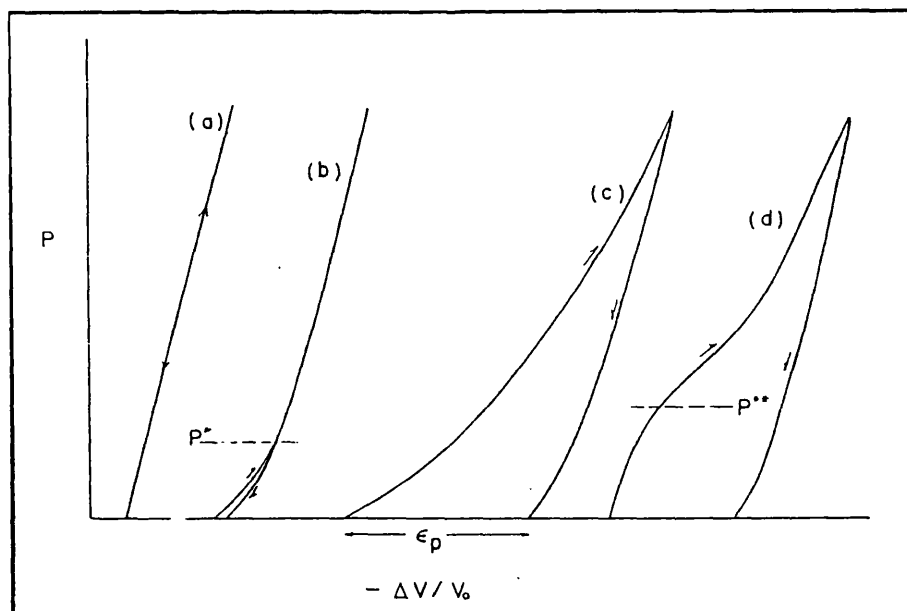


Fig. 6.3.1.1.a. Typical hydrostats for undrained hydrostatic compaction of a porous rock, (After Brace 1978).

Curve (a) shows linear elastic mineral deformation of a typical rock. Curve (b) shows the behaviour of rocks with a pore structure comprising only cracks - in this curve the cracks are initially open until point  $P^*$ , beyond which substantial crack closure occurs. Thereafter the rock deforms in a linear fashion. Upon

unloading a portion of the crack volume is recovered but some pore volume loss is permanent. Curve (c) illustrates a typical hydrostat for rocks with a varied pore structure (cracks and pore), and a porosity of  $\geq 0.05$ . The slope of the curve increases with increasing confining pressure, representing increasing resistance to pore and crack closure. Significant permanent porosity loss occurs upon unloading. Curve (d) represents the hydrostat for rocks with a pore structure comprised principally of spherical pores and porosity  $> 0.05$ . Initially the curve is linear, although after a confining pressure  $P^*$ , pore collapse occurs causing sudden pore volume reduction. After significant pore volume reduction, the slope steepens, representing increasing resistance to pore closure. Upon unloading, significant permanent pore volume reduction is seen, (Brace 1978).

Zhang et al. (1990) investigated the hydrostats of a number of different sandstones. They found the inflection points in the hydrostats coincided with pore collapse. This was confirmed from optical microscope observations of specimen sections. The mechanism for pore collapse was found to be *Hertzian cracking* at the grain

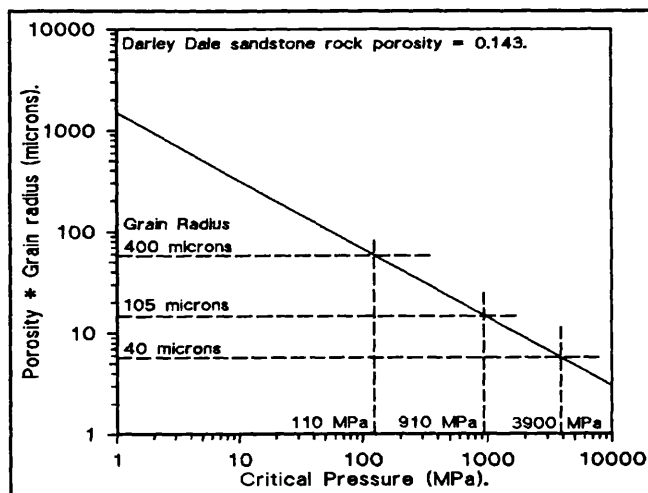


Fig. 6.3.1.1.b. Relationship between product of porosity & grain size, and critical grain crushing pressure, (After Zhang et al. 1990).

contacts. The *critical pressure* was examined with respect to porosity ( $\phi$ ), and a factor  $\alpha$  which equals  $c/R$  (initial crack length at grain contacts ( $c$ ) divided by grain radius ( $R$ )). Using the Hertzian model, the above data, and parameters measured in the laboratory ( $E, K_{IC}$ ), the critical pressure at which grain crushing occurs ( $P_{CR}$ ) was obtained. The ratio  $\alpha$  is assumed constant for a given mineral crystal of all grain sizes. The study found that given this assumption for  $\alpha$ ,  $P_{CR}$  varied inversely with the product of grain size & porosity (fig.6.3.1.1.b.). The lack of a sudden porosity reduction with depth in the field is explained by time dependent chemical action of water on rock causing gradual porosity reduction with burial, (see sections 2.4.3.4. & 2.5.6.), and

pressure dissolution and re-precipitation causes the *rounding* of grains, thus reducing contact pressure and increasing  $P_{CR}$  beyond the lithostatic pressure at a given crustal depth.

### 6.3.1.2. Undrained Hydrostatic Loading on Sandstone.

Fluid pressure increases measured under undrained conditions have been studied theoretically by a number of workers (section 2.3). Experimentally, Green and Wang (1986) measured the  $P_p$  increase for a number of different sandstones, subsequently experimentally obtaining Skempton's  $B$  co-efficient. These results were compared against values of the  $B$  co-efficient calculated from published values for  $K_f$ ,  $K$ ,  $K_u$ , (see glossary).

Experimentally Green and Wang's apparatus differed from the equipment used in this study by the volume of extra fluid necessary to connect the rock specimen to the pressure transducer, the *Upstream Reservoir Volume*, (URV). Green and Wang, and before them Dropek et al. (1978), connected the transducer directly to the end-cap, therefore, in the case of Dropek et al., limiting the URV to 0.002x specimen pore volume. This measures the fluid pressure rise more directly. Larger URV's require a correction factor for the measurement of the  $B$  co-efficient. The results obtained from various studies are given in table 6.3.1.2.a. below.

Effective $C_p$ (MPa)	$B$ (Bruhn '72)	$B$ (Mesri '76)	$B$ (expm'l) (Green & Wang '86)	$B$ (calc)
0.0	0.82	1.00	0.99	0.99
0.9	0.74	0.90	0.95	0.90
2.0	0.68	0.76	0.87	0.85

Table 6.3.1.2.a.

The high values of  $B$  obtained for these rocks are a direct result of the high drained compressibility characteristics of sandstone. The variability noted

above is assumed to be partly due to the URV compensation inaccuracies and to sample variability. The departure of B from unity at low effective confining pressures (0.9MPa) is concerned with the initial closure of compliant voids of low aspect ratio (mainly long thin cracks). Thereafter further compression (and therefore Pore fluid pressure rise), requires greater effective confining pressure. Sample variability (affecting the validity of published bulk moduli data) is considered to be the cause for the small difference between theoretical and experimental derived results for Green and Wang's study shown in the table.

Dropek et al. (1978), conducted a series of experiments to examine, among other parameters, (i) the compressibility of fully saturated samples, (ii) Skempton's B co-efficient, and (iii) the volume strain at which pore pressure begins to build up in partially saturated samples. A B co-efficient of 0.58-0.67 was measured and compared against a value of 0.55 calculated from measured bulk moduli ( $K$ ,  $K_s$ ,  $K_v$ ). The discrepancy was attributed to the assumption of ideal linearly elastic behaviour of rock and fluid in the formulation of B (see eq. 6.3.4.1.a. below). Concerning the pore volume at which pore pressure began to rise for different rock saturation levels (85%, 90% etc.), a linear relationship between bulk strain minus matrix strain ( $\epsilon_{kk} - \sigma_{kk}/K_s$ , i.e. pore strain) and rock saturation (the point at which full saturation occurs) was established. At confining pressures beyond that required for full rock saturation, pore fluid pressure increased initially with a positive curvature and thereafter in a linear fashion. From this the B co-efficient could be determined. The work illustrates that experimental measurement of the B co-efficient compares well with calculated data.

Work on the hydrostatic compaction of Darley Dale sandstone is reported by Jones (1989). P- and S- wave velocity data recorded during compaction indicates an initial increase in  $V_p$  from 2.5km/s to 4.5km/s within the first 50MPa confining pressure increase. Thereafter the rate of  $V_p$  increase slows consistently, rising from 4.5km/s to 5.25km/s only over a  $C_p$  increase from 50MPa to 400MPa. This indicates marked crack closure initially followed by a more gradual closure of cracks and other suitably orientated voids. The lack of inflection point in the  $V_p/C_p$  curve indicates probably no pore collapse during

hydrostatic stressing up to 400MPa. The affect of temperature on deformation has not been reported. However, consisting largely of quartz, Darley Dale sandstone may be vulnerable to stress corrosion cracking under elevated temperature and fluid pressure.

### 6.3.1.3. Microgranodiorite.

To the author's knowledge there is little work on pore volume changes measured under increasing confining pressure for this rock. General behaviour of the rock and experimental data is reported in section 6.1.3.2.

### 6.3.2. Programme of Experiments.

The experiments are broadly divided into four groups, table 6.3.2.a shows information on the experiments and the starting stress conditions (*pre-test* confining pressure - section 5.2.4.4. & 6.3.3.1. - pore fluid pressure, and confining pressure, at commencement of experiment).

Test	Rock	Dr/Udd	Pre-test Cp	Start Pp	Start Cp	Start Cp	Peak Cp	Cyclic Low
			MPa	MPa	MPa	MP/min.	MPa	MPa
0071	DDSS	Udd	30	20	30	2.5	326	-
0073	DDSS	Udd	30	20	30	2.5	327	-
0075	DDSS	Udd	30	20	30	2.5	330	-
0083	DDSS	Udd	30	20	30	2.5	332	75
0085	DDSS	Udd	30	20	30	2.5	327	61
0060	DDSS	Dmd	27	20	24	10	130	24
							334	24
							456	24
0065	DDSS	Dmd	30	20	23	10	73	23
							125	23
							174	23
							225	24
							326	24
							326	-
0067	DDSS	Dmd	29	20	23	10	123	24
							122	24
							122	23
							123	23
							123	23
							120	23
0080	DDSS	Dmd	30	20	23	2.5	487	24
							332	-
0166	Micro.G.	Dmd	30	21	24	2.5	235	36
0185	Micro.G.	Dmd	30	20	23	5	441	23
0077	steel	Dmd	30	20	23	2.5	222	23
0078	steel	Dmd	15	10	13	2.5	210	13
0079	steel	Dmd	30	10	13	2.5	211	13

Table 6.3.2.a. Details of experimental programme investigating pore fluid pressure and volume change with increasing confining pressure.

Tests 0071, 0073, 0075, 0083 and 0085 are *undrained* tests on Darley Dale sandstone. The range of tests allows Skempton's B co-efficient to be examined.

Tests 0060, 0065, 0067, and 0080 are *drained* experiments on Darley Dale sandstone. The variety of experiments conducted here examine the affect of stressing rate on pore volume reduction, of cycling the same confining pressure repeatedly (0067), and of steadily increasing the cyclical confining pressure (0060 and 0067). The range of tests allow elastic pore volume reduction, (recoverable), permanent pore volume reduction, (irrecoverable), total pore volume reduction, and the rate of pore volume reduction, with confining pressure increase at a given confining pressure, to be examined.

Tests 0166 and 0185 are *drained* tests on microgranodiorite. The two tests examine the affect of stressing rate and maximum confining pressure on compaction, and the elastic and permanent components of compaction.

Tests 0077, 0078 and 0079 are drained tests on steel specimens up to confining pressures of  $\approx 220\text{MPa}$ . Their purpose is to examine pore volume reduction due to fluid trapped between the specimen and the copper jacket. The three tests examine the affect of the *pre-test* confining pressure and pore fluid pressure adopted on pore volume loss at various confining pressures.

### 6.3.3. Results and Discussion.

#### 6.3.3.1. Steel Specimens - Calibration Experiments.

The question of the URV and its effect on total pore fluid pressure change has been discussed in section 6.2. for undrained triaxial deformation. The amount of fluid in the sample, tubing, transducers, and between the specimen and jacket has been found to be important with respect to pore fluid pressure change. Many of these volumes can easily be quantified. To quantify the volume of the pore fluid between the jacket and the specimen, and specimen

and the rams, however, a series of calibrations experiments were required on steel samples (zero porosity) under drained conditions.

The results are presented in fig 6.3.3.1.a. Three tests were conducted to establish the affect of the *pre-test* confining pressure and the effective pressure on pore fluid expelled from the jacket/sample space. The graph shows the results of test numbers 0077, 0078 and 0079. It must be noted that a

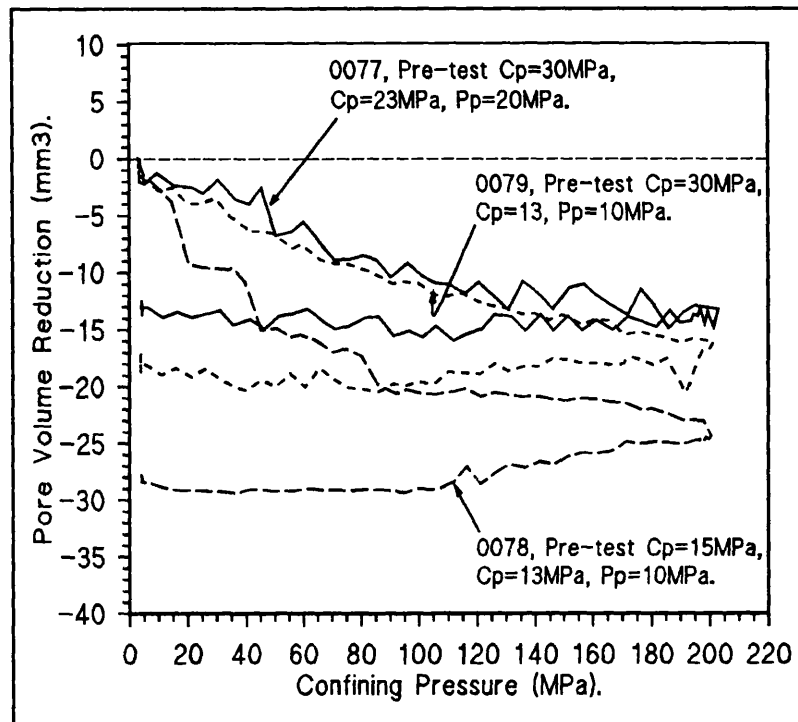


Fig. 6.3.3.1.a. Results of calibration tests on steel specimens to establish volume of fluid between jacket and specimen and experimental starting procedure.

measured fluid volume of  $5\text{mm}^3$  requires movement of 0.2mm of the intensifier piston. This level of accuracy required by the equipment explains the unsteady curve seen in the figure. It can be seen from results 0077 and 0078 that the different confining pressures used (constant effective confining pressures) has no appreciable affect on the total fluid volume expelled or the rate of expulsion. It can be seen that 70% of total fluid expulsion occurs within the first 100MPa, and no recovery is observed upon unloading.

Test 0078 shows the effect of a lower pre-test confining pressure - total pore fluid expelled equals  $25\text{mm}^3$ . Again,  $\approx 80\%$  of this fluid is expelled within the first 100MPa, and upon unloading some fluctuation of the curve, but no recovery, is observed.

Clearly, the higher the pre-test confining pressure, the more *trapped fluid* is expelled prior to the test. This suggests that before experimentation a high confining pressure should be applied just to compact the jacket onto the

sample. In doing this, however, the question of the closure of microcracks in the rock under this initial *pre-test* confining pressure must be considered. This crack volume is impossible to quantify using the present equipment. In setting the starting stress conditions the criteria are, (i) a minimum pore fluid pressure required for reliable pore pressure/volume measurements ( $\approx 10\text{MPa}$ ), and, (ii) a minimum effective confining pressure is required for jacket integrity, ( $\approx 3\text{MPa}$  - double the pore fluid and confining pressure transducer accuracies of  $\approx 1.75\text{MPa}$ ). Adopting  $C_p = 13\text{MPa}$  and  $P_p = 10\text{MPa}$  satisfies these conditions, although fig. 6.3.3.1.a. shows that  $23\text{mm}^3$  of fluid remains between the jacket and the sample when a pre-test confining pressure of  $C_p = 15\text{MPa}$  is adopted. This value is rather high, and it was decided, in order to ensure minimum trapped fluid *and* reliable pore fluid volume/pressure readings, a pre-test confining pressure of  $30\text{MPa}$ , an initial pore fluid pressure  $20\text{MPa}$ , and an initial confining pressure of  $23\text{MPa}$  should be applied at the commencement of a test, see section 5.2.4.4. for the final experimental procedure adopted. Known jacket/sample pore volumes are used to correct all pore volume data.

### 6.3.3.2. Microgranodiorite - Drained Experiments.

Two drained tests (0166 and 0185) were executed on samples of this rock (porosities - 2.0% and 0.9%), at a stressing rate of  $2.5\text{MPa}/\text{min}$ . The results (fig. 6.3.3.2.a.), are corrected for jacket fluid volume loss as per section 6.3.3.1. The two specimens

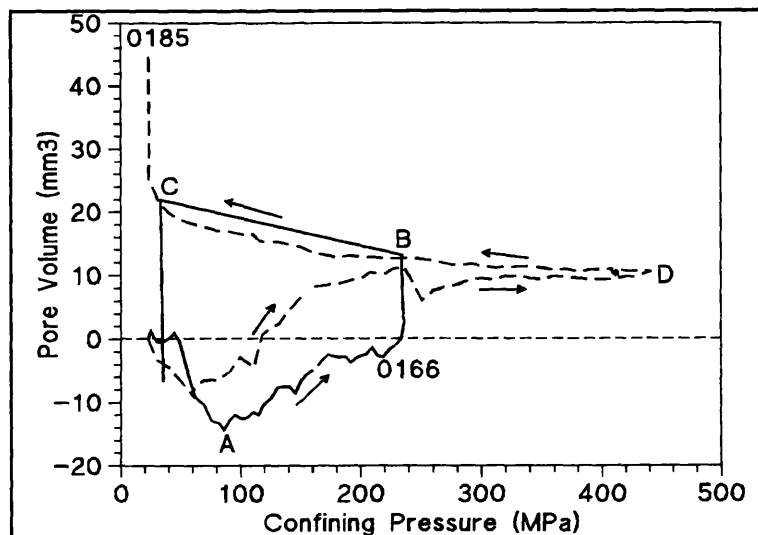


Fig. 6.3.3.2.a. Results of hydrostatic compaction tests on two specimens of Penmaenmawr microgranodiorite. See text.

behaved in a qualitatively similar manner. Experiment 0166 (solid line -  $\phi = 2.0\%$ ) shows compaction of 10% of pore volume up to a confining pressure of  $90\text{MPa}$  (point A), considered due to crack closure. Thereafter, (from  $90\text{MPa}$

to 230MPa), a pore volume increase of  $15\text{mm}^3$  occurs probably due to grain rearrangement. At  $C_p = 230\text{MPa}$  the confining pressure was held constant for thirty minutes during which time water was drawn into the specimen. This might be due to lower permeability at higher confining pressures. It is felt that if the stressing rate were reduced, the rock would have displayed more steady dilatant behaviour, represented by a straight line from point A to point B on the graph. The total dilation at point B exceeds initial pore volume by 10% - equal to  $15\text{mm}^3$ . Unfortunately, the experiment was terminated at this point - at the time the author felt the experiment had been unsuccessful. The confining pressure was released from point B to point C over one minute, which, in fact yielded some interesting results. Initially fluid was drawn into the specimen - as may be expected. During the subsequent few minutes at a confining pressure of 20MPa, fluid was expelled. It is thought that initially the rapid drop of confining pressure caused crack closure and fluid expulsion at the upper end of the specimen where the pore fluid access *hp* tube is located. Internally pore fluid pressure remained high due to poor permeability restricting the fluid escape paths. Over the subsequent two minutes (at point C) high pressure inside the specimen then expelled fluid to yield a final pore fluid volume very close to the initial value. An alternative conclusion concerns the high internal pore fluid pressure causing a breach of the copper jacket and a gradual inflow of  $\text{N}_2$  fluid from the vessel to the sample after point C.

Experiment 0185 (dashed line -  $\phi = 0.9\%$ ), similarly displays initial compaction of  $\approx 10\%$  of pore volume ( $10\text{mm}^3$ ) up to 60MPa, and thereafter fluid intake up to 220MPa, resulting in an absolute intake value of  $22\text{mm}^3$ , at point B. This is similar to test 0166 and again is thought to be the consequence of grain rearrangement, associated cracking and pore volume development. Increasing the confining pressure further from 230MPa to 450MPa (B→D) causes no further appreciable pore volume change. The confining pressure was held constant at 450MPa for 50mins, during which time no pore fluid flow was detected confirming no compaction or dilation from point B to point D. The spike at point B is unexplained at this stage; representing a piston movement of only 0.1mm it could possibly be electrical interference.

Upon unloading at a rate of 2.5MPa/min, sample 0185 behaved similarly to test 0166; fluid being drawn in as elastically closed cracks re-open. At point C, the confining pressure was held constant for a number of minutes and pore fluid was further drawn into the sample. This can be explained by low permeability impeding the intake of fluid initially, and the final pore fluid volume datum representing actual porosity at the end of the experiment. This result reinforces the ruptured jacket theory for experiment 0166 which showed pore volume reduction during the same period.

*In summary*, the similarities of the two sets of results are clear. Ten percent compaction by  $\approx 80\text{MPa}$ , ( $15\text{mm}^3$  and  $9\text{mm}^3$  in the two results of different porosity - 2.0% and 0.9%), and fluid inflow after an increase in confining pressure to 220MPa. Compaction induced microcracking in the rock is thought to induce an increase in permeability sufficiently to allow the flow of fluid into pre-existing rock pore volume. The final pore volume recorded reflects this permanent increase in permeability.

#### 6.3.3.3. Darley Dale Sandstone - Drained Experiments.

Fig. 6.3.3.3.a. and 6.3.3.3.b. display the hydrostats of four experiments. All tests were conducted at the same stressing rate of 10MPa/min, except test 0080 which was conducted at 2.5MPa/min.

The different stressing rate seemed to have little effect on the shape of the hydrostat, probably due to the high porosity and permeability of the sandstone which permits adequate fluid flow even at relatively high stressing rates.

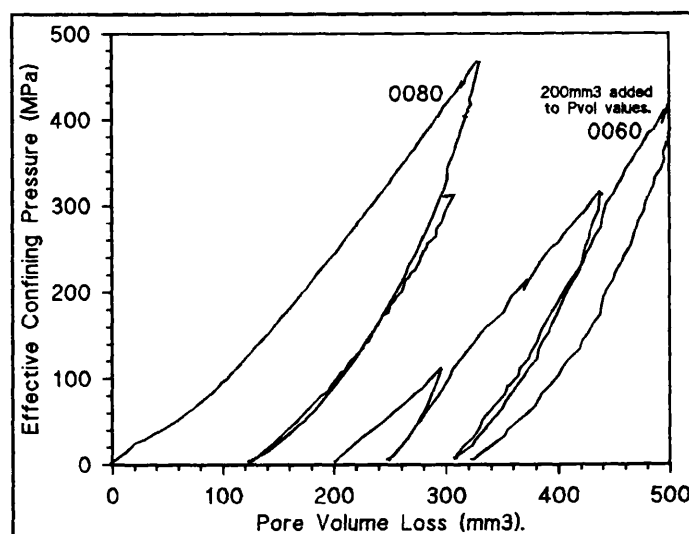


Fig. 6.3.3.3.a. Results of two drained hydrostatic compaction experiments (0060 & 0080), see text.

A smooth positively concave line displaying no inflection point within the range of 0-450MPa is found for each sample.

Acoustic emission results, although not displayed on the figures for clarity, were recorded for many of these tests and similar repeat tests. Fig 6.3.3.3.c. shows the peaks in AE for different confining pressures for all the tests. The lack of definite AE peak from all AE data at any confining pressure, and the smooth

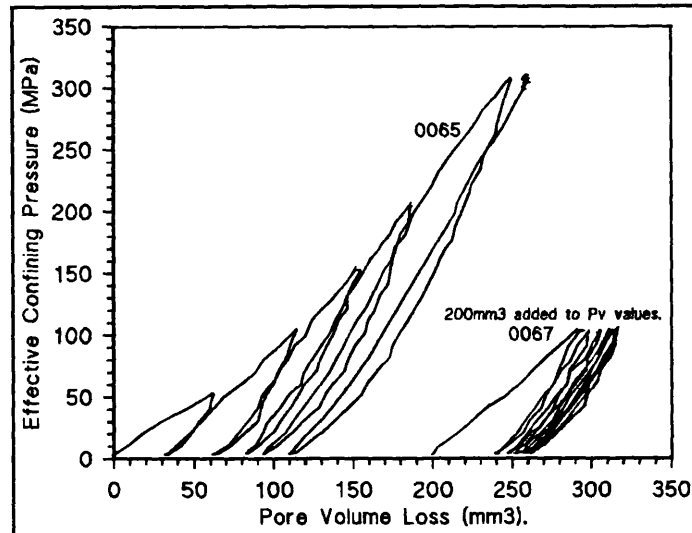


Fig. 6.3.3.3.b. Results of two drained hydrostatic compaction experiments, (0065 & 0067), see text.

curved of the hydrostat verify the lack of a definite critical crushing pressure, and support the notion of continual crushing of different grain sizes at different critical pressures.

This is expected from grain radii data indicating various grain sizes. (further details in section 6.3.4.). Upon unloading a portion of the pore volume loss is recovered (elastic deformation) and a portion is not recovered, (permanent deformation), this is clearly visible from the hydrostats.

For each experiment the

confining pressure was cycled to a different confining pressure in each test. Subsequently reloading the samples caused the hydrostat to retrace the unloading path until the previous maximum is exceeded, after which the original *loading* hydrostat curve is extended.

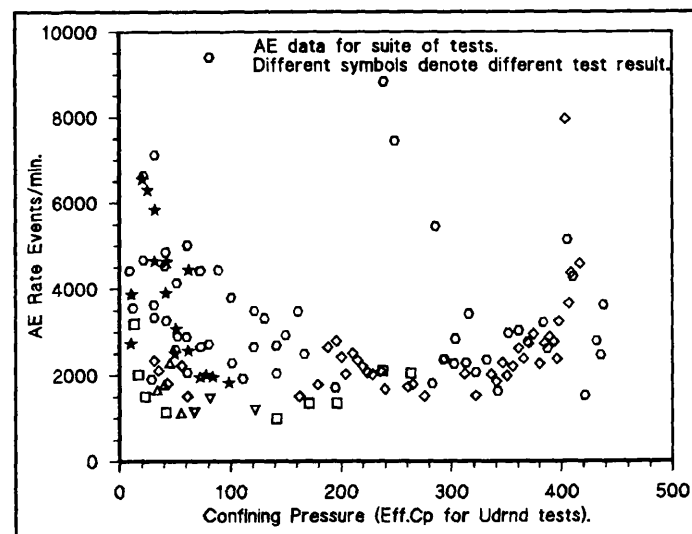


Fig. 6.3.3.3.c. Acoustic emission peaks for whole suite of hydrostatic compaction experiments. No clear peak is seen, see text.

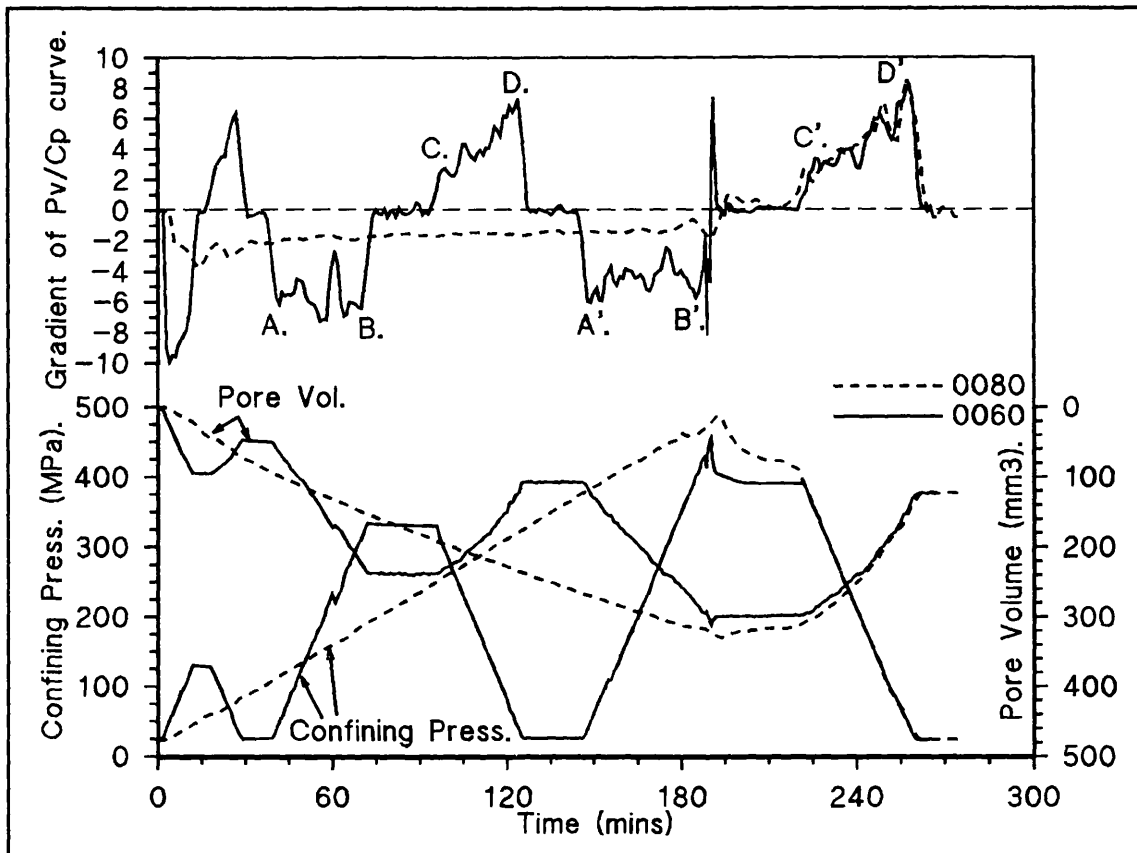


Fig. 6.3.3.3.d. Results of experiments 0060 & 0080 examined with respect to the changing P<sub>v</sub>/C<sub>p</sub> gradient during stress cycling.

Figures 6.3.3.3.d. and 6.3.3.3.e. show the same four tests results as fig.'s 6.3.3.3.a. & b. in a different form. Each figure represents the results of two experiments.

The lower curve shows confining pressure against time. The middle curve shows pore fluid volume change against time. The uppermost curve is the gradient of the pore volume/time ( $P_v/C_p$ ) curve. The solid curves and the dashed curves represent different experiments. It can clearly be seen from fig 6.3.3.3.d. that the  $P_v/C_p$  gradient varies with confining pressure during the unloading cycle ( $C \rightarrow D$ , and  $C' \rightarrow D'$ ) - increasing as confining pressure decreases, whereas the gradient is constant during loading ( $A \rightarrow B$ , and  $A' \rightarrow B'$ ).

This is evident from the three cycles of test 0060, and for the one cycle of test 0080. This varying gradient is also visible from the curved unloading pore fluid volume/time curve for both tests. Fig. 6.3.3.3.e. shows results of tests 0065 & 0067. The  $P_v/C_p$  gradient curves in these figures show an inflection plateau on the unloading cycles, ( $A \rightarrow B$ ,  $A' \rightarrow B'$ ). During unloading, the gradient initially increases, stabilising after  $\approx 20$ MPa of unloading at  $\approx +4$  (point A), and after a further reduction in confining pressure of  $\approx 100$ MPa the gradient then

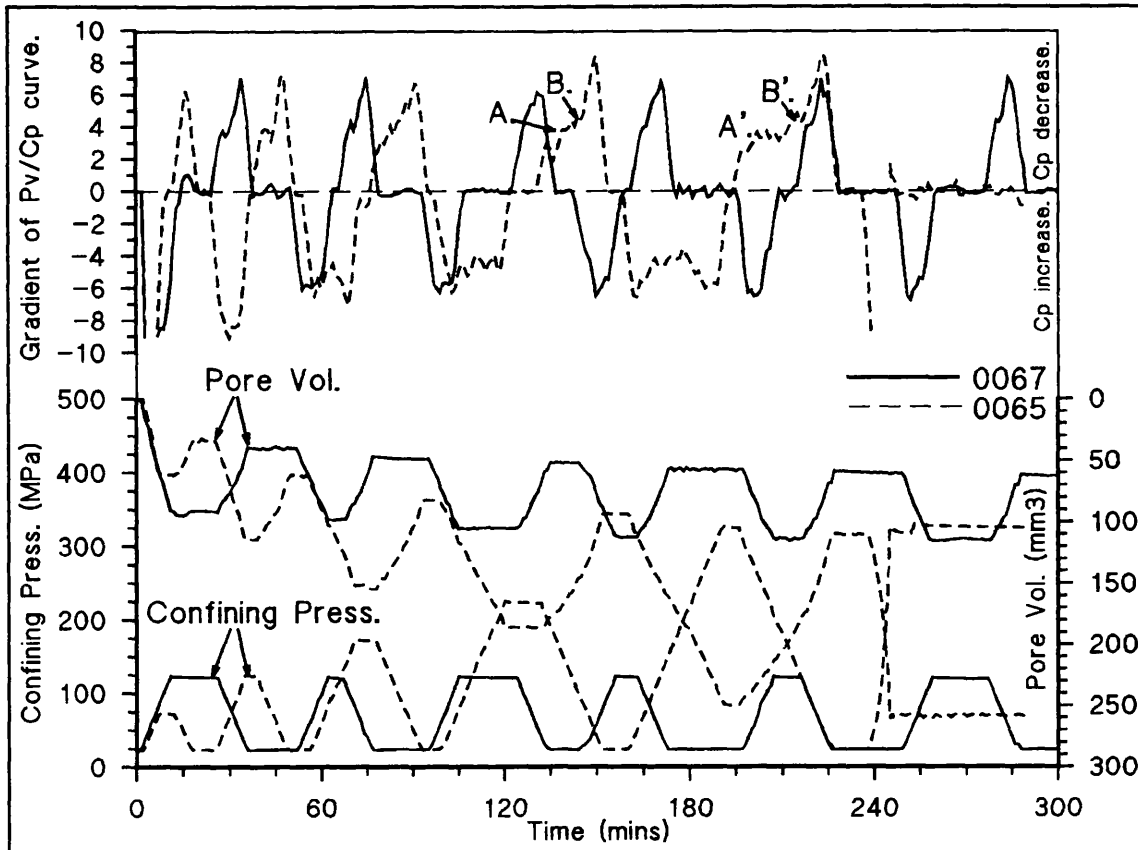


Fig. 6.3.3.3.e. Results of experiments 0065 & 0067 examined with respect to the changing Pvol/Cp gradient during stress cycling.

increases from  $\approx +4$  to  $\approx +7$  (point B). The relationship between permeability and confining pressure explains this phenomenon, (section 2.7.2.4.).

As confining pressure is reduced during unloading, low permeability initially resists fluid outflow. The effective confining pressure in the centre of the sample increases, and after a reduction of  $\approx 100\text{MPa}$  confining pressure, permeability increases sufficiently to allow the escape of trapped pore fluids from the specimen, thus the Pvol/time gradient increases.

The reason that the same effect is not seen in the other two experiments is unknown.

The amount of elastic, permanent, and total, pore volume reduction for all tests is plotted against effective confining pressure in fig. 6.3.4.2.b. on page 209. Where a number of results at a similar effective confining pressure is shown the possible error of the results is indicated, i.e. at  $100\text{MPa}$ . A polynomial best fit line is fitted to the results.

*In Summary*, drained hydrostatic compaction experiments show a smooth curve up to 450MPa indicating no sudden crack closure or pore collapse, fig. 6.3.4.2.b. It is proposed that either sudden pore collapse would occur at a greater effective confining pressure, or that continual pore collapse of different sized pores is occurring continually throughout the increase in confining pressure. When corrected for fluid trapped between jacket and sample, total, elastic, and inelastic deformation of the rock is obtained for any confining pressure. Changes in permeability due to elevated confining pressure initially decreases fluid outflow during unloading. This data is used in subsequent analysis, section 6.3.4., 6.4.3.2.

#### 6.3.3.4. Darley Dale Sandstone - Undrained Experiments.

The results of four undrained hydrostatic experiments are shown in fig. 6.3.3.4.a. For experiments 0083 and 0085, the unloading curve was traced and the experiment stopped as the pore pressure approached confining pressure to prevent the inside of the vessel from fluid contamination. It can be seen that the gradient of the unloading curve varies with confining pressure in a similar fashion to the drained results.

The hysteresis in the loading/unloading behaviour concerns mechanisms of purely elastic crack closure (recoverable) and inelastic crack closure (requiring a further input of energy to re-open cracks). The permanent pore fluid pressure remaining in the sample at the termination of

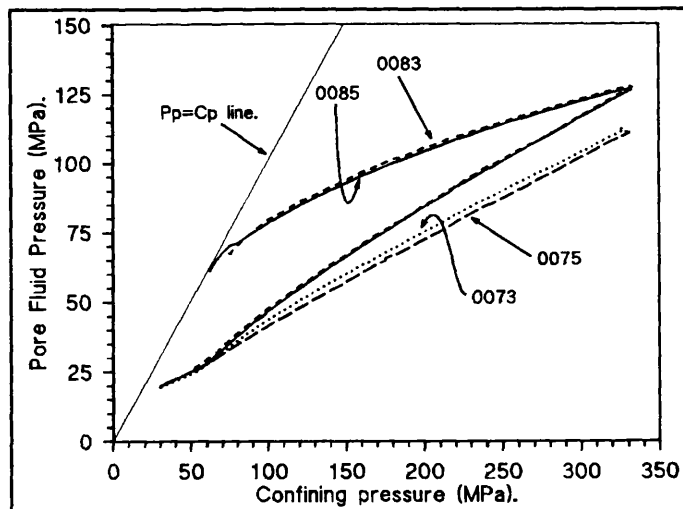


Fig. 6.3.3.4.a. Results of undrained hydrostatic compaction experiments, see text.

the experiment is indicative of the permanent pore volume loss - similarly experienced in the drained results. The apparent variability of the results is thought to be a function of the variability of the rock; different grain sizes suffer deformation at different confining pressures due to differences in grain

contact stress concentrations, and hence the  $P_p/C_p$  curve varies accordingly with specimen variability.

*In Summary*, undrained hydrostatic compression experiments on Darley Dale sandstone reveal a permanent and elastic component of pore volume reduction. This is manifested elevated pore pressure during unloading relative to loading. Sample variability affects these results significantly. The data is used below to calculate Skempton's B coefficient for rock and for further pore-elastic analysis.

#### 6.3.4. Darley Dale Sandstone - Analysis.

##### 6.3.4.1. Consideration of Skempton's "B" Co-efficient for Undrained Hydrostatic Deformation.

Analysis of the undrained hydrostatic compaction data presented in section 6.3.3.4., using established linear poro-elasticity, can yield Skempton's B coefficient of the rock as it varies throughout hydrostatic stressing, (see section 2.3.2.). Following the establishment of the B co-efficient and the correction factor applied to experimentally observed values of the B co-efficient ( $B_{obs.}$ ), to account for the compressibility of the fluid in the URV, more detailed poro-elastic analysis of deformation can be attempted. A prediction of pore volume loss due to elastic and permanent compaction mechanisms under drained hydrostatic stress conditions is possible and attempted here. Accurate values for the bulk moduli of the rock (of the solid component of the rock -  $K_s$ , of the rock as a whole -  $K$ , and of the rock and pressurised fluid phase together under undrained condition -  $K_u$ ), along with rock porosity ( $\phi$ ), and pore fluid bulk modulus ( $K_f$ ), are required for this analysis.

Fig 6.3.4.1.a. illustrates the B co-efficient calculated for the four undrained tests of section 6.3.3.4., and the average values of these tests for a confining pressure between 45MPa and 330MPa is shown in a bold solid line. If the irregularity of the curves is overlooked at this stage, the trend of the B co-

efficient is seen to rise initially from a starting value of  $\approx 0.25$  at a confining pressure of  $\approx 50\text{MPa}$ , to  $\approx 0.425$  at  $75\text{MPa}$ , thereafter steadily decreasing (at a decreasing rate) to a stable value of  $\approx 0.3$  from  $250\text{MPa}$  onwards. This variation in the B

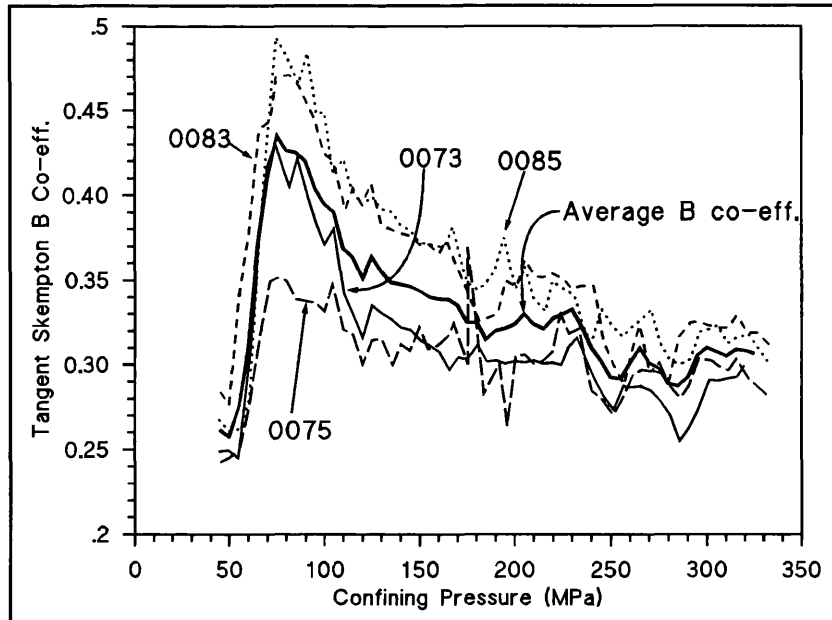


Fig. 6.3.4.1.a. Tangential Skempton B co-efficients for all four undrained hydrostatic compaction experiments. Average (unsmoothed) curve shown in bold, see text.

co-efficient is thought to be caused by two processes, (i) the initial peak in B coefficient is due to the closure of suitably orientated open fluid filled cracks, and (ii) the subsequent fall in B co-efficient starting at  $60\text{MPa}$  is due to the siliceous cementing material of the sandstone deforming (allowing some pore volume reduction), bringing the stiffer quartz grains (which makes up 85% of the rock), into contact, resisting further pore volume reduction and causing the B co-efficient to level off at 0.3. At confining pressures  $>150\text{MPa}$ , as the bulk modulus of the rock rises and pore volume reduction decreases for a given increase in confining pressure, the B co-efficient decreases. The large variability of the B co-efficient results (specimen variability) is discussed in section 6.3.3.4.

Whilst the trend of the B coefficient elucidates much about the behaviour of the rock under the effect of an increasing confining pressure, the absolute B co-efficient values are unrepresentative of true rock behaviour due to the addition of a compressible fluid volume and *hp* tubing system - the URV.

Bishop (1973) formulated an equation for the theoretical B co-efficient in a porous medium which included a term for the bulk modulus of the solid material of the rock ( $\kappa_s$ ). Until this time this  $\kappa_s$  had not been included in the

derivation of theoretical values for B, and soil and rock particles were considered incompressible for Skempton's B co-efficient analysis. The importance of the compressibility of the soil grains could not be ignored, especially as  $\kappa$  approached  $\kappa_s$  under increasing confining pressure. The equation thus derived is;

$$\text{Skempton's B Co-eff.} = 1/[1 + \phi \cdot ((C_w - C_s)/(C - C_s))] \quad (6.3.4.1.a)$$

Where  $C_w$  = compressibility of water ( $=1/\kappa_f$ ),  $C_s$  = compressibility of the solid component of the rock (grains), ( $=1/\kappa_s$ ),  $C$  = the bulk compressibility of the rock ( $=1/\kappa$ ), and  $\phi$  = porosity. Note; compressibility and bulk modulus are interchangeable - compressibility being the reciprocal of bulk modulus. The equation requires precise determination of rock and fluid compressibilities.

### Determination of Bulk Compressibilities of Darley Dale Sandstone, and of the Pore Fluid (Water).

**The compressibility of water**, ( $C_w = 1/\kappa_f$ ), is a non-linear function of fluid pressure and obtained from steam tables for any pore fluid pressure, (fig 4.4.3.2.a.). In this analysis it is calculated for different confining pressures during determination of the B co-efficient. The value of  $\kappa_f$  for water at zero confining pressure and 20°C is  $\approx 2200\text{MPa}$  at  $C_p' = 100\text{MPa}$ , rising to  $2500\text{MPa}$  at  $400\text{MPa}$ . For the calculation following a value of **2500MPa** is taken since the fluid is under pressure.

**The compressibility of the bulk rock**, ( $C = 1/\kappa$ ) is obtained from either  $v_p$  &  $v_s$  data - yielding the *dynamic* bulk modulus - or from the drained hydrostatic compaction data on Darley Dale sandstone given in section 6.3.3.3., giving the *static* bulk modulus. Both these methods are considered here and the value of  $\kappa$  determined from each compared.

(i)  *$v_p$  and  $v_s$  determination of  $\kappa$* . Fig 6.3.4.1.b. shows  $v_s$  and  $v_p$  data (supplied by P. Sammonds), from dry hydrostatic compaction experiments on Darley Dale sandstone. The curve fitted to the data is based on the *bed of nails model* of Carlson and Ganghi (1985). The model assumes that  $v_p$  is a

function of the changing elastic modulus of the rock, and of the changing rock density. These in turn are functions of confining pressure. Furthermore, the elastic modulus of the rock is a weighted composite function of the elastic modulus of the grains (a constant) and the elastic modulus of the cracked

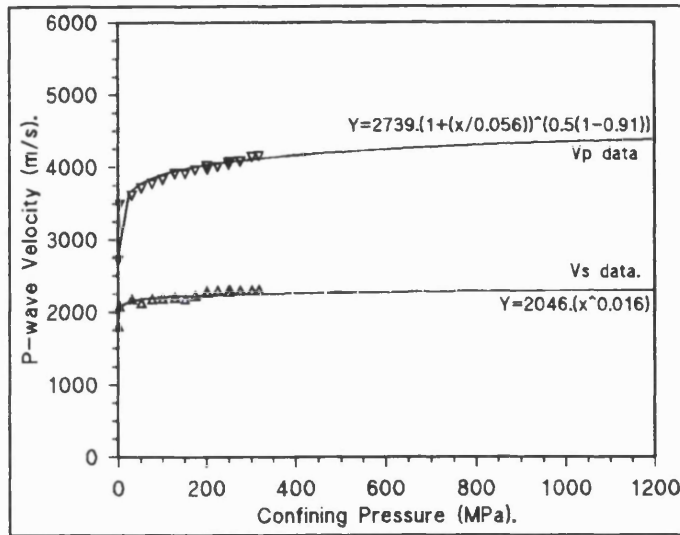


Fig. 6.3.4.1.b. Vp and Vs data for dry Darley Dale sandstone for the determination of the *dynamic* bulk modulus, (supplied by P. Sammonds).

solid, (a function of confining pressure). The variation of Vp therefore is dependent upon the variation of the elastic modulus of the cracked rock/pore system with confining pressure.

Considering crack surfaces to be made up of nails of different length as per fig 6.3.4.1.c., with each nail having a spring constant. As the crack closes more nails come into contact and the system stiffness increases. The variation of Vp with Cp under increasing hydrostatic pressure is then found to satisfy the relation;

$$V_p = V_0 \cdot (1 + (C_p/P_0))^{((1-m)/2)} \tag{6.3.4.1.b.}$$

Where  $V_0$  is the initial P-wave velocity at zero confining pressure, and "m" is a constant relating to the shape of the cracks. A high "m" value indicates narrow cracks with few large asperities which close easily causing a rapid

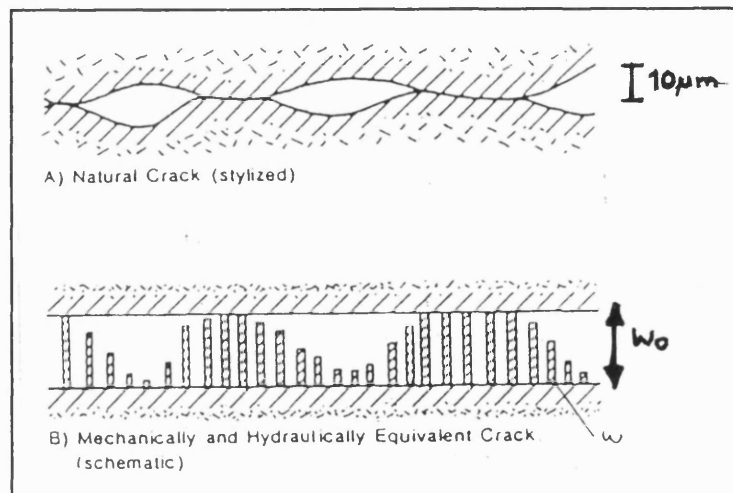


Fig. 6.3.4.1.c. Stylised natural crack and *bed of nails* model. (After Carlson and Gangi 1985).

initial rise in  $V_p$ , and a low "m" value indicates rounded rough walled pores that close with greater resistance and cause a smaller initial rise in  $V_p$  with an increasing confining pressure. The constant  $P_0$  relates to initial crack contact and possibly physically describes the degree of crack cementing (Jones 1989), or crack sealing. The above relationship is fitted to the  $V_p$  data in fig 6.3.4.1.b.,  $V_s$  is a power-law fit. The data is used to calculate  $K$  (the dynamic bulk modulus) of Darley Dale sandstone at any confining pressure using the equation.

$$K = \phi \cdot (V_p^2 - (4/3) \cdot V_s^2) \quad (6.3.4.1.c.)$$

This method yields a value of 9800MPa for  $K$  at zero confining pressure (fig. 6.3.4.1.d. - top curve), increasing rapidly under the influence of an increasing confining pressure as expected from the closure of favourably orientated microcracks and the bedding in of the ram/specimen system.

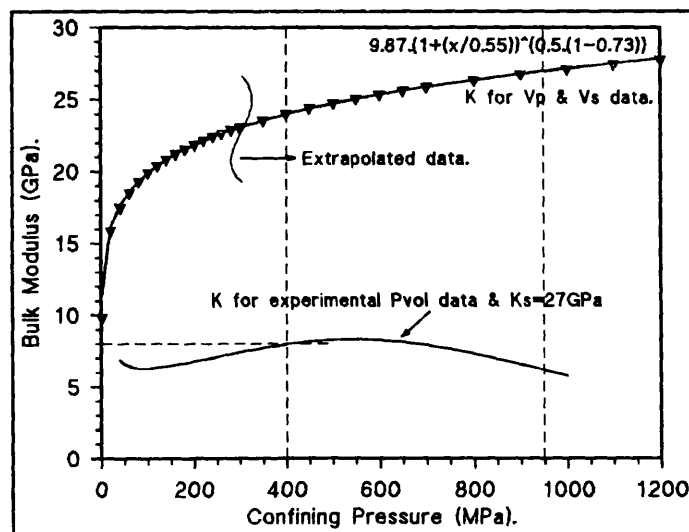


Fig. 6.3.4.1.d. Calculated *dynamic* bulk modulus for  $V_p$  &  $V_s$  data (upper curve), and *static* bulk modulus for experimental data (lower curve), see text.

(ii) *Drained hydrostatic pore volume loss for determination of  $K$ .* The second method calculates the *static* bulk modulus of the rock. Bulk strain under increasing hydrostatic stress and constant pore fluid pressure is a result of pore compression (through rock frame deformation) and elastic grain compression. If these components of bulk strain are known for a given increase in hydrostatic pressure, overall bulk modulus can be obtained from  $K = \delta\sigma / \delta\epsilon$ . Pore volume loss data for an increase in hydrostatic pressure are obtained from drained hydrostatic test results shown in figs. 6.3.3.3.a. & b., and grain bulk strain is obtained from the confining pressure and the bulk modulus of the solid part of the rock -  $K_s$ , (determined later at 27GPa). This

method yields a value of  $K$  of 6,500MPa at zero confining pressure, varying as shown in fig. 6.3.4.1.d. - lower curve.

It can clearly be seen from fig 6.3.4.1.d. that the value for *dynamic*  $K$  is much greater than the *static*  $K$ , a consequence of the *dynamic* loading method involved in its determination. Furthermore, the dynamic  $K$  displays a *doubling* of the value of  $K$  under the initial 100MPa confining pressure, which is not seen in the experimentally derived static bulk modulus.

It must further be noted that the determination of the static bulk modulus of compressibility is based on extrapolated *experimentally* derived pore volume loss data, and *calculated* bulk strain of the solid part of the rock. The experimental pore volume loss data makes up some  $\approx 80\%$  of rock compaction, the grain bulk strain making up  $\approx 20\%$ . This latter component of sample bulk strain requires a value of  $K_s$ , the determination of which is a point of deliberation and is discussed in the next subsection. What can be said with confidence about the data is that the lower curve is reasonably accurate for confining pressures up to 400MPa - the limit of experimental data - whilst beyond this confining pressure the value is vulnerable to inaccuracies in the extrapolation of the experimental data.

Furthermore, the static bulk modulus is determined during the same study (same batch of rock) under saturated conditions, whereas the dynamic bulk modulus is determined from a different batch of rock under dry conditions. Considering that the variability of Darley Dale sandstone between samples and batches is well known, and based on the discussion above, the *static* bulk modulus is used in this analysis, yielding a  $K$  of  $\approx 6,500\text{MPa}$  at

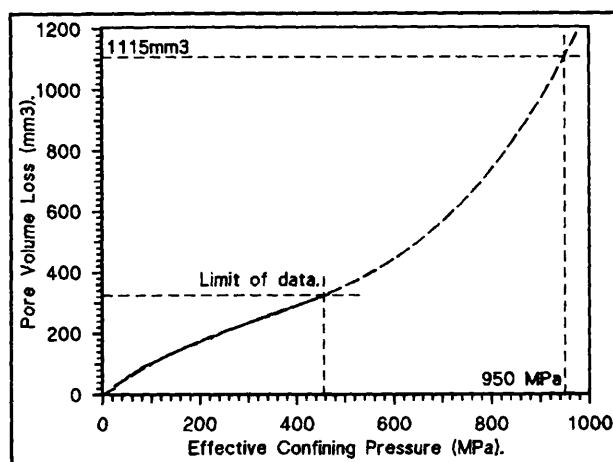


Fig. 6.3.4.1.e. Extrapolation of drained hydrostatic compaction data to establish point at which zero porosity exists in the rock - 1115mm<sup>3</sup> and 950MPa.

zero confining pressure, increasing gradually as a function of confining pressure up to 8000MPa at a confining pressure of 400MPa.

***The compressibility of the solid part of the rock.*** ( $C_s = 1/K_s$ ). This is also obtained from a number of sources. These are examined and compared here.

**(i)** *From  $v_p$  and  $v_s$  data, and drained hydrostatic test results.*  $K_s$  can be obtained from the bulk modulus (K) of the rock under a confining pressure at which full pore volume closure occurs. Considering the pore fluid volume/effective confining pressure curve 0080 of fig. 6.3.3.3.a., and producing the curve to 1115mm<sup>3</sup> pore volume loss (total porosity elimination for Darley Dale sandstone) with a polynomial function, a confining pressure of 950MPa is obtained, (fig 6.3.4.1.e.). The extended curve is smooth and satisfactorily depicts no sudden inflection point, as determined in section 6.3.3.3.

Zhang et al (1990) established a relationship as discussed in section 6.3.1.1. and shown in fig 6.3.1.1.b. Grain radii of 40-400 $\mu$ m found in Darley Dale sandstone (section 5.1.1.) equate to range of critical pressures between 110MPa and 3900MPa. A confining pressure of 950MPa (equal to full pore and crack closure), equates to a minimum grain radius of 105 $\mu$ m - greater than that observed in rock section microscopy analysis. The difference between 40 and 105 $\mu$ m as the smallest grain radius is indistinguishable under optical microscopy and hence 950MPa is accepted as the confining pressure for full pore and crack closure.

If the upper, *dynamic* K/C<sub>p</sub> curve (fig. 6.3.4.1.d.) is extended to 950MPa, a value of K of 27,000MPa is obtained.

**(ii)** Extrapolating the lower static K/C<sub>p</sub> curve of fig. 6.3.4.1.d. yields a value for bulk modulus of  $\approx$  5000MPa.

**(iii) Published mineralogical  $V_p$  and  $V_s$  data for the determination of  $K_s$ .**  $K_s$  can also be obtained from compressional and shear wave velocities through grains of quartz and plagioclase from published data, Carmichael (1989). Using the 85% of the value of  $K$  from  $V_p$  and  $V_s$  data for quartz (determined from the equation 6.3.4.1.c.), and 15% of the value of  $K$  determined from published  $V_p$  and  $V_s$  data for plagioclase (representing the proportions of the main constituents of Darley Dale sandstone), a value of 41,000MPa is found for  $K_s$ .

So, we have three value for  $K_s$  from three different methods ranging from 5000MPa to 41000MPa. Consideration of the physical processes occurring leading up to full pore and crack closure is important for a proper analysis of these values. As rock pore volume approaches zero, the stiffness of the rock should increase rapidly as rock bulk strain is accommodated by grain bulk strain only - already shown to be much less than the contribution to compaction from rock matrix bulk strain. In the static bulk modulus curve (lower curve fig. 6.3.4.1.d.), a *decrease* in  $K$  is seen as confining pressure approaches 950MPa, which puts the extrapolation of this experimental data into doubt. The dynamic bulk modulus (upper curve), whilst not increasing dramatically, is nevertheless increasing, and hence is a better representation of the real physical processes occurring in the rock. The highest value of  $K$  at 41000MPa is for the dynamic bulk modulus of the quartz and plagioclase grains only, and fails to consider cement and minor constituents of the rock which can detract significantly from overall solid rock stiffness. Of the three analyses, in the absence of any better data, the dynamic bulk modulus at 27000MPa is taken as the most appropriate value for  $K_s$ .

Whilst it could further be argued that if the extrapolated pore volume loss data (fig. 6.3.4.1.e.) is poor for the determination of  $K_s$ , i.e. static  $K$  at 950MPa, it must also be poor for the determination of the confining pressure at which full pore closure occurs - i.e. 950MPa. Since the *dynamic* bulk modulus (from  $V_p$  and  $V_s$  data on dry samples, top curve fig. 6.3.4.1.d.) at 27000MPa varies only 4% over the confining pressure range of 1000MPa to 12000MPa, the error in  $K_s$  due to an incorrect determination of the confining pressure for full pore and

crack closure is minimal. Hence a  $K_s$  value of **27,000MPa** is taken for the following analysis.

### Calculation of Skempton's B co-efficient.

Having established values for  $K$ ,  $K_r$ , and  $K_s$ , and knowing the porosity of the rock  $\phi$ , the theoretical values for the B co-efficient under a changing hydrostatic pressure are calculated using equation 6.3.4.1.a., the results of which are shown in fig. 6.3.4.1.f. This theoretical B co-efficient ( $B_{\text{theort'1}}$ ) can be further used to calculate the undrained bulk modulus of the rock ( $K_u$ ) for poro-elastic modelling of undrained compaction data, (see section 6.3.4.2.). The figure shows the theoretical value for the B co-efficient to be twice that of the smoothed observed value of the B co-efficient ( $B_{\text{obs}}$ ).

The correction factor between  $B_{\text{obs}}$  and  $B_{\text{theort'1}}$  calculated for a incompressible or zero URV eq. 6.3.4.1.a., is  $\approx 2$ , i.e. experimentally derived  $B_{\text{obs}}$  values must be doubled due to the effect of the compressible URV.

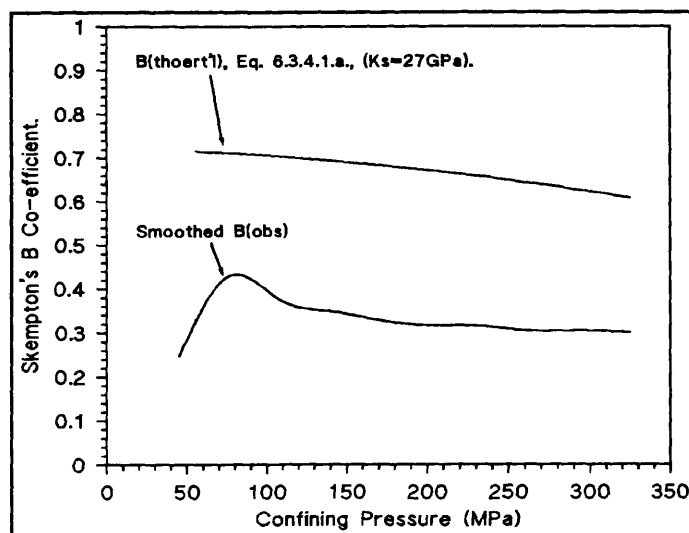


Fig. 6.3.4.1.f. Smooth observed B co-eff. compared against calculated theoretical B co-efficient. Difference is partly due to URV compressibility, see text.

Bishop later extended the work (Bishop 1976), to

consider the effect of the compressibility of the URV (consisting of compressible fluid, and pressure sensitive tubes & transducers). The equation thus derived yields a *corrected B co-efficient* ( $B_{\text{corr}}$ ). The equation was re-derived from first principles based on the following assumptions; (i) interconnecting pores, (ii) elastic and isotropic solid material in the rock, (iii) elastic and isotropic rock skeleton behaviour, (iv) random distribution of pore spaces, and (v) linear elastic fluid compressibility. It considers hydrostatic stress under undrained conditions to be comprised of two components - the

pore fluid pressure and the effective confining pressure. Under these stresses the bulk strain of the pores, of the solid parts of the rock, and of the fluid, is equated to bulk strain of the entire sample to derive the equation below.

$$B = 1/[1/B_{obs.} - (C_w/(C-C_s)) * (System\ Compress.)] \quad (6.3.4.1.d.)$$

Where the "System Compress" means "URV compressibility", and is;

$$((URV/Sample\ Vol) + ((C_L + C_M)/V.C_w)) \quad (6.3.4.1.e.)$$

Where  $C_L$  is the compressibility of the *hp* tubing,  $C_M$  is the compressibility of the pressure transducer, and  $V$  is the specimen volume. In other studies conducted to date (Mesri et al. 1976), system compressibility (the second component of eq. 6.3.4.1.e.), was found to be no more than  $1/6^{th}$  of the fluid compressibility (first term of eq. 6.3.4.1.e.), and indeed, in chapter 4 of this study,  $C_M$  and  $C_L$  for this apparatus were found to be negligible. For this reason the second term in eq. 6.3.4.1.e. is taken as zero in this analysis. The URV/sample volume ratio is equal to 0.25 in the apparatus used in present study, and the compressibilities of the sandstone are as calculated previously for the derivation of the  $B_{theor't}$ . The values for  $B_{corr.}$ , derived from equation 6.3.4.1.d., for confining pressures between 30MPa and 330MPa, are shown in fig. 6.3.4.1.g. The corrected B co-efficient ( $B_{corr.}$ ) meets the theoretical B co-efficient ( $B_{theor't}$ ), only at a confining pressure of 85MPa, and the correction factor between the smoothed  $B_{obs.}$  and  $B_{corr.}$  varies between 1.4 and 1.7. Closer examination of the correction factor data reveals an average value of 1.55.

The errors between the values of  $B_{theor't}$  (top curve) and  $B_{corr.}$  (middle curve) shown in fig. 6.3.4.1.g. are common in this type of analysis. For equation 6.3.4.1.d., Bishop (1976) noted that the system B compressibility should be *matched* to the rock specimen compressibility. The result of a matched system means that the difference between  $B_{obs.}$  and  $B_{corr.}$  should be no more than 10%. In a study by Bruhn (1972), the value of the URV/sample volume ratio was 0.15, and this was found too large to yield comparable  $B_{corr.}$  and  $B_{theor't}$  values from the technique, (i.e. - the URV compressibility and rock

compressibility were unmatched). Mesri (1976), and Wissa (1969), suggest a typical acceptable value for this ratio is 0.015, for which reasonably accurate  $B_{corr.}$  results were obtained. Wissa (1969) suggested for best results, the URV should be no more than 0.003x the rock pore volume. Clearly 0.25 represents an unmatched URV compressibility and this must be borne in mind when viewing the results in fig. 6.3.4.1.g.

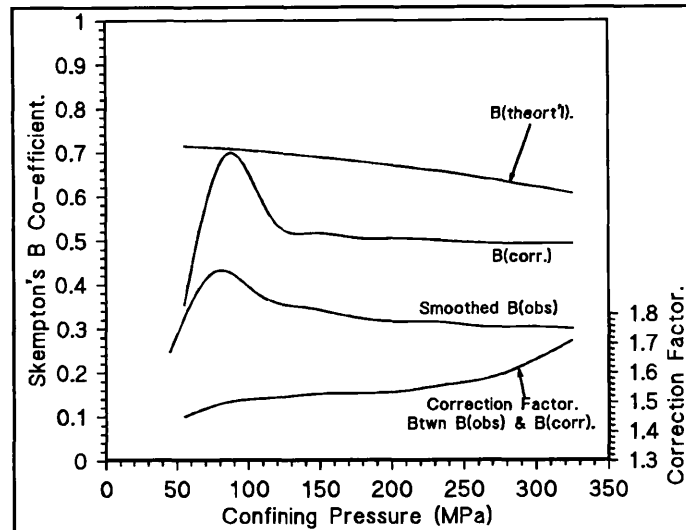


Fig. 6.3.4.1.g. Comparison of smoothed observed and calculated B co-eff.'s from eq 6.3.4.1.a & 6.3.4.1.d.

Nevertheless, errors between  $B_{corr.}$  and  $B_{theort'}$  still occurred in the previous studies as they have in this present study using this technique. Causes postulated by Mesri et al. (1976) are the values of rock bulk compressibilities adopted. The correction factor is highly sensitive to the value of  $c (=1/k)$ , and care must be taken when selecting this variable. In this study, numerous values for this bulk modulus have been considered before a final figure was adopted. Mesri et al. (1976) investigated possible values for fluid compressibility ( $C_w$ ) used in equation 6.3.4.1.d. which would satisfy matching  $B_{theort'}$  and  $B_{corr.}$ , and found a fluid compressibility ( $C_w$ ) 2-3 times that of water was required to eliminate the error. Further sources of discrepancy between  $B_{corr.}$  and  $B_{theort'}$  concern the assumptions made in the derivation of the equations 6.3.4.1.d. However, of those assumptions mentioned above, pore inter-connectivity and grain elasticity behaviour can be assumed valid for Darley Dale sandstone under a confining pressure of only 350MPa, and the assumption of linear elastic fluid behaviour is accounted for by recalculating  $C_w$  for each increment of pore fluid pressure.

To reconcile the differences between theoretical and observed values of the B co-efficient in this study, if the compressibility of the bulk rock ( $c$ ) were to approach the compressibility of the fluid ( $C_w$ ), the correction factor would

approach 1.0, as it can be seen from equation 6.3.4.1.d. This requires a rock bulk modulus in the region of 2,000 to 3,000MPa, or for an increase in the bulk modulus of the fluid by two or three times, as per the findings of Mesri et al (1976). This low value for  $K$  is however unrealistic, as is a higher value for  $K_f$ , hence discrepancies between the theoretical and experimental results remain. Using the form for the change in bulk modulus with confining pressure as seen in fig. 6.3.4.1.d. (dynamic bulk modulus derivation), but adopting the lower values for  $K$  mentioned above (2,000-3,000MPa), one can see how the an increasing  $K$  with increasing confining pressure reduces the compliance of the rock and hence reduces the  $B$  co-efficient as seen in fig. 6.3.4.1.a.

Considering the limitations of the theoretical analysis technique (highly sensitive to bulk moduli -  $K$  and  $K_f$ ), and the apparatus (unmatched URV), the results for  $B_{corr.}$  and  $B_{theor't}$  in fig. 6.3.4.1.g. are thought to be within reasonable limits of each other. The value of a URV correction factor at 1.55 is greater than that determined from the analysis of triaxial experiments under various URV's, at 1.286 (section 6.2.), but considering the method of data extrapolation used in section 6.2., 1.55 does not seem unreasonable.

Accurate determination of the  $B$  co-efficient yields fluid pressure variation under a changing stress for a given rock mass under confined conditions. Since a changing fluid pressure reduces the effective confining pressure this has important implications for the deformation behaviour of rocks when confined by an impermeable surrounding rock. This matter has been discussed in the analysis of results of undrained triaxial experiments in section 6.2.4.1.

*In Summary.* In order to correct the measured  $B$  co-efficient from undrained hydrostatic compaction experiments, a number of methods for determining the bulk modulus of the rock ( $K$ ) and of the grains ( $K_g$ ) have been considered. Experimentally derived static bulk modulus data was judged the most appropriate for  $K$  at 6,500MPa, and, based on extrapolated compaction data to determine the confining pressure for full porosity elimination (i.e. 950MPa), the dynamic bulk modulus from  $v_p$  and  $v_s$  data at 950MPa was used to yield a value for  $K_g$  at 27,000MPa. These values were employed when using Bishop's methods to determine the theoretical and corrected  $B$  co-efficients, fig.

6.3.4.1.g. Correction factors between measured and calculated B co-efficients were found to be  $\approx 2$  and  $\approx 1.55$ . This compares with  $\approx 1.29$  for the URV analysis in section 6.2.5. These values can now be used in the determination of the undrained bulk modulus ( $\kappa_u$ ) which is in turn required to model drained hydrostatic compaction data in the next sub-section.

#### 6.3.4.2. Consideration of Variations in Fluid Mass as a Function of Deformation under Drained Hydrostatic Stress Conditions.

The above analysis relates fluid pressure changes to hydrostatic deformation in the *undrained* case. The analysis of the variation in pore and crack volume

under *drained* hydrostatic loading results in a relationship between fluid volume change, the bulk moduli of rock ( $K_u$ ,  $K_r$ ,  $K$ ), pore fluid pressure  $p$ , the compressibility of the pore fluid  $K_f$ , and porosity  $\phi$ , (see section 2.3.2.), as so;

$$\delta v = \alpha \cdot \epsilon + [(\sigma^2/(K_u - K)) - (\phi/K_f)] \cdot p \quad (6.3.4.2.a.)$$

The equation relies on some parameters already determined, ( $K_f$  &  $K_r$ ), and also  $K_u$ ,  $\alpha$ ,  $p$ , and  $\epsilon$ . For the drained environment under adequate permeability, fluid pressure  $p$ , and hence  $K_f$ , remain constant, and these values have been discussed earlier, (fig. 4.4.3.2.a.). The bulk strain ( $\epsilon$ ) in the rock under hydrostatic stress is easily determined from hydrostatic stress divided by the bulk modulus of the rock ( $\sigma/K$ ), therefore  $\epsilon$  is a function of  $K$ , which is already established for Darley Dale sandstone.

Hence, the two outstanding variables requiring determination are  $\alpha$  and  $K_u$ .

Firstly considering  $\alpha = 1 - K/K_s$ . Both  $K$  and  $K_s$  are already determined to an acceptable degree of accuracy in section 6.3.4.1. Fig. 6.3.4.2.a. shows the variation of  $\alpha$  for two values of  $K_s$ . With increasing confining pressure the value of  $\alpha$  decreases, (as expected from the rise in  $K$  with confining pressure), and for a lower value of  $K_s$ , the value of  $\alpha$  is translated down the alpha axis. For  $K_s = 27,000\text{MPa}$ ,  $\alpha = 0.65 \rightarrow 0.8$  as a function of confining pressure.

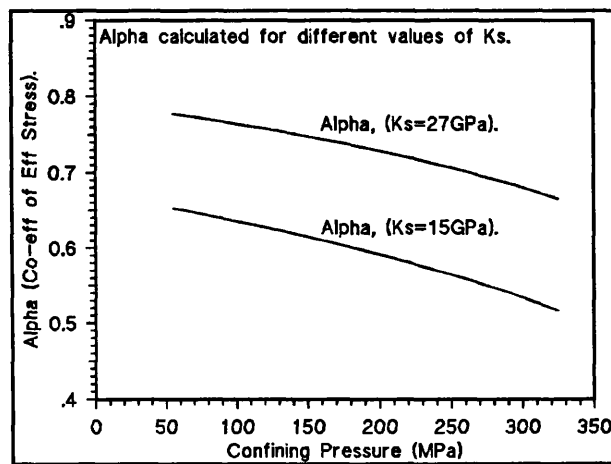


Fig. 6.3.4.2.a. Calculated values of  $\alpha$  for different values of  $K_s$ , see text for details.

$K_u$  is determined from rearranging the equation for Skempton's B co-efficient (eq. 2.3.3.d.), shown below, using experimentally determined B co-efficient data ( $B_{obs.}$ ) corrected for URV compressibility.

$$K_u = -K/(B\alpha - 1) \quad (6.3.4.2.b.)$$

It can therefore be seen from the unknown variables above, that the value of  $\delta v$  (eq. 6.3.4.2.a.), is primarily a function of  $K_s$ ,  $K$ , and the correction factor for  $B_{obs}$ .

The computer software written (by the present author) to analyse the experimental data using equation 6.3.4.2.a. incrementally increases the confining pressure in steps of 5MPa, establishing  $\delta v$  for this applied hydrostatic stress, and recalculating  $K$ ,  $\alpha$ ,  $K_u$  (from experimental derived and corrected  $B_{obs}$ ), & the revised porosity,  $\phi$ , from the value of  $\delta v$  obtained from the last increment of confining pressure.

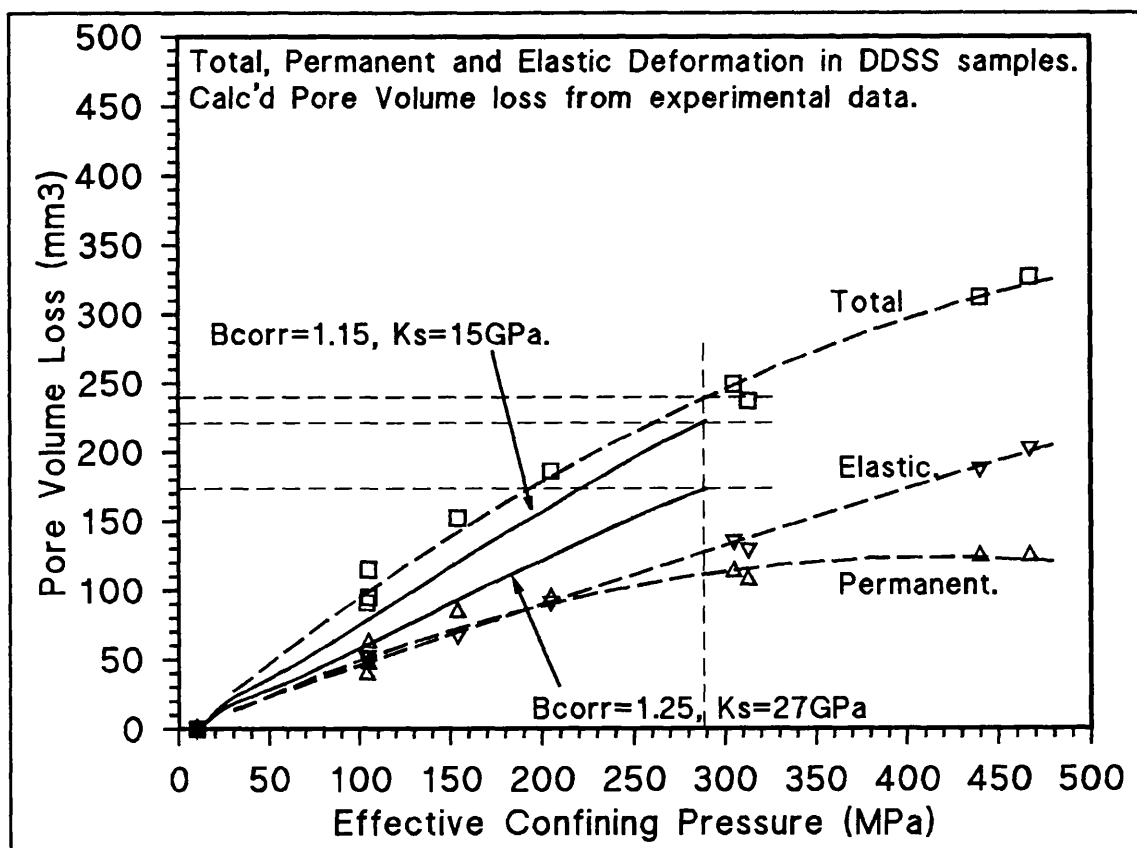


Fig. 6.3.4.2.b. Comparison of experimental and calculated pore volume loss data from fig.6.3.3.3.a. & b., and eq. 6.3.4.2.a. - see text for more details.

Accepting the determined values of  $K$  and  $K_s$  and initially taking the  $B$  coefficient correction factor at 1.25 - established in section 6.2. - the total pore fluid volume loss under a effective hydrostatic stress of  $\approx 300$ MPa is found to be  $\approx 170$ mm<sup>3</sup>, (fig. 6.3.4.2.b. - lower solid line). This compares with an experimental derived result of  $\approx 240$ mm<sup>3</sup>. The calculated value for pore volume loss is some 30% less than the experimental results. Since the derivation of  $K_s$  and  $B_{corr}$  are considered the most unreliably determined

parameters in this analysis, a consideration of the variation of  $\delta v$  at 320MPa with  $B_{obs.}$  correction factor and  $K_s$  using eq. 6.3.4.2.a. is presented in fig. 6.3.4.2.c. to find optimum values for  $K_s$  and  $B_{obs.}$  correction factor to ensure calculated  $\delta v$  values meet experimentally derived  $\delta v$  values.

From earlier discussions,  $K_s$  is involved in many other variables in equation 6.3.4.2.a. -  $\alpha$ ,  $K$ , and hence also  $K_u$ , - and affects the overall value for  $\delta v$  as seen on the figure 6.3.4.2.c. Pore fluid volume expelled ( $\delta v$ ) at first rises with an increasing  $K_s$  to a peak at  $\approx 15$  GPa, and then gradually decreases by approximately the same amount from  $K_s = 15$  GPa to  $K_s = 45$  GPa. Overall, the variation in  $\delta v$  throughout the  $K_s$  range is between 6% and 25% depending on the correction factor adopted. The upper curves in the figure most closely represents the experimentally derived  $\delta v$  values of  $240\text{mm}^3$ , and the variation in  $\delta v$  with  $K_s$  for this curve is  $\approx 6\%$ . Hence the value of  $K_s$  turns out to be less influential in the determination of  $\delta v$  than the correction factor for  $B_{obs.}$ , i.e than  $K_u$ , (since  $K_u$  is determined directly from B co-efficient - eq. 6.3.4.2.b.).

If values for  $K_s$  and the B co-efficient correction factor are *selected* from fig. 6.3.4.2.c. to satisfy the experimentally derived  $\delta v$  value of  $240\text{mm}^3$ , either  $K_s = 45\text{GPa}$  and a correction factor of 1.0, (point A. on the fig.), or  $K_s = 15\text{GPa}$ , and a correction factor of  $\approx 1.05$ , (point B on the

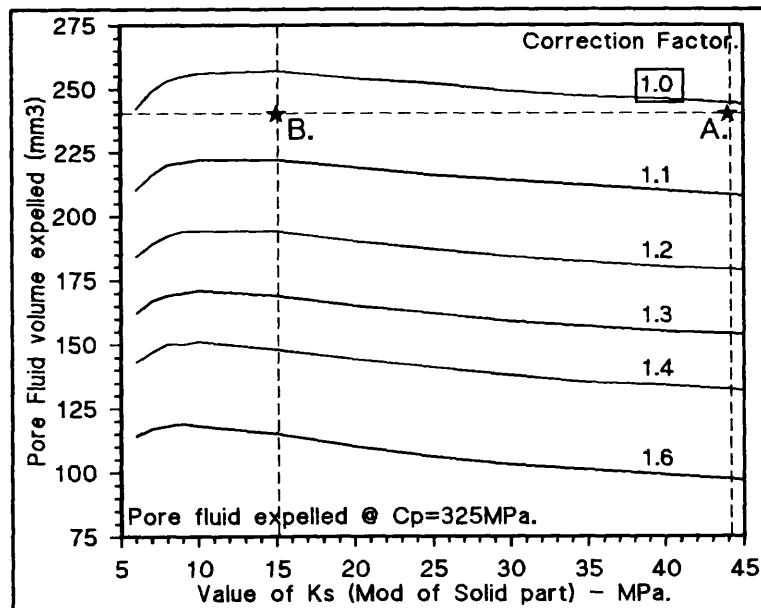


Fig. 6.3.4.2.c. Variation in  $\delta v$  with B co-eff. correction factor and  $K_s$ , from eq 6.3.4.2.a., see text for details.

fig.) are found as extremes in a range of values of both variables. Considering that the compressibility of the URV in the undrained experiments *is* significant in reducing the value of the experimentally measured pore fluid pressure (section 6.2.4.2.) and hence the B co-efficient, the  $K_s = 45\text{GPa}$ , and B co-efficient correction factor = 1.0 combination is not viable, (even though  $K_s$  is close to

the 41GPa obtained for  $K_s$  from mineralogical data - section 6.3.4.1.). Further considering that experimentally, the correction factor for  $B_{obs.}$  to meet  $B_{corr.}$  and  $B_{theor'1}$  (section 6.2. and fig. 6.3.4.1.g.), is  $>1.05$ , the condition from fig. 6.3.4.2.c. of B correction factor of  $\approx 1.15$ , and  $K_s = 15\text{GPa}$ , (point B), is the most probable combination available which satisfies  $\delta v \approx 240\text{mm}^3$ . The results of computed  $\delta v$  analysis using these variables is plotted in fig. 6.3.4.2.b. (upper solid line). This line in the figure follows the *trend* of the experimental data if not meeting the data precisely. The range of experimental points at the effective pressure of 105MPa in the figure represents the error in the experimental data, and this suggests the calculated  $\delta v$  data and experimental  $\delta v$  data are in reasonable agreement

The significance of this *matched*  $\delta v/C_p$  line in fig. 6.3.4.2.b. with respect to the adopted B co-efficient correction factor (1.15) and  $K_s$  (15GPa) is important. Theoretical and corrected values of the B co-efficient based on a  $K_s$  of 15GPa are shown as dashed lines in fig. 6.3.4.2.d. The solid lines in the figure are

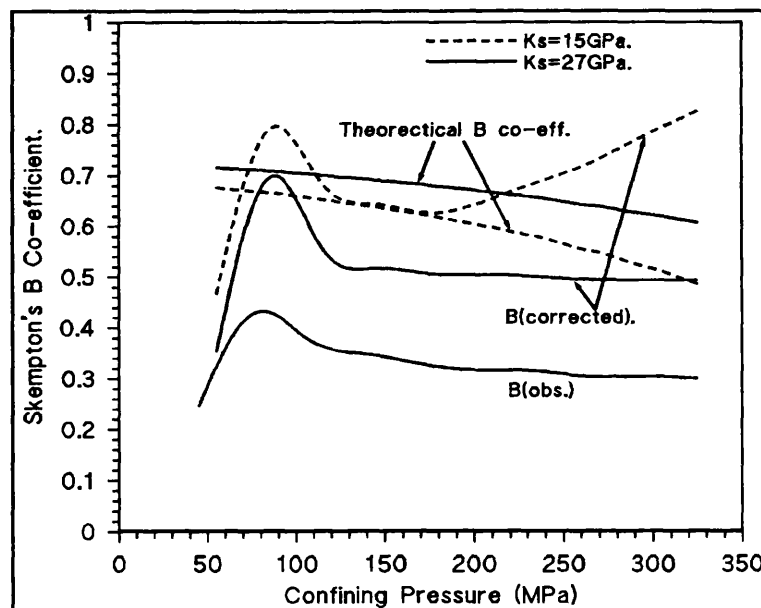


Fig. 6.3.4.2.d. Comparison of observed B co-eff. and calculated from eq. 6.3.4.1.a. and 6.3.4.1.d., and for different values of  $K_s$ . See text for full details.

the theoretical and corrected B co-efficients based on  $K_s = 27\text{GPa}$ , (same as fig. 6.3.4.1.g.) for comparison purposes. The theoretical value of B co-efficient is reduced by the reduction in  $K_s$  from 27GPa to 15GPa, as expected from eq. 6.3.4.1.a., ( $C_v (1/K_s)$  is much smaller than  $C_w (1/K_f)$ , and therefore the second term is reduced by a increase in  $C_s$  (i.e. a decrease in  $K_s$ )).

The decrease in  $B_{theor'1}$  caused by a reduction in  $K_s$  is also *greater* for higher values of confining pressure due to the response of the rock to an increase in  $K$  and  $K_f$  under increasing confining pressure. Physically, this can be

viewed as the relatively lower  $K_s$  value compared to  $K$  value causing relatively more of the deformation to be due to bulk strain of the solid part of the rock, and relatively less to be due to the bulk strain of the frame of the rock. Since the compression of the mineral frame causes pore volume reduction and hence pore fluid pressure rise, a relative decrease in  $K_s$  results in a decrease in pore fluid pressure generated, and hence in  $B_{\text{theort}'1}$ .

In contrast, the  $B_{\text{corr.}}$  (based on equation 6.3.4.1.d.), is *increased* by the reduction in  $K_s$  from 27GPa to 15GPa, which, since  $B_{\text{theort}'1} = B_{\text{corr.}}$  under  $K_s = 15\text{GPa}$ , a lower  $K_s$  than 27GPa may be realistic. However, considering also that the equipment is unmatched and the other values for  $K_s$  determined in section 6.3.4.1., a  $K_s$  of as low as 15GPa is probably too low.

The increased gradient of the  $B_{\text{corr.}}$  curve (at  $K_s = 15\text{GPa}$ ) curve at confining pressures of  $>175\text{MPa}$  is a consequence of an increasing correction factor, dependent as it is on the changing value of  $C (= 1/K)$  and  $B_{\text{obs.}}$ , i.e. as the compressibility of the rock ( $C$ ) decreases ( $K$  increases). Furthermore, if  $B_{\text{obs.}}$  is small and decreasing (as it is at a confining pressure of  $>175\text{MPa}$ ), the effect of even a numerically constant second term in eq. 6.3.4.1.d. is to *increase* the value of  $B_{\text{corr.}}$ . These combined influences cause the increasing  $B_{\text{corr.}}$  seen in the upper dashed curve in fig. 6.3.4.1.d.

The decrease in  $K_s$  from 27GPa to 15GPa for the determination of  $\delta v$  also has the effect of increasing the correction factor between  $B_{\text{obs.}}$  and  $B_{\text{corr.}}$  from an average of 1.55 to an average of 2.2, (not shown in the fig.). This has significant implications if the greater  $B_{\text{corr.}}$  value is used in the calculated value for  $\delta v$ , as seen from fig. 6.3.4.2.c., reducing  $\delta v$  from  $\approx 240\text{mm}^3$  to  $<100\text{mm}^3$ .

Clearly there is a mismatch of bulk modulus values for the theoretical determination of the  $B$  co-efficient and for pore volume reduction under drained conditions,  $\delta v$ . For a given value of  $K_s$ , of 15GPa and an *uncorrected*  $B_{\text{obs.}}$  from hydrostatic undrained experiments (i.e. correction factor = 1.0), (section 6.3.3.4.), a good approximation to pore volume loss,  $\delta v$ , is obtained, (fig. 6.3.4.2.b.). However, the same  $K_s$  value (15GPa) yields good agreement between  $B_{\text{theort}'1}$  and  $B_{\text{corr.}}$  but with a correction factor requirement of  $>2$ .

Possible explanation for the low  $B_{\text{corr.}}$  required to yield accurate  $\delta v$  determination involves the values adopted for the parameter  $K_u$  (based on the  $B_{\text{corr.}}$ ).

$K_u$  depends on the stiffness of the fluid phase and the solid phase of the rock, both of which change with increasing confining pressure under undrained conditions. However, under *drained* conditions the stiffness of the fluid phase ( $K_f$ ) of the rock remains constant, and hence  $K_u$  *should* vary only in response to changes in the stiffness of the solid phase of the rock ( $K$ ). In this analysis,  $K_u$  is based on experimentally derived values of the B co-efficient ( $B_{\text{obs.}}$ ) multiplied by a correction factor to account for the URV compressibility, which is a function of both an *increasing*  $K_f$  and  $K$ . It is postulated, that if  $K_u$  were calculated for a *constant*  $K_f$ , and a *varying*  $K$ , the results for  $\delta v$  would be in better agreement with experimentally obtained  $\delta v$  values.  $K_u$  can be obtained theoretically as a function of  $K$ ,  $K_f$ ,  $K_s$ ,  $\alpha$ , and  $\phi$ , (Guéguen 1994, p142), i.e. allowing  $K$  to increase with confining pressure whilst keeping  $K_f$  constant (a function of  $p$ ). Hence  $K_u$  is then primarily a function of  $K$ . This analysis is not conducted here.

Notwithstanding, the errors involved in taking incorrect values for  $K_u$  are countered by the effect of the URV compressibility reducing otherwise greater values of  $B_{\text{obs.}}$ . Experimentally derived B co-efficients are reduced to approximately half the value expected if experiments were conducted under zero URV (according to fig. 6.3.4.2.d.). The final result is a reasonable estimate of experimentally derived  $\delta v$  results from theoretically calculated analysis based on linear poro-elasticity.

*In Summary.* Using existing poro-elasticity theory (eq. 6.3.4.2.a.), theoretical drained pore volume loss ( $\delta v$ ) is attempted for a variety of  $K_s$  and B-correction factors (the variables found to be the most effectual in controlling  $\delta v$ ). Final values for  $K_u$  and B - correction factor which satisfy experimentally derived  $\delta v$  were  $K=15\text{GPa}$  and correction factor  $\approx 1.05$ , both outside the range derived earlier in the analysis. Using  $K=15\text{GPa}$  means  $B_{\text{theor.}}$  and  $B_{\text{corr.}}$  match, but a correction factor of 2.2 is obtained for  $B_{\text{obs.}}$ , not consistent with the determination of  $\delta v$  (at  $100\text{mm}^3$  under these conditions).

The problem is thought to lie with  $K_v$  being determined from experiments under *undrained* conditions (eq. 6.3.4.2.b.) where both  $K_f$  and  $K$  increase with confining pressure. Under *drained* conditions,  $K_f$  remains constant, hence for this analysis the  $K_v$  values used are too high. In the  $\delta v$  analysis, an incorrect  $K_v$  is countered by an uncorrected B co-efficient, i.e.  $B_{obs.}$ , to yield reasonable  $\delta v$  approximation as seen in fig. 6.3.4.2.b.

### 6.3.5. Future Work.

Further studies could initially involve more tests of the type reported here to confirm repeatability.

Equipment improvements for further tests should provide for the following.

- ▶ *Better confining pressure increase and decrease rate control.* AE were found to be somewhat dependent on the *rate* at which the confining pressure was increased; unavoidable burst in confining pressure caused large AE peaks rendering the use of AE data less valid. By accurately controlling  $C_p$ /time rate, AE would become more reliable, thus aiding the isolation of critical confining pressures at which grain fracturing occurs.
- ▶ *Using heat shrink plastic jackets would hug* the sample better and eliminate the fluid between the jacket and the sample. This would aid absolute pore volume change measurements and reduce AE resulting from the copper jacket pressing into the rock sample under the initial application of confining pressure. These jacket types were not used during these experiments to ensure comparability between tests involving high temperatures and those not.
- ▶ *Achieve higher confining pressures.* Employing a different lower closure to the vessel (section 3.2.) which excludes electrical contacts would (among other modifications including servicing vessel and pump seals and valves), allow greater confining pressures, perhaps up to 1000MPa. This would identify or otherwise any critical confining

pressures beyond 450MPa and allow rocks of well graded small grain radii ( $< 150\mu\text{m}$ ) to be tested.

- ▶ *Measure  $V_p$  &/or  $V_s$  simultaneously with pore volumetry.* This would elucidate changes in pore *shape* and density along with absolute pore volume change from pore volumetry measurements, (see Ayling 1991).
- ▶ *Measurement of permeability* in conjunction with  $V_p$  and  $V_s$  or simply with pore volumetry measurements would explain many of the features observed with the microgranodiorite behaviour. This improvement is under active development using a newly commissioned 40mm diameter specimen sized triaxial cell.

Microscopic observations of post experimental sample sections would clarify many of the hypotheses made in this section. Specifically this could involve.

- ▶ *Terminating the test at different confining pressures* for the Darley Dale sandstone rock and investigating the grain fracture/grain size relationship with respect to the assumptions adopted from the Zhang et al. 1990 publication.
- ▶ *Confirming the effect of cycling the confining pressure* within the same stress range by examining grain rotation, and incremental compaction of pores.

A good method for saturating copper jacket encased samples with low viscosity dyed epoxy resin must be devised for microscopy analysis. A technique was investigated extensively by the author, consisting of pressure assistance upstream and vacuum assistance downstream to force the epoxy resin through the sample. The equipment requires further developmental work.

More general advances to this study could include;

- ▶ ***Using a fluid of higher compressibility.*** This would affect  $K_u$ , and  $K_f$ , and hence  $\delta v$ , both experimentally and theoretically. Attention should be paid to the strain rate adopted for this suite of experiments. The strain rate should be match to the new fluid viscosity and rock permeability to avoid dilatancy hardening.
  
- ▶ Comparing the response of rock deformation using *an inert fluid* and an active fluid is a valid and important development to isolate the chemical affect of the pore fluid on deformation (section 2.4.3.4. and 2.5.6.).
  
- ▶ ***Other rock types*** could be brought into the experimental programme. For example, clastic rocks of different mineralogy, grading, and porosity, could be included to examine the many facets of the behaviour of these rocks under hydrostatic pressure under drained and undrained conditions.

## 6.4. Pore Volume and Pressure Change under Triaxial Stress Conditions.

### 6.4.1. Introduction.

During the deformation of fluid filled porous rocks, pore volume (or pressure) changes occur as a result compaction and dilatant crack growth. For a full examination of the deformation processes it is important to attempt to separate these components. This section examines the results of a whole suite of drained and undrained experiments in this way. First, some recent work is reviewed which has analysed deformation by dividing the pore volume changes during deformation into compaction/dilatancy, and elastic/inelastic mechanisms.

Bernarbé et al. (1994) separated the elastic and inelastic components of deformation through determining the *static* elastic effective Young's modulus of the rock at various stages of deformation (different points on the stress/strain curve), and, based on this, attributed a portion of total specimen strain to elastic deformation and the remainder to inelastic deformation. The point at which inelastic deformation commenced (attributed to frictional sliding on crack faces and between grains), the rock was said to have yielded. They found that inelastic frictional mechanisms occurred during the linear portion of the stress/strain curve at low differential stresses - even during the application of a confining pressure alone for sandstones of high porosity (20%+). It is important to note that the yield stress in the study by Bernarbé et al. is not the *critical pressure*, (section 6.3.1.1.) found during high pressure hydrostatic compaction.

Ayling (1991), used the change in total pore volume during compaction up to the onset of dilatancy (found to be a linear function of differential stress) to predict the components of pore volume change attributable to compaction and to dilatancy. He corrected for linear compaction by subtracting the product of initial linear stress increase and initial linear pore volume decrease per strain increment from the total pore volume change. This can be stated as;

$$\delta V_R = \delta V_T - \delta\sigma(g_1/g_2) \quad (6.4.1.a.)$$

where  $\delta V_R$  is the residual volume change,  $\delta V_T$  is the total volume change, and  $\delta\sigma$  is the change in differential stress,  $g_1$  is the gradient of the linear portion of the total pore volume/strain curve, and  $g_2$  is the corresponding gradient of the linear part of the stress/strain curve. The important assumption implicit in this calculation is that the initial stress and pore volume gradients are the result of elastic pore closure. The data thus derived were very erratic and it was difficult to draw any definite conclusions from some of the results. The method did, however, predict the onset of dilatancy more precisely than AE alone.

## 6.4.2. Programme of Experiments.

A comprehensive suite of triaxial experiments were done under both drained and undrained conditions. Fig. 6.4.2.a. shows the stress conditions for 66 experiments marked in confining pressure/effective confining pressure space. The programme has attempted to address the following areas:

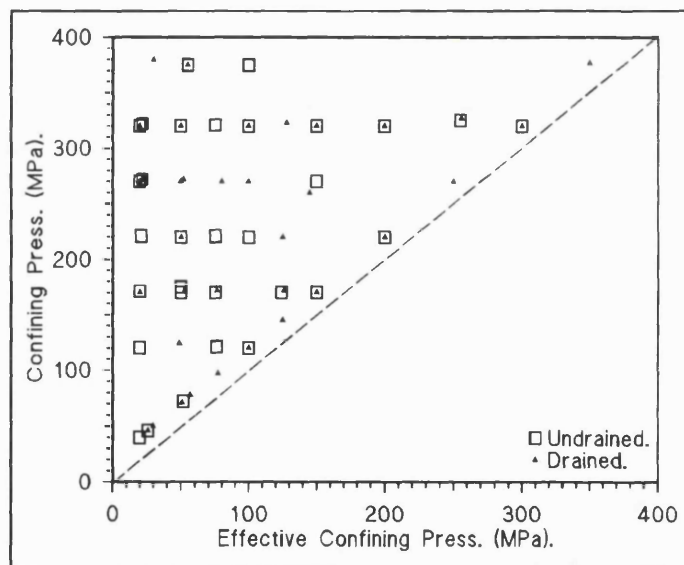


Fig. 6.4.2.a. Full suite of triaxial experiments shown in effective confining pressure/confining pressure space.

- ▶ Examination of the pore volume and pressure changes during cataclastic flow ( $C_p' > 100$ MPa), yielding information on the micro-mechanisms of deformation during stable sliding and strain hardening.
- ▶ Examination of dilatant pore volume increase (by subtracting the compaction component of pore volume change, section 6.3.3.3.), yielding information on the relationship between AE, new dilatant crack growth, and pore volume changes.

- ▶ Examination of the relationship between pore fluid volume, mean stress, and deviatoric stress throughout the deformation cycle in 3-D mean stress/deviatoric stress/pore volume space, allowing the effect of each of the stress components on pore volume to be examined.
- ▶ Examination of the effect of an elevated pore fluid pressure on the chemical activity of fluid during triaxial rock deformation.

### 6.4.3. Results and Discussion.

#### 6.4.3.1. Analysis of Triaxial Deformation under Increasing Pore Fluid Pressure and Constant Effective Pressure.

The pore fluid volume/pressure curves illuminate differences in the micro-mechanisms occurring during deformation not easily seen by observing the stress/strain curve alone. Fig. 6.4.3.1.a. shows five results conducted at an effective confining pressure of 20MPa, and a confining pressures ranging from 40MPa to 322MPa. Strain rate in all the tests was constant at  $10^{-5}/s^{-1}$ .

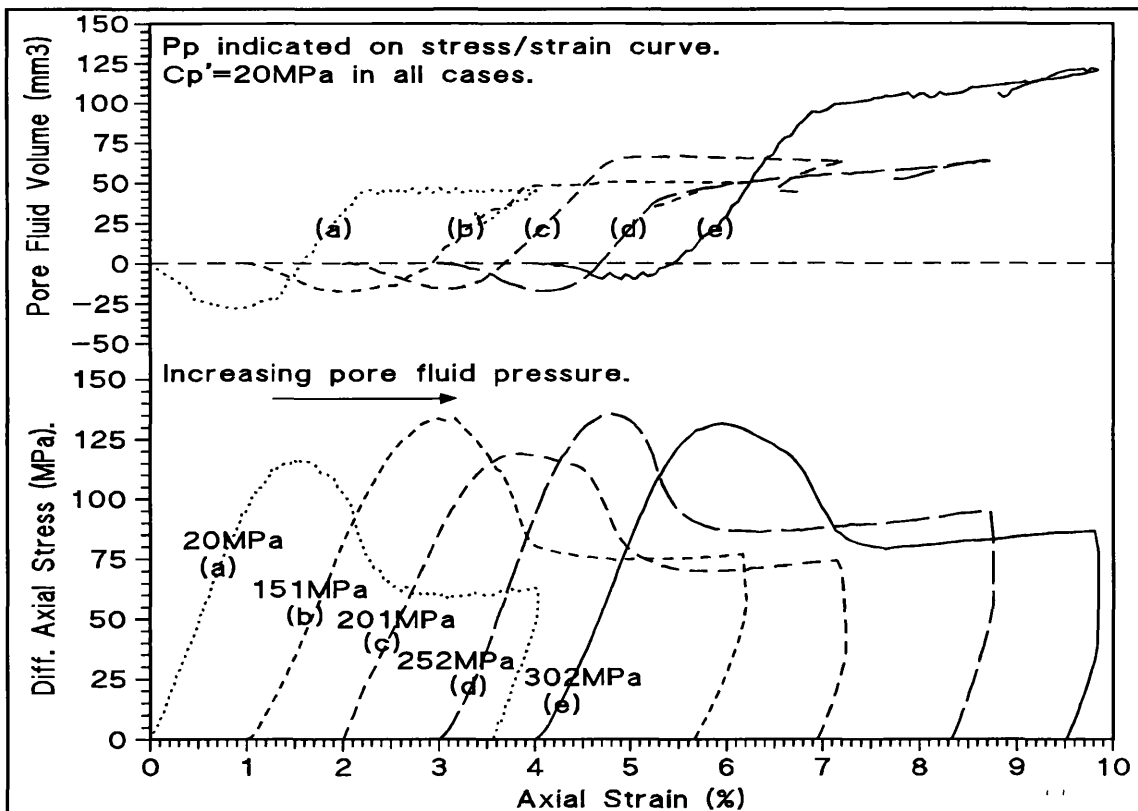


Fig. 6.4.3.1.a. Five triaxial deformation experiments under constant effective confining pressure (20MPa) and various pore fluid pressures to examine the effect of fluid pressure on deformation.

Under a constant effective confining pressure deformation characteristics as shown by the stress/strain curve do not change (within experimental variation) - similar peak strengths, brittle dynamic faulting failure and stable sliding characteristics. The pore fluid volume curve illustrates behaviour seen many times before; initial compaction followed by dilatancy, beginning in all cases at between 1/2 and 2/3 of peak stress as indicated by the deviation in the slope of the pore volume curve from linearity.

The differences found between the pore fluid volume curves of the five results are highlighted below.

- ▶ The degree of initial compaction under increasing differential stress *decreases* with increasing confining pressures (constant effective confining pressure), results (a)→(e).
- ▶ Dilatant crack growth volumes are greater for a greater confining pressure to the extent that at confining pressures of 272MPa and 322MPa results (d) & (e), pore volume increase is seen even during post-dynamic-failure stable sliding.
- ▶ Upon unloading the differential axial stress at the end of the test, the tests conducted at between  $C_p = 40\text{MPa}$  and  $221\text{MPa}$ , (a)→(c) show compaction, whilst those at  $C_p = 272\text{MPa}$  and  $322\text{MPa}$ , (d) & (e), show a degree of further dilatancy followed by compaction.

Based on these results alone the mechanism responsible for this change in pore fluid volume response is difficult to establish with any real degree of conviction. The specimens all show a single fault plane, typical of triaxial deformation at an effective confining pressure of 20MPa, and hence no extra information is gained from the specimens without microscopic section analysis.

The increased fluid reactivity known to occur under elevated pressure increases stress corrosion cracking and mineral dissolution precipitation, which would manifest itself as a time dependent increase in pore volume.

This is seen during stable sliding in curves (d) and (e). If the gradient of the pore fluid volume curve during stable sliding ( $7\text{mm}^3/1\%$  axial strain for results (e) and  $3.8\text{mm}^3/1\%$  axial strain for results (d), or  $17$  and  $9\text{mm}^3/\text{hour}$  at a strain rate of  $10^{-5}/\text{s}^{-1}$  resp.), is subtracted from the measured pore fluid volume curve, the resultant curves resembles typical pore fluid volume responses for lower confining pressures, see fig. 6.4.3.1.b. In conclusion this time-dependent increase in pore volume is the result of stress-corrosion cracking.

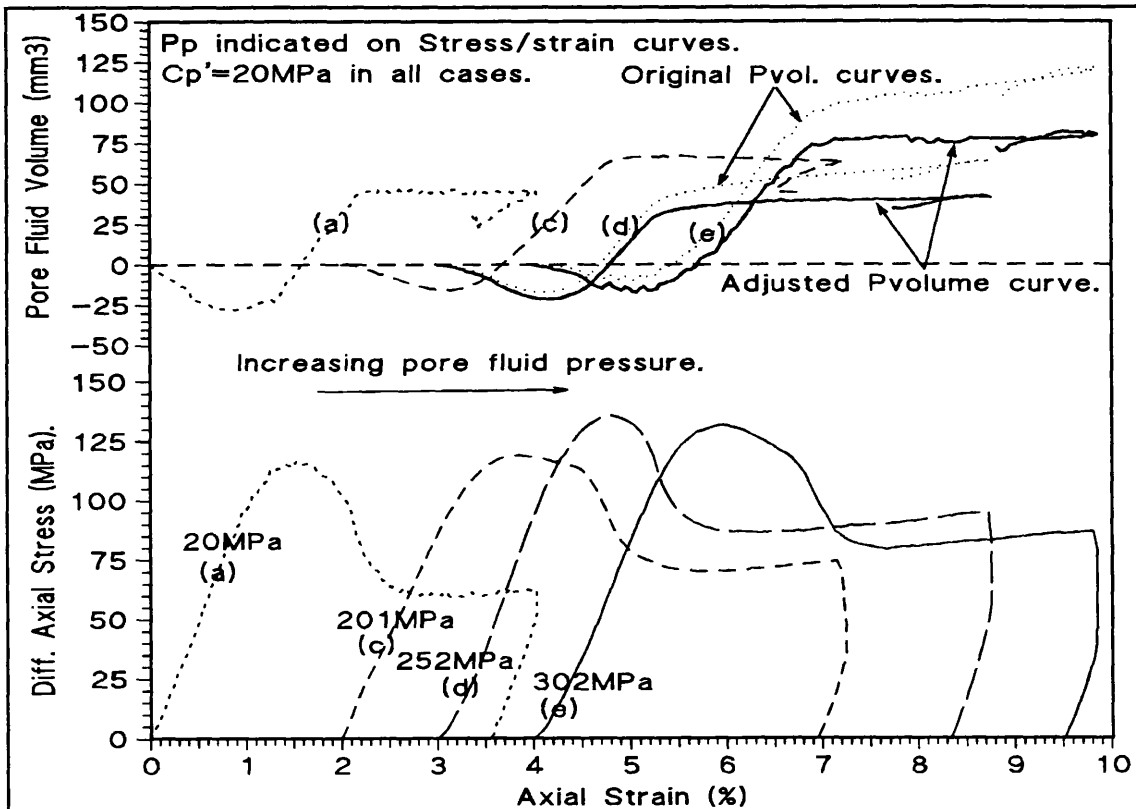


Fig. 6.4.3.1.b. As 6.4.3.1.a. with curves (d) and (e) adjusted for time dependent increase in pore fluid volume due to chemical activity of high pore fluid pressure, see text.

One could argue that the fluid inflow seen in curves (d) & (e) during stable sliding is the result of insufficient equilibration time allowed prior to experimentation. Examination of the equilibration period volumetry data does not confirm this; during post-dynamic failure (nearly two hours after the commencement of the test), delayed fluid inflow resulting from low rock permeability is considered unlikely (based on general experimental experience).

The long term effect of this chemical activity on rocks is a gradual accumulation of damage and subsequent decrease in integrity of the rock. It appears, since the chemical activity of the pore fluid has little effect on

mechanical deformation behaviour of the rock in these tests, that the duration of these experiments is far too short for this chemical activity to have an appreciable effect.

*In summary,* increasing pore fluid pressure (effective confining pressure constant) promotes chemically induced micro-crack damage and causes a time-dependent increase in pore volume of between 9→17mm<sup>3</sup>/hour at pore fluid pressures of 250→300MPa, respectively. Under the short time periods of these laboratory experiments (2.5 hours) the resulting extra cracking has no obvious effect on deformation characteristics.

#### 6.4.3.2. Analysis of Pore Fluid Pressure/Volume Changes and AE During Triaxial Deformation Experiments at High Confining Pressures.

The change in pore volume during cataclastic flow tells us much about the changing dominant deformation mechanisms occurring during the deformation process. Fig.'s 6.4.3.2.a., b., c. & d. show results from eight drained experiments conducted at a constant confining pressure (320MPa), and different pore fluid pressures; the effective confining pressure for each result is indicated against each stress/strain curve in each figure. For each result, stress, pore fluid volume, AE event rate, cumulative AE events, and where data allowed, seismic *b*-value, is shown. Acoustic emission event rate is multiplied by 60 to allow it to be shown on the same axis as cumulative acoustic emissions. The vertical axes scales between the graphs are equal for ease of comparison, and the thick black line on the axial strain axis indicates the start of the second test in each figure. The results illustrate the mechanisms occurring during the shift from brittle failure to cataclastic flow, with pore fluid volumetry and AE events being monitored simultaneously, to the author's knowledge for the first time at these high stresses.

The result at 22MPa (the same as curve (e) of fig. 6.4.3.1.a.), shows behaviour typical of brittle faulting failure rock. The AE event rate and cumulative AE data show that the maximum rate of damage accumulation occurs between

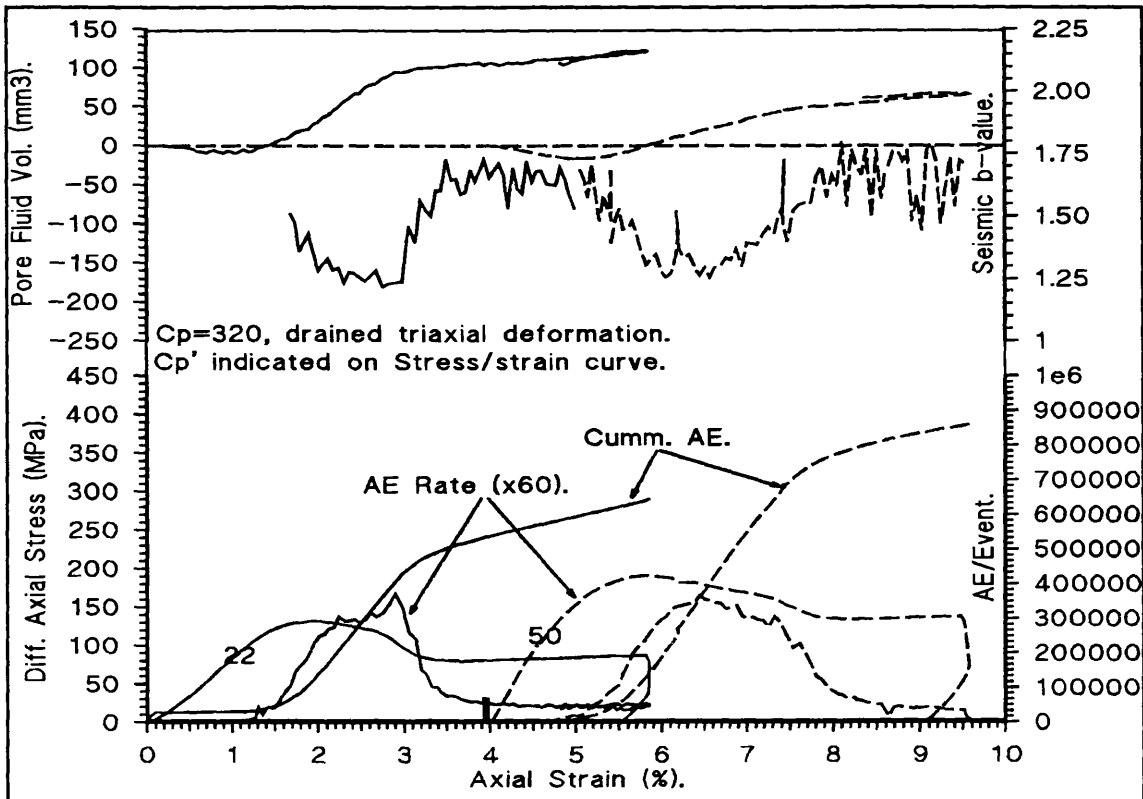


Fig. 6.4.3.2.a. Drained triaxial deformation results on Darley Dale sandstone at  $C_p' = 22$  &  $50$  MPa, see text for details.

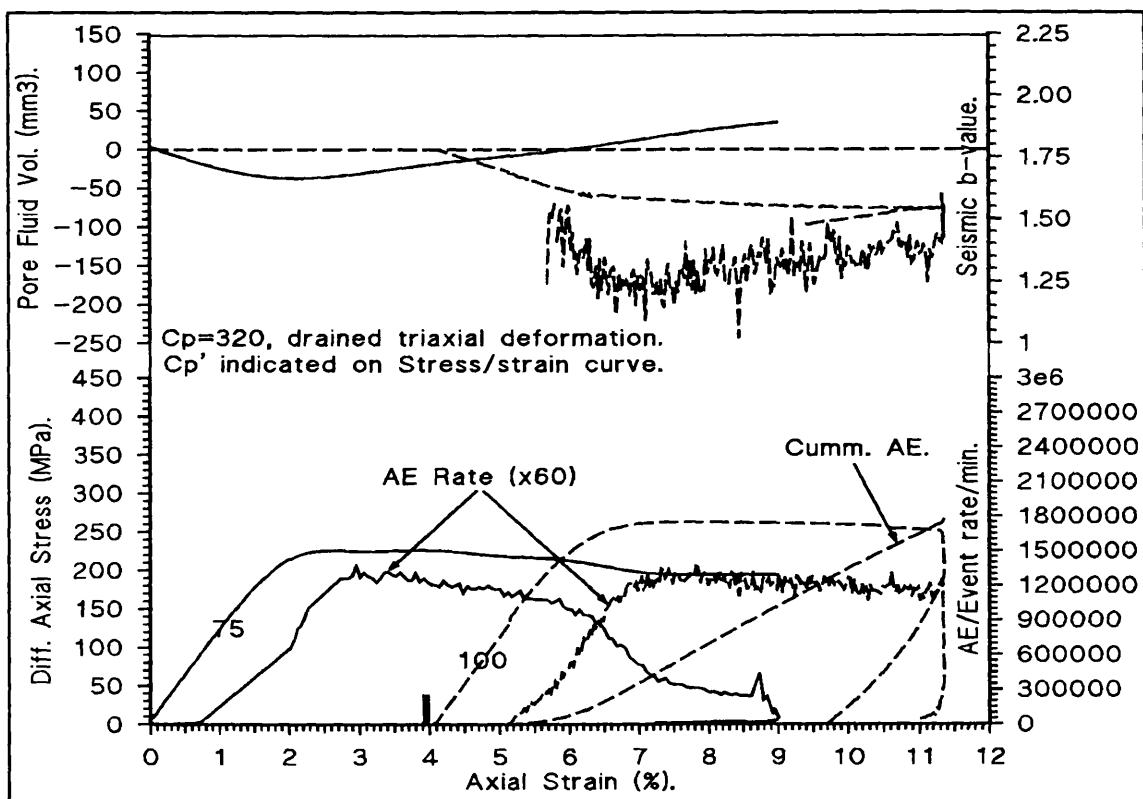


Fig. 6.4.3.2.b. Drained triaxial test result on Darley Dale sandstone at  $C_p' = 75$  &  $100$  MPa, see text for details.

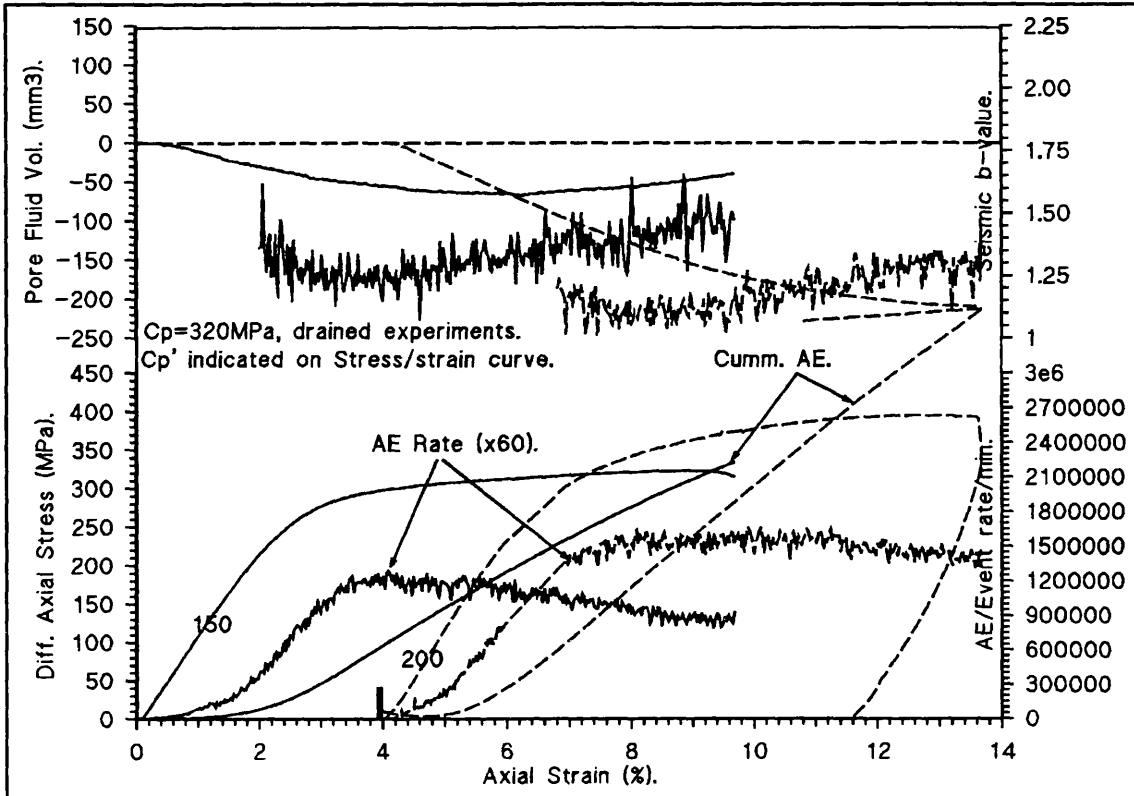


Fig. 6.4.3.2.c. Drained triaxial test results on Darley Dale sandstone at  $C_p' = 150$  &  $200$ MPa, see text for details.

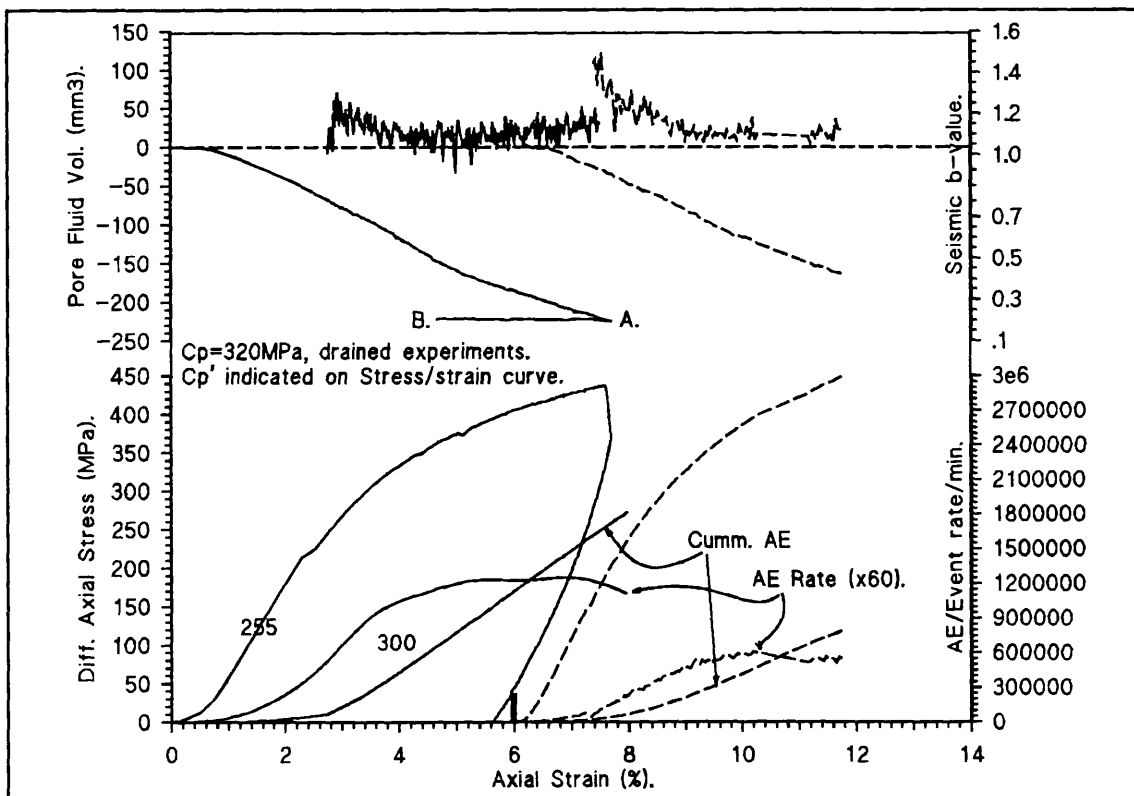


Fig. 6.4.3.2.d. Drained triaxial test results on Darley Dale sandstone at  $C_p' = 255$  &  $300$ MPa, see text for details.

peak stress and dynamic failure - dynamic failure being clearly indicated by a peak in AE event rate and a  $b$ -value minimum. The pore volume changes have been discussed in sections 6.2. and 6.4.3.1.

At an effective confining pressure of 50MPa, deformation characteristics are already showing evidence of transitional behaviour: a broader peak in AE event rate, a  $b$ -value minimum, and reduced dilatancy through the strain softening period. The clearest change in deformation mechanism can be seen in the results at effective confining pressure ( $C_p'$ ) of between 75MPa and 100MPa, (fig. 6.4.3.2.b.); the broad strain softening period at  $C_p' = 75$ MPa followed by faulting failure at  $\epsilon = 6.5\%$ . The pore fluid volume curve shows more compaction than at a lower effective confining pressure, and less dilatancy at the onset of acoustic emissions. At 100MPa, no dynamic faulting occurred in the specimen, and this can be seen by all the indicators discussed above - stress, Pvol., AE and  $b$ -value.

Fig.'s 6.4.3.2.c. & d. ( $C_p' = 150, 200, 255, \& 300$ MPa) show the increasing compaction rate at greater effective confining pressures. Acoustic emissions also commence at an earlier stage in the deformation process under higher effective confining pressures and continues throughout deformation ( $C_p' = 200$ MPa). This is consistent with the findings by Bernabé et al. (1994) which show that the "yield point" of some rocks could be surpassed during the application of a confining pressure alone. The constant accumulation of damage in  $C_p' = 200$ MPa is further indicated by the steady gradient of the cumulative AE curve and the pore fluid volume curve.

Upon unloading, (fig. 6.4.3.2.d.,  $C_p' = 255$ MPa, A→B), pore volume remains constant. This indicates that the majority of deformation is inelastic. The implication of this is that linear elastic deformation includes non-linear deformation too. Another interesting observation is the pore fluid volume curve of the experiment conducted at  $C_p' = 150$ MPa, fig. 6.4.3.2.c. The rock behaves cataclastically, strain hardening after a yield point at  $\epsilon \approx 3\%$ . During deformation pore volume reaches a minimum at  $\epsilon \approx 5.25\%$ , after which an *increase* is observed. This is in agreement with results of Edmond & Paterson (1972). This phenomenon is seen because the specimen was taken to large

enough axial strains. The practice of limiting axial strains to <10% (this study) ensures no breach of the copper jacket. The AE event rate and the *b*-value during cataclastic flow show no clear maximum or minimum indicating only a gradual change in the nature of cracking during deformation.

The pore volume change seen in these four results is a consequence of mean stress causing compaction and deviatoric stress causing new dilatant crack growth. If these components can be separated, more information can be gained concerning the deformation process.

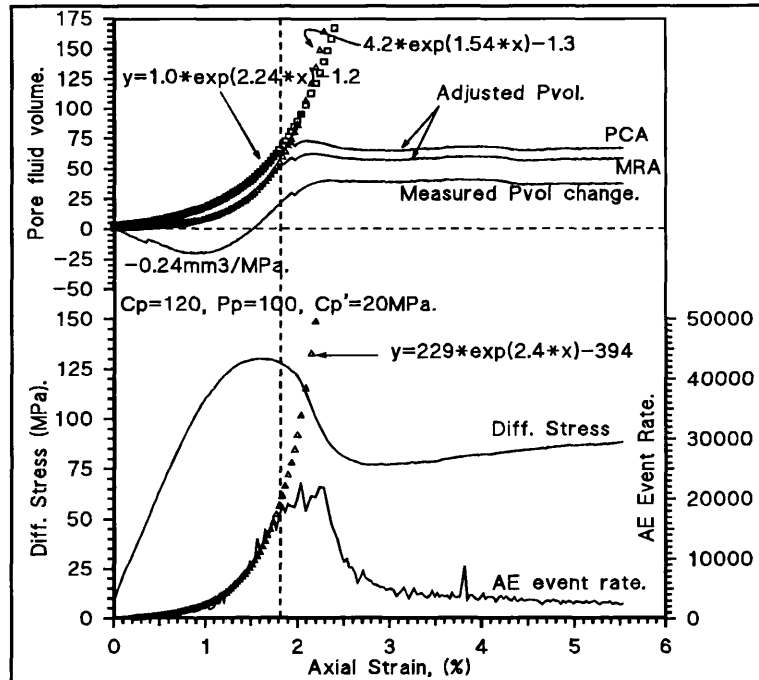


Fig. 6.4.3.2.e. Drained triaxial result at  $C_p' = 20\text{MPa}$ , adjusted pore fluid volume curves attributable to dilatancy alone shown, see text.

In section 6.4.1. the method adopted by Ayling (1991) is reviewed. In fig. 6.4.3.2.e. this method is adopted for the results of a test conducted at  $C_p' = 20\text{MPa}$ , (curve marked MRA). Also presented is an adjusted pore volume curve calculated simply by subtracting *experimentally* derived hydrostatic compaction

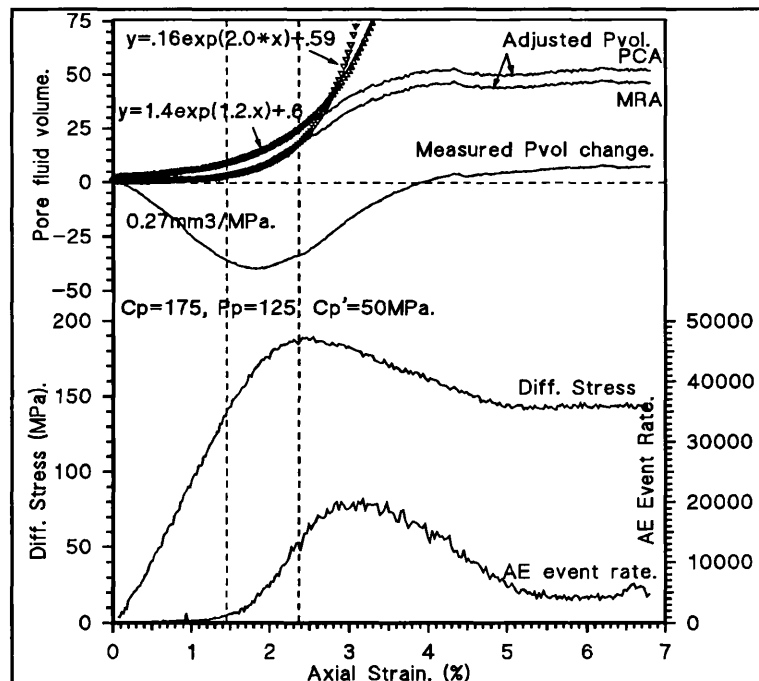


Fig. 6.4.3.2.f. Adjusted (dilatancy) pore volume curve for triaxial test result on Darley Dale sandstone at  $C_p' = 50\text{MPa}$ , see text.

data (a function of mean stress and seen to be non-linear from fig. 6.3.3.3.a. & b.), from the measured pore volume curve for any given mean stress.

The result is seen on the graph as a curve marked "PCA". The difference seen in the two results is due to the MRA method assuming, (i) that the initial compaction period ( $\epsilon = 0.0\% \rightarrow 0.7\%$ ), represents *only* pore compaction and no increase in pore volume due to deviatoric stress induced mechanisms, and, (ii) that this compaction is *linearly* related to differential stress.

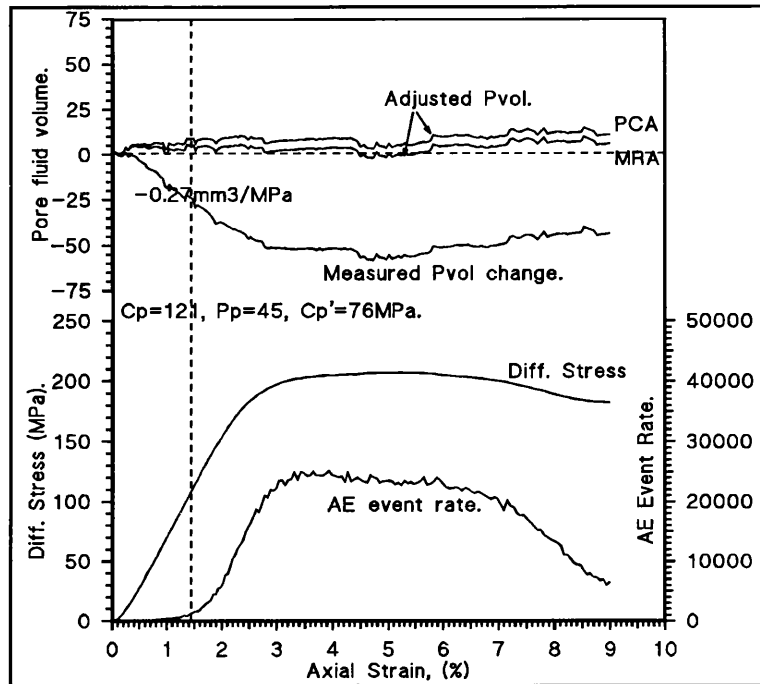


Fig. 6.4.3.2.g. Adjusted pore fluid volume curve (dilatancy) for sandstone at  $C_p' = 75\text{MPa}$ .

The PCA method shows that during the initial stage ( $\epsilon = 0.0 \rightarrow 0.7\%$ ) there *is* some pore volume increase due to the increasing deviatoric stress, probably due to the *bowing* open of cracks orientated parallel to the major principle stress axis. This result shows the change in pore volume is analogous to the change in pore fluid pressure brought about by a differential stress as

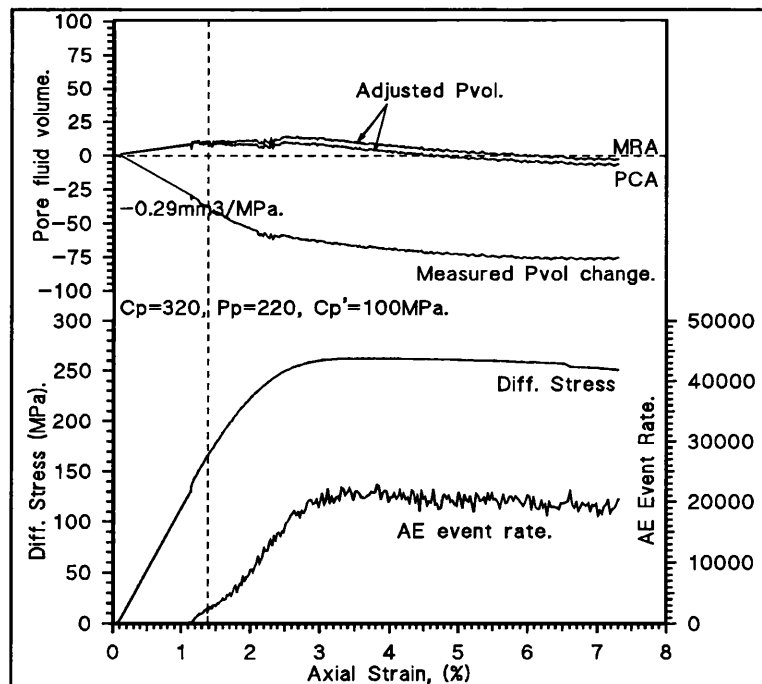


Fig. 6.4.3.2.h. Adjusted pore fluid volume curve (dilatancy) for sandstone at  $C_p' = 100\text{MPa}$ , see text.

described by Skempton's A co-efficient. The A co-efficient is a factor to describing the pore fluid pressure rise due to the the application of a differential load. This is described as;

$$\delta u_3 = B.[\delta\sigma_3 + A(\delta\sigma_1 - \delta\sigma_3)] \quad 6.4.3.2.a.$$

Where  $\delta u_3$  is the overall rise in pore fluid pressure, A & B are Skempton's A and B co-efficients, and  $\delta\sigma_1$  &  $\delta\sigma_3$  are increases in stress in directions 1 and 3.

Fig.'s 6.4.3.2.f., g., h., i., & j., illustrate the

(continued on next page)

same two adjusted pore volume curves for a variety of effective confining pressures (50, 76, 100, 150, & 200MPa).

Fig.'s 6.4.3.2.h., & i., show that both MRA & PCA methods predict some initial pore volume increase.

Although the MRA method predicts this result, due to a poorly selected linear portion of the pore volume curve: the method is designed to accept the initial portion as compaction only, therefore the adjusted MRA curve *should* be flat up to the onset of AE.

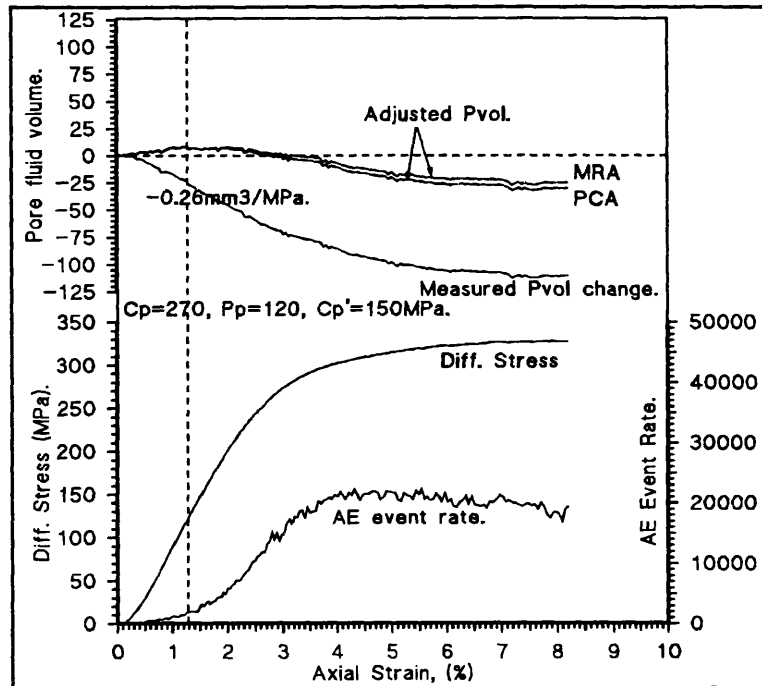


Fig. 6.4.3.2.i. Adjusted pore fluid volume curve for sandstone at  $C_p' = 150\text{MPa}$ , see text.

The largest deviation of the two methods can be seen in fig. 6.4.3.2.j. Here the initial linear portion of the pore volume curve chosen for MRA method was clearly incorrect as seen by the rising adjusted MRA pore volume curve between  $\epsilon = 0.0\% \rightarrow 3.3\%$ . There is also a large difference between the two adjustment methods beyond 3.3%.

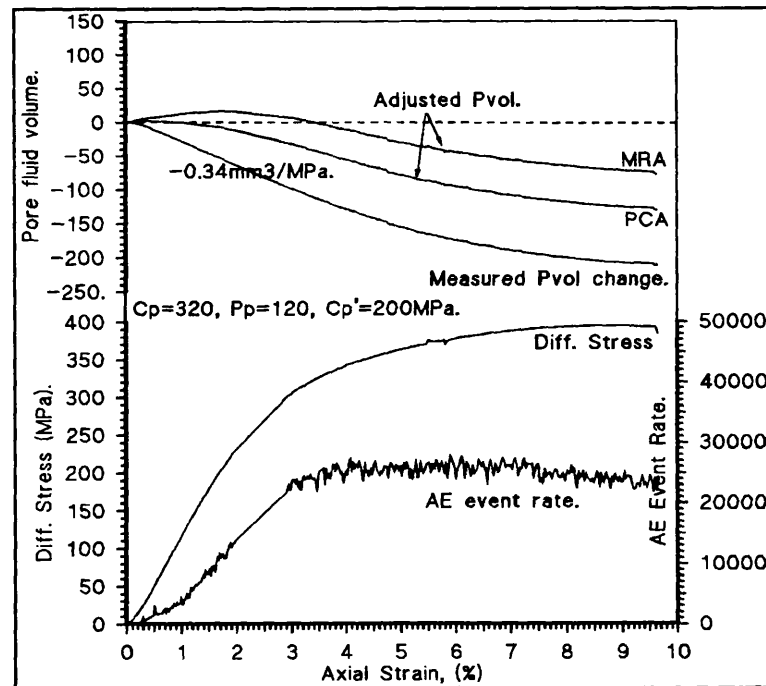


Fig. 6.4.3.2.j. Adjusted pore fluid volume curve for sandstone at  $C_p' = 200\text{MPa}$ , see text.

These six graphs above are summarised in fig.'s

6.4.3.2.k., & l. showing only the adjusted pore fluid volume curves using PCA method. The results show that during cataclastic flow ( $C_p' = 150$  &  $200$ MPa), deviatoric stress actually causes *compaction* of the specimen. It can be concluded that under the effect of an effective confining pressure (mean stress) of  $200$ MPa, the rock yielded and the application of a differential axial stress caused grain rotation and rearrangement, and a reduction in pore volume. At  $C_p' = 76$ , &  $100$ MPa, it appears that deviatoric stress induced mechanisms (rearrangement of fractured grains *and* NDC growth), cancel each other out causing no change in pore fluid volume.

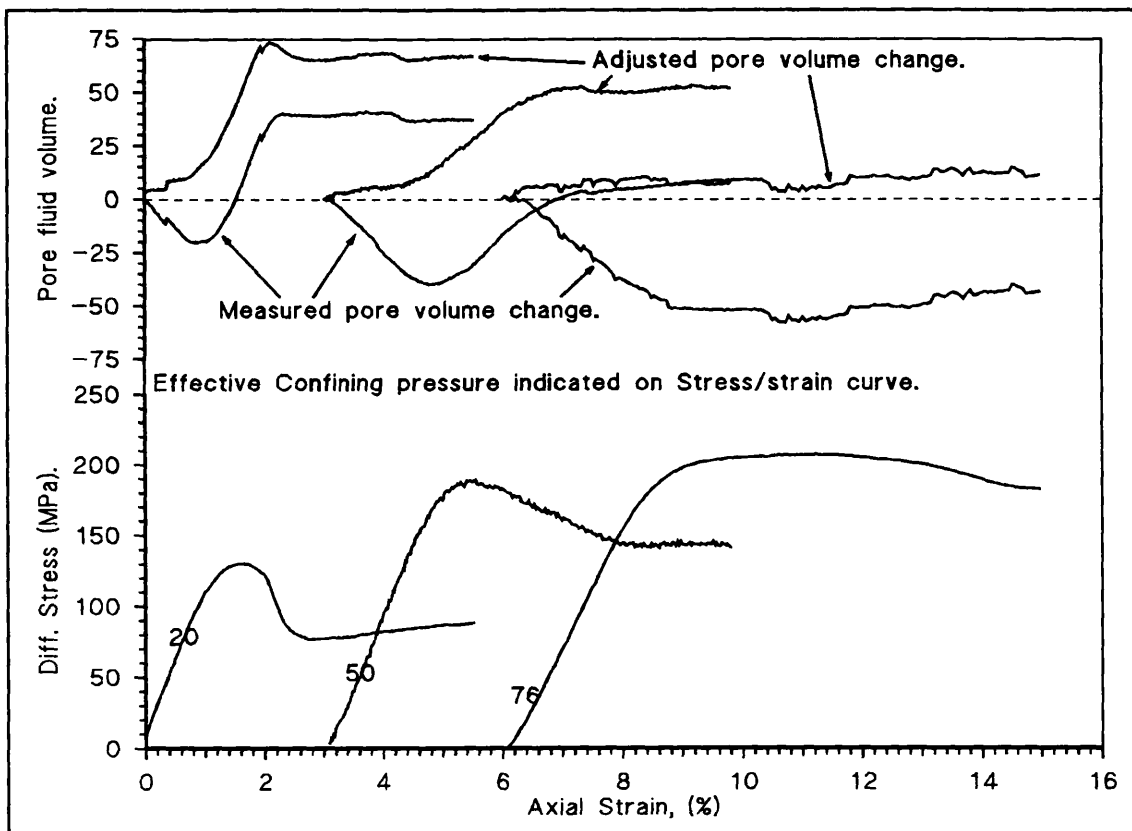


Fig. 6.4.3.2.k. Compilation of figures 6.4.3.2.e., f., & g., "PCA" adjustment method only for comparison purposes, see text.

Finally, in fig.'s 6.4.3.2.e. & f. ( $C_p = 20$  &  $50$ MPa), where deformation is such that the largest component of pore volume change is deviatoric stress induced dilatant crack growth, analysis has been conducted on the rate of increase in dilatant pore and crack volume. Acoustic emissions leading up to peak stress rise exponentially with increasing stress just as in pre-rupture seismicity observations in earthquake prediction (Scholz 1968). In the figures, a simple exponential curve fitting process using commercially available software has been conducted on the *adjusted* pore fluid volume curve, as can be seen by

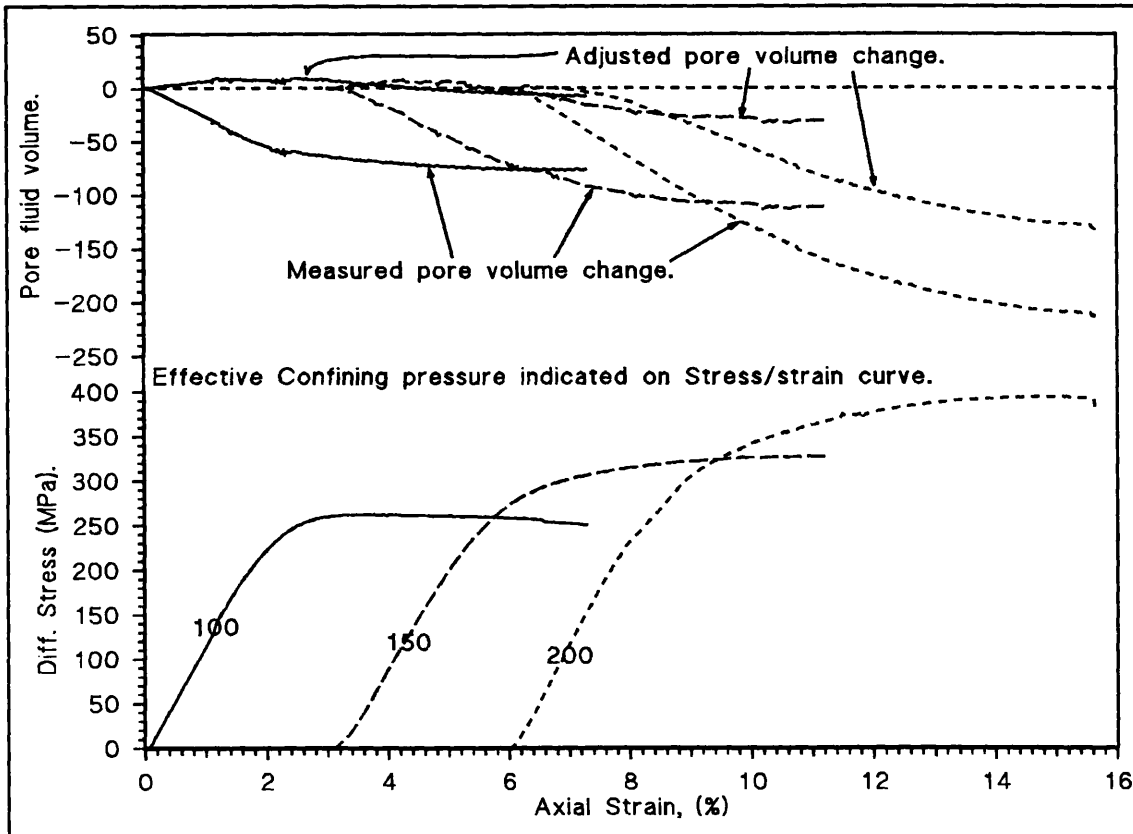


Fig. 6.4.3.2.i. Compilation of figures 6.4.3.2.h., i., & k., "PCA" adjustment method only, for comparison, see text.

data point symbols. Clearly, new dilatant crack growth causes an exponentially increase in pore volume along with AE. This point reinforces the connection between AE and dilatant crack growth in triaxially stress rocks. A power law fit was not attempted and no further analysis has been conducted on this matter in this present study.

*In summary.* Of the two methods for adjusting the measured pore volume curve to eliminate the mean stress induced compaction component of pore volume change under triaxial loading, the method based on experimentally derived compaction data indicates deviatoric stress induced pore volume loss occurs at confining pressures of  $>150$ MPa. The shift from gross brittle fracture to cataclastic deformation is associated with the elimination of dilatant crack growth and the promotion of deviatoric stress induced grain fragment rearrangement and associated pore volume decrease. At large strains ( $>10\%$ ) and  $C_p=76$ MPa, pore volume was seen to increase after initially decreasing. This was found in one result only. At transitional confining

pressures between brittle faulting failure and cataclastic flow, deviatoric stress induced compaction and dilatant crack growth cancel out.

Under triaxial stress conditions conducive to gross brittle fracture, ( $< 100\text{MPa}$ ), the pore volume increase resulting from dilatant crack growth increases exponentially. The equations of the exponential fits are given in fig.'s 6.4.3.2.e. & f.

### 6.4.3.3. Analysis of Elastic and Inelastic Contribution to Pore Volume Change During Triaxial Stressing.

Pore volume reduction of Darley Dale sandstone due to the application of a uniform mean stress of  $400\text{MPa}$  has been shown in fig. 6.3.4.2.b to comprise of  $\approx 2/3$  *elastic* compression of the mineral "frame" or "skeleton", and  $\approx 1/3$  *inelastic* compaction, probably due to pore collapse, micro-fracturing (grain crushing), and rotation and re-arrangement of resultant material.

Under the effect of a differential axial compressive stress, both the mean stress and the deviatoric stress increase causing a complex interplay of pore volume change mechanisms as discussed above in section 6.4.3.2. Whether this pore volume change is elastic or inelastic has been qualitatively investigated in the present study through cycling the differential axial load at various stages of triaxial deformation, - a similar procedure to that conducted by Bernarbé et al. (1994). Elastic/inelastic components of deformation in this case have been observed from the pore fluid volume change under drained conditions.

In fig. 6.4.3.3.a. the stress/strain and pore fluid volume curves of five triaxial deformation test results are shown. The pore fluid pressures in all the tests were  $20\text{MPa}$ . The effective confining pressure is shown against each stress/strain curve (a)→(e). The stress cycling effect on the pore fluid volume is seen circled and numbered on the figure, (aii→ei), and vertical lines connect the axial stress cycle to the pore volume cycle. Salient points from the figure are highlighted below.

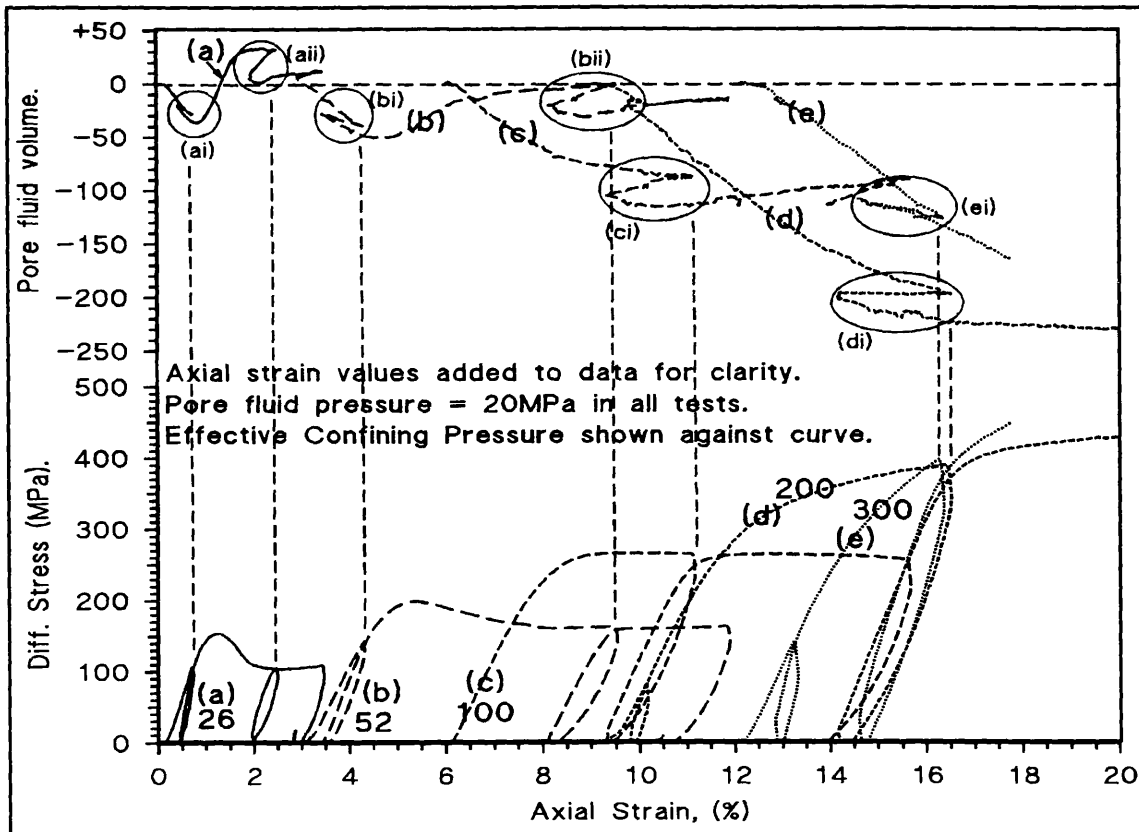


Fig. 6.4.3.3.a. Five triaxial deformation results showing the effect of cycling the differential axial load on the pore fluid volume under different effective confining pressure, see text.

- ▶ It can be seen during shearing failure (curve a), different mechanisms (compaction followed by dilatancy) cause different responses during differential axial stress cycling - (ai) and (aai). The first cycle (ai) shows nearly all the compaction is elastic, whereas the second cycle (aai) shows only ~50% of the dilatant pore volume increase is elastic. Furthermore, this elastic recovery is not regained upon reapplication of differential stress - stable sliding on the fault plane continues at a reduced rock pore volume. The stress cycles during the initial stages of deformation on curves (a) and (b), show a slight change from purely elastic compaction in (ai), to some permanent pore volume loss in (bi).
- ▶ The stress cycles during post-peak/yield deformation (aai, bai, cai, dai, eai), clearly shows a progressive shift in the behaviour of the rock under increasing effective confining pressures. During unloading at low effective confining pressures (aai), a permanent loss in pore volume occurs, at high effective confining pressures (eai), the pore fluid volume curve behaves in a similar fashion to the hydrostatic compaction

cycling curves of fig. 6.3.3.3.a. & b.; some of the pore volume loss is permanent, and some recoverable, with the reloading path following the unloading path. Under effective confining pressure of 200MPa (di), the mechanisms causing permanent loss and temporary loss of pore volume are cancelled to produce *no change* in pore volume during unloading. Reloading invokes further loss in pore volume.

The three pore volume change mechanisms thought to occur during deviatoric and mean stress cycling all contribute during unloading and reloading to different degrees depending on the confining pressure. It is thought that the mechanism of dilatant crack growth (dominant at  $C_p' < 75\text{MPa}$ , curves (a) & (b)), is highly inelastic; permanent pore volume change occurring during an increase *and* a decrease in differential axial load. The mechanism must therefore

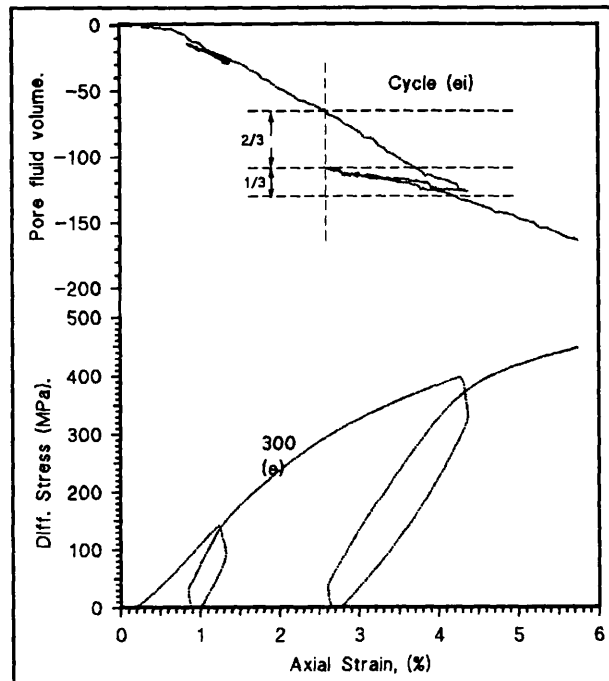


Fig. 6.4.3.3.b. Expanded curve (e) from fig. 6.4.3.3.a., showing elastic and inelastic components of deformation, see text.

comprise of fracture and frictional sliding with very little pore volume loss due to elastic compression of the rock frame or bowing open of suitably orientated cracks. Hydrostatic stress cycling up to 450MPa (fig. 6.3.4.2.b.), shows that  $\approx 3/5$  of pore volume loss is elastic and  $\approx 2/5$  is permanent - *i.e. the majority is elastic*.

Fig. 6.4.3.3.b. (enlargement of curve (ei) in fig. 6.4.3.3.a.), shows, however, that during triaxial stressing of Darley Dale sandstone,  $\approx 1/3$  of pore volume loss is elastic and  $\approx 2/3$  is permanent - *i.e. the majority is inelastic*. Since at  $C_p' = 200\text{MPa}$  in fig. 6.4.3.2.I. the majority of compaction under triaxial loading is deviatoric stress induced ( $\approx 1/3$  mean stress induced and  $\approx 2/3$  deviatoric stress induced), it is therefore reasonable to conclude that deviatoric stress induced compaction is responsible for the permanent pore volume loss in the

cycle of curve (ei). Overall one can say that deviatoric stress induced mechanisms, be they compaction or dilatant, are largely inelastic.

*In summary.*

- ▶ Deviatoric stress induced compaction under the initial stages of deformation is mostly *elastic*, consisting of closure of suitably orientated microcracks (unless at very high confining pressures after which the rock has yielded), see cycles (ai) & (bi).
- ▶ Deviatoric stress induced dilatant crack growth is largely *inelastic*, occurring during the application *and* removal of deviatoric load, and must therefore include energy absorbing mechanisms such as granular and intergranular fracture, and frictional sliding (grain rearrangement), (aii) & (bii).
- ▶ Deviatoric stress induced compaction is largely inelastic and mean stress induced compaction is  $\approx 2/3$  elastic and  $\approx 1/3$  permanent. This latter mechanism is mainly frame compression under the stress levels employed in this study, whilst deviatoric stress induced compaction must be mainly grain fracture and frictional sliding (di) & (ei).

#### 6.4.3.4. Analysis of the Mean-Stress-Induced and Deviatoric-Stress-Induced Pore Volume Change During Triaxial Deformation.

To further examine the influence of deviatoric stress on pore and crack volume change during deformation under a variety of stress conditions, a number of results from the suite of experiments in fig. 6.4.2.a. have been plotted in fig. 6.4.3.4.a. in 3-D space of *effective mean stress*, *deviatoric stress*, and *percent pore fluid volume change from un-stressed state*. The stress paths are shown as lines of dots. The surface connecting the dots (generated using commercially available *Gino-surf* software), shows significant undulations running sub-parallel with the deviatoric stress axis. Unlike many of the smaller undulations, these "ridges" are real phenomena resulting from

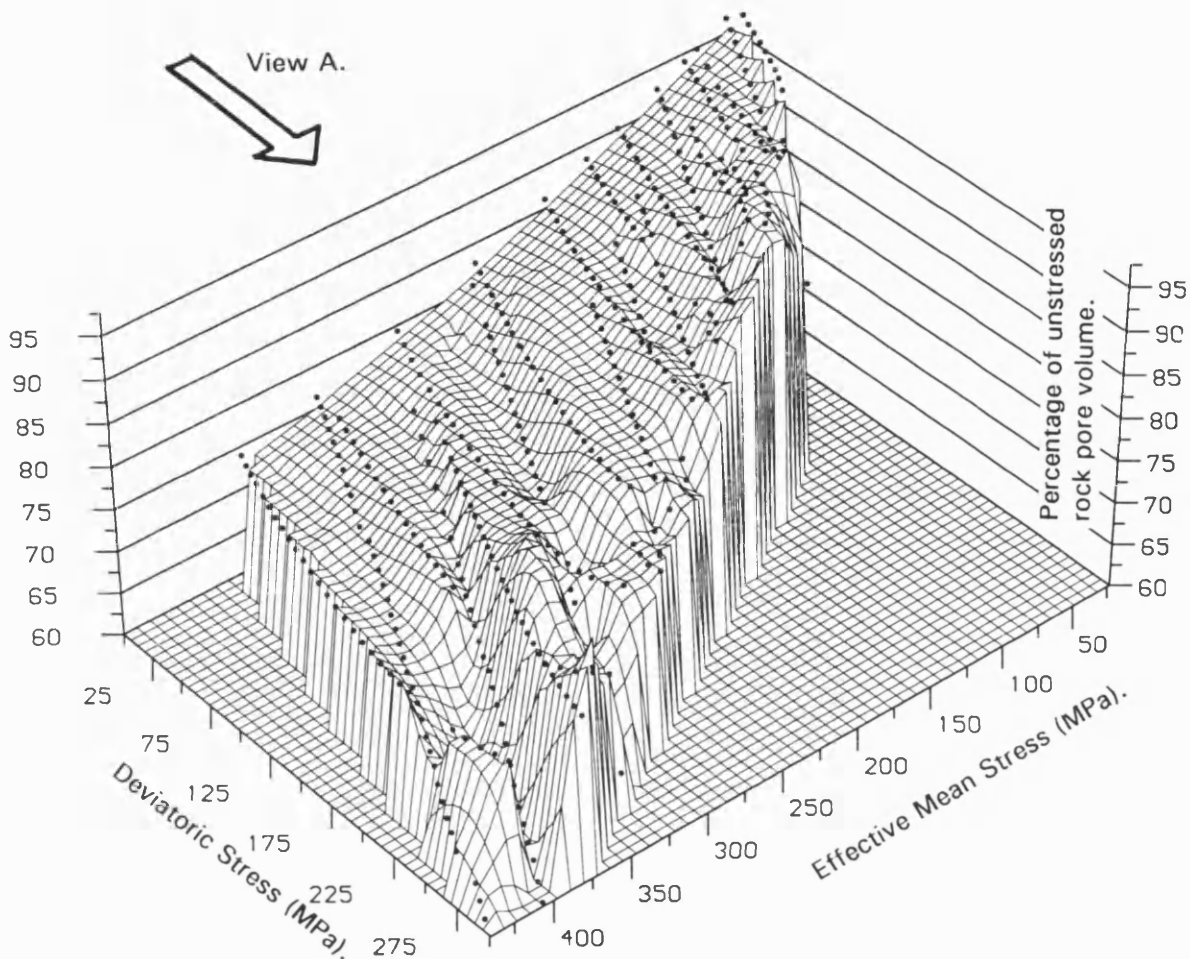


Fig. 6.4.3.4.a. Drained and undrained results plotted in 3-D space of effective mean stress, deviatoric stress, and pore fluid volume change, see text.

the attempt to plot both drained and undrained data on a single surface.

Fig. 6.4.3.4.b. shows view A of fig. 6.4.3.4.a., and displays these ridges more clearly. The stress paths maintaining a constant horizontal displacement (constant pore volume) are the undrained results, and those decreasing with increasing effective mean stress (decreasing pore volume) are the drained results. The reason for the apparent non-conformity between drained and undrained data (not lying on the same surface), lies with the URV affecting the pore fluid pressure generated during undrained experiments, and hence effectively representing a material of different poro-elastic properties (different  $K_v$ ). This reduced pore fluid pressure results in greater effective means stress and deviatoric stress. This displaces the undrained stress paths in the positive mean and deviatoric stress direction. Furthermore, undrained conditions assume constant fluid mass in the sample and near constant pore

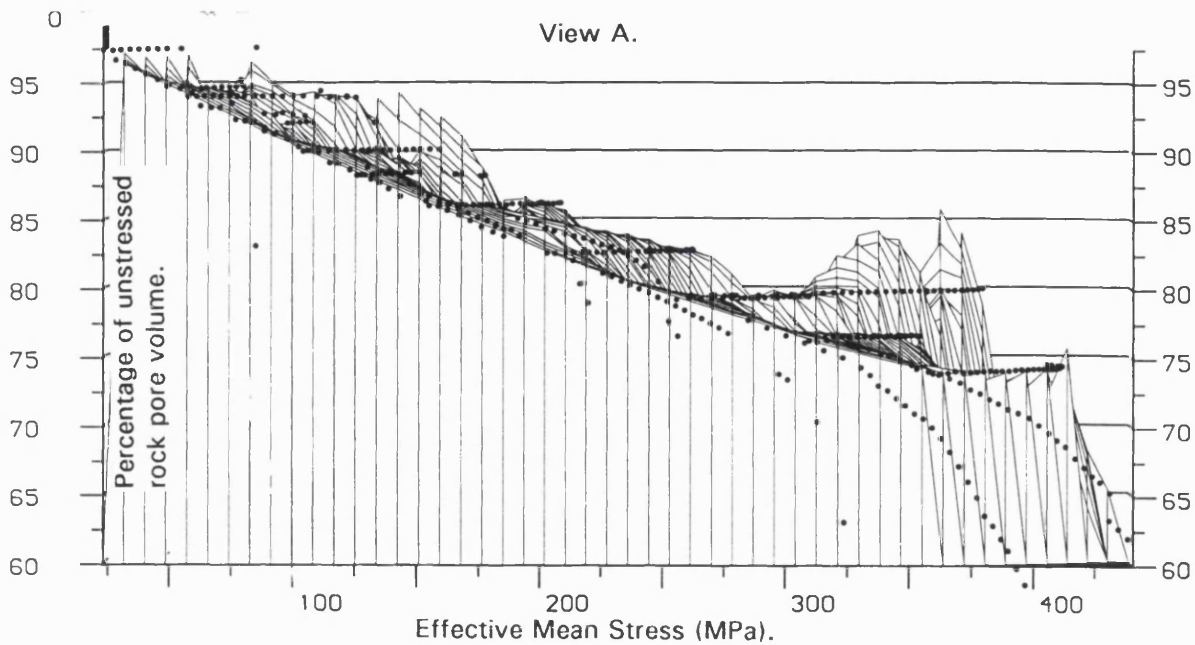


Fig. 6.4.3.4.b. View A of figure 6.4.3.4.a. showing the undrained stress paths deviating from the drained surface due to fluid flow from the specimen to the URV, see text.

volume.

This latter assumption is violated firstly by a rising fluid pressure (hence pore volume must be decreasing), and secondly by fluid flow from the specimen into the URV system, further decreasing actual rock pore volume. These factors result in the stress paths standing out from the surface as seen in the figures 6.4.3.4.a. & b. It must be noted in these plots that the stress paths shown represent deformation up to peak stress only under shear faulting conditions; in the development of fig. 6.4.3.4.a. it became apparent that post-peak deviatoric stress reduction caused the stress paths to curve below the surface seen, and prevented the generation of a smooth surface.

Fig. 6.4.3.4.c. shows the results of the suite of drained tests only. The stress paths in the deviatoric/effective mean stress space (base of plot) are straight as expected, since these stresses are linearly related to differential stress. The surface is also much smoother after the elimination of the undrained results.

If the plot is viewed from "view B", the effect of increasing deviatoric stress alone can be observed under a variety of constant effective mean stresses, (fig. 6.4.3.4.d.). The sub-horizontal mesh-lines seen on the surface represent

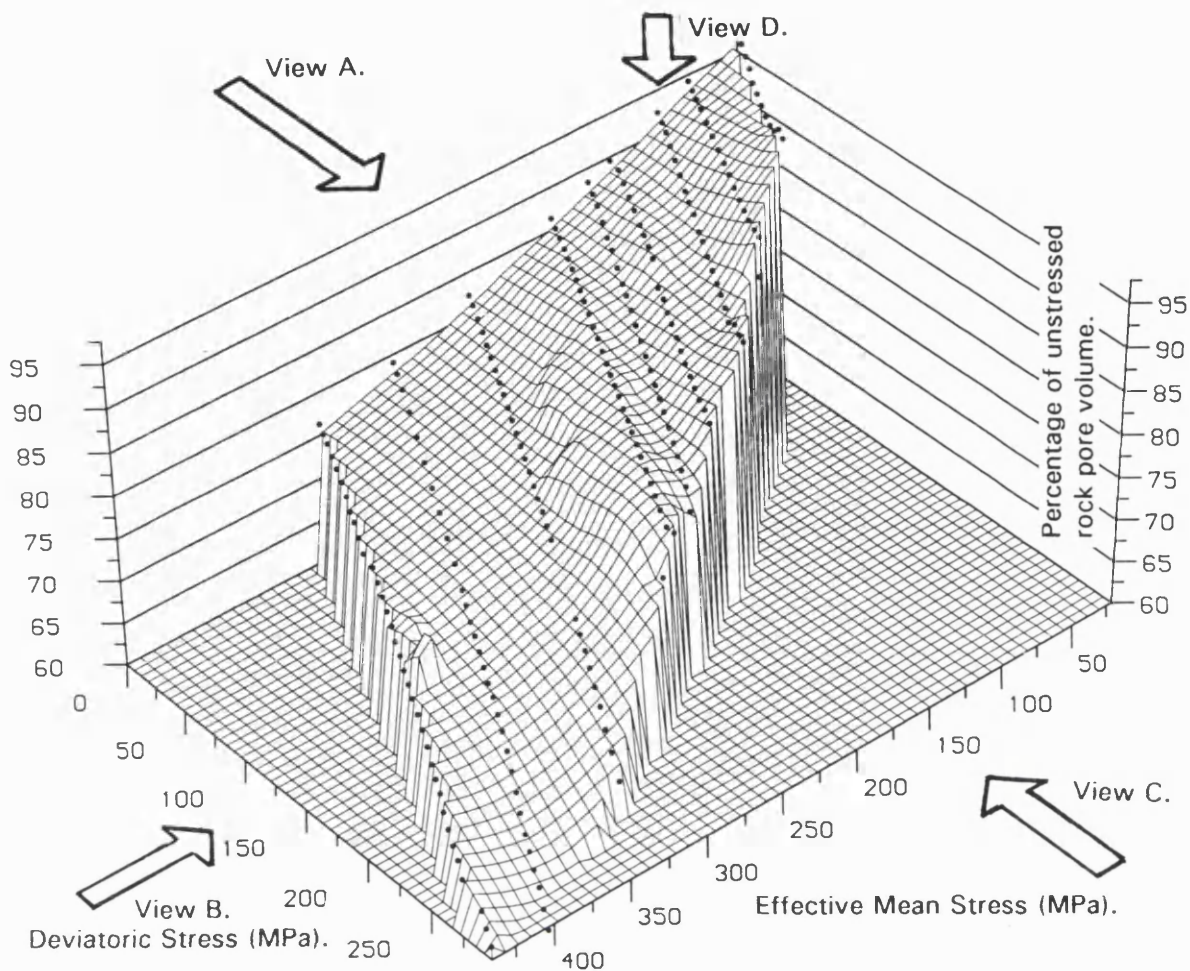


Fig. 6.4.3.4.c. Drained triaxial 3-D surface in deviatoric stress, effective mean stress, and pore fluid volume change, see text.

constant mean stress and increasing deviatoric stress. It can be seen that at low effective mean stresses (near stress path 1→5, corresponding to effective mean stress at the commencement of the tests of 0→125MPa, see fig 6.4.3.4.e.), the effect of increasing deviatoric stress is to *increase* pore volume. For stress path 6, corresponding to effective mean stress of 150MPa, ignoring minor undulations, the effect of deviatoric stress on pore volume change is zero, again due to dilatancy and compaction cancelling out. At effective mean stress of 200MPa+, stress paths 7→9, the effect of deviatoric stress alone causes a decrease in pore volume. This is consistent with results in fig.'s 6.4.3.2.k.→l. The effect of an effective mean stress alone is shown in fig. 6.4.3.4.f. Pre-yield pore volume change with effective mean stress is as found from drained hydrostatic experiments in fig. 6.3.4.2.b. - "total" curve. Post yield pore volume change causes an increase or a decrease in pore fluid volume depending on effective mean stress, (40→150MPa, or 250MPa+, respectively).

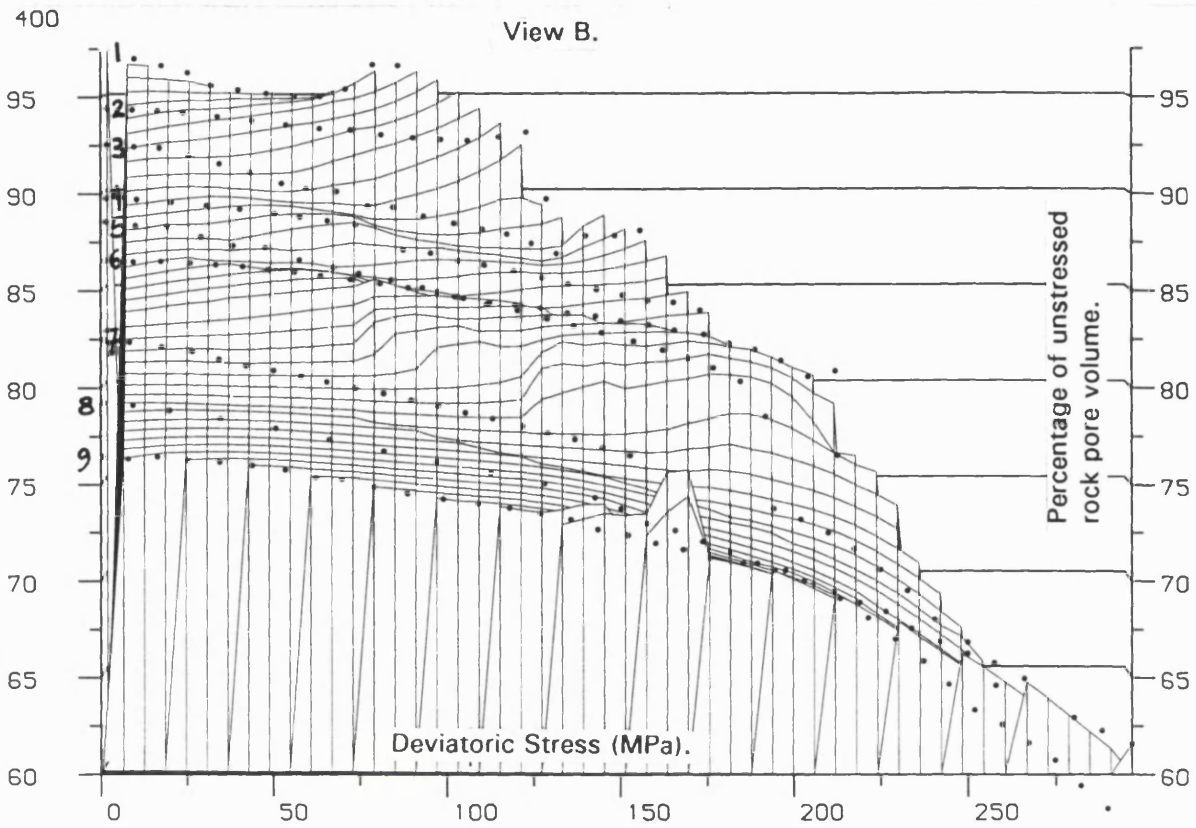


Fig. 6.4.3.1.d. Effect of deviatoric stress on pore volume under different effective mean stress, see text.

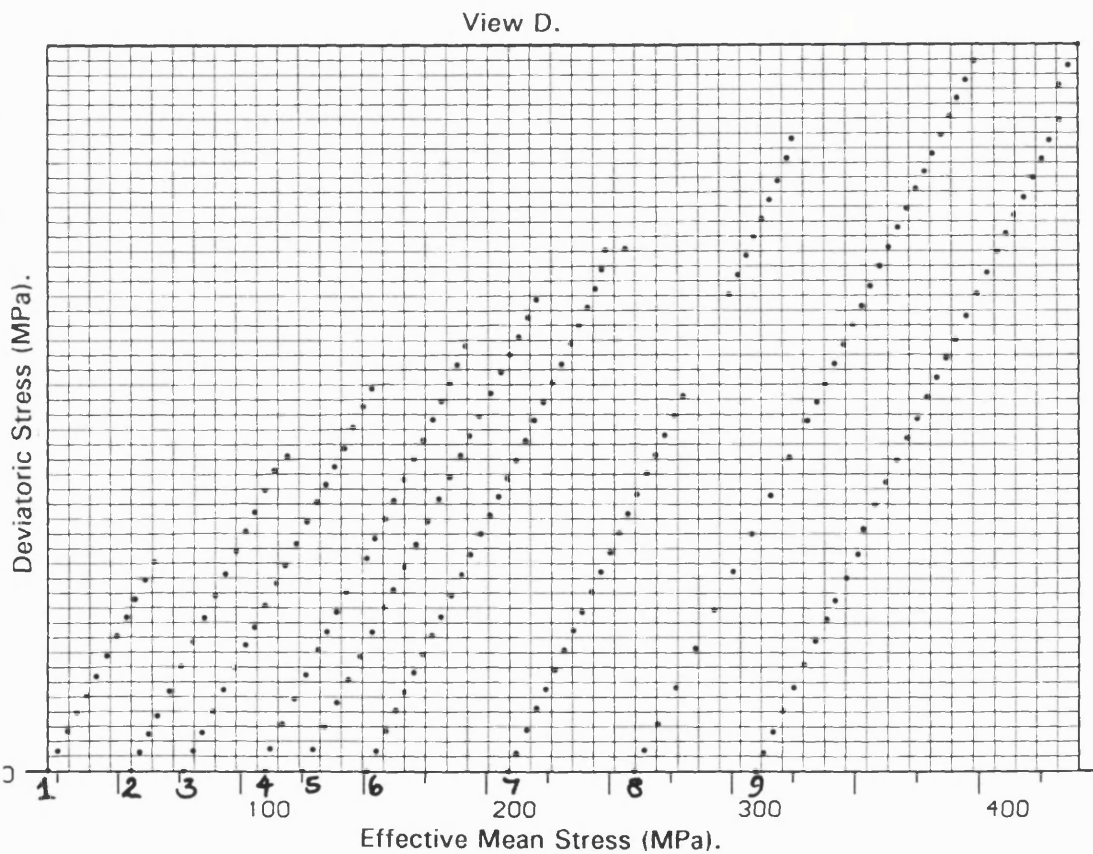


Fig. 6.4.3.4.e. Deviatoric and effective mean stress change due to increasing differential axial compressive stress. Stress paths are linear up to peak of yield stress, see text.

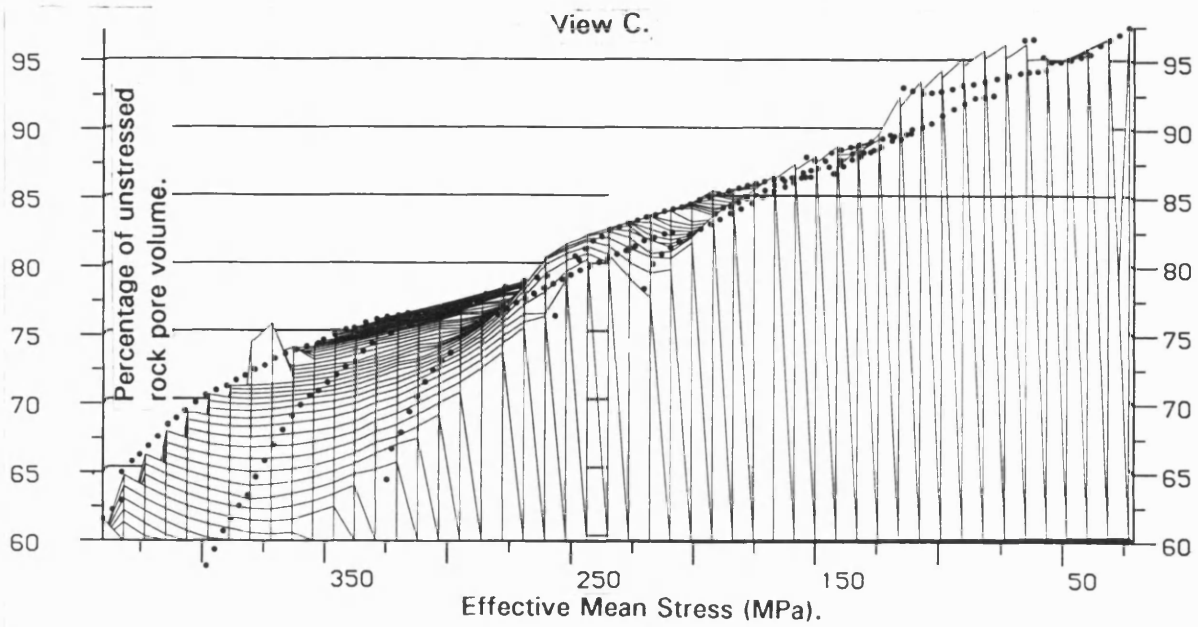


Fig. 6.4.3.4.f. View c. of figure 6.4.3.4.c., showing effect of effective mean stress pore fluid volume, see text.

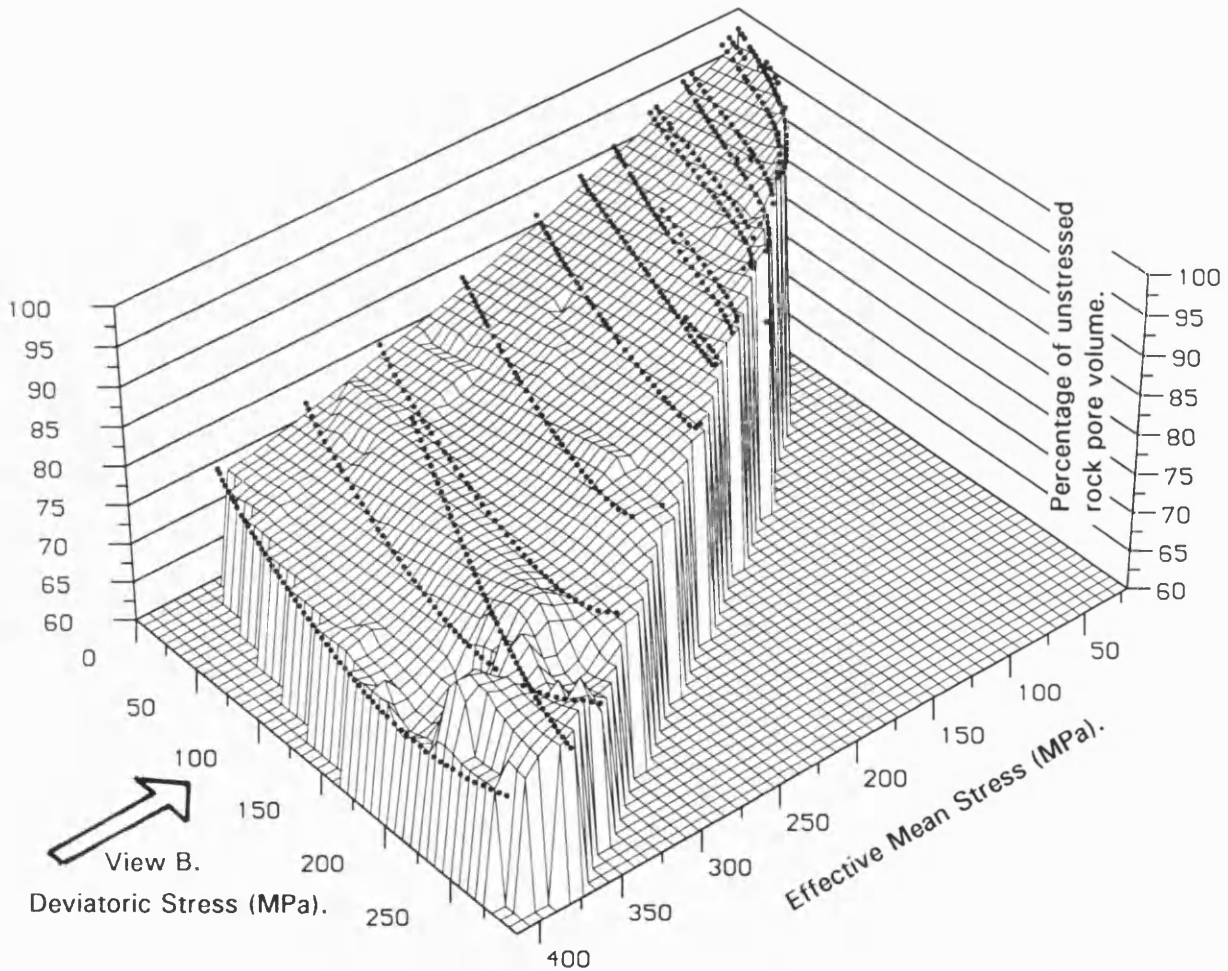


Fig. 6.4.3.4.g. Suite of undrained triaxial deformation results in 3-D space of effective mean stress, deviatoric stress, and pore fluid pressure change, see text.

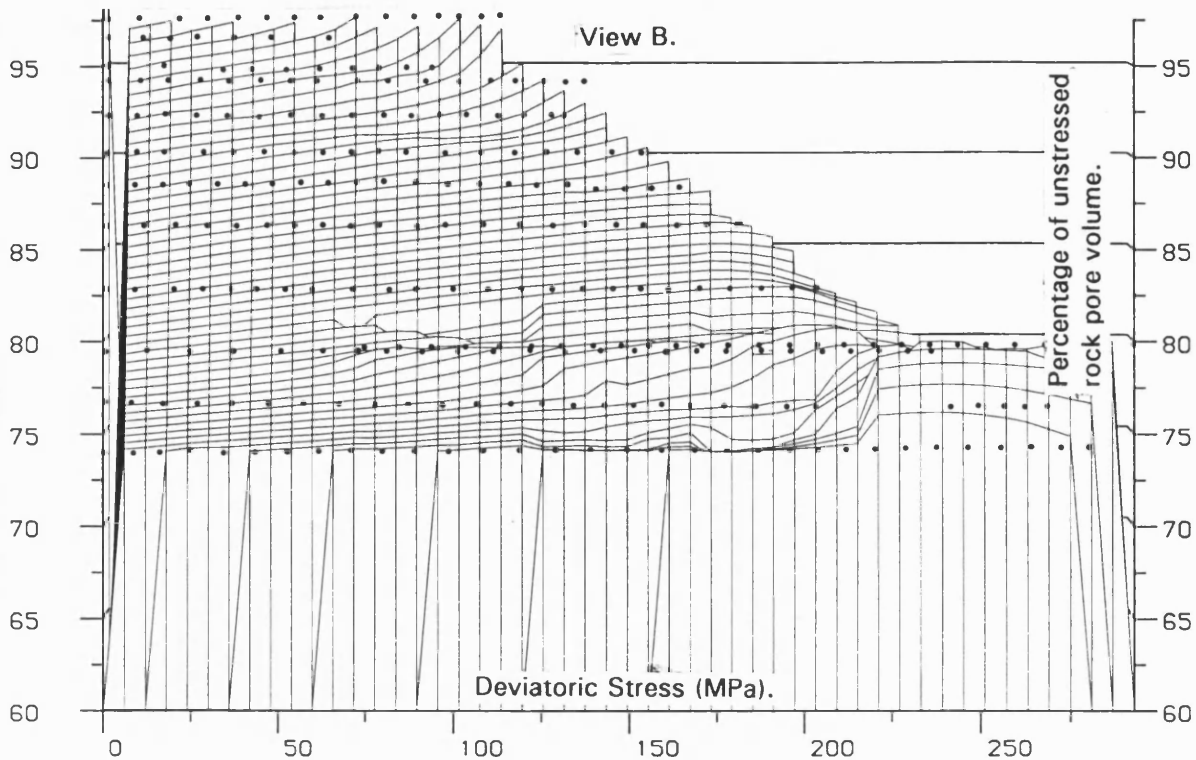


Fig. 6.4.3.4.h. View B. of fig. 6.4.3.4.g., showing effect of deviatoric stress alone on undrained specimens of sandstone, see text.

The undrained results are plotted in fig. 6.4.3.4.g. The stress paths are horizontal in the vertical axis (zero pore fluid volume change) as discussed above. The effect of a deviatoric stress alone (indicated by the sub-horizontal mesh-lines in fig. 6.4.3.4.h.), shows a gradual *increase* in pore volume for an increase in deviatoric stress throughout the effective mean stress range. This is a result of the assumptions of undrained triaxial deformation discussed above; the changing pore volume and elevated deviatoric and effective mean stresses (due to effect of URV). From this analysis it is clear that unless the URV is very small, or pressure and volume change correction factors are used, undrained test results do not accurately represent the behaviour of the rock under stress.

The method of plotting results in this way indicates better the effect of a given stress path on pore volume change and whether deviatoric or mean stress is responsible for a given pore volume change. The method also indicates the need for better control of mean stress and deviatoric stress during deformation to allow the effect of these stresses to be more accurately determined.

*In summary.*

- ▶ Three dimensional plots of pore fluid volumometry against effective mean and deviatoric stress allows better determination of components of pore volume change attributable to deviatoric and effective mean stress.
- ▶ Effective mean stress alone (constant deviatoric stress) reduces pore volume as found in the hydrostatic test results. This persists until yielding, beyond which pore volume decrease accelerates under increasing mean stress.
- ▶ Deviatoric stress causes dilatancy under low effective mean stress (<125MPa - brittle faulting failure), has zero effect (or a cancelling effect) between 125→200MPa (transitional between brittle faulting failure and cataclastic flow), and causes pore volume decrease under higher effective mean stresses, (200MPa+), (fig. 6.4.3.4.d.) This is in agreement with results from section 6.4.3.2.
- ▶ Undrained triaxial pore volumometry results require fluid pressure *and* pore volume correction factors to represent accurately poro-elastic rock behaviour. Without such correction, undrained results only qualitative represent the effect of a confined fluid mass on deformation. In reality this represents the effect of a low permeability confining rock surrounding the deforming rock. Whilst this is important, it is difficult to quantify in these laboratory experiments.

**6.4.4. Future Work.**

The four sub-section of this section have dealt with mechanisms and causes of pore volume change in deforming rocks, and the effect of elevated pore fluid pressure on deformation. The work has led to the following recommendations for future work.

- ▶ **Conducting a more thorough and quantitative examination of elastic and inelastic deformation components under a variety of stress conditions. This will yield information about the nature of the different deformation mechanisms occurring during triaxial stressing.**
  
- ▶ **Control effective confining pressure during the application of a differential stress. This will allow the application of deviatoric or mean stress alone, and yield information on the sensitivity of damage accumulation, and of different mechanisms to different stress paths and magnitudes.**
  
- ▶ **Quantification of, (i) the 3-D surfaces representing the poro-elastic response of the rock to allow prediction of the rock under any stress condition, and (ii) elastic and inelastic response of the rock under changing stress conditions.**
  
- ▶ **Devise a means of removing the effect of an URV interactively during undrained triaxial deformation, e.g. in undrained tests use the servo-controller to ensure that the *mass* fluid in the rock remains constant. This would require that as pore fluid pressure increases due to compaction (fluid expelled from specimen into URV), the intensifier piston moves to force fluid back into the specimen. Similarly, as the pore pressure decreases due to dilatancy and fluid flows from URV into specimen, the intensifier piston should move to reduce pore fluid pressure and allow fluid to flow out of the specimen.**

Alternatively the URV could be eliminated by separating fluid in the intensifier from fluid in the specimen by a membrane strain gauge situated at the end cap. A change in pressure between that in the specimen and that controlled by the intensifier will be detected by strain on the membrane. The servo-controlled intensifier piston would then move to eliminate the pressure difference, and the pressure recorded from the intensifier pressure transducers.

- ▶ An examination of pore fluid volume change under extended axial strain (>20%). One result in this suite of experiments showed pore fluid volume reaching a minimum during cataclastic deformation, rising thereafter. Very few results under cataclastic flow conditions have indicated a final and stable pore volume. Examining the possibility of a *critical pore volume* for sliding is a area of rock physics requiring attention.

## **6.5. Effects of High Temperature on Drained and Undrained Triaxial Deformation.**

### **6.5.1. Introduction and General Review.**

The effect of an increase in confining pressure on compressive triaxial deformation of polycrystalline rock is to change the mode of deformation from brittle faulting, through cataclastic flow, to ductile flow. The exact confining pressure at which the change from cataclastic flow to ductile flow occurs - the brittle/ductile transition (since cataclastic flow is fundamentally brittle) - for any given rock type is strongly dependent upon temperature, strain rate, and grain size. By careful selection of grain size, temperature, or confining pressure, ductile flow mechanisms can be induced in laboratory experiments that only normally occur in the crust at strain rates of  $10^{-14}$ /s or less, i.e. for any given grain size and strain rate, an increase in temperature promotes ductility by lowering the confining pressure at which the brittle/ductile transition occurs (exception where dehydration causes embrittlement).

This brittle/ductile transition pressure can be considered the point at which the applied stress exceeds the plastic flow stress, hence ductile mechanisms (outlined in section 2.4.2.2.) replace distributed microcracking as the dominant cause of rock strain, (Murrell 1990). Approaching the brittle/ductile transition, both micro-cracking *and* ductile mechanisms can occur, and hence at temperatures below the brittle/ductile transition small amounts of creep are observed, (Murrell & Chakravarty, 1973).

Whilst the increase in ductility with confining pressure is well established, experimental evidence suggests for many rocks that an increase in temperature alone is ineffectual in inducing ductile flow, and that a small confining pressure is also required (Murrell & Chakravarty 1973). This is attributed to, among other factors, the suppression of grain boundary parting that otherwise occurs due to differential thermal expansion, and the avoidance of decomposition and hence rock disintegration, (Paterson 1978).

One exceptional case is Solnhofen limestone where ductility is induced at 500°C under zero confining pressure, (Heard 1960).

The presence of a pressurised fluid in the rock pore structure during high pressure/temperature experiments reduces the effective confining pressure as per the effective stress law, so long as strain hardening is avoided with sufficiently low strain rate, (Rutter 1972a). The chemical effect of fluids on rocks is discussed in section 2.5.6. This effect is exacerbated when the fluid is under elevated temperature and pressure. For a full review of ductile mechanisms the reader is referred to Murrell 1990, and Tullis 1990.

From the experimental data reviewed above it is clear that the temperatures employed in this study are far below the brittle/ductile transition, and the *brittle faulting failure/cataclastic flow* transition is more pertinent to this suite of results. The experiments have employed, for the first time in the laboratory at UCL pore volumetry measurement techniques during high temperature triaxial deformation experiments. The mechanisms occurring and factors affecting cataclastic flow and the faulting failure/cataclastic flow transition are covered in section 2.4.

For pore volumetry experiments under high temperature, the question arises concerning the change in fluid specific volume between the specimen at, say, 300°C, and the pore pressure intensifier at 20°C. Fig. 6.5.1.a. shows a part of the phase diagram for water at the pressures and temperatures of concern. Above the critical point ( $\approx 22\text{MPa}$  pressure, and 374°C

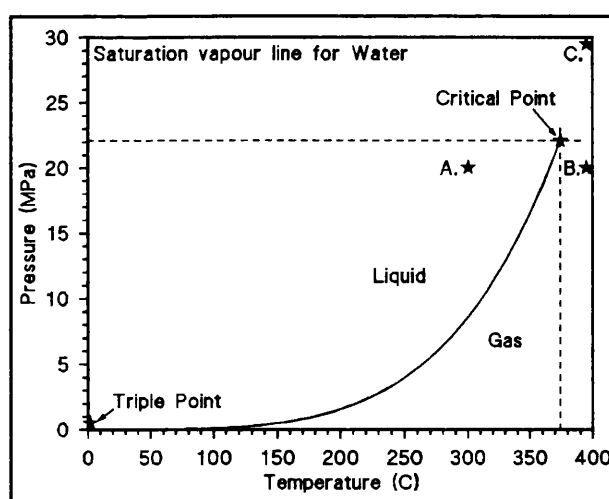


Fig. 6.5.1.a. Saturation vapour line and critical point for water. Three test conditions shown, A, B, & C.

temperature), water becomes super critical and does not suffer a large volume change as either temperature or pressure falls. Below the critical point a large specific volume change occurs at the liquid/ vapour phase boundary.

Figs. 6.5.1.b. & c. shows the specific volume of water against temperature for a variety of confining pressures. From these figures the specific volume of water at any given specimen temperature can be compared against the specific volume of water at 20°C, and the drained pore volumetry measurements multiplied by the factor found to obtain the true pore volume change occurring in the specimen.

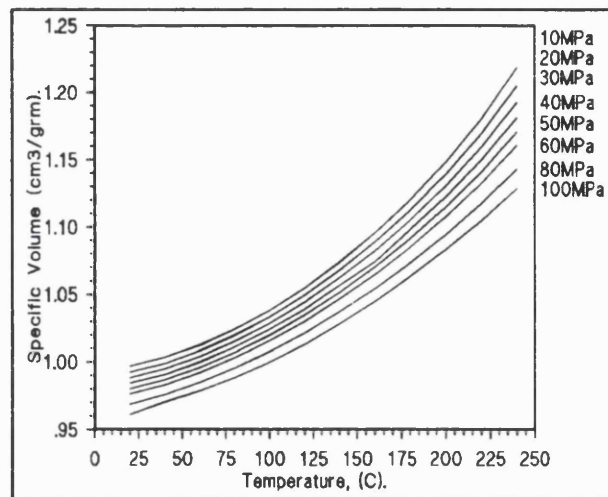


Fig. 6.5.1.b. Specific volume under different pressures and temperatures, 0→250°C.

This matter is made more complicated for the undrained case where the change in temperature between specimen and pressure transducer can cause the water to condense from a vapour (its possible state in the specimen) to a liquid (its state in the *hp* tubing). The changing pore fluid pressure during undrained tests also affects the temperature of condensation, i.e.

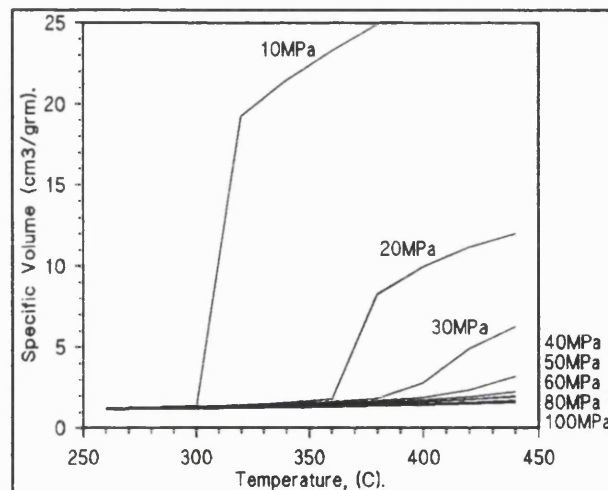


Fig. 6.5.1.c. Specific volume of water under different pressures and temperatures, 250→450°C.

its *position* in the *hp* tubing system. The result is a mobile vapour/liquid interface at a certain temperature/pressure combination at a certain position in the ram/*hp* tubing. For example, in the event of a rise in pore fluid pressure due to a pore volume reduction in the specimen, the liquid/vapour interface will respond by moving to a new position in the temperature graduated *hp* tubing where the temperature corresponds to the new pressure at which the phase change can occur (new position on the liquidus). Water vapour condenses and evaporates as necessary at the mobile interface, resulting in little or no change in the pore fluid pressure reading at the pressure transducer. So whilst pore volume may be changing in the rock specimen,

measured pore fluid pressure remains constant. The following two sections review experimental data at elevated temperature specific to the rocks used in this study.

#### 6.5.1.1. Darley Dale Sandstone.

Quartzite is only marginally ductile at 800MPa confining pressure, at 900-1000°C temperature, and at  $10^{-5}$ /s strain rate, (Heard & Carter, 1968). High confining pressure (1500MPa) and temperature (725-900°C) experiments on quartzo-feldspathic aggregate show little deformation of the quartz component of the aggregate until 800°C, when both cataclastic flow and recrystallisation accommodated creep occurs, (Dell 'Angelo & Tullis, 1982). Clearly high pressures and temperatures are required to deform a quartz rich rock by ductile mechanisms, far beyond those attained in this experimental study.

An important point concerning the possible effect of high temperatures on the deformation of Darley Dale sandstone is that of differential thermal expansion of quartz at  $\approx 100^\circ\text{C}$ . This is discussed in section 5.1.2. concerning the drying of samples based on work by Glover et al. (1995), on granites. They found that quartz bearing rocks display thermal cracking initially at  $100^\circ\text{C}$ , and again commencing at  $\approx 300^\circ\text{C}$ , due to the anomalously high volumetric expansion of quartz.

The effect of an active aqueous solution at high temperature and pressure on rock exacerbates cracking through stress corrosion, (see section 2.5.6.).

#### 6.5.1.2. Penmaenmawr Microgranodiorite.

Penmaenmawr microgranodiorite is reported to have a melting temperature of  $1220^\circ\text{C}$ . The same study (Murrell & Chakravarty, 1973) also found, under the effect of temperature alone, the rock to be brittle to  $1050^\circ\text{C}$ , beyond which partial melting occurred. A study on granite by Griggs, Turner & Heard (1960) showed that under 500MPa confining pressure and temperatures from  $25^\circ\text{C}$  to  $800^\circ\text{C}$ , granite displays a gradual and steady loss of strength with a

transition to ductile flow. From these results it is again clear that a relatively low temperature ( $<400^{\circ}\text{C}$ ) is insufficient to induce ductile behaviour in these rocks.

Fig. 6.5.1.2.a. illustrates the variation of peak strength with temperature for Penmaenmawr microgranodiorite, (Murrell & Chakravarty, 1973).

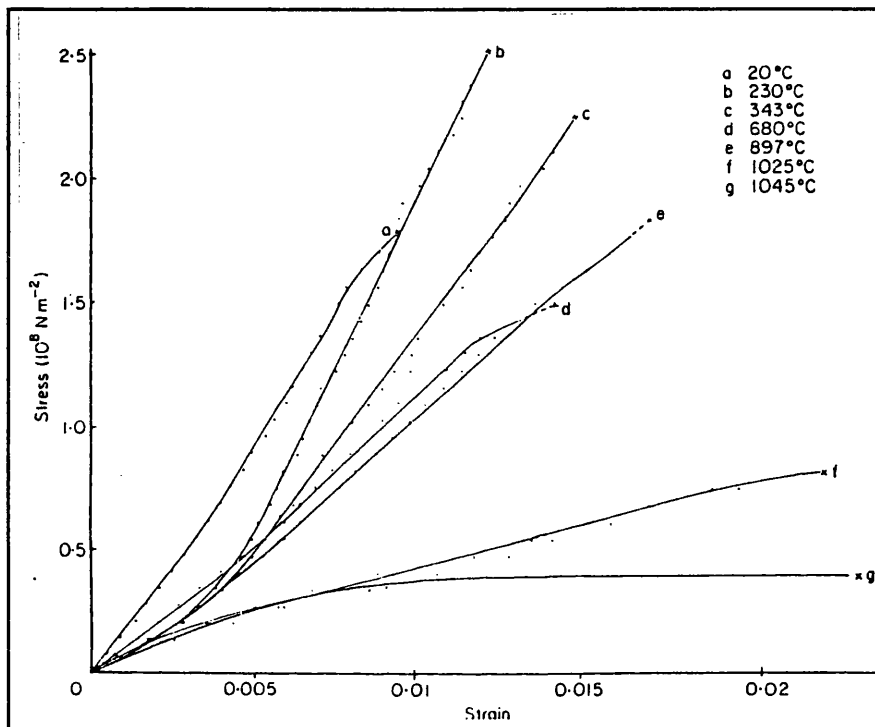


Fig. 6.5.1.2.a. Decrease in peak strength with increase in temperature for Penmaenmawr microgranodiorite, see text. (After Murrell & Chakravarty 1973).

With an increase in temperature ( $20^{\circ}\text{C} \rightarrow 400^{\circ}\text{C}$ ), peak strength and Young's modulus both decrease, and section 6.1.2.2. describes the dehydration characteristics of the rock at  $320^{\circ}\text{C}$ , which was shown to decrease strength through the effective confining pressure law. Studies concerning variations in the Young's modulus of similar rocks (Westerly granite and Stripa granite), show a non-linear decrease of 30% for an increase in temperature to  $300^{\circ}\text{C}$  at a confining pressure of  $\approx 55\text{MPa}$ , and a decrease of 50% for the same increase in temperature under  $\approx 8\text{MPa}$  confining pressure, (Heard & Page, 1982). The results are consistent with expected changes in elastic moduli based on the thermo-elastic response of micro-cracks; opening with increase in temperature, and closing with an increase in confining pressure.

Variations in permeability ( $\kappa$ ), and porosity ( $\phi$ ), with increasing temperature found a general trend of an increase in both  $\kappa$  and  $\phi$  with temperature for Westerly granite, whilst Stripa granite showed an initial *decrease* in  $\kappa$  and  $\phi$  for the first 120°C, followed by an increase thereafter. The effect is most exaggerated under the lowest effective confining pressure (5MPa). The reason for this behaviour is suggested as non-uniform thermal expansion/contraction behaviour of the rock. Studies by Potter (1978) on microgranodiorite also found the same decrease in  $\kappa$  (to 0.1x initial value) at 120°C, followed by a recovery in both with a further increase in temperature. This  $\kappa$  and  $\phi$  behaviour with increasing temperature is also found in other rocks (e.g. gabbro, Page & Heard 1981).

### 6.5.2. Programme of Experiments.

The changing mechanical characteristics of the pore fluid and its effect on Darley Dale sandstone deformation is studied prior to investigating the effect of temperature on the deformation of Darley Dale sandstone and Penmaenmawr microgranodiorite.

The series of experiments conducted are highlighted below.

- ▶ Experiments to determine the effect of a pore fluid of varying mechanical behaviour on rock deformation under drained and undrained conditions. Various heat and pressure conditions with respect to the critical point of water are employed in the investigation.
- ▶ Pore volumetry experiments on microgranodiorite were conducted under drained and undrained conditions.
- ▶ The effect of elevated temperature (20-400°C) on drained triaxial deformation characteristics of both Darley Dale sandstone and Penmaenmawr microgranodiorite. One set of stress conditions were adopted for this suite of experiments. The use of elevated

temperatures and the high strength of microgranodiorite limited the effective confining pressure in these tests to only 5MPa.

### 6.5.3. Results and Discussion.

#### 6.5.3.1. Darley Dale Sandstone.

Dependence of the Mechanical Behaviour of the Pore Fluid on Deformation during Undrained Triaxial Conditions.

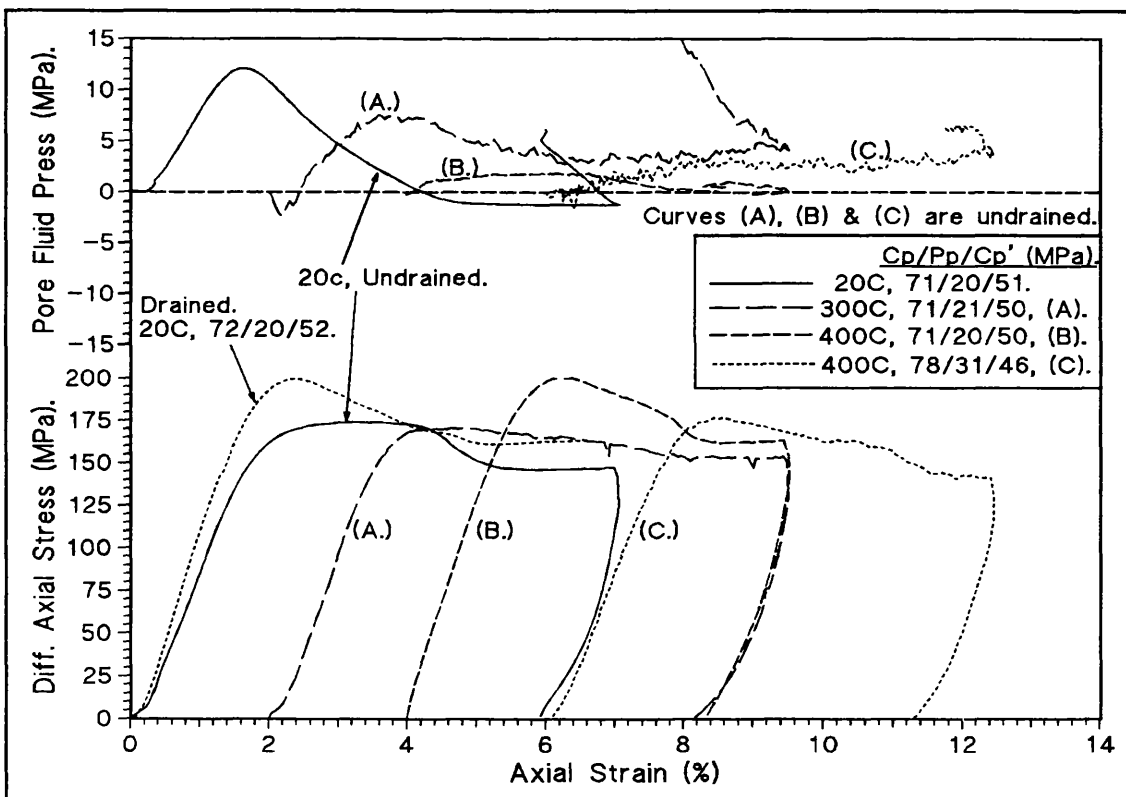


Fig. 6.5.3.1.a. Five triaxial deformation experiments showing the mechanical dependence of the pore fluid on deformation of Darley Dale sandstone, see text for details.

Fig. 6.5.3.1.a shows five experimental results labelled; "drained", "undrained", (A), (B), and (C), conducted at an effective confining pressure of  $\approx 50$ MPa and a pore fluid pressure between 20 & 30MPa. Axial strain values have been added to results A, B, and C for clarity. Pore fluid pressure and temperature conditions under which water exists as a liquid (A), as a vapour, (B), and in a super-critical state (C) in the respective experiments have been adopted to investigate the effect of different mechanical behaviour of the pore fluid on

deformation. These conditions are marked on fig 6.5.1. as A., B., and C. Limitations concerning the choice of the conditions with respect to the critical point of water are, (i) the maximum temperature allowable for ram components used in the test (AE monitoring equipment employed), and, (ii) the lower limit of  $\approx 15\text{MPa}$  pore fluid pressure to ensure accurate pore fluid intensifier piston response. The pore fluid pressure curves display undulations in response to fluctuations in temperature during deformation. The first two curves in fig. 6.5.3.1.a. (marked "drained" and "undrained") were conducted at  $20^\circ\text{C}$  and are presented for comparison with the remainder of the tests. The numerical information adjacent to the curves and in the legend corresponds to the *confining pressure / pore fluid pressure / effective confining pressure*.

The "drained" and "undrained" results at  $20^\circ\text{C}$  show behaviour as expected and as discussed in depth in section 6.2.4.1. for Darley Dale sandstone, i.e. the changing pore fluid pressure in the undrained case alters the effective stress during deformation and affects linear elastic deformation, rock peak strength, strain hardening/softening roll over, and stress drop. The three main results of interest in the figure (curves A, B, and C), shall now be considered.

Result A shows undrained triaxial deformation results for conditions under which water is a liquid. A pressure fall of  $12\text{MPa}$  is necessary before water vapourises at this temperature, and hence the water remains as a fluid in the specimen throughout the experiment. A 30% variation in the specific volume of water occurs between  $20^\circ\text{C}$  (transducer temperature), and  $300^\circ\text{C}$  (specimen temperature), (fig. 6.5.1.a. & b.). This results in the measured pore fluid pressure change at the pressure transducer being reduced compared with the "undrained" result.

The effect on deformation in comparison to the "undrained" result is clear from the pore fluid pressure response and its effect on the peak strength. Unlike the "undrained" result, result A displays little or no stress drop during dynamic faulting. The effect of increased temperature is to induce transitional behaviour in the rock due to increased cracking from differential thermal

expansion of quartz and stress corrosion cracking. This results in a highly fractured rock matrix which then deforms by rearrangement and rotation of the grains and grain fragments, i.e cataclastic deformation.

Result B shows undrained triaxial deformation results for conditions under which water in the specimen is super-critical, but in the pressure transducer is liquid. A change in specific volume of water of a factor of approximately seven occurs during the phase change with decreasing temperature between specimen and transducer, (fig. 6.5.1.b.). The result is little or no change in fluid pressure during undrained deformation. Deformation behaviour (stress/strain curve) is therefore similar to the "drained" result. The effect of differential expansion of quartz grains and stress-corrosion cracking, as evident in result A, is not so evident, and unlike results A the deformed specimen showed no outward signs of cataclastic deformation.

Result C shows the results of undrained deformation at 400°C and 30MPa pore fluid pressure. The effective confining pressure remains the same as the other tests. These conditions place the water in the specimen in a super-critical state throughout the equipment temperature range, with the water suffering a 2.8x volume decrease from specimen temperature to sample temperature. This then has the same effect on deformation as seen in result B, and, indeed, the deformation characteristics are very similar. The result is similar, but weaker than result B, and the deformed specimen also showed some cataclastic deformation along with faulting failure. The pore fluid pressure curve indicates compaction throughout deformation which is indicative of transitional deformation behaviour. Increased chemical activity (stress corrosion cracking), and thermal cracking from the higher pressure and temperature in result C is thought to be the cause of this transitional behaviour and the reduced strength compared to result B.

The precise reason for these different deformation characteristics can be properly discovered through rock section analysis. This has not been conducted in this project.

*In summary.* During high temperature and high pressure *undrained* triaxial deformation, the characteristics of deformation are highly dependent upon the temperature and pressure adopted in relation to the critical point and liquid/vapour phase boundary of water, and the temperature differential throughout the pore fluid pressure measurement system. If a phase change occurs in the water between specimen and transducer under undrained conditions, the resultant deformation behaviour is more akin to drained conditions. The results of B & C compared to A show that thermal and stress-corrosion cracking are far less influential in controlling deformation than the mechanical effect of the effective confining pressure.

### Effect of Temperature on Triaxial Deformation.

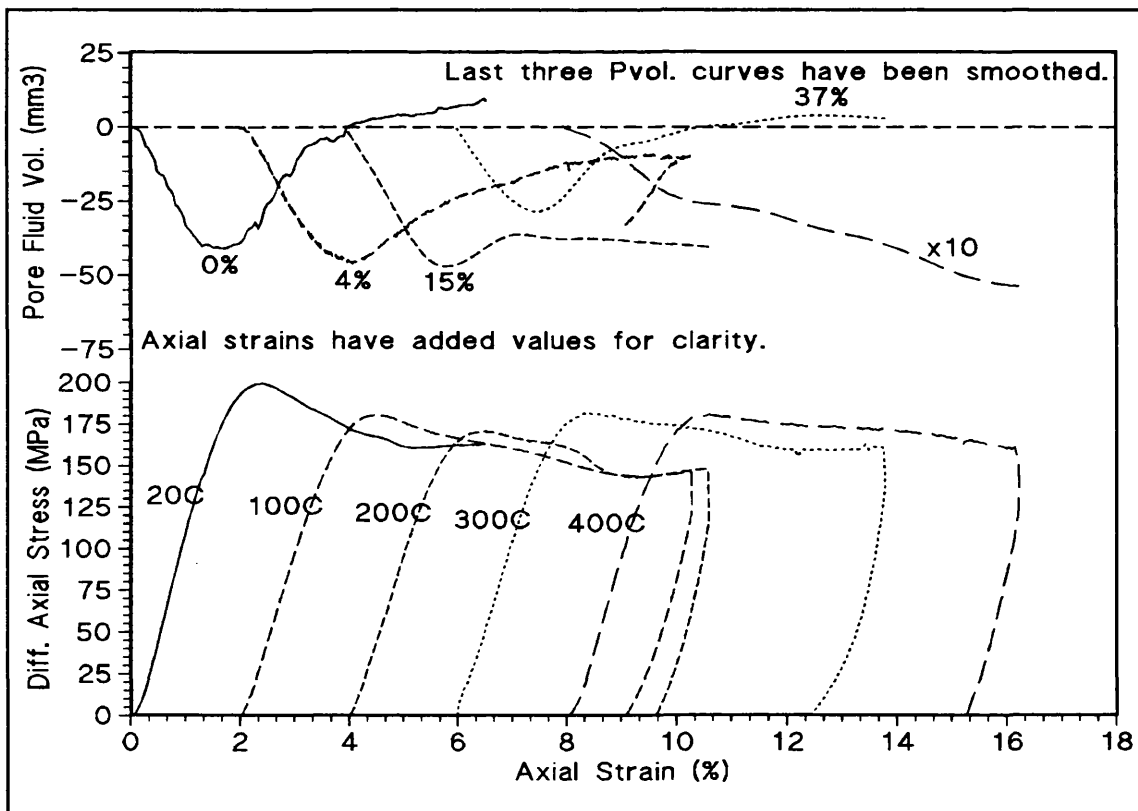


Fig. 6.5.3.1.b. Shows the effect of temperature on drained triaxial deformation of Darley Dale sandstone, 20→400 °C,  $c_p' = 20\text{MPa}$ .

Fig. 6.5.3.1.b. shows five drained experiments conducted under the same effective confining pressure (20MPa), and temperatures ranging from 20 °C to 400 °C. Again, axial strain values have been added to some results for clarity.

The experiment conducted at 400°C employed a pore fluid pressure of 30MPa to avoid a fluid phase change in the *hp* tubing.

The effect of an increasing temperature on deformation is clear; peak strength and the amount of dilatancy is progressively reduced and pore volume compaction increased (dilatant crack growth decreases), to the extent that at 400°C, deformation is undoubtedly transitional between brittle faulting failure and cataclastic flow. Post- experimental specimen observation supports this general trend towards transitional behaviour; less strain being accommodated on the shear fault and more throughout the sample as temperature increases. The pore fluid volume curves must be viewed considering the measured values are less than real pore volume changes, (section 6.5.1. & 6.5.3.1.). The phase change values are indicated against the pore fluid volume curve in the graph. The test conducted at 300°C is anomalous to the trend; the pore fluid volume curve indicating dilatancy and the stress/strain curve displaying a greater peak strength than samples deformed at lower temperatures. The precise cause of this is unknown, but the furnace temperature gradient along the sample was sometimes difficult to control, especially at high temperatures, and it is felt that the temperature of the specimen in result B could perhaps not have been as exactly recorded in the data.

Fig. 6.5.3.1.c. shows the results of three drained triaxial experiments under a confining pressure of  $\approx 75\text{MPa}$ , and temperatures ranging from 20°C to 200°C. Darley Dale sandstone deforms in a transitional fashion at this pressure, as can be seen from the experiment conducted at 20°C, however it can also be seen that increasing the temperature has the effect of promoting cataclastic behaviour. This is illustrated by the stress/strain curve (higher temperatures showing less strain softening), and the pore fluid volume curve which shows increased rate of compaction for higher temperatures. If the pore fluid volume curves are increased as per the change in specific volume of the fluid with temperature as described above (shown in fig.), the increase in compaction with temperature becomes clearer.

The above drained results and a number of similar experimental results under different conditions are compiled on fig. 6.5.3.1.d. The figures against each

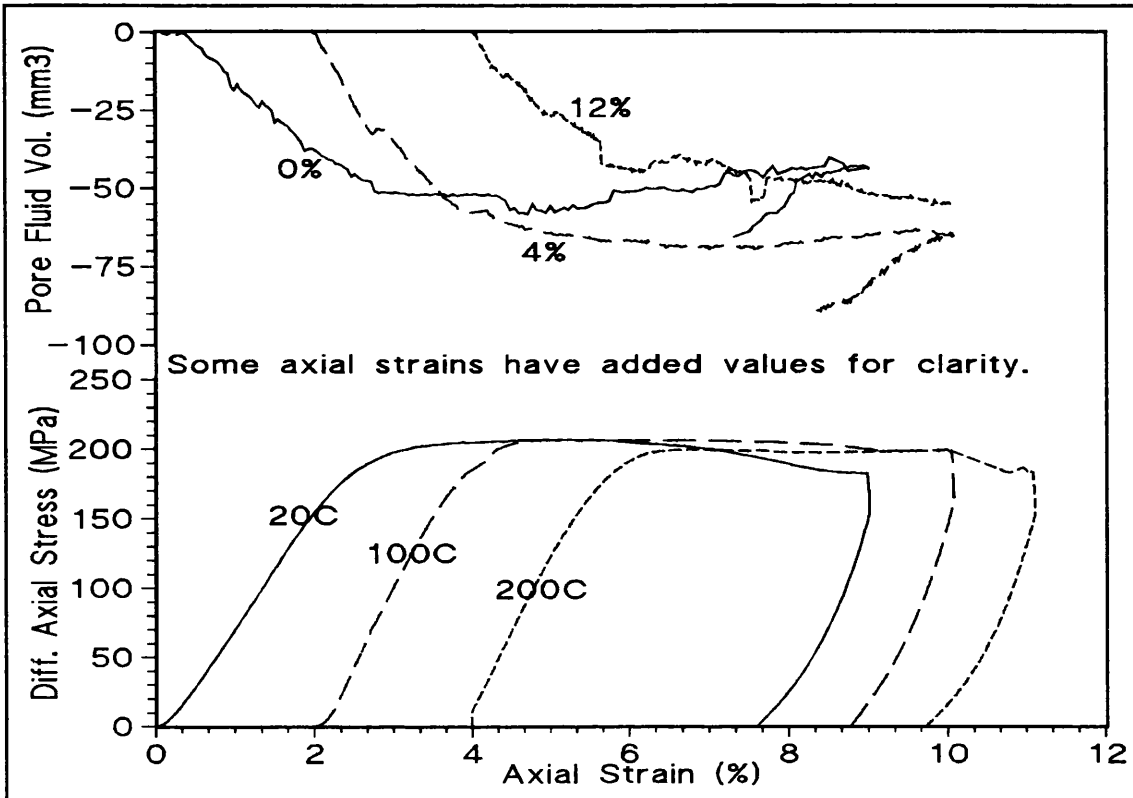


Fig. 6.5.3.1.c. Effect of temperature on drained triaxial deformation of Darley Dale sandstone, 20→200°C,  $C_p = 45\text{MPa}$ .

point represents the stress drop or strain softening (-ve), or strain hardening (+ve), following peak or yield strength, respectively, as a percentage of peak or yield stress. The data map out the change from brittle faulting,

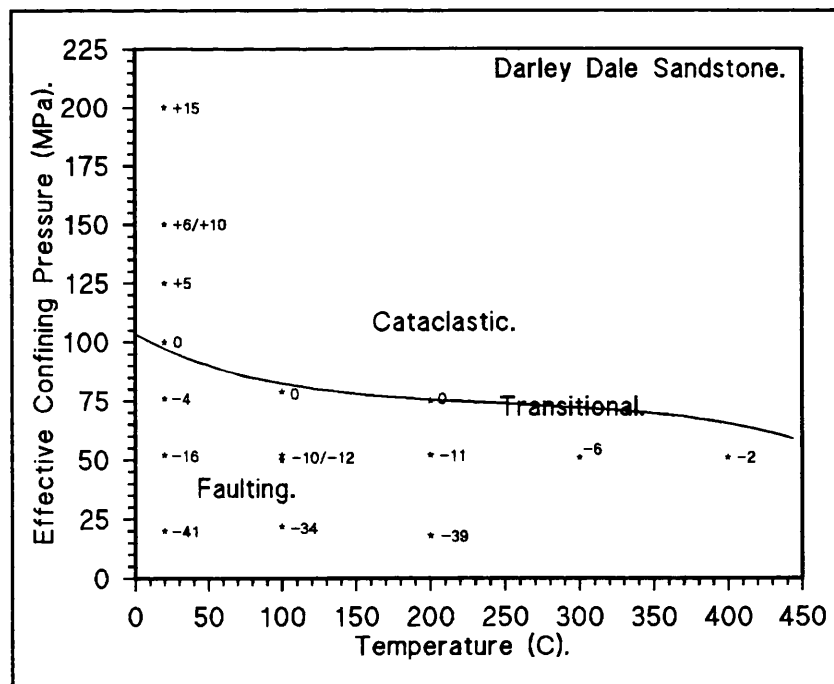


Fig. 6.5.3.1.d. Strain hardening/softening (as a % of peak stress) for Darley Dale sandstone under different temperatures, see text.

through transitional deformation behaviour to cataclastic deformation with increasing temperature and effective confining pressure. In this analysis the effective stress law is assumed valid (i.e.  $\alpha = 1$ ). The effect of temperature on the transitional confining pressure is clear. The promotion of cataclastic flow

is considered due to increased cracking through differential thermal expansion of mineral grains. A fall in the transition pressure occurs at 100°C, and then again at 300°C; both temperatures are coincident with increased AE activity in results by Glover et al. (1995). The differential thermal expansion cracking has the effect of increasing initial porosity for a given stress condition, and under the applied differential stress greater compaction results. Furthermore, the fractured nature of the matrix gives rise to easier grain rotation and re-arrangement, mechanisms associated with cataclastic flow. A linear approximation to the free curve drawn on the graph yields a gradient of  $\approx 1\text{MPa}/11^\circ\text{C}$ .

*In summary.* Temperature promotes cataclastic behaviour by reducing the faulting/cataclastic flow confining pressure by 1MPa/11°C in Darley Dale sandstone. The mechanisms associated with this are thermal cracking and stress-corrosion cracking (to a lesser extent). Through these mechanisms damage is increased to the extent that sliding on the resultant microcrack surfaces and re-arrangement of grains and grain fragments permits distributed deformation throughout the specimen. This temperature/ transition pressure relationship has important implications for the position of the seismic/aseismic boundary in the crust with respect to unusually high temperature gradients. A higher temperature gradient will cause this transitional boundary to be shallower compared to regions with a lower temperature gradient.

#### 6.5.3.2. Penmaenmawr Microgranodiorite.

##### Drained and Undrained Triaxial Deformation of Microgranodiorite.

Fig. 6.5.3.2.a. shows the results of two experiments conducted under the same initial effective confining pressure (5MPa) and temperature (20°C), the solid curve represents drained results and the dashed curve represents undrained conditions. The response of the low porosity (<2%) microgranodiorite is quite different from Darley Dale sandstone tested above.

The striking difference in the deformation characteristics between this rock and previous rocks is peak strength and brittleness of failure; the stress drop occurs very suddenly, perhaps lasting <1sec. The axial deformation of 0.5-1.0% strain occurring during faulting is the consequence of the strain energy released from the system during failure (section 4.2.6.). In both cases there can be seen a non-linear region of deformation within the first 0.5% axial strain. This is a results of the *bedding in* of the sample and ram, and probably less so the closure of favourably

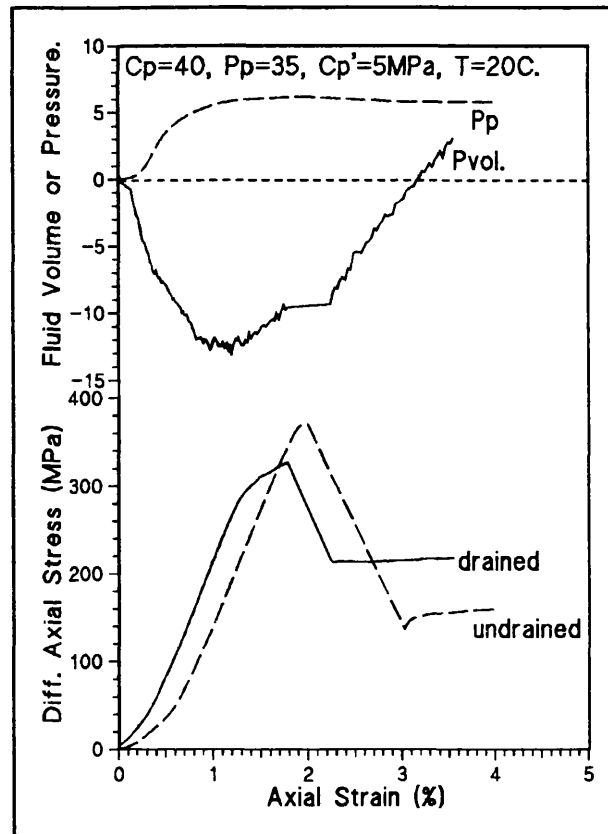


Fig. 6.5.3.2.a. Drained and undrained triaxial deformation results on Penmaenmawr microgranodiorite, see text.

orientated micro-cracks (also observed in the pore fluid pressure response of each result). This is followed by a period of linear elastic deformation which indicates a similar value of Young's modulus in both results. The uneven nature of the pore volume curve is discussed in section 6.3.3.1.

The drained results shows initial compaction until  $\approx 90\%$  peak strength afterwhich dilatant cracking occurs and increases rock pore volume. This is also seen in the strain hardening behaviour of the stress/strain curve. During post-failure deformation, the pore fluid volume curve is seen to gradually rise during stable sliding to a level *greater* than initial pore volume. This behaviour must be attributed to delayed fluid flow into the specimen and fault plane region upon the relaxation of axial load (compaction relaxation - section 6.3.3.2.).

The undrained result shows similar compaction during linear elastic deformation, which raises the pore fluid pressure to 1MPa above the confining pressure. This *negative* effective confining pressure is not significance since

the accuracy of the pressure transducers is  $\pm 1.75\text{MPa}$ . It also appears that similar behaviour as that seen by Ismail and Murrell (1976a) is seen here: excess pore fluid pressure causes fluid to drain into a volume created between the jacket and the rock, and fluid flow into and out of the specimen then occurs during deformation as required, thus a *drained* environment at zero effective confining pressure is created.

Some anomalous features exist in the results which necessitate a note.

- ▶ The undrained test shows a greater peak strength compared to the drained tests, even though from  $\epsilon \approx 1.4\%$  onwards, the undrained specimen is deforming under zero confining pressure. Following stress drop, however, the undrained tests shows a lower residual shear strength than the drained case, as would be expected.
- ▶ The drained result shows some *roll over* leading to dynamic failure, which is not seen in other drained results, and hardly noticed in the undrained result.
- ▶ The undrained result does not show the time delayed increase in specimen porosity following dynamic failure as seen in the drained result. It is assumed that fluid is being drawn from the chamber between the jacket and the specimen, thus not affecting overall pore pressure measured at the transducer. Furthermore, since the pore fluid pressure does not fall after  $\epsilon = 1.4\%$ , it is assumed pore volume created during this period of deformation, unlike in the drained case, is insufficient to accommodate *all* the fluid expelled in the earlier part of the test.

These anomalies illustrate the difficulties involved in conducting pore volumetry experiments with this very stiff, low porosity, high permeability rock in triaxial pore volumetry experiments. The first point concerning the strength of the rock under drained conditions is discussed further below.

### Effect of Elevated Temperature on Drained Triaxial Deformation of Penmaenmawr Microgranodiorite.

Fig. 6.5.3.2.b. shows drained triaxial deformation results for microgranodiorite under conditions of 5MPa effective confining pressure, and temperatures ranging from 20°C to 400°C. The stress/strain (lower curve) and pore fluid volume response (upper curve) is shown.

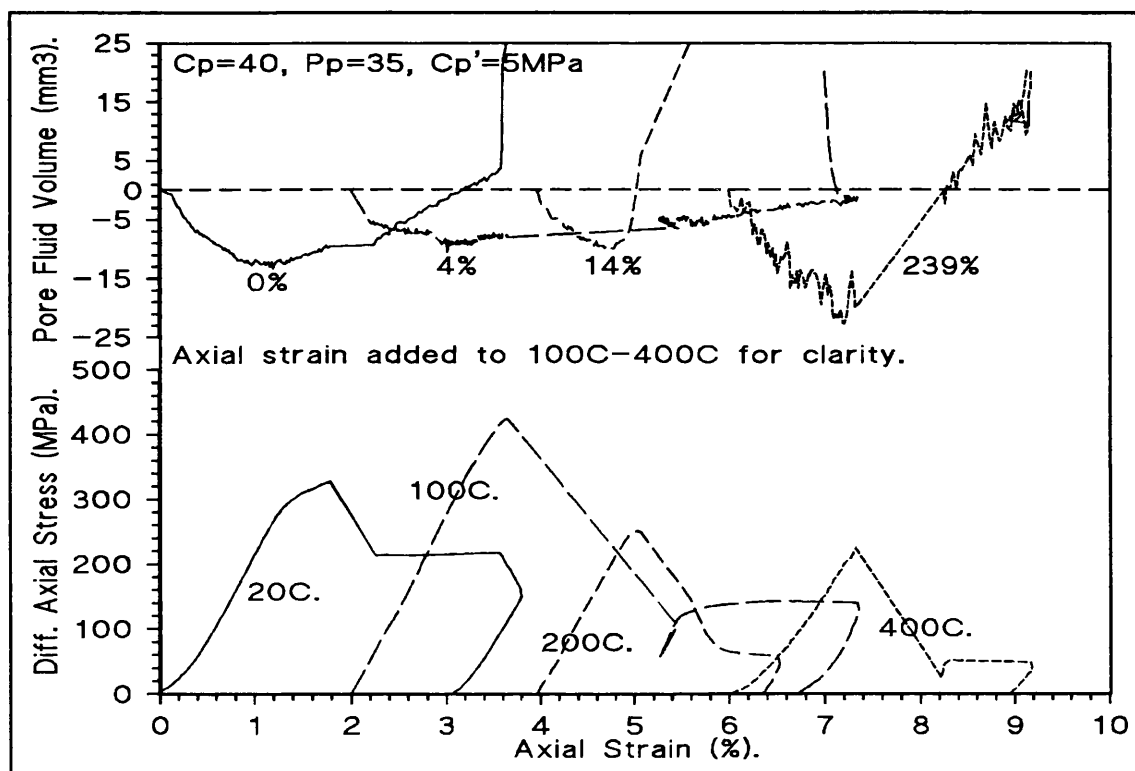


Fig. 6.5.3.2.b. Effect of temperature on drained triaxial deformation of microgranodiorite, see text for details.

The pattern of deformation shows a linear elastic portion of deformation during which compaction occurs, followed by some dilatancy at  $\approx 90\%$  of peak strength, sudden and very dynamic stress drop during which extensive specimen strain occurs as before, followed by stable sliding. During the region of stable sliding pore fluid is seen to be drawn into the specimen. This is assumed to be delayed fluid inflow following the very sudden dynamic failure.

The effect of temperature on deformation is a reduction in peak strength and residual shear strength. The stiffness of the rock appears (from the gradient

of the stress/strain curve), to remain constant for all tests. The specific volume difference between fluid in this specimen and in the pressure intensifier is given against the pore fluid volume curve. If the curves are viewed with these percentage increases in mind a trend can be observed of increasing compaction and dilatancy for experiments conducted at higher temperatures.

The reasons for reduced strength with increasing temperature lie (as with Darley Dale sandstone) with increased thermal cracking rendering the rock matrix extensively fractured and of higher porosity (Heard & Page 1982, Potter 1978). The effect of this higher porosity is seen in the pore fluid volume curve (greater compaction and dilation), and in the stress/strain curves. Dehydration of chlorite (section 6.1.2.2.), causes fluid production, although this is not wholly obvious from the pore fluid volume curves. Unlike Darley Dale sandstone, elevated temperature effects on this rock did not induce transitional behaviour, but reduced strength.

Anomalous results concern the post-dynamic failure pore fluid volume curves, and the trend between the results at 20°C and 100°C.

- ▶ The sudden dynamic failure of the specimens and the large specimen strain during failure (machine strain energy release), risked jacket rupture. This may have occurred in all the tests (except 400°C), where the pore fluid volume curve shows large increases (>25mm<sup>3</sup>) after dynamic failure.
- ▶ The result at 20°C shows reduced peak strength compared to the result at 100°C. Since the 20°C results (the same result as the drained test in fig. 6.5.3.2.a. and shown to be anomalous to the undrained result in that analysis), also shows unusually large strain hardening prior to failure and a stress drop of only  $\approx 1/3$  of peak strength during failure compared to all the other tests which show a stress drop of  $\approx 2/3$  of peak strength, it is suggested that this test result at 20°C is unreliable. If the residual shear strength is accurate (judging from the trend this is likely), and a stress drop of  $\approx 2/3$  peak strength is used to calculate a

true peak strength of the 20 °C result, then a peak strength (at 20 °C and  $C_p' = 5\text{MPa}$ ) of  $\approx 600\text{MPa}$  is expected. This is more in tune with the general trend of the suite of experiments.

However if the variation of porosity (which *may* affect strength), with temperature as obtained by Potter (1978) is correct for Penmaenmawr microgranodiorite, then perhaps the result for the 20 °C test *is* correct. However, the roll over in stress/strain curve and the reduced dynamic stress drop in the 20 °C result make this unlikely, and the above analysis is thought to be more correct.

*In Summary.* Increased temperature on drained triaxial deformation at an effective confining pressure of 5MPa causes increased micro-cracking in the rock and reduces peak and residual strength of the rock. The increased cracking is also seen in greater compaction and dilatancy during deformation. This effect of reducing the peak strength of granite has important implications with respect to the emplacement of heat generating radioactive waste in granitic rock repositories. The resultant thermal fracturing could reduce strength and threaten long term integrity of the rock with respect to gross fracture and associated fluid transport characteristics.

#### 6.5.4. Further Work.

##### 6.5.4.1. Darley Dale Sandstone Experiments.

Further work on Darley Dale sandstone based on the results seen in this section are highlighted below.

- ▶ Expand the study with a wider range of temperatures and pressure to establish fully a faulting/cataclastic transition and brittle/ductile map.
- ▶ Microscopic examination of sections of the deformed rock will verify (or otherwise) the hypotheses regarding micro-cracking induced in the rock

through the temperature, stress corrosion cracking, and deviatoric stress.

- ▶ Conduct a study to isolate the effect of temperature induced chemical activity on rock deformation. The study should employ different confining pressures under dry conditions and water saturated conditions varying the pore fluid pressure for a given effective confining pressure and temperature.

#### 6.5.4.2. Microgranodiorite Experiments.

Areas of further work required based on the results presented above are highlighted below.

- ▶ Initially repeat these experiments to confirm repeatability and validity of these results. Especially, experiment conducted at 20°C and 100°C under drained conditions.
- ▶ Expand the study for a greater temperature and effective confining pressure range. The effect of high temperature under very low effective confining pressure only has been investigated in this section.
- ▶ Microscopic observations of sections of the rock after the experiments will aid confirmation of the micro-mechanisms active during deformation and during the application of heat

## 6.6. Studies of Pore Fluid Generation Due to Chemical Dehydration of Gypsum under Various Confining Pressures and Pore Fluid Pressures.

### 6.6.1. Introduction and Review of Previous Studies.

Hydrates in the crust produce water during metamorphism. Since fluid and fluid pressure in crustal rocks has a marked effect on deformation, the processes of, and environmental factors controlling dehydration are important considerations for fluid/rock interaction studies. Gypsum's *% solid volume loss : % fluid volume gain* ratio at 29.3%:37.1% measured against initial rock volume is typical of many hydrates, and as such represents typical crustal pore pressure build-up due to dehydration, (Ko, 1993). This has important implications with respect to deep radioactive waste storage repositories where the emplacement of heat generating waste material could induce chemical dehydration and embrittlement of the surrounding rock. Whether such high pore pressure conditions are maintained for time periods of geological interest is dependent upon competition between the dehydration reaction rate and fluid pressure dissipation rate.

Section 6.1.3.3. describes the gypsum used in this study with respect to its mineralogy, its dehydration reaction, and its deformation characteristics under triaxial loading. In this section that basic outline is completed with a review of some dehydration studies on the rock.

Murrell & Ismail (1976a) conducted numerous drained and undrained experiments on gypsum. They found that during *undrained* high temperature triaxial deformation, dehydration and the consequential production of water had a marked effect on deformation. At temperatures greater than 130°C, water production reduced the effective confining pressure and changed the failure mode; for example, if  $C_p > 40\text{MPa}$  (the brittle/cataclastic flow transition pressure found for this gypsum), there is a transition from cataclastic strain hardening to brittle faulting. Under *drained* conditions, this was not seen to

happen as the water produced was "drained off" and did not change the effective confining pressure.

Furthermore, peak strengths found for (i) drained dehydrating samples under triaxial stress, and (ii) samples dried after dehydration, and subsequently subjected to triaxial stress, (i.e. constant effective confining pressure in both situations but (i) suffering fluid production), suggested an amount of *compaction softening* occurs during triaxial stressing. During drained dehydration (condition (i)), isolated pores within the rock trapped water raising pore fluid pressure, reducing effective confining pressure, and hence affecting deformation behaviour. In an undrained suite of triaxial experiments at dehydration temperature, increasing the confining pressure failed to affect fracture strength, indicating a constant effective confining pressure for all levels of imposed confining pressures, i.e. a  $P_p$  rising concomitantly with  $C_p$ .

The sigmoidal dehydration/time curve found from drained pore volumetry studies on volterra gypsum (Ko, 1993), can be divided into three sections according to micro-structural changes occurring in the rock, (fig. 6.6.1.a.).

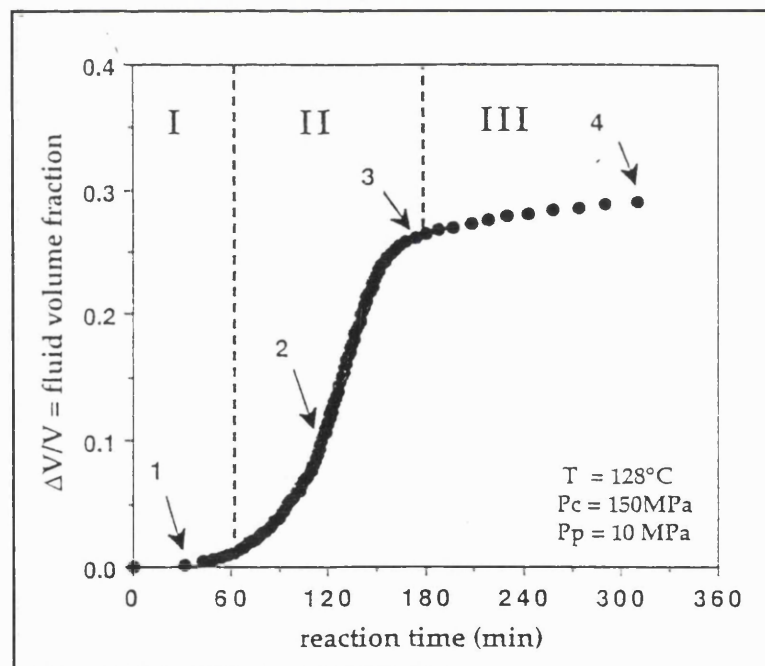


Fig. 6.6.1.a. Drained fluid expulsion/time curve for Volterra Gypsum, see text for details, (After Ko, 1992).

*Stage I*, low fluid

expulsion rate is a consequence of low permeability in the rock.

*Stage II*, sufficient porosity and permeability has occurred (from increased pore fluid pressure and change in micro-structure from gypsum to bassanite) to allow an increased rate of fluid expulsion. Micro-structural analysis at this

stage showed a collapsed solid structure caused by excess connected porosity.

*Stage III*, comparatively little un-dehydrated gypsum remains resulting in low water expulsion.

The undrained dehydration curve also shows a sigmoidal shape (fig. 6.6.1.c.) indicating permeability is not the only factor dictating dehydration rate - gypsum free surface availability should also contribute.

Acoustic compressional wave velocity measurements conducted during gypsum dehydration (increasing temperature) by Jones (1989), showed a slight  $V_p$  fall from 5.5km/s to 5.1km/s as temperature was raised to 110°C, but between 110°C and 130°C,  $V_p$  fell  $\approx 30\%$  from 5.1km/s to 3.5km/s. Thereafter  $V_p$  decreased minimally up to 300°C. The decrease in  $V_p$  in these results is attributed to the opening of pores and cracks through a reduction in effective confining pressure (undrained conditions), caused by the production of water from the dehydration reaction.

Ko (1993), studied the effect of pore fluid pressure and confining pressure on

dehydration of gypsum. She found that when temperature and confining pressure remained constant, an increase in pore fluid pressure causes a *reduction* in water production output rate and in the maximum amount of fluid produced, (fig. 6.6.1.b., curve C→D). The same happened when decreasing the confining pressure for a constant pore fluid pressure (curve A→B). This is due

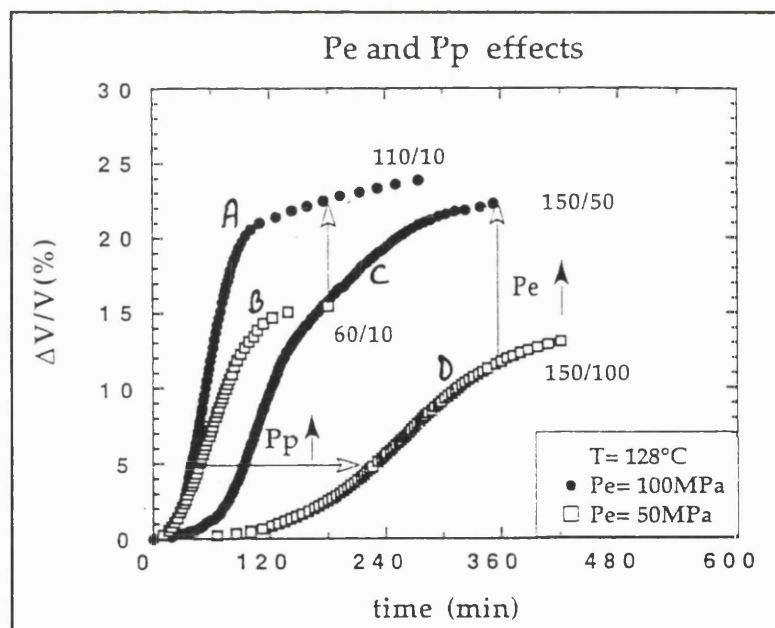


Fig. 6.6.1.b. Dependence of effective confining pressure and pore fluid pressure on drained dehydration of Volterra gypsum, (After Ko, 1992).

to two factors, (i) the increase in fluid pressure affects the dehydration reaction temperature by 8MPa/Kelvin, and (ii) a reduction in the effective confining pressure reduces compaction assisted fluid expulsion, (Murrell 1985, and McConnel 1978). This effect is clearly seen in the *undrained* dehydration curve for Volterra gypsum, fig. 6.6.1.c.; the increasing fluid pressure resulting from dehydration reduces the dehydration rate and compaction assisted fluid expulsion to cause a "rolling over" of the sigmoidal dehydration curve.

A decrease in external confining pressure at constant effective confining pressure (curves A→C, in fig. 6.6.1.b.), was also shown to have an effect on dehydration by decreasing the *rate* of fluid output, although not affecting the final fluid output quantity. This is due to the increased pore fluid pressure (curve C) reducing dehydration reaction rate from the P-T relationship.

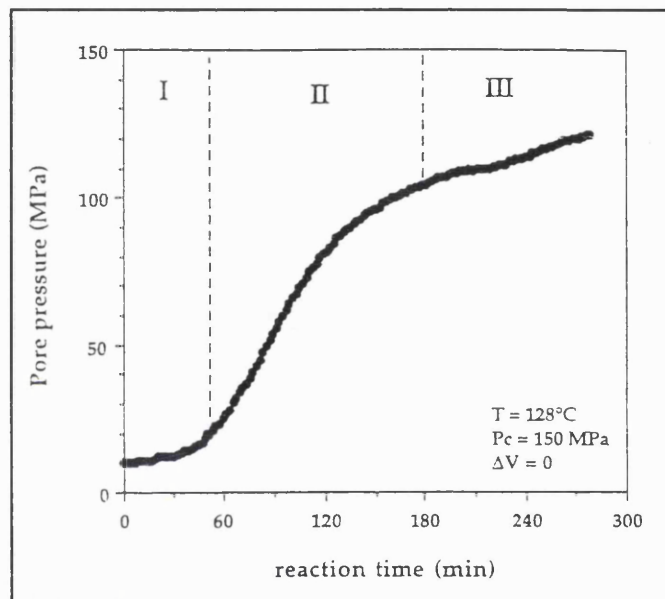


Fig. 6.6.1.c. Pore fluid pressure/time curve for *undrained* dehydrating Volterra gypsum, see text, (After Ko, 1992).

Ko also studied the effect of applying a positive deviatoric axial stress to the specimen during drained dehydration. The rate of fluid expulsion increased by a factor of greater than three due to increased axial permeability and an increase in the specific surface area of gypsum through increased microcracking, (Murrell 1985). The total amount of fluid produced, however, remained unaffected.

The rate of dehydration and amount of fluid produced is also heavily dependent upon the relative timing of dehydration and the application of the differential axial compressive load. If dehydration occurs simultaneously with triaxial loading, fluid production rate is faster throughout dehydration. If dehydration is stimulated *prior* to triaxial loading, as the differential axial load

is applied, water production rate is increased, again by a factor of approximately three.

## 6.6.2. Programme of Experiments Conducted in the Present Study.

The five experiments conducted were designed to investigate the effects of crustal conditions on dehydration rates and total fluid volumes expelled in a drained environment; pore fluid pressure, effective confining pressure, and temperature. To examine the effect of triaxial loading on undrained dehydrating gypsum, one such experiment was conducted.

Samples were all saturated prior to experimentation and therefore fluid expulsion represents the difference between rock mass decrease and fluid production.

## 6.6.3. Results and Discussion.

### 6.6.3.1. Dehydration Experiment Results.

Details of the conditions under which each experiment was conducted is given against each curve in fig. 6.6.3.1.a. as; *confining pressure/pore fluid pressure/effective confining pressure*. Comparison with fig. 6.6.1.b. shows much faster initial reaction rate for Glebe mine

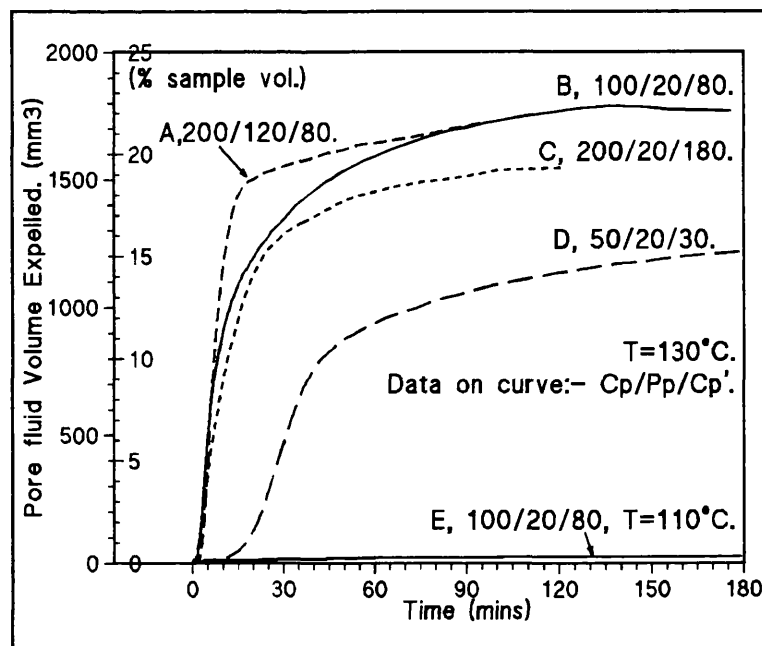


Fig. 6.6.3.1.a. Results of drained dehydration experiments on gypsum. Data in body of graph.

gypsum. This is attributed to rock type variability.

### Effect of Confining Pressures.

It can be seen from curves A & B that an increase in confining pressure (constant effective confining pressure), has no effect on the total fluid expelled, or on the initial rate of dehydration, but an effect is seen on the rate after 50% dehydration. The sample subjected to greater confining pressures shows a constant rate of dehydration to  $\approx 90\%$  of total dehydration (total dehydration for both experiments is measured at 90mins. for comparison purposes, even though curve B shows further dehydration beyond 90mins.), whereas B ( $C_p' = 100\text{MPa}$ ) shows the rate of dehydration tailing off at  $\approx 60\%$  of total dehydration. This result is in contrast those obtained by Ko (1993), who found the same increase in confining pressure (constant effective confining pressure) caused a *reduction* in reaction rate and a retarded commencement of dehydration, (curves A. $\rightarrow$ C. on fig. 6.6.1.b.). Ko's result was attributed to the higher pore fluid pressure affecting dehydration temperature from the P-T phase relationship (a 100MPa increase in pore fluid pressure causes a  $12.5^\circ\text{C}$  increase in dehydration temperature). This, however, is not seen in the result in this study, fig. 6.6.3.1.a., and one concludes that for the particular gypsum used in the present study (Glebe Mine Gypsum - Nottinghamshire), the modified dehydration temperature due to pore fluid pressure increase is still below  $130^\circ\text{C}$ . Explanation for different sigmoidal dehydration curves seen between this study and Ko's results requires further experimentation.

### Effect of Effective Confining pressure.

Curves D $\rightarrow$ B $\rightarrow$ C, fig. 6.6.3.1.a. show a progressively increasing effective confining pressure (50 $\rightarrow$ 100 $\rightarrow$ 200MPa), under a constant pore fluid pressure of 20MPa. From D $\rightarrow$ B an increased dehydration rate initially and a greater maximum volume of fluid expelled is seen. It seems that the greater effective confining pressure in experiment B has increased fluid expulsion rates and total fluid volumes. It is also seen that curve D is still rising at 180mins. An extended tests period may discover that fluid volumes expelled under different

effective confining pressure conditions eventually become equal. It is reasonable to suggest from this that an increase in effective confining pressure increases the *rate* of dehydration but not the total fluid volume produced.

Experiments B.→C. shows that with a further increase in confining pressure the total amount of dehydration is *reduced*, whilst the rate of dehydration remains constant. Since pore pressure and temperature remain constant between the experiments, reaction kinetics should be unchanged. It seems that a *peak* in the dehydration output/effective confining pressure relationship has been exceeded in experiment C. It is postulated that this effect is due to an increase in rock porosity leading to the *structural collapse* of the more fibrous bassanite rock matrix as observed by Ko (1993). Beyond a certain effective confining pressure (i.e. < 180MPa), skeletal collapse of the rock could inhibit fluid flow sufficiently to prevent further fluid expulsion. Under these conditions internal pore fluid pressure could build up and decrease effective confining pressure sufficiently to allow fluid expulsion to resume. This phenomenon is dependent upon sufficient unreacted gypsum remaining in the rock after matrix collapse to produce sufficient fluid pressure. If this is not the case, fluid flow recovery by this mechanism will not occur.

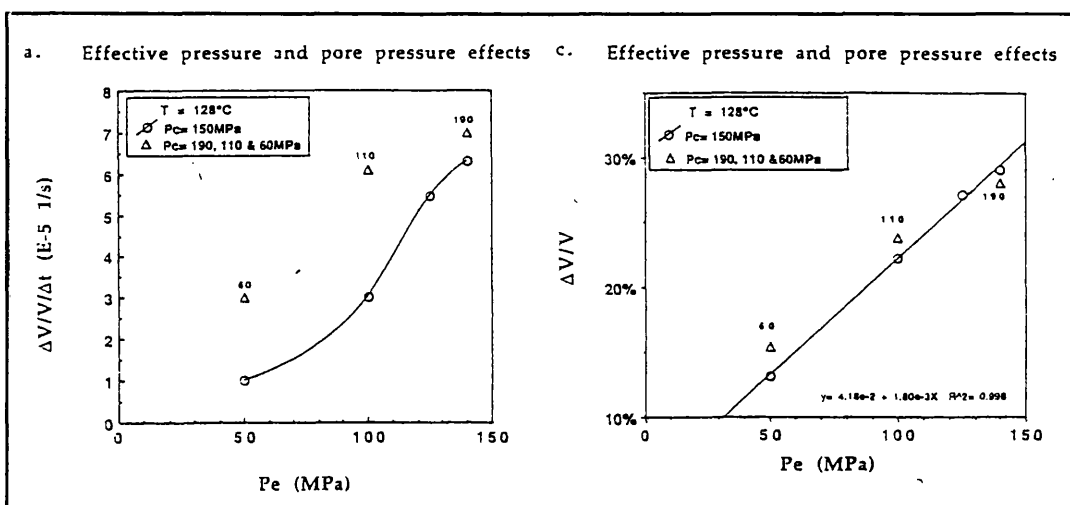


Fig. 6.6.3.1.b. Effective pressure and pore pressure effects on reaction rate and total volumes, see text, (After Ko, 1992).

Ko's results show evidence of a possible peak in the effective confining pressure/dehydration relationship - the dehydration rate against effective confining pressure curve (fig. 6.6.3.1.b.), shows a decrease in gradient at an effective confining pressure approaching 150MPa.

#### Effect of Pore fluid pressure.

Ko's results suggest that the reaction rate is strongly dependent on pore fluid pressure. Experiments C→A, (fig. 6.6.3.1.a.) were conducted to investigate this. Results show that the effect of an increase in pore fluid pressure from 20MPa to 120MPa is to *increase* dehydration rate and total dehydration. This is again in sharp contrast to Ko's findings, although experiment C, at an effective confining pressure of 180MPa, may well have suffered microstructural collapse which inhibits fluid flow. Clearly more tests are required to fully analyse the effect of pore fluid pressure on dehydration.

*In summary*, dehydration reactions under drained conditions are heavily dependent upon the effective confining pressure assisting fluid flow through rock compaction. However, a maximum effective confining pressure is postulated, beyond which structural collapse of the rock frame reduces porosity and permeability, and thus effects fluid expulsion rates. Pore pressure may build up internally under these conditions, but insufficient to recover permeability.

An increase in pore fluid pressure reduces dehydration temperature (ref. the P-T relationship at  $\approx 8\text{MPa/K}$ ). If the resulting dehydration temperature is still less than that experimentally imposed, dehydration continues unhindered and the effect of any change in effective confining pressure dominates.

The results have highlighted an interaction between three mechanisms controlling dehydration. That of the chemical dehydration reaction rate, of compaction assisting fluid expulsion, and of compaction decreasing permeability through bassanite matrix collapse. The complex interaction of these mechanisms could be the explanation for the difference found between

these results and Ko's. Without further experimentation disentanglement of these mechanisms is impossible, (see section 6.6.4.).

### 6.6.3.2. Triaxial Stress and Dehydration Experiment Results.

Fig. 6.6.3.2.a. shows the results of undrained triaxial deformation of dehydrating gypsum. Overall effect of temperature on the effective confining pressure is initially nil, and so deformation is largely unaffected by the rise in temperature until 130°C (dehydration temperature), at which point water production increases pore fluid pressure and decreases effective confining pressure ( $\epsilon = 1.3 \rightarrow 3.8\%$ ). At point A, ( $\epsilon = 3.8\%$ ),

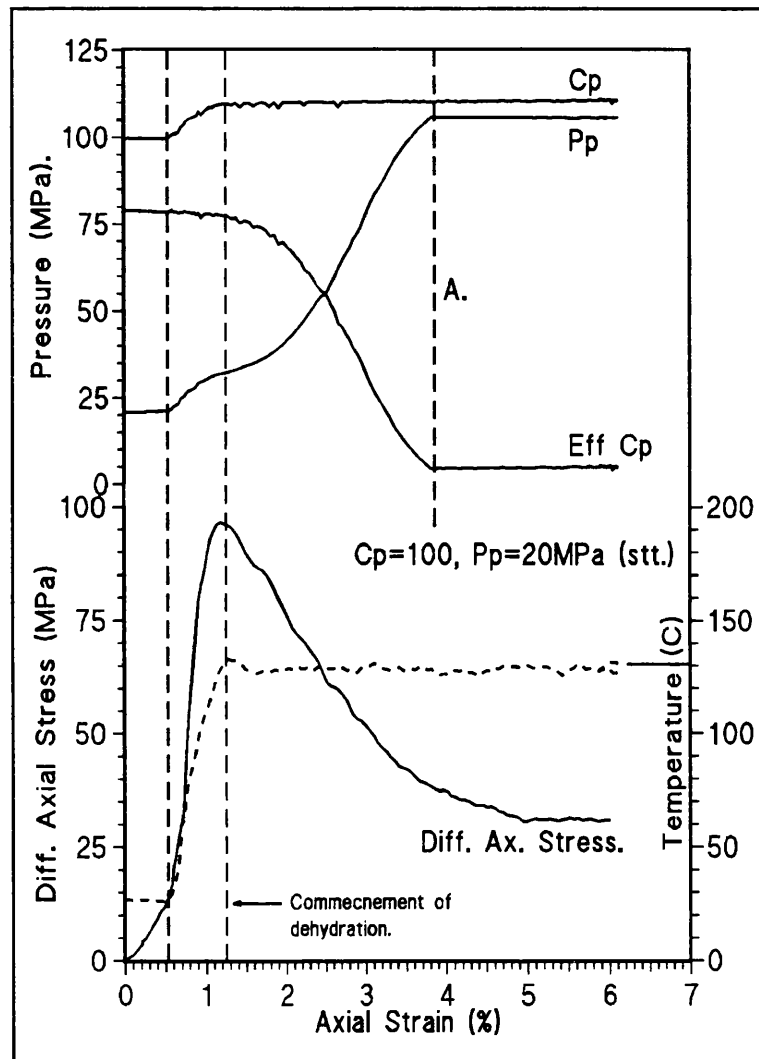


Fig. 6.6.3.2.a. Triaxial deformation and dehydration of gypsum,  $T=130^\circ\text{C}$ ,  $C_p$ ,  $P_p$ , shown in graph. Point A. - changed to drained conditions to avoid jacket leakage.

experimental control was changed to drained conditions to prevent jacket rupture. Ismail & Murrell (1976), showed when fluid pressure exceeds confining pressure, excess fluid can pass into a space created between the specimen and the jacket. Fluid pressure then remains at the level of the confining pressure. In this case, the presence of the energised furnace encouraged caution in that respect

Three important features found in the results are highlighted below.

- ▶ The effect of the falling effective confining pressure on deformation is to increase the magnitude of the stress drop. The residual shear strength ( $\epsilon = 5\% \rightarrow$ ) occurs at an effective confining pressure of 5MPa, whereas peak strength occurred under an effective confining pressure of  $\approx 80\text{MPa}$ .
- ▶ The overall result of decreasing effective confining pressure and increasing pore fluid pressure on dehydration (see section 6.6.1.) is that during undrained dehydration, a feedback mechanism must occur; the product of dehydration (fluid pressure) reduces the rate of compaction of the rock *and* the dehydration reaction rate, and therefore inhibits further dehydration. This phenomenon is dependent on the exact relationships between effective confining pressure & dehydration, and pore fluid pressure & dehydration temperature. For example, if most dehydration occurs before the increasing pore fluid pressure inhibits dehydration, dehydration will stop suddenly, whereas if the increasing pore fluid pressure inhibits dehydration prior to most dehydration, the sigmoidal curve will show a smooth roll-over as dehydration is slowly hindered, fig. 6.6.1.c.
- ▶ In contrast to tests by Ismail and Murrell (1976a), where dehydrated temperature of  $130^\circ\text{C}$  was imposed 1hr. prior to triaxial loading, the specimens in this study were dehydrated *during* triaxial loading, and hence under an increasing pore fluid pressure. Both Ismail and Murrell's specimen and fig 6.6.3.2.a. results show faulting failure, although in fig. 6.6.3.2.a., very little displacement occurred on the failure plane - most strain occurring throughout the specimen as dehydration progressed.

*In summary*, undrained triaxial deformation of dehydrating gypsum increases the magnitude of dynamic stress drop during failure through a decreasing effective confining pressure.

Dehydration under undrained conditions invokes a feedback mechanism; product of dehydration (fluid pressure), decreases compaction of the rock and

the reaction rate, and thus the rate of dehydration and total amount of fluid produced. The details of this phenomenon depend upon the precise nature of the effect of effective confining pressure and pore fluid pressure on dehydration.

#### 6.6.4. Future Work.

The results of the few experiments conducted here have presented some interesting problem worth further analysis. These are highlighted below.

- ▶ Further drained dehydration experiments are required over a greater range on pore fluid and effective confining pressures. Some tests should be conducted with "compensated dehydration temperatures" to account for changes in dehydration temperature brought about from a change in pore fluid pressure, (ref P-T relationship). The programme should also examine further the precise relationship between effective confining pressure and dehydration with respect to a maximum in the dehydration/ effective confining pressure relationship evident from this study.
- ▶ Expand the study to undrained experiments where the *feedback* mechanism of a changing effective confining pressure and pore fluid pressure affects dehydration rates and volumes.
- ▶ The effect of dehydration on *undrained* triaxial deformation characteristics requires further investigation. Under a variety of confining pressures, specimens should be triaxially loaded whilst simultaneously applying high temperatures to initiate dehydration. The pore fluid pressure generated will affect the rate of dehydration as described above, and hence affect triaxial deformation behaviour. Ideally the confining pressure should be accurately controlled to maintain constant *mean stress* during the application of the differential axial load, as dehydration is temperature and pressure dependent as per the P-T relationship.

- ▶ The change in specimen axial or bulk strain during undrained dehydration could be examined from creep experiments, (constant axial load), to study changing specimen volume during dehydration. Thermal expansion will increase specimen volume initially, but competing mechanisms of gypsum decomposition (specimen volume reduction) and fluid production (specimen volume increase) should cause an overall increase in volume. The precise relationship with respect to confining pressure and temperature could be examined.

The above experimental programme will elucidate the behaviour of gypsum under simulated crustal conditions and will go some way to explaining the conditions under which the production of elevated pore fluid pressure in the crust occurs as a result of the dehydration of rocks like gypsum.

## **CHAPTER 7. GENERAL CONCLUSIONS AND FUTURE WORK.**

### **7.1. General Conclusions.**

Compaction and dilatancy are the pore volume change mechanisms that occur during deformation. Isolating the causes of these mechanisms is important for predicting the poro-elastic behaviour of rock under a given stress field. The effect of temperature, of pore fluid and lithostatic pressure, and of a variation in Upstream Reservoir Volume (URV) have been investigated on a variety of crustal rocks to establish their effect on the process of dilatancy and compaction using a recently modified high pressure triaxial deformation vessel. Temperature, fluid pressure, and lithostatic pressure have been applied to specimens of rock to accurately represent real sub-surface deformation conditions. Pore volumetry and acoustic emissions have been employed to monitor changes in pore & crack volume and damage accumulation in the deforming rock specimens.

Building on the discussions in chapter 6, the general conclusions of the study are presented below.

- ▶ Isolation of deviatoric and mean stress components of triaxial stress through 3-D representation and analysis (section 6.4.3.2. & 6.4.3.4.), of drained triaxial test data has shown that deviatoric stress alone has the effect of promoting both dilatancy and compaction. During cataclastic flow deviatoric stress induced compaction occurs, and during brittle faulting failure, deviatoric stress induced dilatancy occurs. In both cases this commences at the onset of acoustic emissions. The mechanisms by which this occurs (both dilatancy and compaction) are shown to be largely inelastic, and thought to be due to energy absorbing intergranular and intragranular fracture and frictional sliding. At the transition from brittle faulting failure to cataclastic flow, pore volume change is due to applied mean stress alone; deviatoric stress has no effect on pore volume. It is thought that this is due to a cancelling-out of deviatoric stress induced dilatancy and compaction.

- ▶ The Skempton B co-efficient calculated from undrained hydrostatic compaction data varies with hydrostatic stress due to the deformation of different components of the rock (grains, cement) of different bulk moduli, (section 6.3.4.1.). Experimentally derived values of the B co-efficient have been compared against calculated *theoretical* and calculated *corrected* values from well known formulations. The results demonstrate the sensitivity of the formulations to the bulk moduli values adopted ( $K_u$ ,  $K_s$ , &  $K$ ), and to the relative compressibilities of the rock and the URV system. The B co-efficient correction factor required to account for the URV in this analysis was found to be  $\approx 1.55$ .
- ▶ Drained hydrostatic compaction of Darley Dale sandstone proved that no pore collapse occurs up to 450MPa hydrostatic pressure (section 6.3.3.3.). Total pore volume reduction as a function of confining pressure has been shown to be non-linear, and the elastic/inelastic components of deformation is 50/50 up to 300MPa hydrostatic stress, thereafter 70/30, - i.e the majority of deformation due to mean stress induced compaction up to 450MPa is elastic, fig. 6.3.4.2.b.
- ▶ Bulk moduli data and the above mentioned B co-efficient data have been used successfully to calculate pore volume changes due to drained hydrostatic compression, (section 6.3.4.2.). Again, careful selection of the bulk moduli data and B co-efficient correction factor proved paramount in the analysis. The results have implications for predicting poro-elastic behaviour of rocks under changing effective confining pressure conditions, i.e. for hydrocarbon recovery.
- ▶ Undrained triaxial stress conditions (confined fluid mass) have been shown to affect rock deformation through an increase in  $K_u$  upon initial deformation, and a decrease in stress drop (decreasing pore fluid pressure) during specimen yielding (pore and crack volume increase), section 6.2.4.2. This can promote cataclastic flow where otherwise brittle faulting failure would occur.

- ▶ A large URV under undrained conditions has been shown to affect deformation by decreasing any fluid pressure change caused by a changing pore and crack volume, (section 6.2.4.2.). This affect has been experimentally quantified using different URV's to yield an URV *correction factor* , of 1.29, (when URV = 2.5x specimen pore volume), see section 6.2.5.
- ▶ A servo-controlled fluid pressure intensifier has been integrated into a high pressure triaxial vessel to create equipment capable of controlling and monitoring confining pressure, pore fluid pressure, temperature, and axial stress & strain, and of monitoring acoustic emissions during triaxial deformation. This has allowed the volume of pores and cracks to be investigated as a function of stress (mean and deviatoric) and temperature and permitted the laboratory investigation reported here.
- ▶ Drained gypsum dehydration data (section 6.6.3.1.) have confirmed that a complicated interplay occurs between mechanisms controlling fluid expulsion,
  - (i) fluid pressure sensitive chemical dehydration rate,
  - (ii) effective confining pressure sensitive compaction assisted fluid expulsion, and
  - (iii) effective confining pressure sensitive permeability restricting fluid expulsion.

The details of this interaction require substantially more experimentation. Undrained triaxial deformation on dehydrating gypsum further highlights this interaction, and the increasing fluid pressure during dehydrating affects the stress/strain characteristics through the effective stress law.

- ▶ A high pore fluid pressure ( $\approx 300\text{MPa}$ , at  $20^\circ\text{C}$ ) has been shown to cause time dependent increase in pore volume at a rate of  $\approx 17\text{mm}^3/\text{hr}$ . during triaxial deformation, (section 6.4.3.1.). This rate is insufficient to effect laboratory triaxial deformation experiments which are conducted at a strain rate of  $10^{-5}/\text{s}^{-1}$ .

- ▶ Elevated temperatures up to 400°C have been shown to reduce the transitional confining pressure in Darley Dale sandstone by 1MPa/11°C, (section 6.5.4.1.). Temperature and pressure conditions corresponding to the critical point of water causes rocks under undrained triaxial conditions to respond as if conditions were drained, due to the large specific volume change of water which occurs between the specimen and the pressure transducer.
  
- ▶ Pore volumetry experimentation on low permeability rocks such as Penmaenmawr microgranodiorite proved difficult due to the large specimen strains incurred during dynamic failure, (section 6.5.4.2.). This affected jacket integrity and caused fluid leakages.

*In summary*, the equipment development programme proved successful although further developments have been identified which would improve the equipment further, (see section 7.2.). The experimental programmes undertaken using the equipment have elucidated the mechanisms occurring during dilatancy and compaction, and whether deviatoric or mean stress is responsible for these mechanisms in Darley Dale sandstone. The effect of heat and dehydrating minerals on deformation has been demonstrated, and a three dimensional representation of triaxial deformation pore volumetry data has been shown to be good a way of presenting the changing pore volume that occurs in a rock under a given stress path or field. Quantification of the 3-D surfaces has implications for the prediction of the poro-elastic response of rock under crustal stress conditions, and for the exact determination of the URV correction factor.

Overall, the work has shown how pore fluid volumetry can be used to monitor rock poro-elastic response to crustal stress and environmental conditions, and how subsequent experimental data can be used to establish poro-elastic properties of rock, which can then be used as a predictive tool for poro-elastic behaviour of rock under given stress conditions.

## 7.2. Future Work.

Each section within chapter 6 includes future work recommendations specific to that suite of experiments. The suggestion generally include; (i) expanding the experimental programme to more extreme conditions, and (ii) microscopy observational work to support (or otherwise) the conclusions already obtained.

Highlighted below are the most significant areas for future study.

- ▶ *Establish servo-control of the confining pressure intensifier.* This would allow control of both the effective mean stress and deviatoric stress, and for the precise determination of the effect of both of these stresses on poro-elastic behaviour of rock. This would also eliminate confining pressure surges causing AE peaks during hydrostatic tests, hence permit pore collapse to be better monitored.
- ▶ *Quantification of the 3-D surfaces* determined in section 6.4.3.4. This would allow the pore volume under any stress condition to be predicted. The difference in the equations for the undrained (involving effect of URV) and drained 3-D surfaces represents the URV correction factor. By determining the pore volume difference between these surfaces for any given stress condition, a correction factor for fluid expulsion under undrained conditions could be established and electronically incorporated into the pore fluid intensifier servo-controller system. Intensifier activation during undrained experimentation would then replace fluid expelled into the URV system, thus simulating constant fluid mass conditions.

Since the URV allows fluid flow from the specimen during experimentation, it simulates different degrees capping rock permeability in the crust. Rock poro-elasticity could theoretically be quantified by *three* environmental factors (assuming bulk moduli are constant), - mean stress, deviatoric stress, and capping rock

permeability. By relating the size of the URV (i.e. fluid expelled during undrained deformation) to capping rock permeability, an accurate attempt at predicting subsurface rock poro-elastic response under changing stress state is possible.

- ▶ *Microscopic observation* of deformed samples for the suites of experiments conducted in the study would verify;
  - (i) lack of pore collapse under drained hydrostatic loading up to 450MPa.
  - (ii) effect of cycling confining pressure on grain and grain fragment rearrangement leading to progressively reduced pore volume.
  - (iii) Verification of the effect mean stress and deviatoric stress induced damage during deformation.
  
- ▶ *Quantification of elastic and inelastic components of deformation* under mean and deviatoric stress. This would also (along with microscopy observations), determine more precisely the nature of the mechanisms occurring during deformation, leading to a better understanding of the processes of deformation in geological materials.
  
- ▶ Devise a means of *removing the effect of an URV* interactively during undrained triaxial deformation using the servo-controller to ensure that the *mass* fluid in the rock remains constant. Alternatively the URV could be eliminated by separating fluid in the intensifier from fluid in the specimen by a membrane strain gauge situated at the end cap; pressure change between that in the specimen and that controlled by the intensifier will be detected by strain on the membrane. See section 6.4.4. for more details.

## Appendix A.

### A.1. Calibration of Load Cell.

The actuator load cell was calibrated after a maintenance service using a certified *proof ring*. The ring was sited axially with the actuator and the load cell and an axial load applied. Proof ring strain was measured using a dial gauge (related to load from the calibration certificate), and the load cell reading was recorded from the servo controller. Fig A.1. shows the deviation between the actuator controller axial load reading and the proof ring axial load reading. This deviation is plotted against proof ring axial load reading. The largest error proved to be only 0.75%.

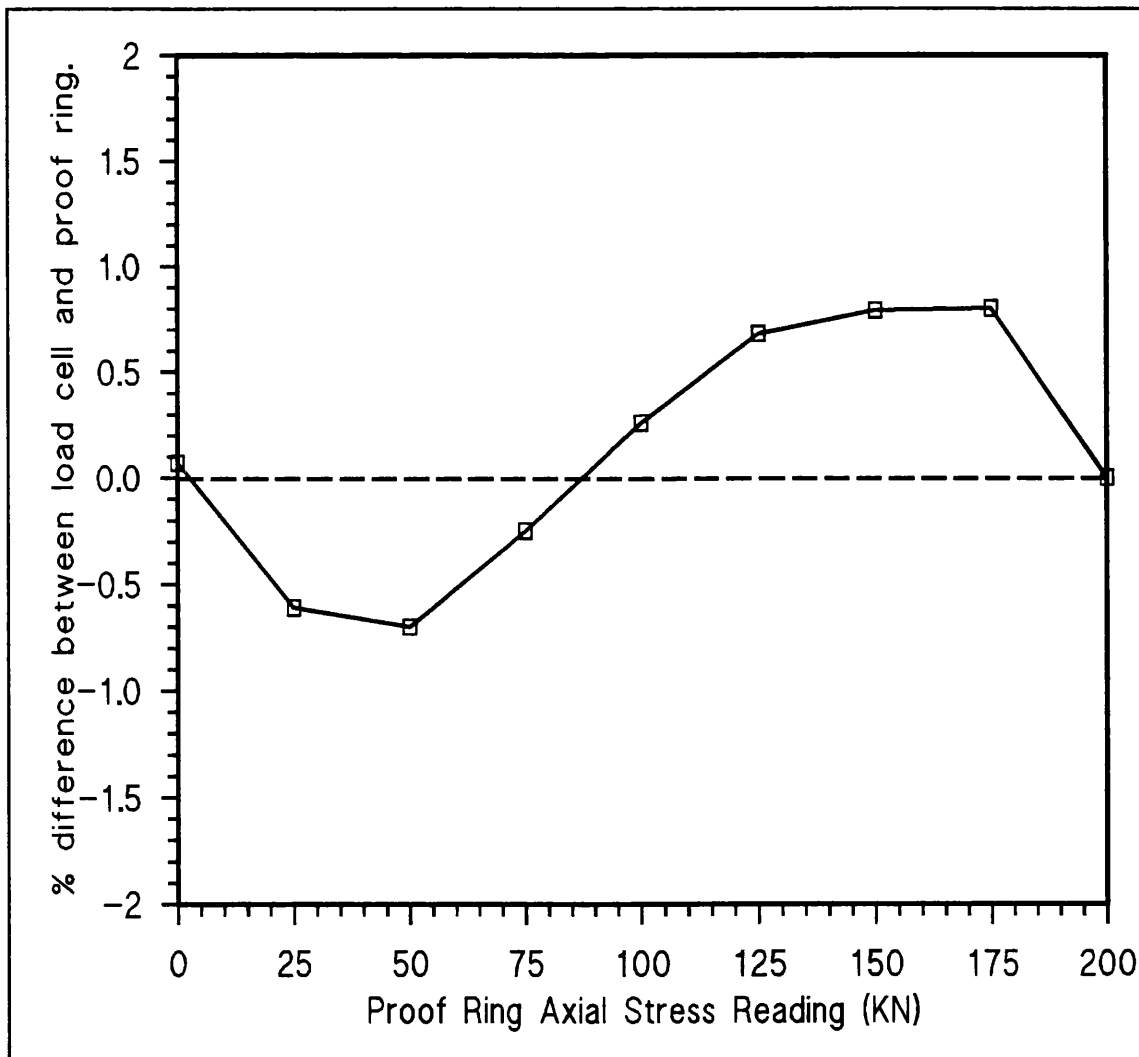


Fig. A.1. The deviation of load cell reading compared with proof ring axial stress reading in KN.

## **Appendix B.**

### **Equipment Development: Pore Fluid and P and S-wave Upper Ram.**

Following from the design objectives and constraints detailed in section 4.7.2., four alternative designs are presented here.

#### **Design 1: Internal Fluid Access Hole.**

Design 1 involves separating the high pressure pore fluid port from the piezo-electric transducer axially along the upper ram. At a position  $\approx 190\text{mm}$  above the transducer (and rock specimen), the diameter of the ram increases from 20mm to 27mm. At this point a high pressure port for 1/8" (1.58mm) tubing is centrally sited. The arrangement is similar to the pore fluid upper ram already employed. The port directs pore fluid into a thin ( $\approx 1.5\text{mm}$  I.D.) tube, bored off-vertical, leading to the platen. The bored tube arrives at the platen to one side of the piezo-electric transducer. A fluid distribution plate sits between the platen and the rock specimen to distribute the fluid evenly over the surface of the rock. An electrical wire serving the transducer runs through another tube bored *off-vertical* through the ram to arrive at one side of the 1/8" *hp* fluid port (190mm from specimen). The end-cap is constructed of a number of parts (similar to the existing arrangement) into which the transducer is fitted. By this design pore fluid is permanently separated from the transducer. The transducer wire passes to one side of the 1/8" port, to continue up the central bore of the piston. The port must necessarily be no further than  $\approx 190\text{mm}$  from the platen, or atmospheric pressure access to the lower chamber of the balanced ram system will be obstructed.

The problem with this design lies in the long narrow bored holes. Holes of this diameter and length (1.5mm diam. x 190mm), are very difficult to manufacture and align accurately. The internal finish of such bored holes is also difficult to control; scores on this surface might lead to sub-critical stress

corrosion crack growth. This work requires the employment of outside specialists.

### Design 2: Wave Guide System for P- and S-wave.

Design 2 involves siting the transducer 150mm axially along the ram and installing a *wave guide* to direct the P-/S-waves with minimal attenuation. The pore fluid arrangement is very similar to design 1. The advantage of this arrangement is the extra space provided by siting both pore fluid and elastic wave components away from the end-cap where the ram diameter is 27mm. The disadvantage of this design is the same as for design one; that of accurately guiding the drilling of the long thin holes and their internal finish. Again, the work requires the services of outside specialists.

### Design 3: Pulse Echo Technique.

In this design the upper ram supplies the pore fluid only, exactly as in the existing arrangement, although to an upgraded specimen diameter size of 20mm. The lower ram incorporates *two* piezo-electric transducers. One of the transducers for *transmitting* the P-/S-wave signal (manufactured from PZT - Lead Zirconate Titanate), and one for *receiving* the reflected wave (Lithium Niobate - gold faced with a resonant frequency of 1MHz). The different transducers are necessary because of the vastly differing performance between transducers depending on their function, Ayling (1991).

The problem with this arrangement concerns *ringing* of the receiving transducer due to the proximity of the transmitting transducer, thus masking the legitimate received wave. Ayling solved the problem of ringing of the receiving transducer when sited opposite the transmitting transducer by backing the transducers with tungsten loaded epoxy resin. Tungsten has similar acoustic impedance characteristics to the transducer (efficiently transferring wave energy from the transducer to the epoxy backing), whilst the epoxy has good energy absorption characteristics. A detailed

investigation into electronic filtering techniques is required to fully address the problem

#### Design 4: Pore Fluid/Transducer End-cap.

This arrangement involves siting both the PZT piezo-electric transducer and the pore fluid access channel at the 20mm diameter platen of the upper ram. This is illustrated in Fig B.a. Siting both transducer and pore fluid access path in the same zone is achieved by passing the wire for the transducer *inside* the high pressure tubing and having the fluid flow *around* the transducer.

The transducer sits centrally in the end-cap, 6mm from the rock specimen set in commercially available adhesive potting resin bonded to the end-cap (between cross-sections B and C'). The resin selected for this function balances a number of required physical characteristics; good adhesive strength, reasonable operating temperatures, adequate stiffness and vibration dampening. The heat and corrosion resistant wire for the transducer signal (1.0mm diameter) passes up the *centre* of the 1/8" (1.51mm I.D.), high pressure tubing. Pore fluid flows *around* the potted transducer, through 0.5mm diameter holes drilled through the platen, via a fluid distribution plate, to the rock specimen. The joints in the construction of the end-cap are sealed using high pressure "O" ring seals and the three separate components interlock with screw threads.

The 1/8" high pressure tube with transducer wire inside passes up the central 4mm bored hole of the piston to a redesigned *piston head block*. Here the wire and the fluid separate. The wire exits through a high pressure electrical seal (similar to the design used in the lower closure), whilst the pore fluid exits from a standard high pressure fitting. The arrangement of the *piston head block* is such that no load is applied to the *hp* tube whilst up to 200KN is applied to the piston.

The problem with this system concerns the availability of *hp* tubing of sufficient working pressure of  $\geq 400\text{MPa}$ , internal diameter of  $> 1\text{mm}$ , and

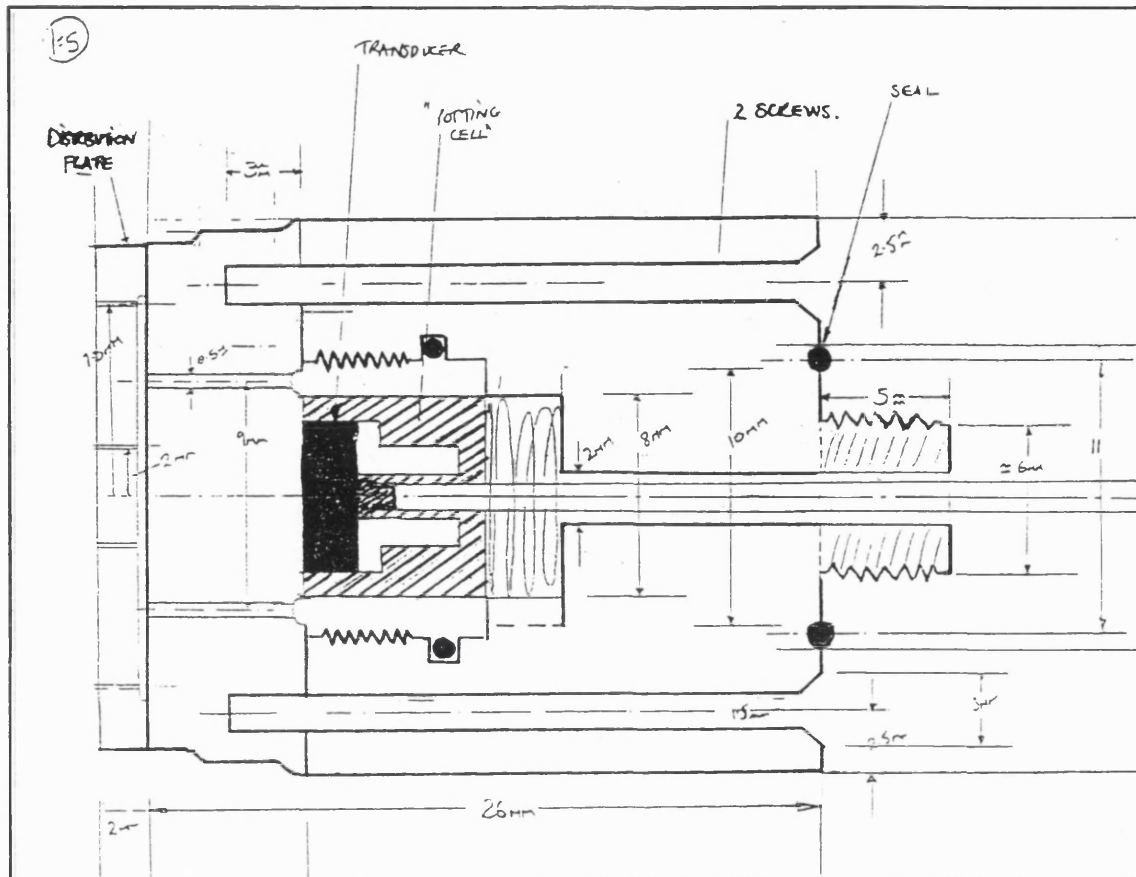


Fig. B.a. Design four - fluid and transducer sited in end-cap.

external diameter of  $<4\text{mm}$ . Current availability of *hp* tubing allows only 100MPa maximum working pressure if the dimensions are satisfied. A second restriction concerns maximum working temperature of the potting compound and electrical wire at  $120^\circ\text{C}$  and  $200^\circ\text{C}$  respectively.

These limitation restrict experimental limits to  $120^\circ\text{C}$  and 100MPa pore fluid pressure.

### Summary.

Of the four designs, the fourth received the most detailed appraisal during which a number of design limitations where uncovered. The proposal is, however, valid within the above mentioned constraints. For future development of the triaxial system, design number three deserves further attention and could well prove to be the best alternative.

## Appendix C.

### Equipment Development; Double Sealing Ring Lower End-cap.

The design for the double sealing ring lower ram is shown in fig. C.1.a. The main features of this component are given below.

- ▶ The end-cap between the platen and cross-section B is constructed from only two parts connected by two 2.5mm diameter screws. This contrasts with the previous design which was constructed of four parts. Improvement is gained by this with the elimination of numerous steel interfaces in the end-cap where confining pressure gas could enter the ram.
- ▶ The transducer is placed in a *well* inside the end-cap. The lower surface of the well is finished to a high standard for a good transducer/steel acoustic transfer, and *access channels* for emplacement and removal of the transducer are detailed, (hatched).
- ▶ Because the second sealing ring requires a minimum diameter of 17.5mm in order to achieve an interference seal with the copper jacket, the diameter of the end cap must be tapered back to 17mm from B-B to where it connects to the existing main body of the lower ram, (fig. C.a.).

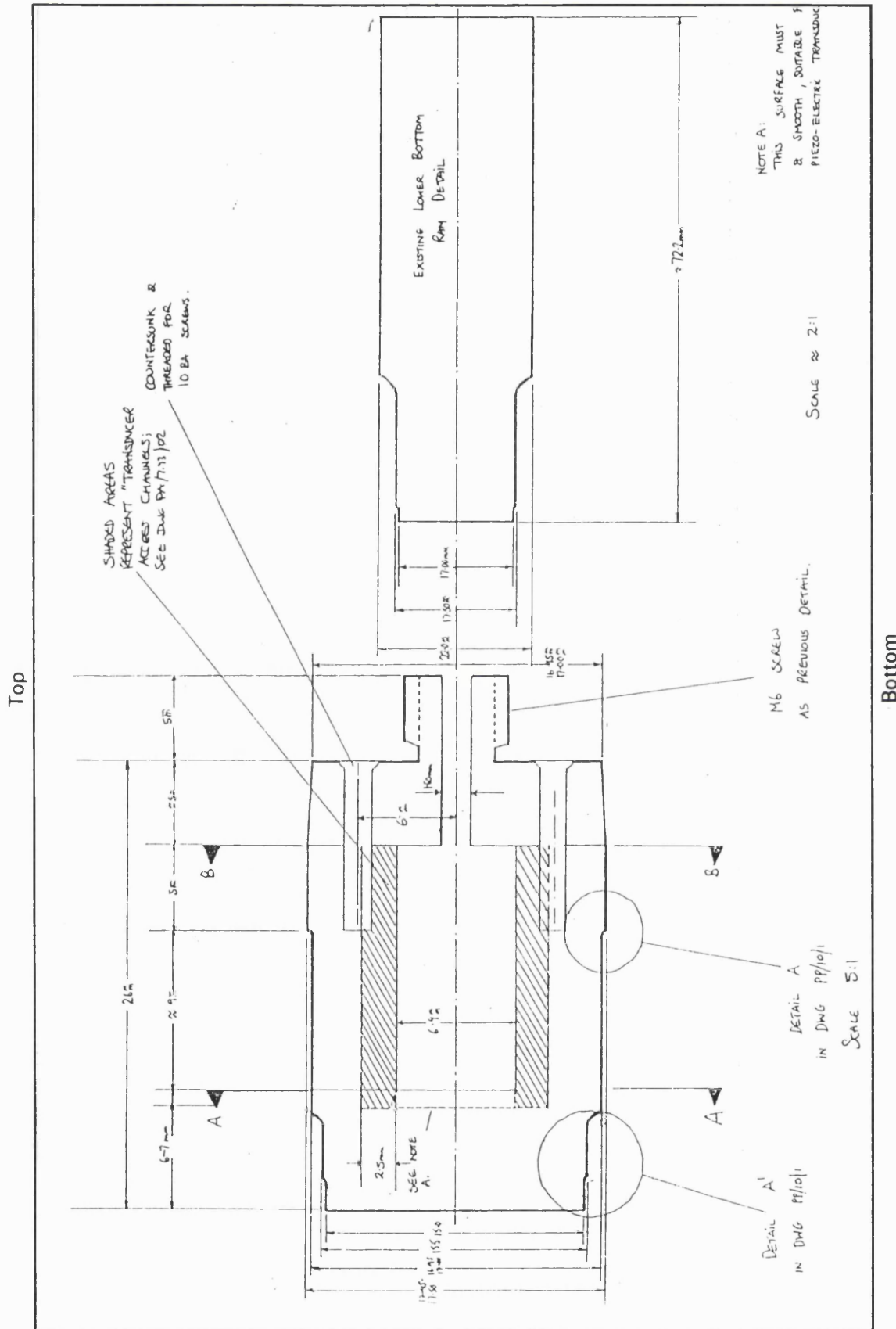


Fig. C.a. The double sealing ring lower ram. See text for details.

**List of References.**

**Aki, K. A., 1965.** Maximum Likelihood Estimate of  $b$  in the formula  $\log N = a - bM$  and its Confidence Limits. *Research Bulletin of the Earthquake Research Institute*. Vol 43, 1965, pp. 237-239.

**Ashby, M. F. & Hallam, S. D., 1986.** The Failure of Brittle Solids Containing Small Cracks under Compressive Stress States. *Acta Metall.*, Vol. 34, pp. 497-510, 1988.

**Atkinson, B. K., 1982.** Sub-critical Crack Propagation in Rocks: Theory, Experimental Results and Applications. *J. Struct. Geol.*, Vol. 4, pp. 41-56, 1982.

**Atkinson, B. K. & Meredith, P. G., 1987.** The Theory of Subcritical Crack Growth with Applications to Minerals and Rocks. In: *Fracture Mechanics in Rocks*. Atkinson, B. K. (ed.), Academic Press Geology Series, London, 1987.

**Ayling, M. R., 1991.** An Experimental Study of Physical Property Changes in Crustal Rocks Undergoing Triaxial Deformation. *Ph.D. Thesis*, University of London, 1991.

**Ayling M. R. et al., 1995a.** (Meredith, P. G. and Murrell, S. A. F.) Microcracking During Triaxial Deformation of Porous Rocks Monitored by Changes in Rock Physical Properties: I - Elastic Wave Propagation Measurements on Dry Rocks. *Tectonophysics - special edition - "The Role of Fluids in Rock Deformation"*, in press, 1995.

**Barber, D. J., 1990.** Regimes of Plastic Deformation. In: *Deformation Processes in Minerals and Rocks*. Barber, D. J., and Meredith P. G., (eds.), Urwin Hyman, London, 1990.

**Barber, D. J. & Meredith, P. G., 1990.** Deformation Processes in Minerals and Rocks. *Unwin Hyman*, London. 1990.

**Batzle, M. L., et al., 1980.** (Simmons, G., and Siegfried, R. W.). Microcrack Closure in Rocks under Stress: Part I. Direct Observations. *J. Geophys. Res.*, Vol. 85, pp. 7072-7090, 1980.

**Bernabé, Y. & Brace, W. F., 1990.** Deformation and Fracture of Berea Sandstone. *The Brittle-Ductile Transition in Rocks - The Heard Volume*, Duba, A. G., Durham, W. B., Handin, J. W. and Wang, H. F., (eds.), *Am. Geophys. Un. Monogr.* Vol. 56, pp. 91-101, Washington D. C., 1992.

**Bernabé, Y., et al., 1994.** (Fryer, D. T. and Shively, R. M.). Experimental Observations of the Elastic and Inelastic Behaviour of Porous Sandstones. *Geophys. J. Int.* Vol. 117, pp. 403-418, 1994.

**Biot, M. A., 1941.** General Theory of Three-Dimensional Consolidation. *Journal of Applied Physics.* Vol 12, pp. 155-164. 1941.

**Bishop, A. W., 1973.** The influence of an Undrained Change in Stress on the Observed Pore Pressure Response to an Undrained Change in Stress in Saturated Rock. *Géotechnique*, vol. 23, No. 3, pp.435-442, 1973.

**Bishop, A. W., 1976.** The influence of System Compressibility on the Observed Pore Pressure Response to an Undrained Change in Stress in Saturated Rock. *Géotechnique*, vol. 26, No. 2, pp.371-375, 1976.

**Blanpied, M. L., Lockner, D. A. & Byerlee, J. D., 1991.** *J. Geophys. Res.* Vol. 18, pp. 609-912, 1991.

**Blanpied, M. L. et al., 1992.** (Lockner, D. A., and Byerlee, J. D.). An Earthquake Mechanism based on Rapid Sealing of Faults. *Nature*, 358, pp. 574-576, 1992.

**Brace, W. F., 1971a.** Resistivity of Saturated Crustal Rocks to 40km Based on Laboratory Measurements. *Am. Geophys. Union Geophys. Monogr. Series*, Vol. 14, pp 243-255, 1971.

**Brace, W. F., 1977.** Permeability from Resistivity and Pore Shape. *J. Geophys. Res.*, Vol. 82, No. 23, pp. 3343-3349, 1977.

**Brace, W. F., 1978.** Volume Changes During Fracture and Frictional Sliding: A Review. *Pageoph*, Vol 116, pp. 603-614, 1978.

**Brace, W. F. & Bombolakis, E. G., 1963.** A Note on Brittle Crack Growth in Compression. *J. Geophys. Res.* Vol. 68, pp. 3709-3713, 1963.

**Brace, W. F. & Martin, R. J., 1968.** A Test of the Law of Effective Stress for Crystalline Rocks of Low Porosity. *Int. J. Rock Mech. Min. Sci.*, Vol 5, pp. 415-426, 1968.

**Brace W. F. et al., 1966.** (Paulding, B. W., Scholz, C.). Dilatancy and the Fracture of Crystalline Rocks. *J. Geophys. Res.* Vol. 77, Vol. 16, pp. 3939-3953, 1966.

**Brown, R. J. S. & Korrington, J., 1975.** On the Dependence of the Elastic Properties of a Porous Rock on the Compressibility of the Pore Fluid. *Geophysics*, Vol. 40, No. 4, pp.608-616, 1975.

**Bruhn, R. W., 1972.** A Study on the effects of pore pressure on the strength and Deformability of Berea Sandstone in triaxial compression: 3<sup>rd</sup>. Interim Rep. *U. S. Army Corps of Engineers, Missouri River Div.* Lab. No.64,493, Omaha, 1972.

**Carlson, R. L. & Ganghi, A. F., 1985.** Affect of Cracks on the Pressure Dependence of P-wave Velocities in Crystalline Rocks. *J. Geophys. Res.* Vol 90, No. B10, pp. 8675-8684, 1985.

**Carmichael, R. S., 1989.** CRC Practical Handbook of Physical Properties of Rock and Minerals. *CRC Press Inc.* ISBN 0-8493-3703-8.

**Cater, N. L., & Kirby, S. H., 1978.** Transient Creep and Semi-brittle behaviour of Crystalline Rocks. *Pure Appl. Geophys.*, Vol. 116, pp. 807-839, 1978.

**Chester, F. M., 1993.** (Evans, J. P. and Biegel, R. J.). Internal Structure and Weakening Mechanisms of the San Andreas "Fault. *J. Geophys. Res.*, Vol. 98, pp. 303-311, 1993.

**Cook, N. G. W., 1981.** Stiff Testing Machines, Stick Slip Sliding and the Stability of Rock Deformation. In: *Mechanical Behavior of Crustal Rocks - The Handin Volume*, 1981. ISBN 0-87590-024-0.

**Costin, L. S., 1983.** A Microcrack Model for the Deformation and Failure of Brittle Rock. *J. Geophys. Res.*, Vol. 88, pp. 9485-9492, 1983.

**Costin, L. S., 1985.** Damage Mechanics in the Post-Failure Regime. *Mech. Mat.* Vol. 4, pp. 149-160, 1985.

**Costin, L. S., 1987.** Time Dependent Deformation and Failure. In *Fracture Mechanics of Rock*, Atkinson, B. K. (ed.), pp. 167-215. London, Academic Press, 1987.

**Cox, S. F., 1993.** Low Friction During Sliding on Simulated Faults in Porous Quartz Sandstones at Hydrothermal Conditions. *Proc. Wkshp LXIII - The Mechanical Involvement of Fluids in Faulting*. USGS, National Earthquake Hazard Reduction Program. pp. 501-508, June 6-10, 1993, Menlo Park, CA. 1993

**Cox, S. J. D. & Meredith, P. G., 1993.** Microcrack Formation and Material Softening in Rocks Measured by Monitoring Acoustic Emissions. *Int. J. Rock Mech. Min. Sci. & Geomech. Abstr.* Vol. 30, pp. 11-24, 1993

**Das, S. & Scholz, C. H., 1981.** Theory of Time Dependent Rupture in the Earth. *J. Geophys. Res.*, Vol. 86, pp. 6039-6051, 1981.

**David, C. & Darot, M., 1989.** Permeability and Conductivity of Sandstones. In: *Rock at Great Depth*, Maury, V. & Fourmaintraux, D. (eds.). Balkema, pp 203-210, 1989.

**Dell'Angelo & Tullis, 1982.** Textual Strain Softening in Experimentally Deformed Aplite. *Trans Am. Geophys. Union*, vol 63, pp. 438, 1982.

**Dey, T. N., & Wang, C-Y., 1981.** Some Mechanisms of Microcrack Growth and Interaction in Compressive Rock Failure. *Int. J. Rock Mech. Min. Sci.*, Vol. 18, pp. 199-209, 1981.

**Dropek, R. K., Johnson, J. N. & Walsh, J. B., 1978.** The Influence of Pore Pressure on the Mechanical Properties of Keyanta Sandstone. *J. Geophys. Res.* Vol 83, No. B6, pp. 2817-2824, 1978.

**Edmond, O. & Murrell, S. A. F., 1973.** Experimental Observation on Rock Fracture at Pressures up to 7kbar and the Implications for Earthquake Faulting. *Tectonophysics*, Vol. 16, pp. 71-87, 1973.

**Edmond, J. M. & Paterson, M. S., 1972.** Volume Changes During the Deformation of Rocks at High Pressures. *Int. J. Rock Mech. Min. Sci.* Vol. 9, pp. 161-182, 1972.

**Fischer, G. J. & Paterson, M. S., 1989.** Dilatancy and Rock Deformation at High Temperatures and Pressures. *J. Geophys. Res.* Vol. 94, No. B12, pp. 17,607-17.617, 1989.

**Fischer, G. J. & Paterson, M. S., 1992.** Measurements of Permeability and Storage Capacity in Rocks During Deformation at High Temperature and Pressure. In: *Fault Mechanics and Transport Properties of Rock*. Evans, B. and Wong, T.-F. (eds.), Academic Press. 1992, ISBN 0-12-243780-2.

**Franklin, J. A. et al., 1979.** (Volger, U. W., Slavin, J., Edmond., J. M. and Bieniawski, Z. T.) Suggested Methods for Determining Water Content, Porosity, Density, Absorption and Related Properties and Swelling and Slake-

Durability Index Properties. *Int. J. Rock Mech. & Min. Sci. & Geom. Abstr.*, Vol. 16, No. 2, pp. 141-156, 1979.

Fonseka, G. M., Murrell, S. A. F. & Barnes, P., 1985. Scanning Electron Microscope and Acoustic Emission Studies of Crack Development in Rocks. *Int. J. Rock Mech. Min. Sci. & Geomech. Abstr.*, Vol. 22, No. 5, pp. 273-289, 1985.

François, D. & Wilshaw, T. R., 1968. The Effect of Hydrostatic Pressure on the Cleavage Fracture of Polycrystalline Materials. *J. Appl. Phys.*, Vol. 39, pp. 4170-4177, 1968.

Freiman, S. W. & Swanson, P. L., 1990. Fracture of Polycrystalline Ceramics. In: *Deformation Processes in Minerals, Ceramics and Rocks*, Barber, D. J., and Meredith P. G., (eds.), Urwin Hyman, London, 1990.

Frohlich, C. & Davis, S., 1993. Teleseismic *b*-value; or Much ado about 1.0. *Geophys. Res. Vol.* 98, pp. 631-644, 1993.

Glaser, S. D. & Nelson, P. P., 1989a. Characterisation of Acoustic Emission Waveforms Produced by Rock During Mode I and Mode II Crack Propagation. Conf. Paper, *Rock at Great Depth -Rock Mechanics and Rock Physics at great Depth*, Maury and Fourmaintraux (eds.), 1989, Balkema, Rotterdam. Vol. I, pp. 249-256.

Glaser, S. D. & Nelson, P. P., 1989b. Characterisation of Acoustic Emission Waveforms Produced by Rock Fracture During Mode I and Mode II Loading. Conf. Paper, *Proc. Rock. Mechanics as a Guide for Efficient Utilization of Natural Resources*. Khair (ed.), Balkema, Rotterdam, 1989. (find rest of reference)

Glover, P. J. W. et al., 1995. (Baud, P., Darot, M., Meredith, P. G., LeRavelec, M., Zoussi, S., and Reuschlé, T.) Alpha-Beta Phase Transition Monitored Using Acoustic Emissions. *Geophys. J. Int.*, Vol. 112, pt. 3, pp. 775-782, 1995.

**Green, D. H. & Wang H. F., 1986,** Fluid Pressure Response to Undrained Compression in Saturated Sedimentary Rock. *Geophysics*, Vol. 51, No. 4, pp. 948-956, 1986.

**Griggs, D. T., Turner, F. J. & Heard, H. C., 1960.** Deformation of Rocks at 500°C to 800°C. In *Rock Deformation, Geol. Soc. Am. Mem. 79*, pp. 39-104, 1960.

**Guéguen, Y. & Palciauskas, V., 1994.** Introduction to the Physics of Rocks. Princeton University Press, ISBN 0-691-03452-4.

**Gueguen, Y., Reuschlé, T. & Darot, M., 1990.** Single Crack Behaviour and Crack Statistics. In: *Deformation Processes in Minerals, Ceramics and Rocks*, Barber, D. J., and Meredith P. G., (eds.), Urwin Hyman, London, 1990.

**Hallam, S. D. & Ashby, M. F., 1990.** Compressive Brittle Fracture and the Construction of Multi-axial Failure Maps. In: *Deformation Processes in Minerals, Ceramics and Rocks*, Barber, D. J. & Meredith, P. G. (eds.), Unwin Hyman Ltd., London, 1990.

**Handin et al. 1963.** - See page 303.

**Hatton, C. G., 1992.** Structure and Seismic Signature of Subsidiary Damage around Natural and Artificial Fractures. Ph.D. Thesis, University of Edinburgh, (1992).

**Heard, H. C., 1960.** Transition from Brittle Fracture to Ductile Flow in Solenhofen Limestone as a Function of Temperature, Confining Pressure, and Interstitial Fluid Pressure. In: *Rock Deformation*. Griggs, D. & Handin, J. (eds.), Geol. Soc. Am., Memoir 79, pp. 193-226, 1960.

**Heard, H. C. & Page, L., 1982.** Elastic Moduli, Thermal Expansion, and Inferred Permeability of Two Granites to 350°C and 55MPa. *J. Geophys. Res.* vol 87, No. B11, pp. 9340-9348, 1982.

**Holcomb, D. J., 1993.** Observations of the Kaiser Effect under multiaxial Stress States: Implications for its Use in Determining In-situ Stress. *Geophys. Res. Lett.*, requires full reference.

**Holcomb, D. J. & Costin L. S., 1986.** Detecting Damage Surfaces in Brittle Materials Using Acoustic Emissions. *J. App. Mech.* Vol. 53, pp. 536-544, 1986.

**Horii, H. & Nemat-Nasser, S., 1986.** Brittle Failure in Compression: Splitting, Faulting and the Brittle-Ductile Transition. *Phil Trans R. Soc. Lond. Ser. A.*, Vol. 319, p 337-374, 1986.

**Hubber, M. K. & Rubey, W. W., 1959.** Role of Fluid Pressure in the Mechanics of Overthrust Faulting. *Geol.Soc. Am. Bull.*, Vol. 70, pp. 115-166, 1959.

**Hudson, J. A., Couch, S. L. & Fairhurst, C., 1972.** Soft, Stiff and Servo-controlled Testing Machines: a Review with Reference to Rock Failure. *Eng. Geol.* 6, pp. 155-189, 1972.

**Ingraffea, A. R., 1987.** Theory of Crack Initiation and Propagation in Rock. In: *Fracture Mechanics in Rocks.* Atkinson, B. K. (ed.), Academic Press, 1987.

**Ismail, I. H. A., 1974.** Experimental Studies of Mechanical Instabilities in Rocks. Ph.D. thesis, University of London, 1974.

**Ismail, I. A. H. & Murrell, S. A. F., 1976.** Dilatancy and the Strength of Rocks Containing Pore Water under Undrained Conditions. *Geophys. J. R. astr. Soc.*, Vol. 44, pp. 107-134, 1976.

**Ismail, I. A. H. & Murrell, 1989.** The Effect of Confining Pressure on Stress-drop in Compressive Rock Fracture. *Tectonophysics*, Vol. 175, pp. 237-248, 1989.

**Jaeger, J.C. & Cook, N. G. W., 1979.** Fundamentals of Rock Mechanics, Third Edition. *Chapman and Hall*, London. 1979.

**Jones, C., 1989.** An experimental Study of the Relationship Between P-wave Velocity, Acoustic Emission and Deformation in Rocks under Simulated Crustal Conditions. Ph.D. Thesis, University of London, 1974.

**Jones, C. & Murrell, S. A. F., 1989.** Acoustic Compressional Wave Velocity and Dilatancy in Triaxially Stressed Rock. Conf. Paper, *Rock at Great Depth - Rock Mechanics and Rock Physics at great Depth*, Maury and Fourmaintraux (eds.), 1989, Balkema, Rotterdam. Vol. I, pp. 241-247.

**Kemeny, J. M. & Cook, N. G. W., 1987.** Crack Models for Failure of Rocks in Compression. *Proc. 2<sup>nd</sup>. Int. Conf. on Constitutive Laws for Engineering Materials*, Tuscon, Arizona.

**Ko, S-c, 1993.** Dehydration-induced Pore Fluid Pressure Anomolies and the Weakening of Rocks. *Ph.D. Thesis*, Swiss Federal Institute of Technology Zürich, 1993.

**Kranz, R. L., 1983.** Microcracks in Rocks: A Review. *Tectonophysics*, Vol. 100, pp. 449-480, 1983.

**Lawn, B. R. 1993.** Fracture of Brittle Solids, (2<sup>nd</sup>. ed.). *Cambridge University Press*. Cambridge, 1993.

**Locker, D. A., 1993.** The Role of Acoustic Emissions in the Study of Rock Fracture. *Int. J. Rock Mech. Min. Sci. & Geomech Abstr.* Vol. 30, No. 7, pp. 883-899, 1993.

**Lockner, D.A. & Byerlee, J.D., 1977.** Acoustic Emissions During Fluid Injection into Rock. In *Proc. First Conf. on Acoustic Emissions/Micro-seismic Activity in Geological Structures and Materials*. Hardy & Leighton (eds.), pp. 87-98, Tech Publications, Germany, 1977.

**Lockner, D. A. et al., 1992.** (Byerlee J. D., Kuksenko, V., Ponomarev, A. and Sidorin, A.). Observations of Quasi-static Fault Growth from Acoustic Emissions. In: *Fault Mechanics and Transport Properties of Rocks*, Evans, B., & Wong, T-f., (eds.), Academic Press, London, 1992.

**Main, I. G. et al., 1989.** (Meredith, P. G., Jones, C.). A Reinterpretation of the Precursory Seismic *b*-value Anomoly from Fracture Mechanics. *Geophysical Journal*, Vol. 96, pp. 131-138, 1989.

**Main, I. G. et al., 1990.** (Meredith, P. G., Sammonds, P. R. and Jones, C.). Influence of Fractal Flaw Distribution on Rock Deformation in the Brittle Field. In: *Deformation Mechanisms, Rheology and Tectonics*. Knipe, R. J. and Rutter E. H. (eds.), Geol Soc. Spec. Pub., No. 54, pp. 71-79, 1990.

**McConnel, J. D. C., Astill, D. M. and Hall, P. L., 1987.** The Pressure Dependence of the Dehydration of Gypsum to Bassanite. *Minerogical Magazine*, Vol. 51, pp. 453-457, 1987.

**Meredith, P. G. & Atkinson, B. K., 1983.** Stress Corrosion and Acoustic Emissions During Tensile Crack Propagation in Whin Sill Dolerite and other Basic Rocks. *Geophys. J. R. Astr. Soc.*, Vol. 75, pp.1-21, 1983.

**Meredith, P. G., Main, I. & Jones, C. J., 1990.** Temporal Variations in Seismicity During Quasi-static and Dynamic Rock Failure. *Tectonophysics*, Vol 175, pp.249-268, 1990.

**Mesri, G., Adachi, K. & Ullrich, C. R., 1976.** Pore Pressure Response in Rock to Undrained Change in All-round Stress. *Geotech.* Vol. 26, pp.317-330, 1976.

**Mogi, K., 1962c.** Magnitude-Frequency Relation for ELastic Shocks Accompanying Fractures of Various Materials and Some Related Problems in Earthquakes, (2nd. paper). *Bull Eathquake Res. Inst.*, Vol. 40, pp. 831-853, 1962.

**Muir Wood, R., 1994.** Earthquakes, Strain-cycling and the Mobilisation of Fluids. In: *Geofluids; Origins, Migration and the Evolution of Fluids in Sedimentary Basins*, Parnell, J, (ed.), Geol. Soc. Spec. Publ. No. 78, pp. 85-98, 1994.

**Murrell, S. A. F., 1963.** A Criterion for Brittle Fracture of Rocks and Concrete under Triaxial Stress, and the Effect of Pore Fluid Pressure on the Criterion. In; *Rock Mechanics*. Fairhurst, C., (ed.), Proc. 5<sup>th</sup> Symp. Rock Mech., New York: Pergammon Press, pp. 563-577.

**Murrell, S. A. F., 1965.** The Effect of Triaxial Stress System on the Strength of Rocks at Atmospheric Temperatures. *Geophys. J. R. Astron. Soc.* Vol. 10, pp. 231-281, 1965.

**Murrell, S. A. F., 1985.** Aspects of Relationships Between Deformation and Prograde Metamorphism that Causes Evolution of Water, In: *Metamorphism Reactions: Kinetics, Textures, and Deformation*. Thompson, A. B., & Rubie, D. C. (eds.), New York, Springer-Verlang, pp. 211-241, 1985.

**Murrell, S. A. F., 1989.** General Report: The Measurement of the Properties at Great Depth of Rocks and Rock Masses. Conf. Paper, *Rock at Great Depth - Rock Mechanics and Rock Physics at great Depth*, Maury and Fourmaintraux (eds.), 1989, Balkema, Rotterdam. Vol. III, pp. 1219-1226.

**Murrell, S. A. F., 1990.** Brittle-to-Ductile Transitions in Polycrystalline Non-metallic Materials. In: *Deformation Processes in Minerals, Ceramics and Rocks*, Barber, D. J., and Meredith P. G., (eds.), Urwin Hyman, London, 1990.

**Murrell, S. A. F., & Chakravarty, S., 1973.** Some New Rheological Experiments on Igneous Rocks at Temperatures up to 1120°C. *Geophys. J. R. Astr. Soc.*, vol. 34, pp. 211-251, 1973.

**Murrell, S. A. F. & Digby, P.J., 1970.** The Theory of Brittle Fracture Initiation under Triaxial Stress Conditions. *J. Geophys. J. R. Astron. Soc.* Vol. 19, pp. 309-334; II *ibid*, pp. 499-512, 1970.

**Murrell, S. A. F. & Ismail, I. A. H., 1976a.** The Effect of Decomposition on the Mechanical Properties of Rocks at High Pressures and Temperatures. *Tectonophysics*, Vol. 31, pp. 207-258, 1976.

**Murrell, S. A. F. & Ismail, I. A. H., 1976b.** The Effect of Temperature on the Strength at High Confining Pressure of Granodiorite Containing Free Water and Chemically-Bound Water. *Contrib. Miner. Petrol.* Vol 55, pp. 317-330, 1976.

**Nur, A. & Byerlee, J. D., 1971.** An Exact Effective Stress Law for Elastic Deformation of Rock with Fluids. *J. Geophys. Res.* Vol. 76, pp. 6414-6419, 1971.

**Obert, L. & Duvall, W., 1942.** Use of Subaudible Noise for Prediction of Rockbursts. U.S. Bur. Mines Rept. Invest. 3634, 13 pp., 1942.

**Ollson, W. & Peng, S., 1976.** Microcrack Nucleation in Marble. *Int. J. Rock Mech. & Min. Sci.*, Vol. 18, pp. 53-59, 1976.

**Paterson, M. S., 1978.** Experimental Rock Deformation - *The Brittle Field*, Springer-Verlag, 1978. ISBN 3 540 08835 0.

**Page, L. & Heard, H. C., 1981.** Elastic Moduli, Thermal Expansion and Inferred Permeability of Climax Quartz Monzonite and Sudbury Gabbro to 500°C and 55MPa. *Proc. Symp. Rock Mech.* 22., pp. 97-104, 1981.

**Potter, J. M., 1978.** Experimental Permeability Studies at Elevated Temperature and Pressure in Granitic Rocks, *Rep. LA-7224-T*, Los Alamos Natl. Lab., Los Alamos, N.M., 1978.

**Quist, A. S. & Marshall, W. L., 1968.** Electrical Conduction of Aqueous Sodium Chloride Solution from 0°C to 800°C and at Pressures to 4000bar. *J. Phys. Chem.*, Vol. 72, p. 684, 1968.

**Read, M. D. et al., 1989.** (Meredith, P.G., Murrell, S.A.F.). Permeability Measurement Techniques under Hydrostatic and Deviatoric Stress Conditions. Conf. Paper, *Rock at Great Depth - Rock Mechanics and Rock Physics at great Depth*, Maury and Fourmaintraux (eds.), 1989, Balkema, Rotterdam. Vol I, pp. 211-217.

**Read, M. D. et al., 1995.** (Ayling, M. R., Meredith, P. G. and Murrell, S. A. F.) Microcracking During Triaxial Deformation of Porous Rocks Monitored by Changes in Rock Physical Properties: II - Pore Volumetry and Acoustic Emissions Measurements on Water Saturated Rocks. *Tectonophysics - special edition - "The Role of Fluids in Rock Deformation*, in press, 1995.

**Rist, M. A. et al., 1991.** (Sammonds, P. R. Murrell, S. A. F.) Strain Rate Control During Deformation of Ice: An Assessment of the Performance of a New Servo-controlled Triaxial Testing System. *Cold Regions Science and Technology*, Vol. 19, pp. 189-200, 1991.

**Rutter, E. H., 1972a.** Effect of Strain Rate Changes on the Strength and Ductility of Solenhofen Limestone at Low Temperatures and Confining Pressures. *Int. J. Rock Mech. Min. Sci.*, Vol. 9, pp. 183-189, 1972.

**Sammis, C. G. & Ashby, M. F., 1986.** The Failure of Brittle Porous Solids under Compressive Stress States. *Acta Metall.* Vol. 34, pp. 511-526, 1986.

**Sammonds, P. R. et al., 1989.** (Ayling, M.R., Meredith, P.G., Murrell, S.A.F., Jones, C.). A Laboratory Investigation of Acoustic Emissions and Elastic Wave Velocity Changes During Rock Failure under Triaxial Stresses. Conf. Paper, *Rock at Great Depth - Rock Mechanics and Rock Physics at great Depth*, Maury and Fourmaintraux (eds.), 1989, Balkema, Rotterdam. Vol. 1, pp. 233-240.

**Sammonds, P. R., Meredith, P. G. & Main, I. G., 1992.** Role of Pore Fluids in the Generation of Seismic Precursors to Shear Fracture. \*\*\*\*\*

**Sammonds, P. R., et al., 1994.** (Meredith, P. G., Gomez, J. and Main, I.) The Interaction Between Pore FLuid Pressure Changes and Crack Damage Evolution in Rocks and Sunsurface Rock Structures Modelled from Acoustic Emission Data. *Journal of Acoustic Emissions*, Vol. 13, No. 1/2, pp. 521-528, 1994.

**Savage, J. C., 1972.** Relation of Corner Frequency to Fault Dimensions. *J. Geophys. Res.*, Vol. 77, pp. 3788-3795, 1972.

**Savanick, G. A. & Johnson, D. I., 1974.** Measurements of the Strength of Grain Boundaries in Rock. *Int. J. Rock Mech. Min. Sci. & Geomech. Abstr.* , Vol. 11, pp. 173-180, 1974.

**Scholz, C. H., 1968a.** Microfracturing and the Inelastic Deformation of Rocks in Compression. *J. Geoph. Res.* Vol. 73, No. 4 pp. 1417-1432, 1968.

**Scholz, C. H., 1968b.** The Frequency-Magnitude Relation of Microfracturing in Rock and its Relation to Earthquakes. *Bull. Seismol. Soc. Am.*, Vol. 58, pp. 399-415, 1968.

**Scholz, C. H., 1968c.** Experimental Study of the Fracturing Process in Brittle Rock. *J. Geoph. Res.* Vol. 73, No. 4 pp. 1447-1454, 1968.

**Scholz, C. H., 1992.** Earthquakes - Weakness amidst Strength. *Nature*, Vol. 359, pp. 677-678.

**Sibson, R. H., et al., 1975.** (Moore, Mc. M. and Rankin, A. H.). Seismic Pumping - A Hydrothermal Fluid Transport Mechanism. *J. Geol. Soc. Lond.*, Vol. 131, pp. 653-659, 1975.

**Skempton, A. W. 1954.** The Pore Pressure Co-efficients A & B. *Geotechnique*, Vol. 4, No. 4, pp. 143-147, 1954.

**Sleep, N. H. & Blanpied, M. L., 1992.** Creep, Compaction and the Weak Rheology of Major Faults. *Nature*, 359, pp. 687-692, 1992.

**Sondergeld, C. H., & Estey, L. H. 1984.** Source Mechanisms and Microfracturing During Uniaxial Cycling of Rock. In: *Third Conf. on Acoustic Emissions/Micro-seismic Activity in Geol. structures*. Hardy and Leighton (eds.), pp. 131-145, Trans Tech Publications, Germany, 1984

**Spetzler, H. et al., 1974.** (Scholz, C. H. and Lu, C-p, J.). Strain and Creep Measurements on Rocks by Holographic Interferometry, *Pure and Appl. Geophys.*, Vol. 112, p. 571, 1974.

**Stevens, J. D. & Holcomb, D. J., 1980.** A Theoretical Investigation into the Sliding Crack Model of Dilatancy. *J. Geophys. Res.*, Vol. 85, pp. 7091-8000, 1980.

**Stuart, C. E., 1992.** Evolution of Anisotropic Microcrack Damage in Cyclically Stressed Rock, Charaterised by Comtemperaneous Acoustic Emission and Elastic Wave Velocity Measurements. *Ph.D. Thesis*, University of London, 1992.

**Stuart, C. E., et al., 1993.** (Meredith, P. G. M., Murrell, S. A. F. and Munster, J. G. van). Anisotropic Crack Damage and Stress-Memory Effect in Rocks under Triaxial Loading. *Int. J. Rock Mech. Min. Sci.* Vol. 30, No. 7, pp. 937-941, 1993.

**Swan, G., 1975.** Observations of Crack Propagating in Rock Plates. *Int. J. Rock Mech. Min. Sci.*, Vol. 12, pp. 329-334, 1975.

**Swanson, P. L., 1987.** Tensile Fracture Resistance Mechanisms in Brittle Polycrystalline Materials: an Ultrasonic and *insitu* Microscopy Investigation. *J. Geophys. Res.* Vol. 92, pp. 8015-8036, 1987.

**Tapponier, P. & Brace, W. F., 1976.** Development of Stress Induced Microcracks in Westerly Granite, *Int. J. Rock Mech. Min. Sci.* Vol. 13, p. 103, 1976.

**Todd, T. P. 1973.** Effect of Cracks on the Elastic Properties of Low Porosity Rocks. Ph.D. Thesis, Mass. Inst. Tech. Cambridge, Mass.

**Tóth, J., 1963.** A Theoretical Analysis of Ground water Flow in Small Drainage Basins. *Journal of Geophysical Research*, Vol 68, pp.4795-4812, 1963.

**Tullis, J., 1990.** Experimental Studies of Deformation Mechanisms and Microstructures in Quartzo-feldspathic Rocks. In: *Deformation Mechanisms in Minerals, Ceramics and Rocks*, Barber, D. J. & Meredith P. G. (eds.), Urwin Hyman, London, 1990.

**Walsh, J. B., 1965.** The Effect of Cracks on the Uniaxial Elastic Compression of Rocks. *J. Geophys. Res.* Vol. 70, pp. 399-411, 1965.

**Walsh, J. B., 1981.** Effect of Pore Pressure and Confining Pressures on Fracture Permeability. *Int. J. Rock Mech. Min. Sci. & Geomech. Abstr.* Vol. 18, pp. 429-435, 1981.

**Zhang, J. et al., 1990.** Micromechanics of Pressure Induced Grain Crushing in Porous Rocks. *J. Geophys. Res.* Vol. 95, No. B1, pp 341-352, 1990.

**Zoback, M. D. & Byerlee, J. D., 1975a.** Permeability and Effective Stress. *Bull. Am. Assoc. Petrol. Geol.*, Vol. 59, pp. 154-158, 1975.

N.B.

**Handin, J. et al., 1963.** (Hagar, J. R., Friedman, M. and Feather, J. N.) Experimental Deformation of Sedimentary Rocks under Confining Pressure: Pore Pressure Tests. *Bull. Am. Assoc. Petrol. Geol.*, Vol. 47, No. 5, pp. 717, 1963.